

**ANODE CATALYST DEVELOPMENT FOR LOW-TEMPERATURE  
FUEL CELLS:  
FUNDAMENTALS AND SYNTHESIS**

by

Jie Zheng

A dissertation submitted to the Faculty of the University of Delaware in partial fulfillment of the requirements for the degree of Doctor of Philosophy in Chemical Engineering

Winter 2016

© 2016 Jie Zheng  
All Rights Reserved

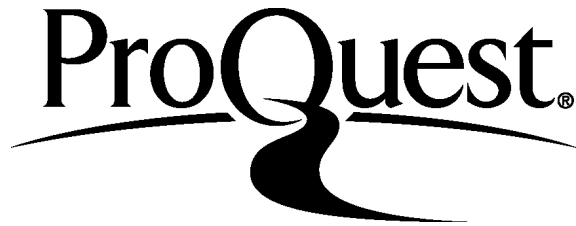
ProQuest Number: 10055793

All rights reserved

INFORMATION TO ALL USERS

The quality of this reproduction is dependent upon the quality of the copy submitted.

In the unlikely event that the author did not send a complete manuscript and there are missing pages, these will be noted. Also, if material had to be removed, a note will indicate the deletion.



ProQuest 10055793

Published by ProQuest LLC (2016). Copyright of the Dissertation is held by the Author.

All rights reserved.

This work is protected against unauthorized copying under Title 17, United States Code  
Microform Edition © ProQuest LLC.

ProQuest LLC.  
789 East Eisenhower Parkway  
P.O. Box 1346  
Ann Arbor, MI 48106 - 1346

**ANODE CATALYST DEVELOPMENT FOR LOW-TEMPERATURE  
FUEL CELLS:  
FUNDAMENTALS AND SYNTHESIS**

by

Jie Zheng

Approved: \_\_\_\_\_  
Abraham M. Lenhoff, Ph.D.  
Chair of the Department of Chemical and Biomolecular Engineering

Approved: \_\_\_\_\_  
Babatunde A. Ogunnaike, Ph.D.  
Dean of the College of Engineering

Approved: \_\_\_\_\_  
Ann L. Ardis, Ph.D.  
Interim Vice Provost for Graduate and Professional Education

I certify that I have read this dissertation and that in my opinion it meets the academic and professional standard required by the University as a dissertation for the degree of Doctor of Philosophy.

Signed:

---

Yushan Yan, Ph.D.  
Professor in charge of dissertation

I certify that I have read this dissertation and that in my opinion it meets the academic and professional standard required by the University as a dissertation for the degree of Doctor of Philosophy.

Signed:

---

Bingjun Xu, Ph.D.  
Professor in charge of dissertation

I certify that I have read this dissertation and that in my opinion it meets the academic and professional standard required by the University as a dissertation for the degree of Doctor of Philosophy.

Signed:

---

Raul F. Lobo, Ph.D.  
Member of dissertation committee

I certify that I have read this dissertation and that in my opinion it meets the academic and professional standard required by the University as a dissertation for the degree of Doctor of Philosophy.

Signed:

---

Feng Jiao, Ph.D.  
Member of dissertation committee

I certify that I have read this dissertation and that in my opinion it meets the academic and professional standard required by the University as a dissertation for the degree of Doctor of Philosophy.

Signed:

---

Hansan Liu, Ph.D.  
Member of dissertation committee

## ACKNOWLEDGMENTS

First of all, I would like to express my sincere gratitude to my Ph.D. advisors Prof. Yushan Yan and Prof. Bingjun Xu for their excellent guidance and mentorship throughout my Ph.D. studies. The “VISA-PhD” (which is short for vision, innovation, speed, accuracy, passion, humility and discipline) philosophy Dr. Yan shared with us from the first day we joined his group has been an important guiding principle for my Ph.D. life. What I have learned from them both research-wise and life-wise will be beneficial for the rest of my life.

I would also like to thank my committee members Prof. Raul Lobo, Prof. Feng Jiao and Dr. Hansan Liu for their useful suggestions and feedback on my research.

My special thanks goes to Dr. Wenchao Sheng who trained me the techniques of performing electrochemical measurements and shared with me knowledge of electrochemistry. I would like to thank Dr. Zhongbin Zhuang for all the discussions we have for the progress of my research. In addition, I am grateful for the support and the good research atmosphere provided by all my other lab members from both Yan and Xu groups, including Shuang Gu, Qianrong Fang, Laj Xiong, Kurt Jensen, Yanqi Zhang, Bingzi Zhang, Junhua Wang, Yun Zhao, Qian Xu, Robert Kasper, Melissa Gettel, Shaun Alia, Ke Gong, Mariah Woodroof, Xiaoya Ma, Andrew Tibbits, Marco Dunwell, Stephen Giles, Shuyuan Zhou, Mingchuan Luo, Minrui Gao, Jun Jiang, Jianyu Cao, Brian Murphy, Matthew Cilkey, Jared Nash, Hao Wang, Hongxia Guo and Yan Wang.

I would like to thank Dr. Piotr Zelenay from Las Alamos National Lab for useful discussion and suggestions, Dr. David Cullen from Oka Ridge National Lab for the

transmission electron microscopy characterization and Robert Forest for the X-ray photoelectron measurement for one of my projects.

I would also like to extend my thanks to my fellow friends in University of California, Riverside, especially Charles Cai, Gen Yin and Jia Fu, for their continuous encouragement and being good friends.

Most importantly, I would like to give my biggest thanks to my parents, to whom this dissertation is dedicated, for their unconditional love and support throughout all the years.

Finally, I would like to thank the Fuel Cell Technologies program and ARPA-E program of U.S. Department of Energy and University of Delaware for funding my Ph.D. research and American Chemical Society for permitting me to reprint the following publications:

Zheng, J.; Zhuang, Z.; Xu, B.; Yan, Y. Correlating Hydrogen Oxidation/Evolution Reaction Activity with the Minority Weak Hydrogen-Binding Sites on Ir/C Catalysts, *ACS Catalysis* 2015, 4449, and Zheng, J.; Cullen, D. A.; Forest, R. V.; Wittkopf, J. A.; Zhuang, Z.; Sheng, W.; Chen, J. G.; Yan, Y., Platinum–Ruthenium Nanotubes and Platinum–Ruthenium Coated Copper Nanowires As Efficient Catalysts for Electro-Oxidation of Methanol, *ACS Catalysis* 2015.

## TABLE OF CONTENTS

LIST OF TABLES .....	xi
LIST OF FIGURES .....	xiii
ABSTRACT .....	xxiv

### Chapter

1	INTRODUCTION .....	1
1.1	Fuel Cells.....	1
1.1.1	H <sub>2</sub> -Fueled Fuel Cells: PEMFC vs. HEMFC .....	4
1.1.2	Direct Methanol Fuel Cells .....	8
1.2	Hydrogen Oxidation Reaction .....	9
1.2.1	Reaction Mechanisms.....	9
1.2.2	Hydrogen Binding Energy (HBE) as the Descriptor for HOR Activity .....	12
1.2.3	Kinetic Study of HOR/HER .....	15
1.3	Methanol Oxidation Reaction.....	17
1.4	Structure of Current Dissertation.....	20
2	CORRECTING DIFFUSION LIMITATION IN ROTATING DISK ELECTRODE MEASUREMENT OF HYDROGEN OXIDATION/EVOLUTION REACTION KINETICS .....	22
2.1	Introduction .....	23
2.2	Materials and Methods .....	25
2.2.1	Preparation of Electrodes and Electrolytes.....	25
2.2.2	Electrochemical Measurements.....	26
2.3	Results and Discussion .....	27
2.3.1	Identification of Diffusion Limitation in Measured HER Currents .....	27

2.3.2	The Origin of the Diffusion Limitation in HER Currents .....	35
2.3.3	Impact of Diffusion Limitation of H <sub>2</sub> on Determination and Interpretation of Tafel Slopes .....	36
2.3.4	Correction of Diffusion Limitation for Both HOR and HER Branches .....	40
2.3.5	Diffusion Limitation Correction for HER Branch Using Different Approaches .....	46
2.3.6	Comparison of the Three Methods of Calculating the Kinetic Current and the Exchange Current ( <i>i</i> <sub>0</sub> ) of HOR/HER .....	52
2.4	Conclusion.....	62
3	<b>CORRELATING HYDROGEN OXIDATION/EVOLUTION ACTIVITY WITH THE MINORITY WEAK HYDROGEN BINDING SITES ON IRIDIUM/C CATALYSTS .....</b>	<b>63</b>
3.1	Introduction .....	64
3.2	Materials and Methods .....	66
3.2.1	Preparation and Characterization of Ir Nanoparticle with Different Sizes .....	66
3.2.2	Electrochemical Measurements.....	66
3.3	Results and Discussion .....	68
3.3.1	Characterization of Ir Particle Size.....	68
3.3.2	HOR/HER Activity of Supported Ir Catalysts with Varying Particle Sizes .....	74
3.3.3	Correlating H <sub>upd</sub> Peaks in Cyclic Voltammogram with HBE of Active Sites.....	78
3.3.4	Identifying True Active Sites for HOR/HER via Peak Deconvolution .....	81
3.4	Conclusion.....	90
4	<b>SIZE-DEPENDENT HYDROGEN OXIDATION AND EVOLUTION REACTION ACTIVITY ON PALLADIUM NANOPARTICLES IN ACID AND BASE .....</b>	<b>92</b>
4.1	Introduction .....	93
4.2	Materials and Methods .....	94
4.2.1	Preparation and Physical Characterization of Palladium Nanoparticles with Different Size .....	94

4.2.2	Electrochemical Measurements.....	95
4.3	Results and Discussion .....	96
4.3.1	Characterization of the Particle Size of All Pd/C Samples .....	96
4.3.2	Measurement of HOR/HER Kinetics .....	101
4.3.3	Particle Size Effect for HOR/HER Activity .....	105
4.3.4	HOR/HER Activities: Acid vs. Base.....	111
4.4	Conclusion.....	113
5	UNIVERSAL DEPENDENCE OF HYDROGEN OXIDATION AND EVOLUTION REACTION ACTIVITY OF PLATINUM-GROUP- METALS ON PH AND HYDROGEN BINDING ENERGY .....	114
5.1	Introduction .....	115
5.2	Materials and Methods .....	116
5.2.1	Materials and Characterization.....	116
5.2.2	Preparation of Electrolytes .....	117
5.2.3	Electrochemical Measurements.....	117
5.3	Results and Discussion .....	120
5.3.1	Particle Size Characterization of Pt, Ir, Pd and Rh Nanoparticles .....	120
5.3.2	pH-Dependent HBE of Carbon Supported Pt, Ir, Pd and Ir Nanoparticles Determined from Cyclic Voltammograms .....	124
5.3.3	pH-Dependent HOR/HER Activity on Carbon Supported Pt, Ir, Pd and Ir Nanoparticles.....	127
5.3.4	Correlation of HOR/HER Activity with HBE.....	133
5.3.5	pH-Dependent CO-Stripping Onset Potential .....	138
5.3.6	Discussion about pH-Dependent HBE and HOR/HER Activity .....	144
5.4	Conclusion.....	149
6	PLATINUM-RUTHENIUM NANOTUBES AND PLATINUM- RUTHENIUM COATED COPPER NANOWIRES AS EFFICIENT CATALYSTS FOR ELECTRO-OXIDATION OF METHANOL .....	150
6.1	Introduction .....	151
6.2	Materials and Methods .....	153

6.2.1	Preparation of CuNWs, PtRuNTs and PtRu/CuNWs.....	153
6.2.1.1	Synthesis of CuNWs.....	153
6.2.1.2	Synthesis of PtRuNTs and PtRu/CuNWs.....	153
6.2.2	Characterization.....	154
6.2.2.1	Electron Microscopy Characterization .....	154
6.2.2.2	X-ray Diffraction and X-ray Photoelectron Spectroscopy.....	154
6.2.2.3	Electrochemical Measurements.....	155
6.3	Results and Discussion .....	156
6.3.1	Electron Microscopy and Elemental Characterization of Synthesized Catalysts .....	156
6.3.1.1	PtRu Nanotubes (PtRuNTs) .....	157
6.3.1.2	PtRu Coated Copper Nanowires (PtRu/CuNWs).....	161
6.3.2	X-ray Spectroscopy Analysis .....	165
6.3.2.1	X-ray Diffraction Pattern.....	165
6.3.2.2	X-ray Photoelectron Spectroscopy .....	167
6.3.3	Cyclic Voltammograms and CO-Stripping of PtRuNTs and PtRu/CuNWs .....	169
6.3.4	Performance of PtRuNTs and PtRu/CuNWs Towards Methanol Oxidation Reaction.....	171
6.3.4.1	Activity of Methanol Oxidation Reaction of PtRuNTs and PtRu/CuNWs .....	171
6.3.4.2	Durability of Methanol Oxidation Reaction on PtRuNTs and PtRu/CuNWs .....	174
6.3.4.3	Activation Energy of Methanol Oxidation Reaction on PtR/CuNWs and PtRu/C.....	175
6.3.5	Originality of the Enhanced MOR Activity of PtRuNTs and PtRu/CuNWs .....	177
6.4	Conclusion.....	181
7	CONCLUSIONS AND PERSPECTIVES .....	182
7.1	Conclusions .....	182

7.2	Perspectives .....	184
7.2.1	Fundamental Studies of Hydrogen Oxidation Reaction .....	184
7.2.2	Catalysts Development for Hydrogen Oxidation Reaction in Base .....	185
7.2.3	PtRu Catalysts for Methanol Oxidation Reaction .....	187
REFERENCES .....		188
Appendix		
A	ABBREVIATIONS AND IMPORTANT VARIABLES .....	202
B	DERIVATION OF EQUATIONS .....	204
B.1	Derivation of HBE and $E_{\text{peak}}$ Relationship .....	204
B.2	Derivation of Exchange Current Density and $E_{\text{peak}}$ Relationship (Eq. 5.6).....	207
B.3	Derivation of $\Delta E_a$ and $\Delta E_{\text{peak}}$ Relationship (Eq. 5.7).....	208
C	REPRINT PERMISSIONS .....	209

## LIST OF TABLES

Table 1.1 Rate equation for HOR/HER with different RDS in the reaction pathway..	11
Table 1.2 Summary of exchange current density ( $i_0$ ), anodic transfer coefficient ( $\alpha_a$ ), activation energy ( $E_a$ ) and technique for HOR/HER kinetic study on Pt, Ir, Pd, Rh and Ru in alkaline or acidic electrolytes.....	16
Table 2.1 Comparison of exchange currents ( $i_0$ ) from three different diffusion-correction methods for HOR/HER on a 5 mm diameter Pt disk in electrolytes with different pHs. ....	60
Table 2.2 Comparison of exchange current ( $i_0$ ), transfer coefficient ( $\alpha$ ) and exchange current density ( $j_0$ ) from three different diffusion-correction methods for HOR/HER on a 5 mm diameter glassy carbon electrode with different Pt loadings in 0.1 M KOH at 1600 rpm.....	61
Table 3.1 Number averaged ( $d_n^{\text{TEM}}$ ) and volume/area averaged ( $d_{v/a}^{\text{TEM}}$ ) particle size from TEM, volume averaged particle size from XRD ( $d_v^{\text{XRD}}$ ), surface areas calculated from $d_{v/a}^{\text{TEM}}$ ( $S_{v/a}^{\text{TEM}}$ ), $d_v^{\text{XRD}}$ ( $S_v^{\text{XRD}}$ ) and measured electrochemically ( $S_v^{\text{XRD}}$ ) .....	72
Table 3.2 Summary of average specific exchange current densities based on t-ECSA and mass exchange current densities of HOR/HER on all Ir samples and their corresponding transfer coefficients ( $\alpha$ ) .....	75
Table 3.3 FWHM and peak position of deconvoluted peak H1, H2 and H3 for all samples .....	83
Table 3.4 FWHM and peak positions of deconvoluted peak H1a, H1b, H2 and H3 for all samples .....	83
Table 4.1 Number averaged ( $d_n^{\text{TEM}}$ ) and volume/area averaged ( $d_{v/a}^{\text{TEM}}$ ) particle size determined from TEM, volume averaged particle size from XRD ( $d_v^{\text{XRD}}$ ), specific surface area calculated from $d_{v/a}^{\text{TEM}}$ ( $S_{v/a}^{\text{TEM}}$ ), $d_v^{\text{XRD}}$ ( $S_v^{\text{XRD}}$ ) and electrochemically measured from cyclic voltammograms ( $S^{\text{EC}}$ ).....	101

Table 4.2 Summary of specific and mass exchange current densities determined from linear fitting in low micropolarization regions for all Pd samples in 0.1 M KOH and 0.1 M HClO <sub>4</sub> .....	108
Table 4.3 Summary of transfer coefficients ( $\alpha$ ) .....	108
Table 5.1 Number averaged ( $d_n^{\text{TEM}}$ ) and volume/area averaged ( $d_{v/a}^{\text{TEM}}$ ) particle size from TEM, surface area calculated from $d_{v/a}^{\text{TEM}}$ ( $S_{v/a}^{\text{TEM}}$ ) and electrochemical surface area determined from CV in 0.1 M KOH (ECSA <sub>CV</sub> ) and CO stripping in 0.1 M KOH (ECSA <sub>CO-stripping</sub> ) of Pt/C, Ir/C, Pd/C and Rh/C. ....	121
Table 5.2 $\beta$ and A from fitting $i_0$ to $E_{\text{peak}}$ using expression $i_0 = A \exp(-\beta FE_{\text{peak}}/RT)$ , activation energy ( $E_a$ ) measured by RDE in 0.1 M KOH from this work and by H <sub>2</sub> -pump from ref[38], difference in H <sub>upd</sub> desorption peak potentials ( $\Delta E_{\text{peak}}$ ) in 0.1 M KOH and acid with pH $\approx$ 0, and $\beta_{E_a}$ calculated by $(E_a(0.1 \text{ M KOH}) - E_a(\text{H}_2 \text{ pump}))/F\Delta E_{\text{peak}}$ ....	138
Table 5.3 Surface area measured from H <sub>upd</sub> adsorption and desorption peaks, potentials for Pt(110) and Pt(100) and the corresponding exchange current densities ( $i_0$ ) in 0.1 M KOH with addition of various salts .....	148
Table 6.1 Elemental composition of PtRuNTs, PtRu/CuNWs by EDX or XPS .....	165
Table 6.2 Summary of MOR activation energies ( $E_a$ ) at 0.5 V and 0.6 V vs. RHE on PtRu/CuWs with different Pt/Ru atomic ratio and PtRu/C .....	175

## LIST OF FIGURES

- Figure 1.1 Gravimetric and volumetric energy densities of various fuels/devices. Solid points represent fuels of technical interest for low-temperature fuel cells. .... 3
- Figure 1.2 Schemes of the structure of a H<sub>2</sub>-fueled (a) proton exchange membrane fuel cell (PEMFC) and (b) hydroxide exchange membrane fuel cell (HEMFC)..... 5
- Figure 1.3 Simulated polarization curves of HOR and ORR in PEMFC and HEMFC operating at 353 K. The HOR polarization curves are simulated based on a Pt loading of 5  $\mu\text{g}/\text{cm}^2_{\text{disk}}$  which corresponds to a roughness factor of about 3 if the ECSA of Pt/C is 60  $\text{m}^2/\text{g}_{\text{Pt}}$ , and estimated HOR exchange current densities in the HEMFC and PEMFC of 3.7  $\text{mA}/\text{cm}^2_{\text{Pt}}$  and 433  $\text{mA}/\text{cm}^2_{\text{Pt}}$  at 353 K based on  $i_0$  and activation energies from Ref[2,3]..... 6
- Figure 1.4 Volcano plots constructed by (a) theoretical calculation based on the kinetic equations derived by Parson assuming Volmer, Heyrovsky or Tafel step as rate determining, respectively,[30] (b) correlating HER exchange current densities on various metals in acidic electrolytes collected by Trasatti[29] vs. metal-hydrogen bond strength measured from gas phase[35], (c) correlating HER exchange current densities on various metals in acidic electrolytes collected by Trasatti[29] vs. hydrogen binding energy (HBE) calculated using density functional theory (DFT) by Nørskov et al. (black circles)[31], red hollow squares represent exchange current densities on Pt, Ir, Rh and Pd determined using H<sub>2</sub>-pump in a proton exchange membrane fuel cell configuration,[33,38] and (d) correlating HER exchange current densities on various metals in 0.1 M KOH vs. DFT-calculated HBE by Sheng et al.[32]..... 14
- Figure 1.5 Detailed pathway for methanol oxidation. Possible products besides CO<sub>2</sub> are indicated in blue. The pathway with formation of adsorbed CO species (CO<sub>ad</sub>) is called indirect pathway, while that without formation of CO<sub>ad</sub> is called direct pathway..... 19

- Figure 2.1 HOR/HER polarization curves on a Pt disk in H<sub>2</sub>-saturated 0.1 M HClO<sub>4</sub>, at a rotating speed of 1600 rpm and a scanning rate of 10 mV/s before (blue dashed line) and after (red solid line) iR-correction. The black dashed line is the calculated concentration overpotential curve, and the green dashed line is the simulated kinetic current using the Butler-Volmer equation (Eq. 2.4) assuming  $i_0 = 70 \text{ mA/cm}^2$  and  $\alpha = 0.5$ . ..... 28
- Figure 2.2 iR-corrected HOR/HER polarization curves at different rotating speeds (100 rpm to 3600 rpm) on a polycrystalline Pt disk in H<sub>2</sub>-saturated 0.1 M HClO<sub>4</sub> at a scanning rate of 10 mV/s. Dashed grey lines are the diffusion overpotential curves at different rotating speeds. The inset shows a Koutecky-Levich plot at 0.08 V vs. RHE, yielding a straight line with  $Bc_0$  value of  $0.075 \text{ mA}/(\text{cm}^2_{\text{disk}}\text{rpm}^{1/2})$ . ..... 30
- Figure 2.3 iR-corrected HOR/HER polarization curves at different rotating speeds (100 rpm to 3600 rpm) on Pt/C (loading:  $10 \mu\text{g}_{\text{Pt}}/\text{cm}^2_{\text{disk}}$ ) in H<sub>2</sub> – saturated 0.1 M KOH at a scanning rate of 10 mV/s. Dashed grey lines are the diffusion overpotential curves at different rotating speeds. The inset shows a Koutecky-Levich plot at 0.5 V vs. RHE, yielding a straight line with  $Bc_0$  value of  $0.069 \text{ mA}/(\text{cm}^2_{\text{disk}}\text{rpm}^{1/2})$ . ..... 32
- Figure 2.4 HOR/HER polarization curves on a) Pt disk in 0.1 M HClO<sub>4</sub> and b) Pt/C (loading:  $10 \mu\text{g}_{\text{Pt}}/\text{cm}^2_{\text{disk}}$ ) in 0.1 M KOH, in H<sub>2</sub> at a scanning rate of 10 mV/s and rotating speeds of 0 rpm (dash black line) and 100 rpm (solid red line). ..... 33
- Figure 2.5 HER polarization curves on Pt disk in a) Ar-saturated 0.1 M HClO<sub>4</sub> at a scanning rate of 10 mV/s at different rotating speeds. Dash magenta line represent HOR/HER polarization curve on Pt disk in H<sub>2</sub>-saturated 0.1 M HClO<sub>4</sub> at 2500 rpm and 10 mV/s as comparison, and b) Ar-saturated and H<sub>2</sub>-saturated 0.1 M KOH at 2500 rpm and 10 mV/s. .... 34
- Figure 2.6 (a) HER polarization curves on Pt disk in H<sub>2</sub> – saturated 0.5 M H<sub>2</sub>SO<sub>4</sub> at a scanning rate of 10 mV/s, and a rotating speed of 1600 rpm before (blue dash line), after (red line) iR correction and concentration overpotential curve (black dash line), (b) Tafel plot of HER before (blue line) and after (red line) iR correction, black line represents concentration overpotential curve. .... 39

Figure 2.7 Schematic illustration of two methods of converting a measured polarization curve ( $\eta$ ,  $i$ ) to a plot of kinetic overpotential vs. kinetic current ( $\eta_k$ ,  $i_k$ ), based on which electrokinetic parameters can be extracted by fitting with the Butler-Volmer equation. (a) Method 1:  $i_k$  is obtained according to the reversible Koutecky-Levich equation ( $1/i = 1/i_k + 1/i_d$ ), and the measured overpotential  $\eta$  is the kinetic overpotential  $\eta_k$ ; (b)  $i_k$  and  $\eta_k$  are obtained according to  $i_k = 1/(1 - i/i_{l,a})^{1-\alpha}$  and  $\eta_k = \eta - \eta_d$ , respectively. The two methods are largely equivalent, except that Method 1 does not require the prior knowledge of the  $\alpha$ . ..... 46

Figure 2.8 (a) HOR/HER polarization curves on a Pt disk in H<sub>2</sub>-saturated phosphoric acid/phosphate buffer solution (pH = 2.4) at 10 mV/s and rotating speeds from 900 to 3600 rpm. Dash lines represent the concentration overpotential curves. (b) Tafel plots of HOR/HER when both HOR and HER kinetic currents were calculated with the irreversible Koutecky-Levich equation (Eq. 2.2), and the dashed lines represent the experimental net-HER currents, the kinetic overpotential  $\eta_k$  is the iR-corrected overpotential ( $E_{iR-free}$  vs. RHE), (c) Tafel plots of HOR/HER when both HOR and HER kinetic currents were calculated with the reversible Koutecky-Levich equation (Eq. 2.11), and the dashed lines represent the experimental net-HER currents, and  $\eta_k = E_{iR-free}$  vs. RHE, (d) Tafel plots of HOR/HER when both HOR and HER overpotentials are corrected by diffusion overpotential ( $\eta_d$ ) ( $\eta_k = E_{iR-free}$  vs. RHE -  $\eta_d$ ) and the HOR and HER currents were converted to kinetic current by Eq. 2.35, the gray dashed line represents the  $|i_k|$  vs  $E_{iR-free}$  curve in (c) at a rotating speed of 3600 rpm for comparison. .. 48

Figure 2.9 Tafel plots for HOR/HER on Pt/C (loading: 10  $\mu\text{g}_{\text{Pt}}/\text{cm}^2_{\text{disk}}$ ) in H<sub>2</sub> saturated 0.1 M KOH at a scanning rate of 10 mV/s at different rotating speeds. (a) Both HOR and HER kinetic currents were calculated with the irreversible Koutecky-Levich equation (Eq. 2.2), dashed lines represents experimental net-HER currents, and  $\eta_k = E_{iR-free}$  vs. RHE, (b) Both HOR and HER kinetic currents were calculated with the reversible Koutecky-Levich equation (Eq. 2.11), and  $\eta_k = E_{iR-free}$  vs. RHE, and (c) Both HOR and HER currents were uncorrected while the overpotential is corrected by diffusion overpotential ( $\eta_d$ ), so  $\eta_k = E_{iR-free}$  vs. RHE -  $\eta_d$ . (d) Both HOR and HER overpotentials are corrected by diffusion overpotential ( $\eta_d$ ) and the HOR and HER currents were converted to kinetic current by Eq. 2.35,  $\eta_k = E_{iR-free}$  vs. RHE -  $\eta_d$ , and gray dashed line represents the  $|i_k|$  vs.  $E_{iR-free}$  curve in (b) at a rotating speed of 3600 rpm for comparison. .... 49

Figure 2.10 (a) HOR/HER polarization curves on Pt(pc) disk in H <sub>2</sub> -saturated 0.1 M KOH, 0.1 M HClO <sub>4</sub> and phosphoric acid/phosphate buffer solutions with different pHs, tested at a scanning rate of 10 mV/s and a rotating speed of 1600 rpm, (b) HOR/HER polarization curves on carbon supported Pt nanoparticles from Tanaka Kikinzo International, Inc. (TKK Pt/C) with different Pt loadings tested in H <sub>2</sub> -saturated 0.1 M KOH, at 1 mV/s and 1600 rpm.....	55
Figure 2.11 Tafel plots of HOR/HER kinetic currents and their corresponding fitting into a Butler-Volmer equation calculated from HOR/HER polarization curves measured on a Pt disk in electrolytes with different pHs at 10 mV/s and 1600 rpm, when (a1 – a6) both HOR and HER kinetic currents were calculated using the reversible Koutecky-Levich equation ( $1/i = 1/i_k + 1/i_d$ ), (b1 – b6) both HOR and HER overpotentials are corrected by diffusion overpotential, and both HOR and HER currents were converted to kinetic currents using $i/i_k = (1 - i/i_{l,a})^{0.5}$ , and (c1- c6) the HOR kinetic currents were calculated using irreversible Koutecky-Levich equation ( $1/i = 1/i_k + 1/i_l$ ) and the HER kinetic currents were the measured ones corrected for internal resistance (iR). All overpotentials were iR-corrected. ....	57
Figure 2.12 Tafel plots of HOR/HER kinetic currents and their corresponding fitting into a Butler-Volmer equation calculated from HOR/HER polarization curves measured on Pt/C in 0.1 M KOH with Pt loadings from 4 to 40 $\mu\text{g}_{\text{Pt}}/\text{cm}^2_{\text{disk}}$ at 1 mV/s and 1600 rpm, when (a1 – a5) both HOR and HER kinetic currents were calculated using the reversible Koutecky-Levich equation ( $1/i = 1/i_k + 1/i_d$ ), (b1 – b5) both HOR and HER overpotentials are corrected by diffusion overpotential, and both HOR and HER currents were converted to kinetic currents using $i/i_k = (1 - i/i_{l,a})^{0.5}$ , and (c1- c5) the HOR kinetic currents were calculated using irreversible Koutecky-Levich equation ( $1/i = 1/i_k + 1/i_l$ ) and the HER kinetic currents were the measured ones corrected for internal resistance (iR). All overpotentials were iR-corrected. ....	59
Figure 3.1 TEM images of (a) 20 wt. % Ir/C, (b) Ir/C-300C, (c) Ir/C-500C, (d) Ir/C-600C, and (e) Ir/C-800C. (f) Average particle size determined from TEM images for all Ir/C samples. Insets of (a-e) are the histograms of particle size for the corresponding sample counted over 300 particles...	69
Figure 3.2 X-ray diffraction (XRD) patterns of 20 wt. % Ir/C, Ir/C-300C, Ir/C-500C, Ir/C-600C and Ir/C-800C.....	71

- Figure 3.3 Cyclic voltammograms of Ir/C, Ir/C-300C, Ir/C-500C, Ir/C-600C and Ir/C-800C conducted in Ar saturated 0.1 M KOH at a scan rate of 50 mV/s. The Ir loading for all samples is 10  $\mu\text{g}/\text{cm}^2_{\text{disk}}$ ..... 73
- Figure 3.4 (a) HOR/HER polarization curve (positive scan) on Ir/C in 0.1 M KOH saturated with  $\text{H}_2$  (1 atm) at a scan rate of 1 mV/s with a rotation speed of 1600 rpm at r.t. (293K) before (black line) and after (red line) iR correction. The blue dashed line is the concentration overpotential curve. The loading of Ir was 10  $\mu\text{g}/\text{cm}^2_{\text{disk}}$ . (b) The measured HOR/HER kinetic current density (black solid line) and the corresponding Butler-Volmer equation (Eq. 3.4) fitting (red dashed line) with  $\alpha = 0.47$ . (c) HOR/HER polarization curves on Ir/C in 0.1 M KOH saturated with  $\text{H}_2$  (1 atm) at scan rate of 1 mV/s at r.t. with rotation speeds ranging from 400 rpm to 2500 rpm. The inset shows a Koutecky-Levich plot at 0.25 V vs. RHE. (d) HOR/HER polarization curves on Ir/C in 0.1 M KOH saturated with  $\text{H}_2$  (1 atm) at a scan rate of 1 mV/s with a rotation speed of 1600 rpm at temperatures ranging from 275 K to 313 K. The inset shows the Arrhenius plot with the slope corresponding to  $-E_a/R$ , giving an activation energy of  $32.9 \pm 1.5$  kJ/mol..... 76
- Figure 3.5 (a) iR-corrected HOR/HER polarization curves (positive scan) and (b) measured kinetic current on Ir/C samples with different sizes. All measurements were performed in 0.1 M KOH saturated with  $\text{H}_2$  (1 atm) at a scan rate of 1 mV/s with a rotation speed of 1600 rpm at r.t. (293 K). Specific (c) and mass (d) exchange current densities of HOR/HER on Ir/C samples normalized to t-ECSA as a function of t-ECSA. The red dashed lines serve as eye guiding lines for the trends. .... 77
- Figure 3.6 (a) Cyclic voltammograms of Ir/C (loading: 10  $\mu\text{g}/\text{cm}^2_{\text{disk}}$ ) measured in Ar-saturated 0.1 M KOH at various scanning rates from 5 to 50 mV/s, 0 rpm, (b)  $\text{H}_{\text{upd}}$  desorption profiles from CV in (a) normalized to peak current of  $\text{H}_2$  after double-layer correction, and (c)  $\text{H}_{\text{upd}}$  adsorption profiles from CV in (a) normalized to peak current of  $\text{H}_2$  after double-layer correction..... 80
- Figure 3.7 Deconvolution of hydrogen desorption peaks into three peaks centered at 0.16 V (H1), 0.24 V (H2) and 0.32 V (H3) for (a) Ir/C, (b) Ir/C-300C, (c) Ir/C-500C, (d) Ir/C-600C, and (e) Ir/C-800C. (f) Fractions of deconvoluted peak H1, H2 and H3 defined by the ratio of deconvoluted peak area and total area..... 82

Figure 3.8 (a) $i_0$ as a function of fraction of peak H1 with three peak deconvolution, and (b) $i_0$ normalized to surface area of site H1 (peak potential at 0.16 V) ( $i_{0(H1)}$ ) as a function of t-ECSA. ....	84
Figure 3.9 Deconvolution of hydrogen desorption peaks into four peaks centered at 0.13 V (H1a), 0.18 V (H1b), 0.24 V (H2) and 0.32 V (H3) for (a) Ir/C, (b) Ir/C-300C, (c) Ir/C-500C, (d) Ir/C-600C and (e) Ir/C-800C. (f) Fraction of peaks H1a, H1b, H2 and H3 among different samples.....	86
Figure 3.10 Correlation between the exchange current density ( $i_0$ ) normalized to t-ECSA and the fraction of peak H1a. ....	87
Figure 3.11 $i_0$ normalized to surface area of H1a (peak potential 0.13 V), H1b (peak potential 0.18 V), H2 (peak potential 0.24 V) and H3 (peak potential 0.32 V) as a function of t-ECSA. ....	87
Figure 3.12 Experimental exchange current densities (black circle dots) and simulated exchange current densities (bars) with contribution from H1a (red bars), H1b (green bars), H2 (blue bars) and H3 (black bars) of all the samples. ....	89
Figure 3.13 Surface averaged distribution (SAD) of square, triangle, edge and vertex sites of particles with a cubo-octahedron structure as a function of particle size. The method for calculating the site distribution can be found in the supporting information of ref.[90] .....	89
Figure 4.1 Transmission electron microscopy (TEM) images of (a) Pd/C, (b) Pd/C-300C, (c) Pd/C-400C, (d) Pd/C-500C, (e) Pd/C-600C and (f) number averaged particle size determined from TEM images for all Pd/C samples. Insets of (a-e) are the histograms of the particle size for each sample counted over 300 particles. ....	97
Figure 4.2 X ray diffraction (XRD) patterns of Pd/C, Pd/C-300C, Pd/C-400C, Pd/C-500C and Pd/C-600C. ....	98
Figure 4.3 Cyclic voltammograms of Pd/C, Pd/C-300C, Pd/C-400C, Pd/C-500C and Pd/C-600C measured at a scanning rate of 50 mV/s in (a) Ar-saturated 0.1 M KOH and (b) Ar-saturated 0.1 M HClO <sub>4</sub> . ....	100

Figure 4.4 Polarization curves of Pd/C, Pd/C-300C, Pd/C-400C, Pd/C-500C and Pd/C-600C measured at r.t. with a scanning rate of 1 mV/s, a rotating speed of 1600 rpm in (a) H <sub>2</sub> -saturated 0.1M KOH with a Pd loading of 20 μg <sub>Pd</sub> /cm <sup>2</sup> <sub>disk</sub> , and (b) H <sub>2</sub> -saturated 0.1M HClO <sub>4</sub> with the Pd loadings of 5 μg <sub>Pd</sub> /cm <sup>2</sup> <sub>disk</sub> for Pd/C, Pd/C-300C, Pd/C-400C, 20 μg <sub>Pd</sub> /cm <sup>2</sup> <sub>disk</sub> for Pd/C-500C, and 30 μg <sub>Pd</sub> /cm <sup>2</sup> <sub>disk</sub> for Pd/C-600C. The grey-dash lines represent concentration overpotential curve. Representative linear plots of kinetic current densities as a function of overpotential in (c) 0.1 M KOH and (d) 0.1 M HClO <sub>4</sub> . Representative Tafel plots of kinetic current densities in (e) 0.1 M KOH and (f) 0.1 M HClO <sub>4</sub> . All the potentials are iR-corrected.....	102
Figure 4.5 HOR/HER (a) specific and (b) mass exchange current densities in terms of as a function of Pd particle size (volume/area averaged particle size) in both 0.1 M KOH and 0.1 M HClO <sub>4</sub> . The specific exchange current densities were determined from different methods including linear fitting in the micropolarization regions, Butler-Volmer fitting with $\alpha_a + \alpha_c = 1$ and $\alpha_a, \alpha_c$ unconstrained, and the mass exchange current densities were determined from linear fitting in the micropolarization regions.....	106
Figure 4.6 H <sub>upd</sub> desorption profiles for all the Pd samples from cyclic voltammograms measured in 0.1 M HClO <sub>4</sub> where the current is normalized to the peak current after double layer current deduction....	109
Figure 4.7 Arrhenius plots of HOR/HER activities on Pd/C (about 3 nm diameter) measured in 0.1 M HClO <sub>4</sub> and 0.1 M KOH. ....	112
Figure 5.1 TEM image and the corresponding histograms of particles size (inset) of (a) Pt/C, (b) Ir/C, (c) Pd/C and (d) Rh/C. The number average particle size is 1.9 ± 0.4 nm for Pt/C, 2.9 ± 0.8 nm for Ir/C, 3.2 ± 0.6 nm for Pd/C and 3.4 ± 0.7 nm for Rh/C.....	122
Figure 5.2 Cyclic voltammograms (CVs) of a) Pt/C, b) Ir/C, c) Pd/C and d) Rh/C measured in Ar-saturated 0.1 M KOH with a scanning rate of 50 mV/s. The dash line represents CV scans in a small potential range to avoid the contribution of oxide reduction current to the H <sub>upd</sub> adsorption current. Currents were normalized to the surface area determined from CV.....	123
Figure 5.3 CO-stripping on (a) Pt/C, (b) Ir/C, (c) Pd/C and (d) Rh/C in 0.1 M KOH. Currents were normalized to the surface area determined from CO-stripping.....	124

Figure 5.4 Representative cyclic voltammograms (CVs) of (a) Pt/C, (b) Ir/C, (c) Pd/C and (d) Rh/C in electrolytes with different pHs (currents were normalized to ECSA <sub>CV</sub> measured in 0.1 M KOH).....	126
Figure 5.5 Underpotential deposited hydrogen (H <sub>upd</sub> ) desorption peak potentials from cyclic voltammograms of (a) Pt/C, (b) Ir/C, (c) Pd/C and (d) Rh/C from CVs as a function of pH. ....	127
Figure 5.6 CVs (a1-e1), HOR/HER polarization curves (a2-e2), and kinetic current densities with fittings based on the Butler-Volmer equation with $\alpha_a + \alpha_c = 1$ (a3-e3) on Pt/C in electrolytes at different pHs. CVs were measured in Ar at a scanning rate of 50 mV/s. HOR/HER polarization curves were collected in H <sub>2</sub> -saturated electrolytes at a scanning rate of 1 mV/s and a rotating speed of 1600 rpm. ....	128
Figure 5.7 CVs (a1-e1), HOR/HER polarization curves (a2-e2), kinetic current density with their fitting into the Butler-Volmer equation with $\alpha_a + \alpha_c = 1$ (a3-e3) on Ir/C in electrolytes with different pH. CVs were measured in Ar at a scanning rate of 50 mV/s, HOR/HER polarization curves were collected in H <sub>2</sub> -saturated electrolytes at a scanning rate of 1 mV/s and a rotating speed of 1600 rpm. ....	129
Figure 5.8 CVs (a1-e1), HOR/HER polarization curves (a2-e2), kinetic current density with their fitting into the Butler-Volmer equation with $\alpha_a + \alpha_c = 1$ (a3-e3) on Pd/C in electrolytes with different pH. CVs were measured in Ar at a scanning rate of 50 mV/s, HOR/HER polarization curves were collected in H <sub>2</sub> -saturated electrolytes at a scanning rate of 1 mV/s and a rotating speed of 1600 rpm. ....	130
Figure 5.9 CVs (a1-e1), HOR/HER polarization curves (a2-e2), kinetic current density with their fitting into the Butler-Volmer equation with $\alpha_a + \alpha_c = 1$ (a3-e3) on Rh/C in electrolytes with different pH. CVs were measured in Ar at a scanning rate of 50 mV/s, HOR/HER polarization curves were collected in H <sub>2</sub> -saturated electrolytes at a scanning rate of 1 mV/s and a rotating speed of 1600 rpm. ....	131
Figure 5.10 Exchange current densities ( <i>i</i> <sub>0</sub> ) of HOR/HER on (a) Pt/C, (b) Ir/C, (c) Pd/C and (d) Rh/C as a function of pH of electrolyte. HOR/HER polarization curves were measured using rotating disk electrode (RDE) method in H <sub>2</sub> -saturated electrolytes at a scanning rate of 1 mV/s and a rotation speed of 1600 rpm at 293 K. Grey stars represent HOR/HER exchange current densities at 293 K estimated from the Arrhenius plot in ref.[38], in which all the activities were measured using an H <sub>2</sub> -pump configuration. ....	133

Figure 5.11: Exchange current densities of HOR/HER on (a) Pt/C, (b) Ir/C, (c) Pd/C and (d) Rh/C as a function of underpotential deposited hydrogen ( $H_{\text{upd}}$ ) desorption peak potential ( $E_{\text{peak}}$ ) from CVs. Gray dash lines in the four figures are linear fittings of the data. ....	135
Figure 5.12: Exchange current densities of HOR/HER ( $i_0$ ) on Pt/C, Ir/C, Pd/C and Rh/C as a function of the lowest underpotential deposited hydrogen ( $H_{\text{upd}}$ ) desorption peak potential ( $E_{\text{peak}}$ ) from CVs. Dash line represents linear fitting of all data points. ....	136
Figure 5.13: Arrhenius plot of HOR/HER activities on Pt/C (a), Ir/C (b), Pd/C (c) and Rh/C (d) in 0.1 M KOH.....	137
Figure 5.14 CO stripping profiles on Pt/C in various electrolytes with different pHs.....	140
Figure 5.15 CO stripping profiles on Ir/C in various electrolytes with different pHs.....	141
Figure 5.16 CO stripping profiles on Pd/C in various electrolytes with different pHs.....	142
Figure 5.17 CO stripping profiles on Rh/C in various electrolytes with different pHs.....	143
Figure 5.18 CO stripping onset potentials as a function of pH on Pt/C (magenta squares), Ir/C (red diamonds), Pd/C (olive up-triangles) and Rh/C (blue down-triangles). ....	144
Figure 5.19 CVs and the HOR/HER polarization curves on a Pt disk in 0.1 M KOH with additional salts of (a, b) KCl, (c, d) $K_2SO_4$ , and (e, f) $NaClO_4$ . ....	147
Figure 6.1 (a) Scanning electromicroscopy (SEM) image and (b) transmission microscopy image of CuNWs. ....	156
Figure 6.2 SEM images and corresponding EDX spectra of (a,b) PtRu(1-1)NTs, (c,d) PtRu(3-1)NTs, (e,f) PtRu(6-1)NTs and (g, h) PtRu(9-1)NTs.....	158
Figure 6.3 (a, b, c) TEM images of a PtRu(6-1)NT in size view with different magnifications. (d) TEM image of a PtRu(6-1)NT in a cross-sectional view. HRTEM image of a PtRu(6-1)NT surface from (e) side view and (f) cross-sectional view.....	159

Figure 6.4 HAADF-STEM image (a, e) and corresponding elemental Pt (b,f), Ru (c, g), overlapping of Pt and Ru (d, h) spectrum images of a PtRu(6-1)NTs in side and cross-sectional view, (i) line scan along the direction shown in (h) of Pt(red) and Ru(green). .....	160
Figure 6.5 SEM images and EDX spectra of (a) PtRu(1-1)/CuNWs, (b) PtRu(3-1)/CuNWs, (c) PtRu(4-1)/CuNWs, (d) PtRu(6-1)/CuNWs and (e) PtRu(9-1)/CuNWs. ....	162
Figure 6.6 (a, b) TEM images of a PtRu(4-1)/CuNW, (c) TEM image of a PtRu(4-1)/CuNW surface, (d) HRTEM image of a PtRu(4-1)/CuNW.....	163
Figure 6.7 HAADF-STEM image (a) of a PtRu/(4-1)CuNW and the corresponding elemental Pt (b), Ru (c), Cu (d) and overlapping of Pt, Ru and Cu (e) spectrum images in side view. (f) Line scan along the diameter direction of a PtRu(4-1)/CuNW in (e).....	164
Figure 6.8 X-ray diffraction (XRD) patterns of (a) CuNWs, (b) PtRu(6-1)NTs and (c) PtRu(4-1)/CuNWs.....	166
Figure 6.9 XPS of Pt 4f of (a) PtRu(6-1)NTs, (b) PtRu/C, (c) PtRu(1-1)/CuNWs, (d) PtRu(3-1)/CuNWs, (e) PtRu(4-1)/CuNWs, (f) PtRu(6-1)/CuNWs and (g) PtRu(9-1)/CuNWs.....	168
Figure 6.10 Cyclic voltammograms of (a) PtRuNTs and (c) PtRu/CuNWs with various PtRu ratios tested in Ar-saturated 0.1 M HClO <sub>4</sub> at a scanning rate of 50 mV/s. CO stripping curves (Solid curves) and cyclic voltammograms directly after CO stripping (dash curves) of (b) PtRuNTs and (d) PtRu/CuNWs with various PtRu ratios. Comparison of (d) cyclic voltammograms and (e) CO-stripping curves of PtRu(4-1)/CuNWs, PtRu(6-1)NTs and PtRu/C. Inset of (e): zoom in of CO stripping curves in 0.25 - 0.5 V vs. RHE. ....	170
Figure 6.11 Cyclic voltammogram (forward scan) of PtRuNTs and PtRu/CuNWs with various PtRu ratios and PtRu/C in terms of (a, c) specific activity and (b, d) mass activity in Ar-saturated 0.1 M HClO <sub>4</sub> with 1 M CH <sub>3</sub> OH at a scanning rate of 5 mV/s. Plot of specific MOR activities at (e) 0.5 V vs. RHE and (f) 0.6 V vs. RHE as a function of PtRu atomic ratio on PtRu/CuNWs, PtRuNTs and PtRu/C. Error bars represents three independent measurements of each sample. ....	173
Figure 6.12 Chronoamperometry of PtRu(4-1)/CuNWs, PtRu(6-1)NTs and PtRu/C measured at 0.6 V vs. RHE for 1800 s. ....	174

Figure 6.13 Cyclic voltammogram (forward scan) and Arrhenius plots of MOR activities at 0.5 and 0.6 V vs. RHE in the inset of (a) PtRu(1-1)/Cu NWs, (b) PtRu(3-1)/CuNWs, (c) PtRu(4-1)/CuNWs, (d) PtRu(6-1)/CuNWs, (e) PtRu(9-1)/CuNWs and (f)PtRu/C measured in Ar-saturated 0.1 M HClO<sub>4</sub> with 1 M CH<sub>3</sub>OH at a scanning rate of 5 mV/s 176

Figure 6.14 Plot of specific MOR activities at 0.6 V vs. RHE as a function of PtRu atomic ratio on PtRu/CuNW at 20 °C (black), 40 °C (blue), 60 °C (green) and 80 °C (red). Hollow dots represents MOR activity of PtRu/C for comparison..... 177

Figure 6.15 SEM images of (a) PtNTs and (b) Pt/CuNWs. (c) Cyclic voltammograms of Pt/CuNWs(Pt 25 wt.%) , PtNTs, Pt disk and TKK Pt/C tested in 0.1 M HClO<sub>4</sub>, 1 M CH<sub>3</sub>OH, Ar, 5 mV/s, activities were normalized to surface area of Pt calculated from H<sub>ads</sub> and H<sub>des</sub> peaks, (d) CO stripping of Pt/CuNWs(Pt 25 wt.%) , PtNTs, Pt disk and TKK Pt/C tested in 0.1 M HClO<sub>4</sub>, 20 mV/s, CO was pre-adsorbed at 0.1 V vs. RHE for 10 min followed by another 10 min Ar-purging. .... 178

Figure 6.16 XPS spectra of PtRu/C, PtRu(6-1)NTs and PtRu(4-1)/CuNWs: (a) Pt 4f, (b) Ru 3p<sub>3/2</sub>..... 180

## ABSTRACT

Commercialization and mass adoption of low temperature fuel cells have been hampered by the large cell voltage loss, which can be largely blamed on the sluggish electrode reaction kinetics even with the state-of-the-art Pt catalysts. Significant progress has been made in the development of cathode catalysts for the oxygen reduction reaction (ORR), whereas the search for efficient anode catalysts has not been as fruitful. Therefore, the rational design and development of efficient anode catalysts are of vital importance, which hinge on two key factors: 1) fundamental understanding of the reaction mechanism and 2) synthesis of catalysts with well-defined structures.

Hydrogen oxidation reaction (HOR,  $H_2 \leftrightarrow 2H^+ + 2e$ ) is roughly two orders of magnitude slower in base than in acid electrolytes on Pt-group metal (PGM) catalysts, which demands either a substantial anodic overpotential or a high PGM loading for hydroxide exchange membrane fuel cells (HEMFCs). Fundamental understanding HOR kinetics is a prerequisite in the design of highly active HOR catalysts. To achieve this goal, my research established protocols to reliably remove the contribution of diffusion in the HOR/HER activity measurement with the rotating disk electrode (RDE) method, based on which intrinsic kinetic information can be extracted.

The effect of particle size on HOR/HER activities were explored on carbon supported Ir and Pd nanoparticles: the specific HOR/HER activities increase as particle size increase. The most active sites for HOR/HER on Ir/C were identified to be the sites with lowest hydrogen binding energy (HBE) (most likely the low-index facets), based on the observation that the activities normalized to the surface area of weakly binding

sites are independent of particle size. Consistent with the results on Ir, the increased HOR/HER activity on larger Pd nanoparticles correlates with an increased ratio of the sites with lower HBE. These findings suggest that future catalyst design should focus on increasing the density of sites with low HBE, e.g., low-index facets.

To establish the generality of the pH effect on the HOR/HER activity, a reliable and easily accessible method to experimentally determine the pH-dependent HBE was developed. In addition, HOR/HER activities on monometallic PGM (Pt, Pd, Ir and Rh) nanoparticles were mapped out over a broad pH range (1-13), which are then correlated with HBE. A universal correlation between the HOR activity and HBE is obtained on all PGMs evaluated, which offers strong evidence that HBE is the dominating descriptor for the performance of HOR catalysts. It follows that tuning of HBE could be a key strategy in the future design of HOR catalysts.

Aside from hydrogen, methanol is a promising liquid fuel for fuel cells. A key challenge in the development of active catalysts for methanol oxidation reaction (MOR,  $CH_3OH + H_2O \rightarrow CO_2 + 6H^+ + 6e$ ), which is the anode reaction of direct methanol fuel cells (DMFCs), is the structural sensitive nature of the catalytic performance. Hence, synthesis of catalysts with tailored structures is critical. Extended surface nanostructures, e.g., PtRu nanotubes (PtRuNTs) and PtRu coated Cu nanowires (PtRu/CuNWs), were synthesized by galvanically displacing the CuNWs template, which showed higher specific MOR activity than that of the benchmark PtRu/C. We attribute the enhanced activity to the weakened Pt-CO bonding through the modification of d-band center of Pt.

# Chapter 1

## INTRODUCTION

### 1.1 Fuel Cells

Developing efficient, cost-effective and environmentally friendly renewable energy conversion and storage devices is of great necessity in order to meet the rapidly increasing demand for energy globally and to replace the unrenovable fossil fuels. While a variety of renewable energy sources including solar, wind, hydropower, and geothermal energies have been explored, their application is limited by the diffuse and intermittent natures. However, the excess energies produced from those renewable sources could be stored in the chemical form, e.g.  $H_2$  produced from water by an electrolyzer, which can be used to generate power through an energy conversion device when needed. Among various energy conversion devices, a fuel cell is one of the most promising ones because of its high efficiency and low or even zero greenhouse gases emission.

A fuel cell is a device which converts the chemical energy in the fuels directly into electricity. It is constructed by two electrodes separated by an electrolyte in the form of either liquid or solid. The electrode where fuel oxidation reaction takes place is called anode and the one where oxygen reduction reaction takes places is called cathode. The electrons produced at the anode are transferred through the outer circuit to the cathode and produce electricity, while the ions are transported through the electrolytes. Since the process involves no combustion the efficiency of fuel cells is not limited by the Carnot cycle, which can be greater than 80% under certain conditions. Besides the

high efficiency, fuel cells generate zero or less pollutions compared with internal combustion engines depending on the type of fuels, are more reliable and mechanically simple since there is no moving parts, and can be operated longer as long as the fuels are fed continuously.

The major types of fuel cells developed includes polymer electrolyte membrane fuel cells, alkaline fuel cells (AFCs), phosphoric acid fuel cells (PAFCs), molten carbonate fuel cells (MCFCs) and solid oxide fuel cells (SOFCs). The AFC is operated at 50 – 200 °C with concentrated (30 – 50%) KOH as its electrolyte, and find its application in space program for producing electricity and drinking water.[1] PAFC, MCFC and SOFC are usually operated at high temperatures (150 – 220 °C for PAFC, 600 – 700 °C for MCFC and 700 – 1000 °C for SOFC), and are applied for stationary power generation.[1] Polymer electrolyte membrane fuel cells are typically operated at temperatures ranging from 20 – 100 °C, which are referred to as low-temperature fuel cells. Depending on the nature of the polymer electrolyte membrane, i.e., whether it transports proton ( $H^+$ ) or hydroxide ( $OH^-$ ), the polymer electrolyte membrane fuel cells can be divided into proton exchange membrane fuel cells (PEMFCs) or hydroxide exchange membrane fuel cells (HEMFCs). Alternatively, the low-temperature fuel cells have a variety of fuel choices with different energy densities for different applications (Figure 1.1), among which  $H_2$  and methanol are the most widely studied ones. The fuel cells with  $H_2$  as the fuel are termed as  $H_2$ -fueled PEMFCs/HEMFCs and with methanol as the fuel termed as direct methanol fuel cells (DMFCs). DMFC is a special type of PEMFC or HEMFC, however, PEMFC/HEMFC are conventionally used to denote the  $H_2$ -fueled ones.

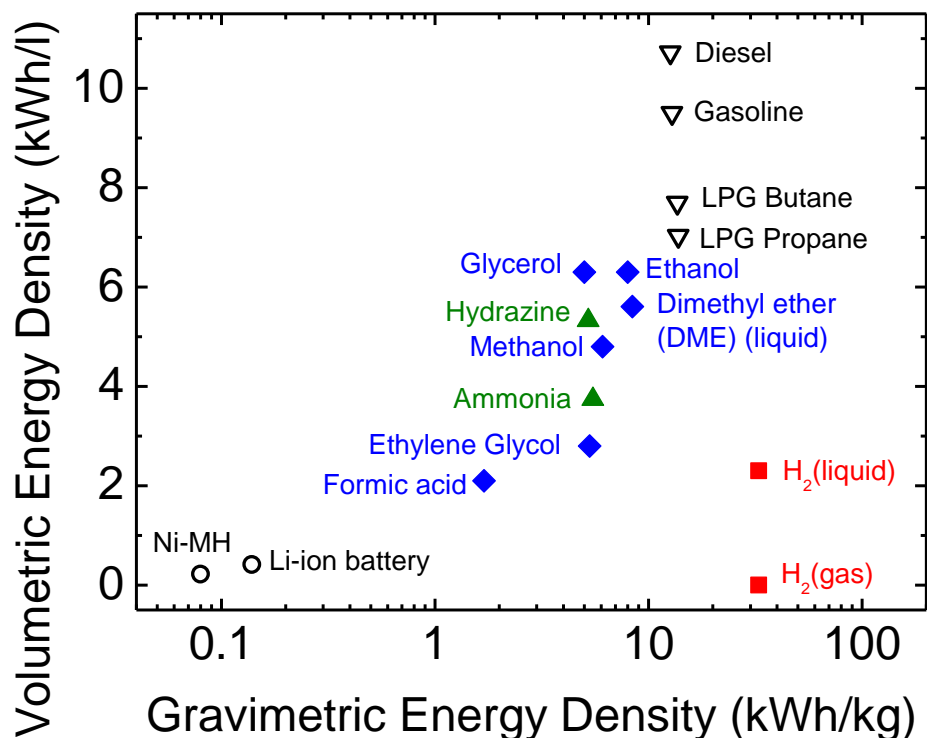


Figure 1.1 Gravimetric and volumetric energy densities of various fuels/devices. Solid points represent fuels of technical interest for low-temperature fuel cells.

The energy density of the fuel is an important parameter from practical application perspective, which is defined with respect to the weight (kWh/kg) or volume (kWh/L) as

$$W_e = (-\Delta G/3600 M) \text{ or } W_s = (-\Delta G \rho/3600 M) \quad (1.1)$$

where  $W_e$  and  $W_s$  are the gravimetric and specific energy density, respectively,  $\Delta G$  is the Gibbs free energy of fuel oxidation,  $M$  is the molecular weight (g/mol) and  $\rho$  is the density (g/L). Among various fuels,  $H_2$  has the highest gravimetric energy density, which is about one order of magnitude higher than those of small organic compounds (blue diamonds and green triangles in Figure 1.1). The liquid small organic fuels such

as methanol, ethanol, glycerol, ethylene glycol and formic acid have comparable or much higher volumetric energy densities compared with H<sub>2</sub> (Figure 1.1). Methanol is the most widely studied one among the liquid fuels due to its higher selectivity to CO<sub>2</sub> compared with other alcohols with more than one carbons.

### 1.1.1 H<sub>2</sub>-Fueled Fuel Cells: PEMFC vs. HEMFC

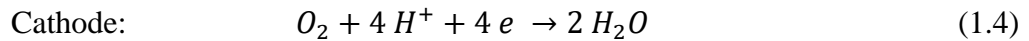
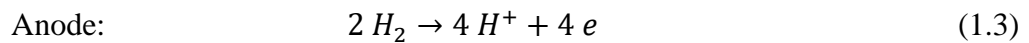
The H<sub>2</sub>-fueled fuel cells are very promising due to the high gravimetric energy density of H<sub>2</sub> as well as its zero-emission nature. The PEMFC and HEMFC share the same overall reaction (Eq. 1.2).



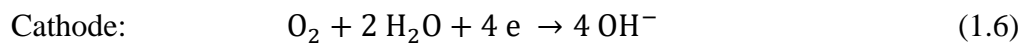
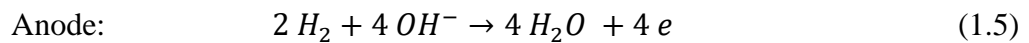
Figure 1.2 depicts the structures of PEMFC and HEMFC: the major component is the membrane electrode assembly (MEA), which is a membrane coated with anode and cathode catalysts on its both sides. The membrane in PEMFCs is a proton-exchange membrane (PEM) which transports H<sup>+</sup>, while that in HEMFCs is a hydroxide exchange membrane (HEM) which conveys OH<sup>-</sup>. The nature of the PEM and HEM determine that the PEMFCs have an acidic operating environment whereas HEMFCs have an alkaline operating environment.

The half-reactions at anode and cathode for PEMFCs and HEMFCs are:

PEMFCs



HEMFCs



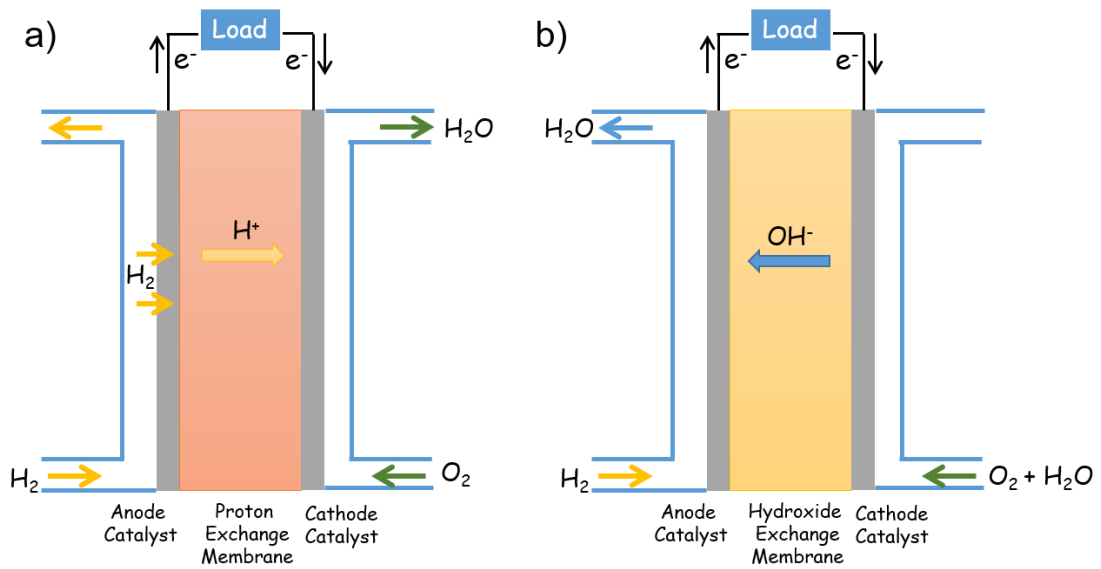


Figure 1.2 Schemes of the structure of a H<sub>2</sub>-fueled (a) proton exchange membrane fuel cell (PEMFC) and (b) hydroxide exchange membrane fuel cell (HEMFC).

The cell voltage ( $E$ ) is related to the Gibbs free energy of overall reaction ( $\Delta G$ ) by Eq. 1.7,

$$E = -\Delta G/nF \quad (1.7)$$

where  $E$  is the cell voltage,  $n$  is the number of electron transferred and  $F$  is the Faraday constant (96485 C/mol). Additionally, the cell voltage is temperature-dependent according to Eq. 1.8 estimated assuming that the reaction enthalpy ( $\Delta H$ ) and reaction entropy ( $\Delta S$ , -163 J/mol/K) are temperature independent.

$$E(T) = E(T_0) + \Delta S (T - T_0)/nF \quad (1.8)$$

Therefore, the cell voltage is 1.23 V at 298 K, 1 atm  $P_{H_2}$  and 1 atm  $P_{O_2}$  and 1.18 V at 353 K. However, the actual cell voltage is smaller than its theoretical value due to voltage losses including kinetic losses from both anode and cathode, internal resistance ( $iR$ ) loss and mass transport loss. Catalysts have to be used at both anode and cathode

to facilitate the electrochemical reactions and reduce kinetic losses. Pt is the state-of-art catalysts for both HOR and ORR.

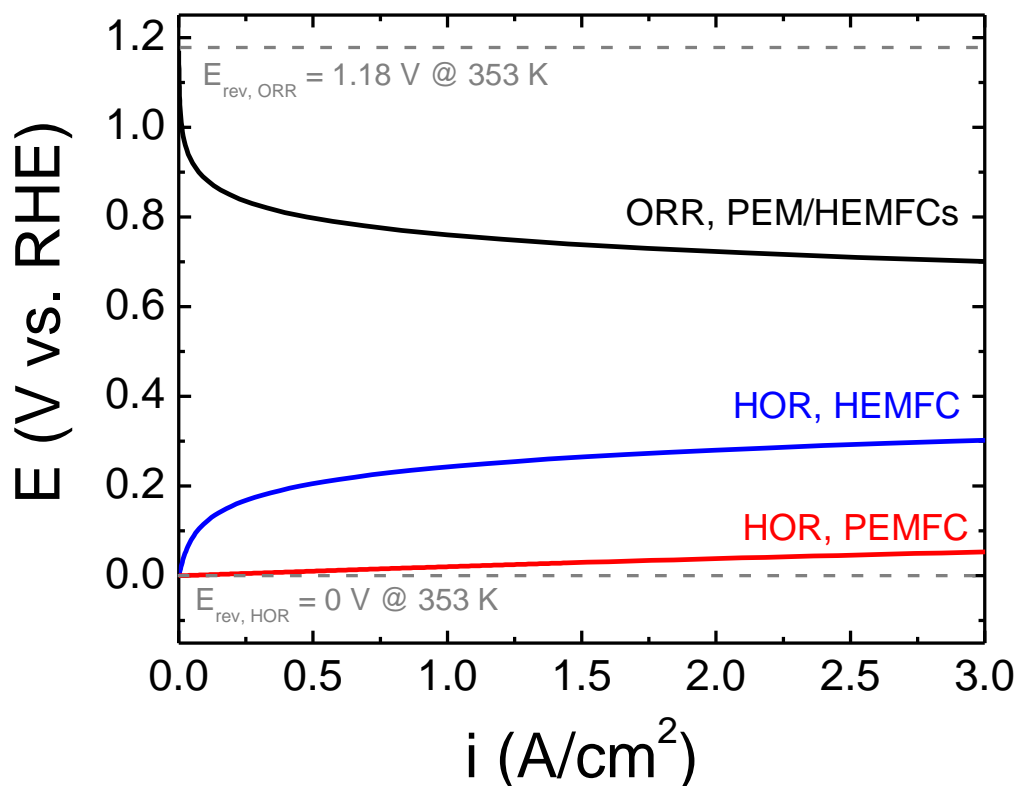


Figure 1.3 Simulated polarization curves of HOR and ORR in PEMFC and HEMFC operating at 353 K. The HOR polarization curves are simulated based on a Pt loading of  $5 \mu\text{g}/\text{cm}^2_{\text{disk}}$  which corresponds to a roughness factor of about 3 if the ECSA of Pt/C is  $60 \text{ m}^2/\text{g}_{\text{Pt}}$ , and estimated HOR exchange current densities in the HEMFC and PEMFC of  $3.7 \text{ mA}/\text{cm}^2_{\text{Pt}}$  and  $433 \text{ mA}/\text{cm}^2_{\text{Pt}}$  at 353 K based on  $i_0$  and activation energies from Ref[2,3].

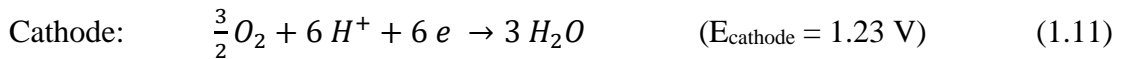
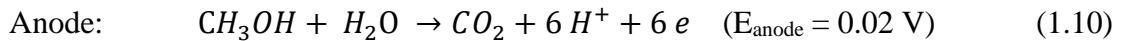
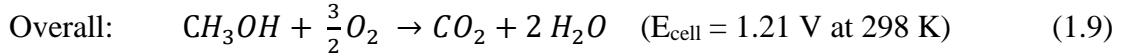
PEMFCs are extensively researched over the decades, which are characterized with high peak power density and are promising for powering automobiles. The sluggish ORR kinetics contributes to about 300 – 400 mV potential loss compared on the cathode

compared with negligible HOR potential loss on the anode (Figure 1.3), therefore, efforts are mainly devoted to the development of ORR catalysts, and a 10 to 20 times enhancement in ORR specific activity has been achieved on Pt-transition metal alloy such as PtNi and PtY.[4-6] Toyota has launched its PEMFC powered vehicle Mirai at the end of 2015. However, only precious metal catalysts can survive the acidic nature of PEMFCs, and the high cost and scarcity of Pt remains a drawback in the long-term economic consideration.

HEMFCs, on the other hand, offer the opportunity to replace the costly precious metal catalysts with non-precious metal or metal free catalysts, which could greatly reduce the cost of fuel cells. Progress has been achieved on the development of HEMs.[7-9] Although the ORR overpotential in HEMFC is still as large as that in PEMFC due to the same kinetics in acid and base on Pt (Figure 1.3), it is considered a less issue since non-precious metal catalyst for ORR have been developed with compared activity as Pt with a loading of 300 – 400  $\mu\text{g}/\text{cm}^2$  for HEMFC application.[10-13] Contrarily, there is very few reports on non-precious metal for HOR. Additionally, the kinetics of HOR on Pt-group metals (PGMs) is about one to two orders of magnitudes slower in base than in acid,[2,3] resulting in a significantly larger HOR overpotential in HEMFC than in PEMFC with the same PGM loadings (see an example on Pt/C in Figure 1.3). To achieve the same HOR performance of PEMFCs, a much higher Pt amount is demanded for HEMFCs, which is not cost effective. Fundamental studies on understanding the puzzling pH-dependent HOR activity and revealing the active sites towards HOR will be beneficial for future design and development of novel HOR catalysts especially non-precious metal catalysts for application in HEMFCs.

### 1.1.2 Direct Methanol Fuel Cells

DMFC is an interesting alternative to H<sub>2</sub>-fueled fuel cells for powering vehicles and portable devices.[14,15] The structure of a DMFC is similar to that of H<sub>2</sub>-fueled fuel cells, except that methanol is fed as the fuel. The overall reaction as well as the anode and cathode reactions in a DMFC are



The benefits of using methanol as the fuel include, 1) methanol has a high energy density (gravimetric energy density 6.1 kWh/kg, volumetric energy density 4.8 kWh/L), 2) methanol is liquid and thus easy to handle, store and transport, which can be easily distributed by the present infrastructure for liquid fuels, 3) methanol is cheap and can be obtained from sustainable sources through fermentation of agricultural products, 4) methanol can be completely oxidized to CO<sub>2</sub> compared with ethanol. Despite those advantages of methanol, DMFCs are characterized with lower energy density and efficiency compared with H<sub>2</sub>-fueled PEMFCs due to the sluggish methanol oxidation reaction (MOR) at anode as well as the crossover of methanol from the anode to the cathode.[14] The slow MOR kinetics lead to a large overpotential at the anode of about 350 mV even with the state-of-art PtRu catalyst. Therefore, developing MOR catalysts with high activity is of great necessity for commercialization of DMFCs.

## 1.2 Hydrogen Oxidation Reaction

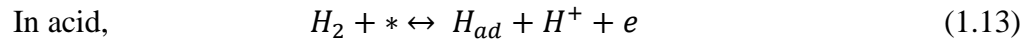
### 1.2.1 Reaction Mechanisms

Hydrogen oxidation/evolution reaction (HOR/HER) (Eqs. 1.3 and 1.5) is a two-electron transfer, multistep reaction, which is generally considered to go through either a Tafel-Volmer pathway or a Heyrovsky-Volmer pathway.[16]

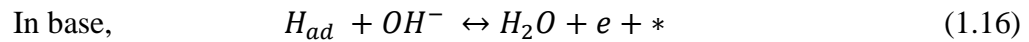
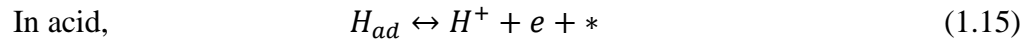
Tafel:



Heyrovsky:



Volmer:



where \* represents a free surface site, and  $H_{ad}$  represents an adsorbed hydrogen atom on the electrode surface. Permutations of these three steps lead to four possible reaction pathways include Tafel (rate determining step, RDS)-Volmer, Tafel-(Volmer), Heyrovsky (RDS)-Volmer, Heyrovsky-Volmer (RDS), and their respective rate equations are summarized in Table 1.1 (Eq. 1.17 to Eq. 1.19). (See Refs[17,18] for more detailed derivation) More mathematically involved rate expressions are needed when the rates of the two elementary steps involved in the mechanism are comparable.[19] When the reaction is completely limited by the diffusion of  $H_2$  or  $H^+$ , the rate equation is shown as Eq. 1.20 in Table 1.1.

Despite the seemingly straightforward reaction pathways and the large amount of research effort devoted to these two reactions, there is still much debate regarding the

reaction mechanism and RDS, as well as key descriptors to predict catalysts' HOR/HER activities. Tafel slope (TS), the potential needed for one order of magnitude increase in current, could be used to differentiate potential RDSs[20]: TS is  $2.303RT/2F$  (~29 mV/dec at 293 K) when the Tafel step is the RDS, while TS is  $2.303RT/\alpha F$  (~116 mV/dec at 293 K for  $\alpha = 0.5$ ) when Volmer or Heyrovsky is rate limiting. Tafel-Volmer (RDS), Heyrovsky-Volmer (RDS) and Heyrovsky (RDS)-Volmer have similar rate equations and identical TS, and therefore, these reaction pathways cannot be differentiated by measuring TS. It is worth noting that the TS for diffusion-limited reactions is identical to the cases when Tafel is RDS, which underscores the importance of obtaining intrinsic kinetic information. Vogel et al. studied the hydrogen oxidation reaction mechanism by comparing the kinetic parameters obtained both electrochemically in 96 wt%  $H_3PO_4$  electrolyte and from the gas-phase from  $H_2$ - $D_2$  exchange on Pt, and concluded that the dual-site dissociation adsorption of  $H_2$  (or the Tafel step) is the rate determining rate based on the similar kinetic rates obtained from both methods as well as the well-established  $H_2$ - $D_2$  exchange mechanism.[21] An additional limiting current was observed below the diffusion limiting current at low overpotential region in the HOR polarization curve on a Pt microelectrode in acid, which has been attributed to the limiting rate of the Tafel step.[22,23] Meanwhile, Sheng et al. argued against the hypothesis of the Tafel step being the RDS in alkaline electrolyte (0.1 M KOH) on Pt on the basis of the excellent fitting of the kinetic current into a Butler-Volmer equation with  $\alpha = 0.5$  (similar to Eq. 1.18 or 1.19) assuming the Tafel step is not rate determining.[2] Satisfactory fitting was also obtained for the HOR/HER kinetic current on Pt/C measured using  $H_2$ -pump in a PEMFC configuration,[3] indicating that Tafel step is not the RDS in acid either. Sheng et al. tentatively

hypothesize that Heyrovsky (RDS)-Volmer is the reaction pathway based on the significantly higher activation barrier of the Heyrovsky step ( $\sim 0.8$  eV) than that of the Volmer step ( $\sim 0.15$  eV) from density functional theory (DFT) calculations on Pt(111).[2] Higher exchange current density was obtained for the Tafel step than Heyrovsky step by fitting the experimental HOR data into a dual-pathway model,[23,24] indicating the Tafel-Volmer pathway is preferred. More recently, the Volmer step is considered to be rate determining deduced from observations of: 1) the correlation between the HOR/HER activity and the binding energy of underpotential deposited hydrogen ( $H_{\text{upd}}$ ) from cyclic voltammogram (CV), which is identical to the Volmer step,[3,25] and 2) identical activity determined electrochemically from HOR/HER measurement and from  $H_{\text{upd}}$  charge transfer resistance (CTR).[3,26,27]

Table 1.1 Rate equation for HOR/HER with different RDS in the reaction pathway

Reaction pathway	Rate equation
Tafel (RDS)-Volmer	$i_k = i_{0,T} \frac{\exp\left(\frac{2F\eta}{RT}\right) - 1}{[\theta_H^0 + (1 - \theta_H^0) \exp\left(\frac{F\eta}{RT}\right)]^2} \quad (1.17)$
Tafel – Volmer (RDS) or Heyrovsky-Volmer (RDS)	$i_k = 2 i_{0,V} \left[ \frac{\theta_H}{\theta_H^0} \exp\left(\frac{\alpha_V F \eta}{RT}\right) - \frac{1 - \theta_H}{1 - \theta_H^0} \exp\left(\frac{(\alpha_V - 1) F \eta}{RT}\right) \right] \quad (1.18)$
Heyrovsky(RDS)-Volmer	$i_k = 2 i_{0,H} \left[ \frac{1 - \theta_H}{1 - \theta_H^0} \exp\left(\frac{\alpha_H F \eta}{RT}\right) - \frac{\theta_H}{\theta_H^0} \exp\left(\frac{(\alpha_H - 1) F \eta}{RT}\right) \right] \quad (1.19)$
Diffusion as RDS	$\eta = -\frac{RT}{2F} \ln\left(1 - \frac{i}{i_{l,a}}\right) + \frac{RT}{2F} \ln\left(1 - \frac{i}{i_{l,c}}\right) \quad (1.20)$

\*  $i_k$  is the kinetic current,  $i_{0,T}$ ,  $i_{0,V}$  and  $i_{0,H}$  are the exchange current for Tafel, Volmer and Heyrovsky step, respectively,  $F$  is the Faraday constant,  $\eta$  is the overpotential,  $\theta_H^0$  is the equilibrium hydrogen coverage,  $\theta_H$  is the hydrogen coverage,  $\alpha_V$  and  $\alpha_H$  are the anodic transfer coefficient for Volmer and Heyrovsky step, respectively, and  $i_{l,a}$  and  $i_{l,c}$  are the limiting current for HOR and HER.

### 1.2.2 Hydrogen Binding Energy (HBE) as the Descriptor for HOR Activity

The adsorbed hydrogen ( $H_{ad}$ ) is the key reaction intermediate in HOR/HER (Eqs. 1.12 to 1.16). To achieve high activity, the interaction between the intermediate species and the catalyst surface should be neither too weak nor too strong according to Sabatier's principle.[28] Therefore, the strength of the  $H_{ad}$  – metal interaction, i.e., hydrogen binding energy (HBE) or Gibbs free energy of hydrogen adsorption ( $\Delta G_{H_{ad}}$ ), could be a good descriptor for HOR/HER activity. Exchange current densities ( $i_0$ ) for HER on various metals have been plotted as a function of metal-hydrogen binding energy,[29-33] which yields a “volcano-shaped” correlation, known as the volcano plot (Figure 1.4). The relationship between HER activity and  $\Delta G_{H_{ad}}$  was first derived mathematically by Parsons in 1957,[30] which provided a theoretical foundation for the volcano plot with its peak at  $\Delta G_{H_{ad}} = 0$ . A volcano plot can be generated in each case, i.e., with Volmer, Heyrovsky or Tafel step being RDS (Figure 1.4a, normalized to the maximum of each  $i_0$ ). Assuming a transfer coefficient of 0.5, the slopes of the volcano plot are  $\pm 0.5/2kT$  when Volmer or Heyrovsky is the RDS, whereas slopes of  $0.5/kT$  are expected when Tafel is RDS. The fact that volcano plots could be derived with a single RDS shows that shifting RDSs is not a prerequisite for volcano plots. A further implication is that the RDS on a catalyst cannot be determined solely based on the relative positions of the peak of the volcano plot and the catalyst. A modified volcano plot with a plateau on top was also proposed by Parsons when a Temkin isotherm was used to describe hydrogen adsorption.[30] However, there is no compelling evidence for the existence of the plateau based on the correlation between  $i_0$  and metal-H binding energy/ $\Delta G_{H_{ad}}$ . [29] An early version of volcano curve was created by plotting the  $i_0$  of HER on different metals in acidic electrolytes against the M-H bond strength either determined electrochemically or derived from metal hydride formation (Figure

1.4b).[29,34,35] Later on, Nørskov et al. plotted the same set of  $i_0$  data against the hydrogen chemisorption energies obtained by density functional theory (DFT) based calculations (black circles in Figure 1.4c).[34] It was recently recognized that  $i_0$  of the PGMs (Pt, Pd, Ir and Rh) obtained in early studies with the rotating disk electrode (RDE) method are likely underestimated due to the facile kinetics of HER on those metal surfaces and the mass transport limitation of  $H_2$ . [2,3,36] Durst et al. recently re-determined the HER activities on Pt, Pd, Ir and Rh in acid, and obtained slope of  $\ln(i_0)$  vs.  $\Delta G_{H_{ad}}$  approaching  $1/kT$  (red open squares in Figure 1.4c).[33] Considering the difference in HER activity between acidic and alkaline electrolyte, Sheng et al. plotted the  $i_0$  for HER in 0.1 M KOH vs. calculated HBE, and verified that HBE was also a good descriptor for HER activity in alkaline electrolytes.[32] It is worth noting that Co, Ni and Fe are located in the weakly bonded branch when the gas-phase M-H bond energies are used as the descriptor (Figure 1.4b), but in the strongly bonded branch plotting against the DFT-calculated HBEs (Figure 1.4c and 1.4d). The discrepancy could be attributed to the fact that Co, Ni and Fe absorb large amounts of hydrogen, resulting in weakened measured M-H bond strengths compared with the calculated ones.[37] Although  $i_0$  in the volcano plots were measured for HER, the definition of exchange current density and the highly reversible nature of HOR and HER entail that the measured exchange current density represents the intrinsic activity the catalyst for both HOR and HER.

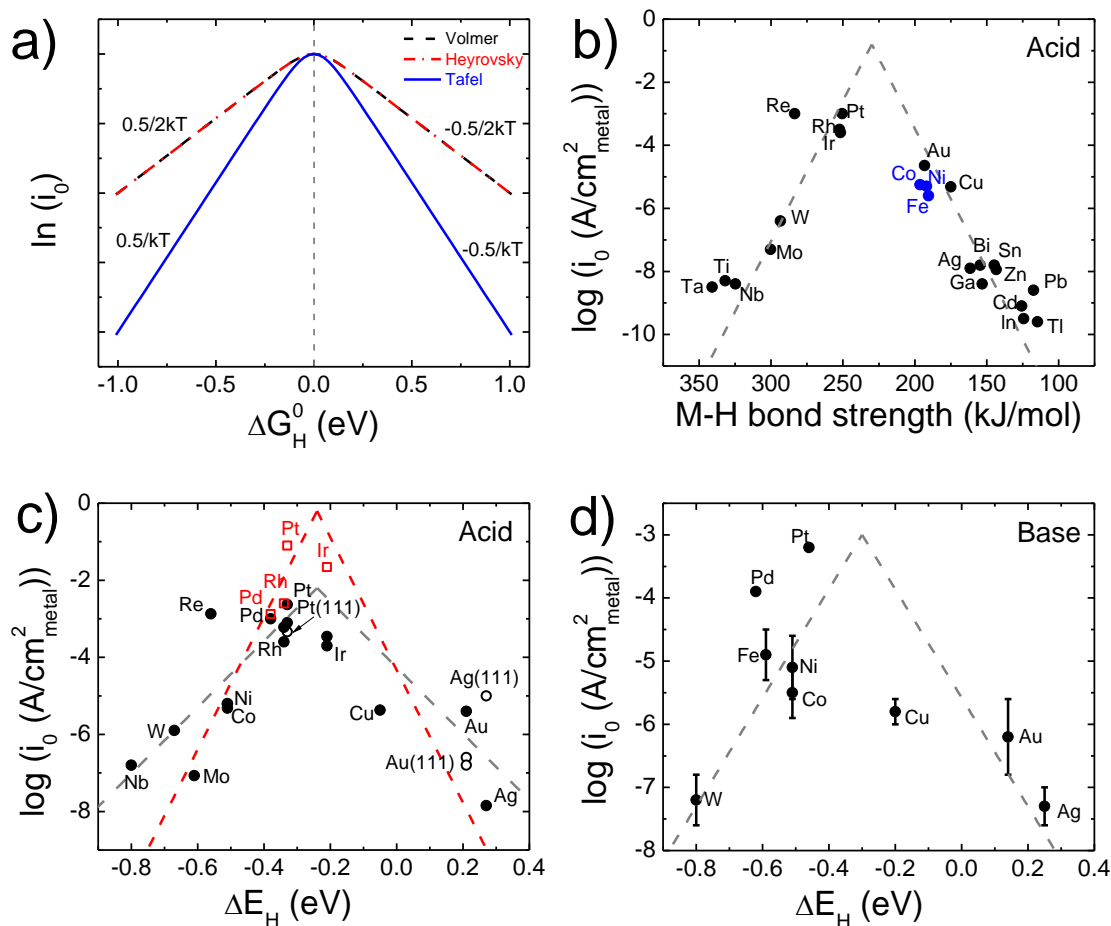


Figure 1.4 Volcano plots constructed by (a) theoretical calculation based on the kinetic equations derived by Parson assuming Volmer, Heyrovsky or Tafel step as rate determining, respectively,[30] (b) correlating HER exchange current densities on various metals in acidic electrolytes collected by Trasatti[29] vs. metal-hydrogen bond strength measured from gas phase[35], (c) correlating HER exchange current densities on various metals in acidic electrolytes collected by Trasatti[29] vs. hydrogen binding energy (HBE) calculated using density functional theory (DFT) by Nørskov et al. (black circles)[31], red hollow squares represent exchange current densities on Pt, Ir, Rh and Pd determined using H<sub>2</sub>-pump in a proton exchange membrane fuel cell configuration,[33,38] and (d) correlating HER exchange current densities on various metals in 0.1 M KOH vs. DFT-calculated HBE by Sheng et al.[32]

### 1.2.3 Kinetic Study of HOR/HER

Kinetic studies of HOR/HER are key to evaluating the intrinsic activity of catalysts and elucidating reaction mechanisms. The intrinsic HOR/HER activity is typically expressed in terms of the exchange current density ( $i_0$ ), which is defined as the HOR and HER current densities at the equilibrium potential when the net current is zero. Most HOR kinetic studies focus on the Pt-group metals (PGMs, Pt, Ir, Pd, Rh and Ru), because other metals either barely show any HOR activity or are unstable under HOR conditions.  $i_0$ , transfer coefficients ( $\alpha$ ) and activation energies ( $E_a$ ) obtained with a variety of different methods on PGMs are summarized in Table 1.2. HOR/HER activities on PGMs follow the sequence of Pt > Ir  $\approx$  Rh  $\gg$  Pd  $\approx$  Ru, and Pt > Ir > Rh  $\approx$  Pd in the alkaline in acidic electrolytes, respectively (Table 1.2). HOR/HER activities on Pt, Ir and Rh in acid were determined to be on the order of 1 mA/cm<sup>2</sup><sub>M</sub> with the rotating disk electrode (RDE) method in several reports,[39-41] which are likely underestimated. Gasteiger et al. measured the PEMFC performance with varied anode catalyst (Pt) loadings, and observed no obvious performance loss when the anode Pt loading was reduced from 0.40 to 0.05 mg<sub>Pt</sub>/cm<sup>2</sup>, which led to the conclusion that the intrinsic HOR/HER activity of Pt is  $\sim$ 27 mA/cm<sup>2</sup><sub>Pt</sub>. [36] This discrepancy in HOR/HER activities was resolved by Sheng et al. by pointing out the difficulty in quantifying HOR/HER kinetics on Pt in acidic electrolyte with RDE measurements because the HOR/HER rate is completely diffusion limited.[2] Using high mass transport HOR/HER measurements, such as H<sub>2</sub>-pump, ultramicroelectrode (UME) and scanning electrochemical microscopy (SECM), HOR/HER activities on Pt in acid were determined to be in the range of 20 to 70 mA/cm<sup>2</sup><sub>Pt</sub> at r.t. (Table 1.2). Therefore, HOR/HER activities determined from RDE measurements ( $\sim$ 1 mA/cm<sup>2</sup>) are likely significantly underestimated, which will be discussed in detail in Chapter 2.

Table 1.2 Summary of exchange current density ( $i_0$ ), anodic transfer coefficient ( $\alpha_a$ ), activation energy ( $E_a$ ) and technique for HOR/HER kinetic study on Pt, Ir, Pd, Rh and Ru in alkaline or acidic electrolytes.

Metal	Electrolyte	$i_0$ (mA/cm <sup>2</sup> <sub>M</sub> )	$\alpha_a$	$E_a$ (kJ/mol)	Technique	Ref
Pt (pc)	0.1 M KOH	0.69 ± 0.03	0.5	28.9 ± 4.3	RDE	[2]
Pt/C	0.1 M KOH	0.57 ± 0.07	0.5	29.5 ± 4.0	RDE	[2]
Pt(111)	0.1 M KOH	0.035	-	46	RDE	[42]
Pt(100)	0.1 M KOH	0.05 (273 K)	-	-	RDE	[42]
Pt(110)	0.1 M KOH	0.3	-	23	RDE	[42]
Pt(pc)	0.1 M KOH	0.7 ± 0.1	-	30 ± 3	RDE	[43]
Pt/C	0.1 M KOH	1.0 ± 0.1 (313 K)	0.38 ± 0.08	-	RDE	[3]
Pt/C	Base (pH = 14)	2.60 ± 0.03 (333 K)	0.5	-	H <sub>2</sub> -pump, HEMFC	[44]
Pt(111)	0.05 M H <sub>2</sub> SO <sub>4</sub>	0.45 (303 K)	-	18	RDE	[45]
Pt(100)	0.05 M H <sub>2</sub> SO <sub>4</sub>	0.60 (303 K)	-	12	RDE	[45]
Pt(111)	0.05 M H <sub>2</sub> SO <sub>4</sub>	0.98 (303 K)	-	9.5	RDE	[45]
Pt(pc)	0.01 M HClO <sub>4</sub> / 0.1 M NaClO <sub>4</sub>	60 ± 20	0.5	-	SECM	[46, 47]
Pt/C	0.1 M HClO <sub>4</sub>	27.2 ± 3.5	-	43	RDE	[48]
Pt/C	0.1 M H <sub>2</sub> SO <sub>4</sub>	19 - 40	-	-	UME	[22]
Pt/C	Acid (pH = 0)	216 ± 50 (313 K)	0.52 ± 0.06	-	H <sub>2</sub> -pump, PEMFC	[3]
Pt/C	Acid (pH = 0)	120 ± 40 (313 K)	-	16 ± 2	H <sub>2</sub> -pump, PEMFC	[38]
Ir/C	0.1 M NaOH	0.37 ± 0.12 (313 K)	0.48 ± 0.02	-	RDE	[3]
Ir/C	0.1 M KOH	0.21 ± 0.02	0.56 ± 0.03	32.9 ± 1.5	RDE	[49]
Ir/C	0.5 M H <sub>2</sub> SO <sub>4</sub>	1.34 (298 K)	-	-	RDE	[50]
Ir/C	Acid (pH = 0)	45 ± 8 (313 K)	0.51 ± 0.01	-	H <sub>2</sub> -pump, PEMFC	[3]
Ir/C	Acid (pH = 0)	36 ± 3	-	19 ± 3	H <sub>2</sub> -pump, PEMFC	[38]
Pd/C	0.1 M NaOH	0.06 ± 0.02 (313 K)	0.43 ± 0.07	-	RDE	[3]
Pd/C	Acid (pH = 0)	5.2 ± 1.2 (313 K)	0.35 ± 0.1	-	H <sub>2</sub> -pump, PEMFC	[3]
Pd/C	Acid (pH = 0)	3.0 ± 0.6 (313 K)	-	31 ± 2	H <sub>2</sub> -pump, PEMFC	[38]
Rh/C	0.5 M H <sub>2</sub> SO <sub>4</sub>	0.677 (298 K)	-	-	RDE	[41]

Rh/C	Acid (pH = 0)	$5.2 \pm 0.2$ (313 K)	-	$28 \pm 1$	H <sub>2</sub> -pump, PEMFC	[38]
Ru/C	0.1 M NaOH	0.03 (298 K)	-	-	RDE	[51]

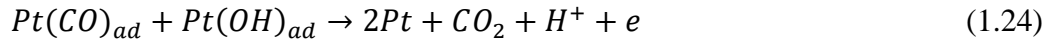
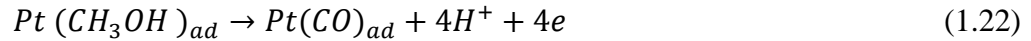
HOR/HER activities on PGMs in acidic electrolyte are much higher than those in alkaline electrolyte (Table 1.2). Debates exist on whether the HBE is the sole and unique descriptor for HOR/HER activity and much lower activity in alkaline electrolyte is attributed to the stronger HBE or there is a change in reaction mechanism from acid to base.[3,25,52,53] A systematic HOR/HER kinetic studies on PGMs over a wide range of pH will be beneficial.

### 1.3 Methanol Oxidation Reaction

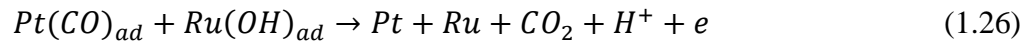
The methanol oxidation pathway is very complex since the complete oxidation of methanol is a six-electron transfer, multistep reaction (Figure 1.5). Besides CO<sub>2</sub> as the product for a complete oxidation reaction of methanol, HCHO, HCOOH and HCOOCH<sub>3</sub> are also detected (Figure 1.5). MOR is considered to go through dual pathways including indirect pathway via formation of adsorbed CO species (CO<sub>ad</sub>) as intermediate and direct pathway via intermediates such as HCHO and HCOOH.[54] For both pathways, the oxidation of methanol consists of the following steps 1) methanol adsorption and dehydrogenation, 2) water dissociation and 3) CO<sub>2</sub> formation. Pt is a good catalyst for methanol adsorption and C-H bond breaking, which has been widely adopted for MOR mechanistic studies. For Pt, the direct pathway dominates at low overpotential where CO<sub>ad</sub> is very stable with a relatively low rate, while both pathways occur at high overpotential.[55,56] Therefore, the indirect pathway is focused.

In an indirect pathway, methanol, upon adsorption on Pt (Eq. 1.21), goes through a series of dehydrogenation steps to form CO<sub>ad</sub> (Eq. 1.22). The CO<sub>ad</sub> is a poisoning intermediate species binding strongly to the Pt surface and blocking the active sites,

which can be removed by adsorbed OH formed through water dissociation (Eqs. 1.23 and 1.24). On pure Pt, it is only possible to have sufficient water-catalyst surface interaction at potentials greater than 0.45 V,[54] therefore, the dissociation of water on Pt surface is the rate determining step at potentials of technical interest for DMFCs (< 0.6 V vs. RHE).



The MOR activity of Pt can be promoted by introducing other metals such as Ru, Sn, Mo, Bi and Os in the forms of either adatoms or alloys.[15] PtRu alloys are considered to be the best bimetallic catalyst for MOR.[57] The promotional effect of Ru can be explained by the “bifunctional” mechanism and/or ligand (electronic) mechanism.[54,58] For “bifunctional” mechanism, Pt adsorbs and dehydrogenates methanol while Ru dissociates water to form OH<sub>ad</sub> at a relatively lower overpotential (Eq. 1.25), which facilitates the removal of CO<sub>ad</sub> on Pt (Eq. 1.26).



Meanwhile, Ru could alter the electronic structure of Pt by lowering the d-band center of Pt, which weakens the Pt-CO bonding and makes the CO<sub>ad</sub> easier to be removed.

PtRu nanoparticles supported on high surface area carbon is the state-of-art catalyst for MOR. Despite of the much enhanced activity of PtRu compared with Pt, the onset potential of MOR is still as high as 300 mV, which needs to be lowered. The catalytic activity of PtRu is known to be dependent on the PtRu composition, structure,

morphology, particle size and alloy degree.[57] Extended PtRu nanostructures such as PtRu nanotubes and nanowires are of particular interest for preferentially exposing of certain facets and facilitating mass transport when applied into a real fuel cell,[59] which will be explored in this dissertation.

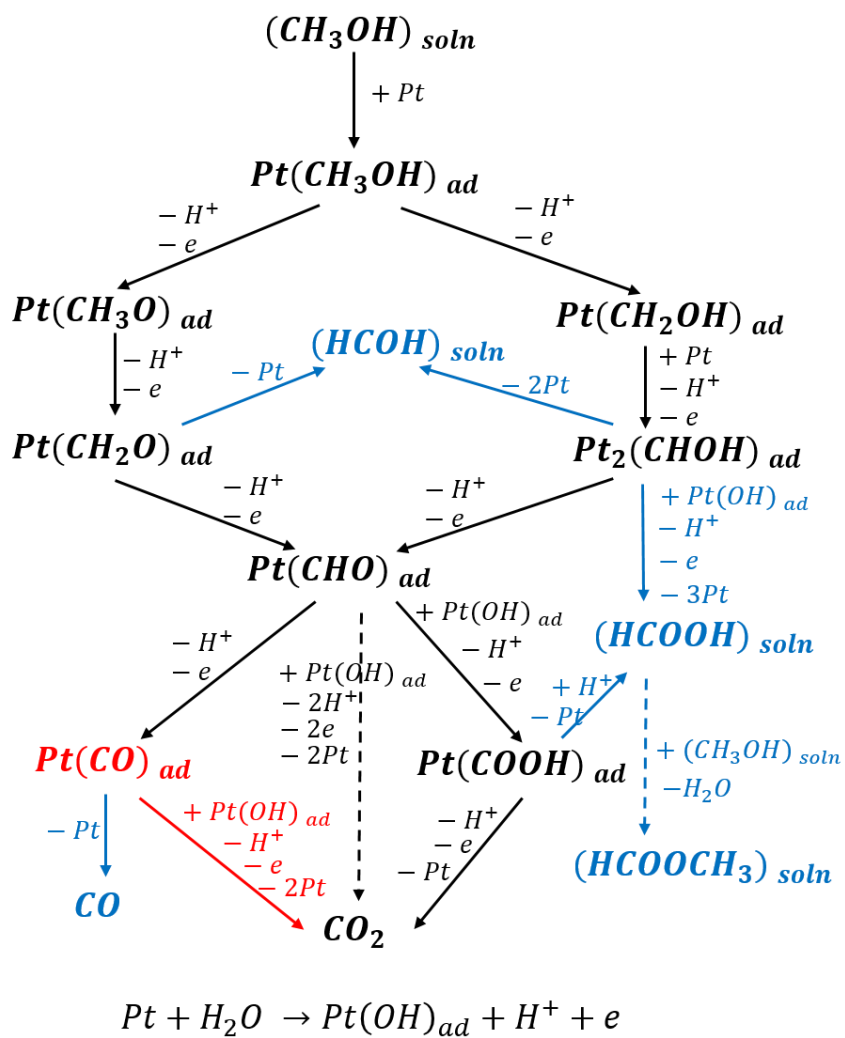


Figure 1.5 Detailed pathway for methanol oxidation. Possible products besides  $CO_2$  are indicated in blue. The pathway with formation of adsorbed CO species ( $CO_{ad}$ ) is called indirect pathway, while that without formation of  $CO_{ad}$  is called direct pathway.

## 1.4 Structure of Current Dissertation

Fundamental understanding of the reaction kinetics and synthesizing nanomaterials with well-defined structure are the two important aspects of catalyst design and development. This dissertation is mainly focused on the anode catalyst development and structured as follows with Chapter 2 to Chapter 5 dealing with the fundamental studies of HOR for HEMFC and Chapter 6 presenting the study on synthesizing nanomaterials for MOR for DMFC.

In Chapter 2, we identified that HER can also be limited by diffusion when its kinetic is facile and established the protocol for correcting the HOR/HER diffusion limitation in RDE measurements for HOR/HER. The origin of HER diffusion limitation was discussed, and the impact of the failure to correct the HER diffusion overpotential or correcting the HOR/HER overpotential using the widely-used irreversible Koutecky-Levich equation on the HOR/HER activity determination and mechanistic interpretation was also demonstrated. The protocol provided in this chapter has been adopted in Chapter 3 to 5 for calculating HOR/HER kinetic currents.

In Chapter 3, efforts were devoted on the identification of the most active sites for HOR/HER on carbon supported iridium nanoparticles (Ir/C) by correlating the HOR/HER activities on Ir/C with varying sizes from 3-12 nm with the amount of sites with different HBEs quantified from  $H_{\text{upd}}$  desorption profiles in CVs. A detailed HOR/HER kinetic study was carried out on Ir/C in 0.1 M KOH and the particle size effect on HOR/HER activity was explored which could potentially bridge the activity gap between bulk electrode and supported nanoparticles.

In Chapter 4, we extended the particle size effect on HOR/HER activities investigation to carbon supported palladium nanoparticles with size ranging from 3 to 42 nm in both acid and base using RDE measurement. The exchange current densities

( $i_0$ ) were determined using three different methods. The HOR/HER activation energies on Pd/C in acid and base were determined and correlated with the activity difference between acid and base.

In Chapter 5, the pH-dependent HBE and HOR/HER activities were explored on supported Pt-group metals (Pt/C, Ir/C, Pd/C and Rh/C) in electrolytes with a broad pH range from 0 to 13, and a universal correlation between  $i_0$  and HBE was established quantitatively. The HOR/HER activation energies on the four metals were determined in 0.1 M KOH and compared with the values measured using H<sub>2</sub>-pump in a PEMFC configuration (which is equivalent to pH = 0) from literature. In addition, the pH-dependent CO-stripping onset potentials were also investigated in order to address whether OH<sub>ad</sub> plays a role in promoting HOR/HER.

In Chapter 6, we synthesized platinum-ruthenium nanotubes (PtRuNTs) and platinum-ruthenium coated copper nanowires (PtRu/CuNWs) via complete and partial galvanic displacement reactions using CuNWs as templates, evaluated their performance towards methanol oxidation and compared their MOR activities with the benchmark MOR catalyst PtRu/C. The Pt/Ru compositional effect on MOR activity was also explored. The electronic properties were measured by X-ray photoelectron spectroscopy (XPS) and used to explain the activity enhancement on PtRuNTs and PtRu/CuNWs.

Chapter 7 summarizes the studies in this dissertation and gives future perspectives.

## Chapter 2

### **CORRECTING DIFFUSION LIMITATION IN ROTATING DISK ELECTRODE MEASUREMENT OF HYDROGEN OXIDATION/EVOLUTION REACTION KINETICS**

Rotating disk electrode (RDE) method is widely employed in studies on the hydrogen oxidation/evolution reaction (HOR/HER) owing to its well-defined mass transport behaviors. While it is accepted that the measured HOR current is controlled by both the electrode kinetics and the diffusion of  $H_2$ , HER is typically assumed free of diffusion limitation. Here we demonstrate that HER could also be diffusion limited when the electrode kinetics is fast, as evidenced by the rotating speed dependent HER current on Pt in acid ( $pH = 1$ ) and the overlap of the HER polarization curve with the concentration overpotential curve. The HER diffusion limitation originates from the insufficient mass transport of produced  $H_2$  from the electrode surface to the bulk electrolyte and the highly reversible nature of HOR/HER. Kinetic analyses based on HER polarization curves on Pt in acid without correcting for the diffusion limitation could lead to inaccurate Tafel slopes and mechanistic interpretations, and significantly underestimated HER activities. A general data analysis protocol based on the reversible Koutecky-Levich equation is developed to obtain accurate kinetic information of HOR/HER even when electrode kinetics is facile. This new method is compared with other existing methods on Pt disk electrodes at different pHs and thin-film electrodes with different Pt loadings.

## 2.1 Introduction

Rotating disk electrode (RDE) method is widely adopted to quantitatively evaluate the intrinsic kinetics of electrochemical reactions, including HOR/HER[2,60,61] and oxygen reduction/evolution reaction (ORR/OER),[62,63] owing to its well-defined mass transport behaviors that can be rigorously derived from hydrodynamics.[64] While ORR activities are typically determined by converting the measured currents at a fixed potential (e.g., 0.9 V vs. RHE) to kinetic currents due to its sluggish reaction kinetics,[65,66] exchange current density ( $i_0$ ) is the more adopted measure of the HOR/HER activity.[2,38] Exchange current density can be determined by either fitting the kinetic current density with the Butler-Volmer equation or extrapolating the Tafel slope to zero overpotential. Accurate measurement of kinetic currents, which is free of the contribution from the mass transport of H<sub>2</sub> to and from the electrode, is key to the reliability of both methods. It is well accepted that HOR can be severely limited by the mass transport of H<sub>2</sub> to the electrode surface, as evidenced by the plateau in the polarization curve or the anodic limiting current at large overpotentials. The mass transport limitation of H<sub>2</sub> in HOR is primarily attributed to the limited solubility of H<sub>2</sub> (<1 mmol/L at room temperature), following the Levich equation[64] as in Eq. 2.1,

$$i_l = 0.62nFAD^{2/3}\nu^{-1/6}c_0\omega^{1/2} = ABC_0\omega^{1/2} \quad (2.1)$$

where  $i_l$  is the limiting current,  $D$  is the diffusivity of hydrogen in electrolyte,  $n$  is the number of electrons transferred in HOR ( $n = 2$ ),  $A$  is the area of the electrode,  $\nu$  is the kinematic viscosity of the electrolyte and  $c_0$  is the solubility of H<sub>2</sub> in electrolyte,  $\omega$  is the rotating rate and  $B = 0.62nFD^{2/3}\nu^{-1/6}$ . The kinetic current for thin-film electrode is then calculated using the Koutecky-Levich equation[60] as in Eq. 2.2,

$$\frac{1}{i} = \frac{1}{i_k} + \frac{1}{i_l} = \frac{1}{i_k} + \frac{1}{ABc_0\omega^{1/2}} \quad (2.2)$$

where  $i$  and  $i_k$  are the measured current and kinetic current, respectively. In contrast, HER is generally assumed to be free of diffusion limitation and indeed no cathodic limiting current is observed in RDE measurements. The lack of diffusion limitation is attributed to the high concentration of  $H^+$  or  $H_2O$  in acidic or alkaline electrolyte. Therefore, measured currents, compensated for the ohmic loss, in the HER branch are considered to be kinetic currents.[67]

The RDE method is unable to quantify the HOR activity on Pt in acid due to the combination of mass transport limitation of  $H_2$  and fast reaction kinetics. The measured current is dominated by the rate of  $H_2$  diffusion to the electrode surface, as evidenced by the overlapping HOR polarization curve and concentration overpotential curve, as defined in Eq. 2.3,[2]

$$\eta_d = -\frac{RT}{2F} \ln\left(1 - \frac{i_d}{i_l}\right) \quad (2.3)$$

where  $\eta_d$  is the diffusion overpotential,  $i_d$  is the diffusion limited current,  $i_l$  is the maximum current from polarization curves,  $R$  is the universal gas constant (8,314 J/(mol·K)),  $T$  is the temperature in Kelvin and  $F$  is the Faraday's constant (96,485 A·s/mol). Thus, the kinetic current of HOR on Pt in acid must be determined by methods free of mass transport limitations, such as  $H_2$ -pump method,[3,38,68] ultramicroelectrode (UME),[22,69] scanning electrochemical microscopy (SECM)[46,47] and floating electrode method.[70] The  $i_0$  of HOR/HER on Pt/C in acid obtained using the  $H_2$ -pump method in a proton exchange membrane fuel cell (PEMFC) configuration is  $\sim 70 \text{ mA/cm}^2_{Pt}$  at 293 K (extrapolated from the Arrhenius plot), with the transfer coefficient ( $\alpha$ ) and Tafel slope determined to be  $\sim 0.5$  and  $\sim 120 \text{ mV/dec}$ , respectively, by fitting the polarization curve with the Butler-Volmer equation.[38]

Several studies of HER on Pt in acid using RDE report Tafel slopes around 30 mV/dec and exchange current densities on the order of 1 mA/cm<sup>2</sup><sub>Pt</sub>,[71-76] which are inconsistent with the results obtained from H<sub>2</sub>-pump measurements.[38] In this chapter, we demonstrate that RDE measurements of HER kinetics on Pt are also limited by mass transport of the produced H<sub>2</sub> from the electrode surface to the bulk electrolyte because the HER kinetics is facile. The evidence collected includes the overlapping of the HER polarization curve with the diffusion overpotential curve and the rotating speed dependence of HER activity. The inefficient diffusion of H<sub>2</sub> formed at the electrode to the bulk electrolyte is proposed to be the origin of HER mass transport limitation. A general data analysis protocol based on Koutecky-Levich equation for reversible reactions is developed to obtain accurate HOR/HER kinetic information. Through comparison with a recently reported method, we show that our proposed approach is equally accurate and more general in extracting kinetic parameters.

## **2.2 Materials and Methods**

### **2.2.1 Preparation of Electrodes and Electrolytes**

The polycrystalline Pt disk was polished using 0.05 μm alumina polishing suspension (Buehler) to a mirror finish prior to electrochemical testing, and the glassy carbon electrodes were pre-polished similarly before preparing thin-film electrodes. Ink suspension of high surface area carbon supported Pt catalyst was prepared by dispersing Pt/C (46.6 wt.%, Tanaka Kikinzoku International, Inc.) into DI water to achieve a concentration of 0.1 mg<sub>Pt</sub>/mL followed by ultrasonication for 1 h to obtain a uniform suspension. Thin-film Pt/C electrodes were prepared by pipetting different amounts of ink solution onto pre-polished glassy carbon electrodes to achieve a final loading of 4

to  $40 \mu\text{g}_{\text{Pt}}/\text{cm}^2_{\text{disk}}$ . 0.1 M  $\text{HClO}_4$ , 0.5 M  $\text{H}_2\text{SO}_4$  and 0.2 M  $\text{H}_3\text{PO}_4$  were prepared by diluting  $\text{HClO}_4$  (67-72%, TraceSELECT, Sigma Aldrich),  $\text{H}_2\text{SO}_4$  (95%, TraceSELECT, Sigma Aldrich) and  $\text{H}_3\text{PO}_4$  (80 %, Sigma Aldrich) with DI water. 0.1 M KOH and 4 M KOH were prepared from KOH tablets (85 wt% and 99.99 % metal trace, Sigma Aldrich). Phosphoric acid/phosphate buffer solutions were prepared by adding different volumes (2 to 10 mL) of 4 M KOH into 100 mL 0.2 M  $\text{H}_3\text{PO}_4$ .

### 2.2.2 Electrochemical Measurements

The electrochemical measurements were performed in a glass cell for rotating electrodes (PINE Research Instrumentation), with a double junction silver/silver chloride ( $\text{Ag}/\text{AgCl}$ ) electrode as the reference electrode, a Pt wire as the counter electrode and a 5 mm diameter polycrystalline Pt disk or a 5 mm diameter glassy carbon as the working electrode using a multichannel potentiostat (Princeton Applied Research). Cyclic voltammograms (CVs) of Pt disk and Pt/C were recorded between  $\sim -0.03$  to 1.1 V vs. RHE in Ar-saturated electrolytes at a scanning rate of 50 mV/s. Hydrogen oxidation/evolution reaction (HOR/HER) polarization curves were obtained by RDE measurement in electrolyte with saturated  $\text{H}_2$ , at a scanning rate of 10 mV/s (for measurement on Pt disk) or 1 mV/s (for measurement on Pt/C electrodes) and rotating speeds ranging from 100 rpm to 3600 rpm at r.t. (293 K). All potentials reported in this work were converted to the reversible hydrogen electrode (RHE) scale. Potential ranges for HER scans were chosen such that no excessive  $\text{H}_2$  bubbling occurred.

The internal resistance was measured after HOR/HER measurement by electrochemical impedance spectroscopy (EIS) from 200 kHz to 100 mHz at open circuit voltage (OCV) and used to obtain internal resistance free (iR-free) potential of

the working electrode. The resistances for 0.1 M HClO<sub>4</sub>, 0.5 M H<sub>2</sub>SO<sub>4</sub> and 0.1 M KOH at 293 K are about 25 Ω, 5 Ω and 40 Ω, respectively.

## 2.3 Results and Discussion

### 2.3.1 Identification of Diffusion Limitation in Measured HER Currents

The HOR/HER polarization curve on Pt disk after internal resistance correction in 0.1 M HClO<sub>4</sub> reaches the plateau at ~-0.06 V vs. RHE and completely overlaps with the concentration overpotential curve as defined by Eq. 3.3 (Figure 2.1), suggesting that both HOR and HER are completely mass transport controlled. To ensure accurate comparison between the polarization curve and diffusion overpotential curve, *i*R correction is essential even for highly conductive electrolytes, e.g., 0.1 M HClO<sub>4</sub> (25 Ω),[2] as evidenced by the significant difference of the polarization curves before and after *i*R correction (blue dashed curve and red solid curve in Figure 2.1, respectively). The lack of *i*R correction in several early studies could be a main cause for not recognizing that the current was completely controlled by the mass transport limitation, which in turn led to significant underestimations of the HOR/HER activity on Pt.[45,77]

Measured currents for the highly reversible HOR/HER are the sum of the anodic (positive) and cathodic (negative) currents from HOR and HER, respectively, according to:  $i = i_{HOR} + i_{HER}$ . Conventionally, the polarization curve at positive overpotentials with positive currents (HOR polarization curve) is referred to as the HOR branch, while the part at negative overpotentials (HER polarization curve) is referred to as the HER branch. It is important to note that HOR and HER occur simultaneously in both branches, albeit with different rates. In this work, we denote the current in the HOR and HER branches as net-HOR and net-HER currents, respectively, to differentiate from the

pure HOR and HER currents. The HOR/HER exchange current density ( $i_0$ ) at 293 K on Pt/C and transfer coefficient ( $\alpha$ ) were determined to be  $\sim 70 \text{ mA/cm}^2_{\text{Pt}}$  and  $\sim 0.5$  respectively, using the  $\text{H}_2$ -pump method in a PEMFC configuration (with an equivalent pH of 0).[38] Since no particle size effect has been observed for Pt regarding HOR/HER,[2,33] the exchange current density and transfer coefficient determined on Pt/C can be used to calculate the kinetic current density ( $i_k$ ) on Pt disk in the HER branch (dashed green line in Figure 2.1) following the Butler-Volmer equation (Eq. 2.4),

$$i_k = i_0 \left[ \exp\left(\frac{\alpha F \eta}{RT}\right) - \exp\left(\frac{(\alpha-1)F \eta}{RT}\right) \right] \quad (2.4)$$

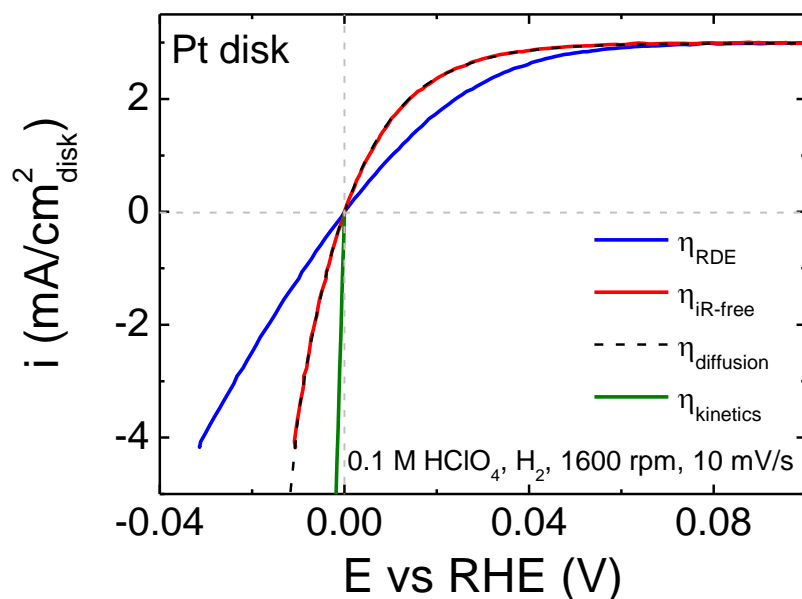


Figure 2.1 HOR/HER polarization curves on a Pt disk in  $\text{H}_2$ -saturated  $0.1 \text{ M HClO}_4$ , at a rotating speed of  $1600 \text{ rpm}$  and a scanning rate of  $10 \text{ mV/s}$  before (blue dashed line) and after (red solid line)  $iR$ -correction. The black dashed line is the calculated concentration overpotential curve, and the green dashed line is the simulated kinetic current using the Butler-Volmer equation (Eq. 2.4) assuming  $i_0 = 70 \text{ mA/cm}^2$  and  $\alpha = 0.5$ .

The measured current in the HER branch should be equal to the kinetic current in the absence of diffusion limitation; however, the calculated kinetic overpotential curve (dashed green line) deviates significantly from the measured polarization curve (solid red line), confirming that the net-HER current is not free of diffusion limitation.

The diffusion current ( $i_d$ ) is proportional to the limiting current ( $i_l$ ) at a given potential, according to Eq. 2.5:

$$i_d = i_l \left( 1 - \exp\left(-\frac{2F\eta}{RT}\right) \right) \quad (2.5)$$

Thus,  $i_d$  should share the same rotation speed dependence as  $i_l$  (Eq. 2.1). It follows that measured currents will also be rotation speed dependent if HER/HOR is completely diffusion limited on Pt disk in acidic media ( $i_{exp} = i_d$ ). Indeed, the HOR/HER polarization curves on Pt disk in 0.1 M HClO<sub>4</sub> at rotating speeds of 100 rpm, 400 rpm, 900 rpm, 1600 rpm, 2500 rpm and 3600 rpm match well with their corresponding diffusion overpotential curves in the entire HOR/HER potential window scanned (Figure 2.2), which is strong evidence that the net-HER current is diffusion limited. Furthermore, a Koutecky – Levich plot at 0.08 V vs. RHE (Figure 2.2, inset) yields a straight line passing through origin, and a  $Bc_0$  value of 0.075 mA/(cm<sup>2</sup><sub>disk</sub>rpm<sup>1/2</sup>), in reasonable agreement with the values reported previously.[2,60,78] Furthermore, the diffusion limited nature of the HER branch on Pt in acid suggests that supersaturation of H<sub>2</sub> is likely in the vicinity of the electrode, which provides the driving force of transport H<sub>2</sub> produced at the electrode to the bulk. Chen et al. reported that the supersaturation of H<sub>2</sub> could be as high as 300 times relative to saturation concentration at room temperature and pressure before nucleation and bubble formation on Pt nanoelectrodes.[79,80]

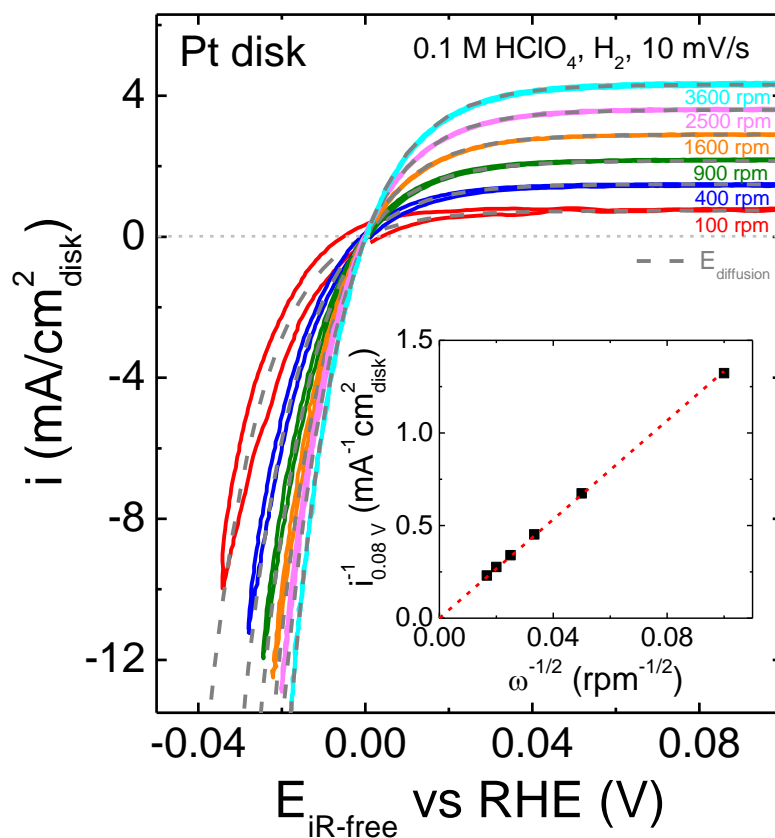


Figure 2.2  $iR$ -corrected HOR/HER polarization curves at different rotating speeds (100 rpm to 3600 rpm) on a polycrystalline Pt disk in  $H_2$ -saturated 0.1 M  $HClO_4$  at a scanning rate of 10 mV/s. Dashed grey lines are the diffusion overpotential curves at different rotating speeds. The inset shows a Koutecky-Levich plot at 0.08 V vs. RHE, yielding a straight line with  $Bc_0$  value of  $0.075 \text{ mA}/(\text{cm}^2_{\text{disk}} \text{rpm}^{1/2})$ .

HER on Pt in base is much slower than in acid, and thus HER currents determined by the RDE in base could be kinetics, rather than diffusion, limited.[2] Indeed, the HOR/HER polarization curves on Pt/C in 0.1 M KOH at different rotating speeds from 100 rpm to 3600 rpm deviate significantly from their corresponding concentration overpotential curves (Figure 2.3), owing to the sluggish kinetics on Pt in

the alkaline electrolyte. In addition, the HER polarization curves at different rotating speeds essentially overlap within experimental errors (Figure 2.3), consistent with a previous report.[67] The independence of the net-HER current on the rotating speed is also due to the sluggish HER kinetics on Pt in base, which makes the net-HER current kinetics rather than diffusion controlled: the HER overpotential at  $-5 \text{ mA/cm}^2_{\text{disk}}$  at 3600 rpm is about 44 mV, less than a quarter of which is from  $\text{H}_2$  mass transport ( $\eta_d = 10 \text{ mV}$ ). Although the kinetic overpotential is dominant when the HER kinetics is sluggish, the contribution of  $\eta_d$  in the overall overpotential in the HER branch could still be sizable: The diffusion overpotential ( $\eta_d$ ) at  $-5 \text{ mA/cm}^2_{\text{disk}}$  increases from 10 mV at the rotating speed of 3600 rpm to 26 mV at 100 rpm. Therefore, a high rotating speed is recommended to facilitate the mass transport of  $\text{H}_2$  and minimize  $\eta_d$  in the RDE measurements of HOR/HER activities. It should be noted that the Levich equation (Eq. 2.1) does not apply when the rotating speed ( $\omega$ ) is small, because the hydrodynamic boundary layer becomes large compared with the disk radius, and the assumption used in derivation of the Levich equation no longer holds.[81] It has been pointed out by Galus et al. that the RDE without rotating will approach unshielded liner diffusion conditions, leading to a finite limiting current.[64] Indeed, rather than the infinitely large diffusion overpotential and zero net-HER current predicted by the Levich equation, finite net-HER currents are observed when the electrode is not rotating in both 0.1 M  $\text{HClO}_4$  and 0.1 M  $\text{KOH}$  on Pt (black dashed line in Figure 2.4). In addition, limiting current densities without rotation in 0.1 M  $\text{HClO}_4$  ( $\sim 0.60 \text{ mA/cm}^2_{\text{disk}}$ ) and 0.1 M  $\text{KOH}$  ( $0.45 \text{ mA/cm}^2_{\text{disk}}$ ) are comparable to those obtained at  $\omega = 100 \text{ rpm}$  (Figure 2.4). Moreover, it is important that constant  $\text{H}_2$  pressure is maintained throughout the experiment to obtain accurate HER polarization curves even though  $\text{H}_2$  is not a reactant

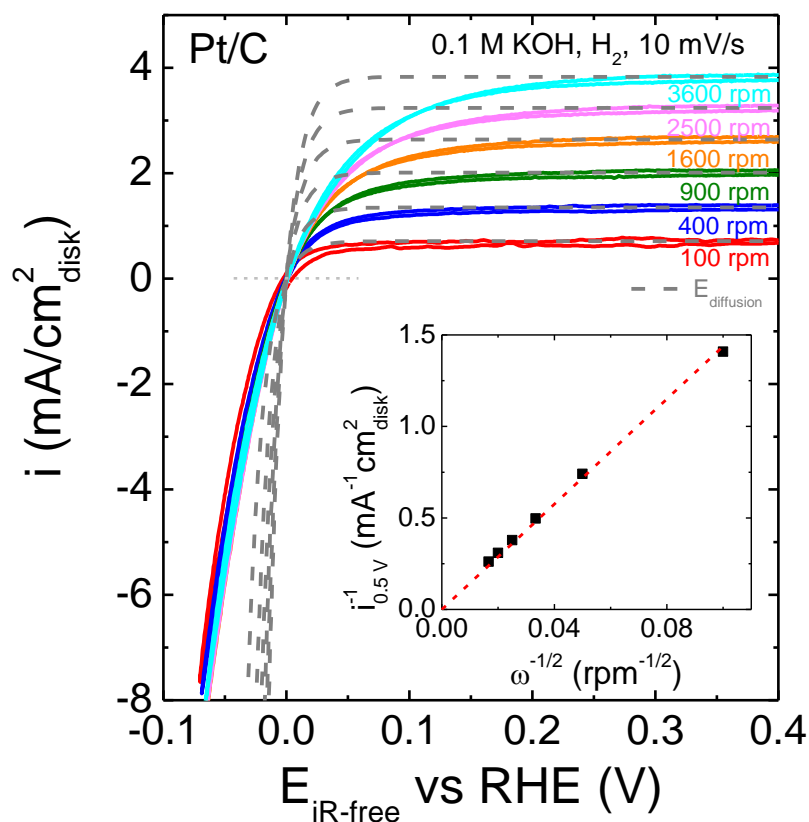


Figure 2.3  $iR$ -corrected HOR/HER polarization curves at different rotating speeds (100 rpm to 3600 rpm) on Pt/C (loading:  $10 \mu\text{g}_{\text{Pt}}/\text{cm}^2_{\text{disk}}$ ) in  $\text{H}_2$  – saturated 0.1 M KOH at a scanning rate of 10 mV/s. Dashed grey lines are the diffusion overpotential curves at different rotating speeds. The inset shows a Koutecky-Levich plot at 0.5 V vs. RHE, yielding a straight line with  $Bc_0$  value of  $0.069 \text{ mA}/(\text{cm}^2_{\text{disk}}\text{rpm}^{1/2})$ .

for HER. Conducting RDE experiments in Ar leads to higher onset potentials for HER ( $\sim 60$  mV vs. RHE in both 0.1 M  $\text{HClO}_4$  and 0.1 M KOH on a Pt disk) (Figure 2.5) due to the positive shift of the  $\text{H}_2/\text{H}^+$  equilibrium potential at  $\text{H}_2$  partial pressure less than 1 atm, which explains the “superior” net-HER current in Ar vs.  $\text{H}_2$  at a rotating speed of 2500 rpm. Moreover, the ill-defined equilibrium potential makes it impossible to reveal kinetic information out of the HER polarization curves obtained in Ar. In 0.1 M KOH,

the HER polarization curves measured in H<sub>2</sub> and Ar match better than in acid, especially at higher overpotentials ( $\sim -25$  mV) (Figure 2.5b). This shows that the error caused by the lower H<sub>2</sub> partial pressure in HER polarization curves is less when the electrode kinetics is sluggish.

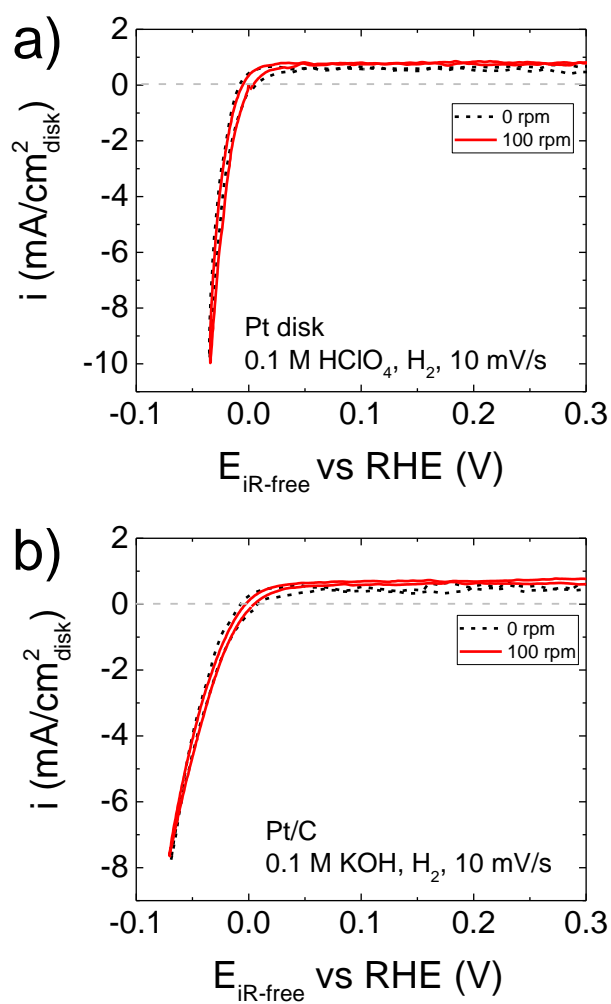


Figure 2.4 HOR/HER polarization curves on a) Pt disk in 0.1 M HClO<sub>4</sub> and b) Pt/C (loading: 10  $\mu\text{g}_{\text{Pt}}/\text{cm}^2_{\text{disk}}$ ) in 0.1 M KOH, in H<sub>2</sub> at a scanning rate of 10 mV/s and rotating speeds of 0 rpm (dash black line) and 100 rpm (solid red line).

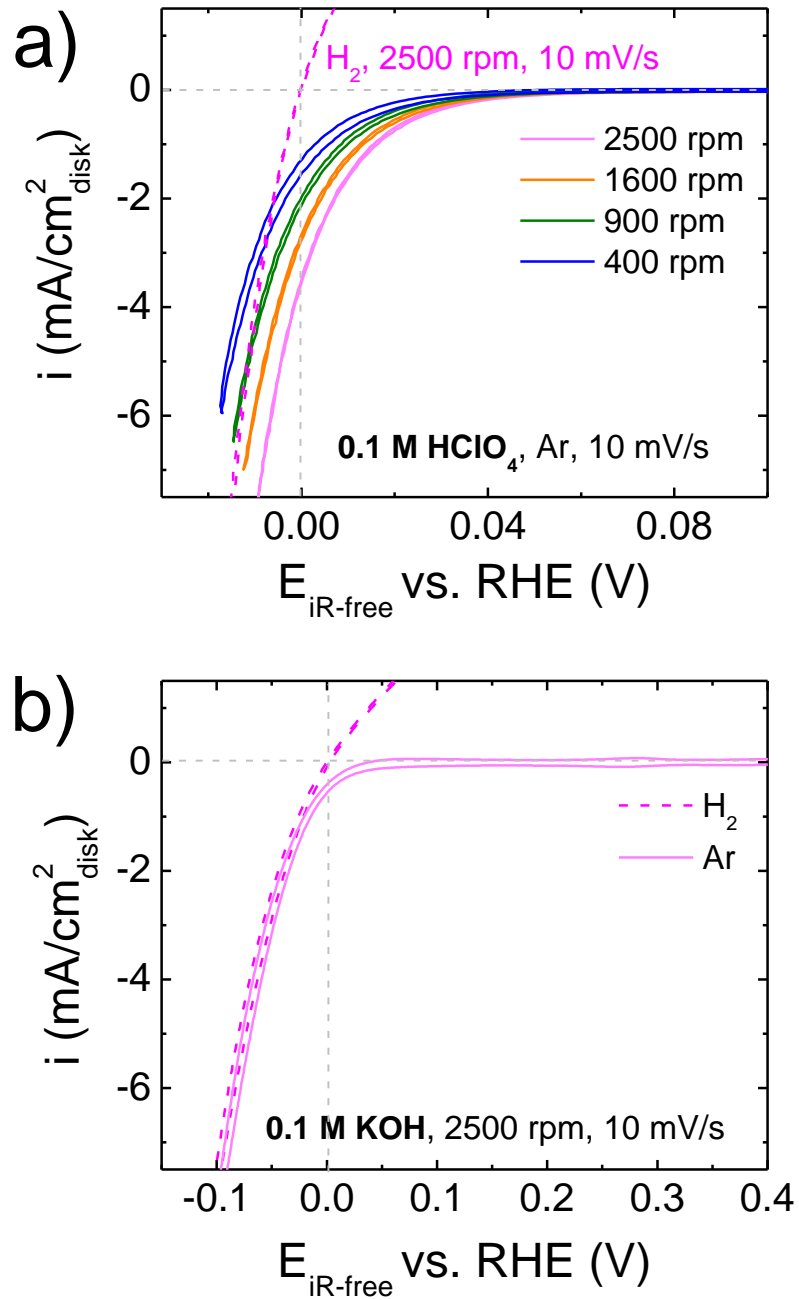


Figure 2.5 HER polarization curves on Pt disk in a) Ar-saturated 0.1 M HClO<sub>4</sub> at a scanning rate of 10 mV/s at different rotating speeds. Dash magenta line represent HOR/HER polarization curve on Pt disk in H<sub>2</sub>-saturated 0.1 M HClO<sub>4</sub> at 2500 rpm and 10 mV/s as comparison, and b) Ar-saturated and H<sub>2</sub>-saturated 0.1 M KOH at 2500 rpm and 10 mV/s.

### 2.3.2 The Origin of the Diffusion Limitation in HER Currents

The highly reversible nature of HOR/HER is key to understanding the diffusion limited behavior of HER. We propose that the diffusion limitation in the HER branch when the electrode kinetics is facile, as in the case Pt electrode in acid, originates from the slow diffusion of the  $H_2$  produced on the electrode in HER to the bulk of the electrolyte. The abundance of the reactant,  $H^+$ , in acid makes the mass transport limitation of the reactant to the electrode unlikely. Meanwhile, the highly reversible nature of HOR/HER makes the efficient transport of product away from the electrode crucial, because the contribution of the pure HOR current to the net-HER current could be significant, especially at low overpotentials. We will discuss only HER in acidic media because the diffusion limitation is more prominent. HER in base ( $2 H_2O + 2 e \rightarrow H_2 + OH^-$ ) can be considered as a combination of a surface reaction step ( $2 H^+ + 2 e \rightarrow H_2$ ) and a  $H_2O$  dissociation step ( $2 H_2O \rightarrow 2 H^+ + 2 OH^-$ ), as suggested by Durst et al.[3] The HOR/HER current can be expressed as follows assuming a first order reaction for  $H_2$ , and an  $\varepsilon$  order reaction for  $H^+$ ,

$$i = nFA(k_{HOR}c_{H_2,surf} - k_{HER}c_{H^+,surf}^\varepsilon) \quad (2.6)$$

where  $k_{HOR}$  and  $k_{HER}$  are the rate constants for HOR and HER, and  $c_{H_2,surf}$  and  $c_{H^+,surf}$  are the surface concentrations of  $H_2$  and  $H^+$ , respectively, and  $\varepsilon$  is the reaction order with respect to  $H^+$ . The assumption of first order reaction with respect to  $H_2$  will be justified by our analysis in the following section. In strongly acidic media (Figures 2.1 and 2.2), the high concentration of  $H^+$  makes a steep concentration gradient from bulk to electrode surface unlikely. Therefore,  $c_{H^+,surf}$  in the second term of Eq. 2.6 can be replaced by the bulk  $H^+$  concentration ( $c_{H^+,bulk}$ ), which is independent of rotating speed. In contrast, the slow mass transport of  $H_2$  could result in a significant difference in  $H_2$  concentrations at the electrode surface, where  $H_2$  is produced, and in the bulk

electrolyte, especially at low rotating speeds. Since H<sub>2</sub> is the reactant of the reverse reaction of HER, i.e., HOR, higher concentration of H<sub>2</sub> at the electrode surface leads to larger HOR currents and in turn lower net-HER currents (Figure 2.2). Surface and bulk H<sub>2</sub> concentrations are related through the constraints of mass transport, as Eq. 2.7,

$$i = nFAm_{H_2}(c_{H_2,bulk} - c_{H_2,surf}) \quad (2.7)$$

where  $m_{H_2}$  is the mass transport coefficient of H<sub>2</sub> and  $c_{H_2,bulk}$  and  $c_{H_2,surf}$  are the bulk and surface concentrations of H<sub>2</sub>, respectively. Substituting the expression for  $c_{H_2,surf}$  derived from Eq. 2.7 into Eq. 2.6, and assuming  $c_{H^+,surf} = c_{H^+,bulk}$ ,

$$i = nFA(k_{HOR}c_{H_2,bulk} - k_{HER}c_{H^+,bulk}^{\varepsilon})/(1 + \frac{k_{HOR}}{m_{H_2}}) \quad (2.8)$$

$$i_{HOR} = nFAk_{HOR}c_{H_2,surf} = nFAk_{HOR}[c_{H_2,bulk} + c_{H^+,bulk}^{\varepsilon} \frac{k_{HER}}{m_{H_2}}]/(1 + \frac{k_{HOR}}{m_{H_2}}) \quad (2.9)$$

$$i_{HER} = nFAk_{HER}c_{H^+,bulk}^{\varepsilon} \quad (2.10)$$

Therefore, the net-HOR/HER and the pure HOR currents are  $m_{H_2}$  or rotating speed dependent (Eqs. 2.8-2.9), because  $m_{H_2}$  is proportional to  $\omega^{1/2}$  according to the Levich equation (Eq. 2.1). When the rate of HOR is much smaller than that of H<sub>2</sub> diffusion, i.e.,  $k_{HOR} \ll m_{H_2}$ , Eq. 2.8 becomes  $i = nFA(k_{HOR}c_{H_2,bulk} - k_{HER}c_{H^+,bulk}^{\varepsilon}) = i_k$ , which is consistent with the observation that HER polarization curves on Pt in base are independent of the rotating speed. Hence, the experimental net-HER currents in base can be considered as kinetic current without introducing significant errors.[2,67]

### 2.3.3 Impact of Diffusion Limitation of H<sub>2</sub> on Determination and Interpretation of Tafel Slopes

Correction for internal resistance (iR) is an indispensable step in obtaining reliable Tafel slopes. To illustrate its importance, we chose to present data obtained in

0.5 M H<sub>2</sub>SO<sub>4</sub> (a typical choice of electrolyte in many HER studies,[71,73-76] Figure 2.6a) with an internal resistance of 5 Ω instead of 25 Ω in the case of 0.1 M HClO<sub>4</sub> (Figures 2.1 and 2.2). The iR-corrected HER polarization curve on Pt disk in H<sub>2</sub>-saturated 0.5 M H<sub>2</sub>SO<sub>4</sub> at 1600 rpm and 10 mV/s deviates significantly from the iR-uncorrected HER polarization curve (Figure 2.6a). Like in 0.1 M HClO<sub>4</sub> (Figure 2.1), the iR-corrected HER polarization curve in 0.5 M H<sub>2</sub>SO<sub>4</sub> also almost overlaps with the concentration overpotential curve. The difference in overpotentials obtained with and without iR correction is about 65 mV at  $-60 \text{ mA/cm}^2_{\text{disk}}$ , demonstrating the importance of iR correction in obtaining accurate kinetic information. The “Tafel slope” of iR-uncorrected HER polarization curve can give rise to a value of  $\sim 30 \text{ mV/dec}$  or  $306 \text{ mV/dec}$  depending on the choice of overpotential range (from the solid blue line in Figure 2.6b), both of which are incorrect.

Correction for diffusion limitation also plays an important role in accurate Tafel analysis, especially when HER kinetics is facile. When the kinetics of HER is sluggish, e.g., in base, the contribution of diffusion overpotential to the overall overpotential is insignificant, and thus the experimental net-HER current can be approximated as the kinetic current. Similar simplification will lead to substantial underestimation of kinetic currents when the rate of HER becomes significant relative to the rate of H<sub>2</sub> mass transport. The overlap between the polarization curves and the concentration overpotential curve on Pt in acid (Figure 2.2 and 2.6a) suggests the measured currents are diffusion limited (Eq. 2.5), i.e.,  $i_{exp} = i_d$ . Thus the apparent Tafel slope determined under this condition ( $2.303RT/2F$  or  $\sim 30 \text{ mV/dec}$  at 293 K) (from solid red line in Figure 2.6b) reflects the Tafel slope for H<sub>2</sub> diffusion, rather than HOR/HER kinetics. Since Tafel slope is frequently used as a diagnostic parameter in mechanistic studies,

especially in the identification of the rate determining step (RDS), incorrect interpretation of measured Tafel slope could lead to misleading mechanistic interpretations. For example, a Tafel slope of 30 mV/dec caused by H<sub>2</sub> diffusion limitation, if interpreted as a Tafel slope that reflects the intrinsic HER kinetics, could lead to the conclusion that HER on Pt in acid follow a Tafel-Volmer pathway with Tafel step being the RLS. Using the diffusion-free H<sub>2</sub>-pump method in a PEMFC configuration, with the equivalent electrolyte pH = 0, assuming a transfer coefficient of about 0.5, a Tafel slope of 120 mV/dec ( $2.303RT/\alpha F$ ) has been obtained,[3,38] suggesting that the Volmer step is likely the RLS. Since exchange current densities of HER are supposed to be obtained by extrapolating the Tafel slope to  $\eta = 0$  V vs. RHE, the 30 mV/dec Tafel slope has led to substantial underestimation of  $i_0$  reported in the literature.[71-76] True HER kinetic parameters can only be extracted after the HER branch of the polarization curves are corrected for the overpotential caused by diffusion ( $\eta_d$ ), which will be discussed in the next section.

Another important consideration is that Tafel behavior reflects irreversible kinetics, which only occurs at high overpotentials for reversible reactions when the contribution from either the anodic or cathodic reaction to the total current is negligible. It follows that Tafel slopes for reversible reactions, e.g., HOR/HER, should be calculated only at high overpotential regions. Assuming negligible mass transport limitation in the HER branch, the contribution of the pure HOR current drops to less than 1 % to the total current when  $\eta < -118$  mV at 298 K ( $e^{\frac{\alpha F \eta}{RT}} / e^{\frac{(\alpha-1)F \eta}{RT}} = e^{\frac{F \eta}{RT}} < 0.01$ ). For HER entirely controlled by mass transport, as indicated in Eq. 3, Tafel slope no longer reflect the reaction kinetics. However, apparent Tafel slope could be useful for revealing the diffusion limitation. To that end, it is still necessary to draw the Tafel

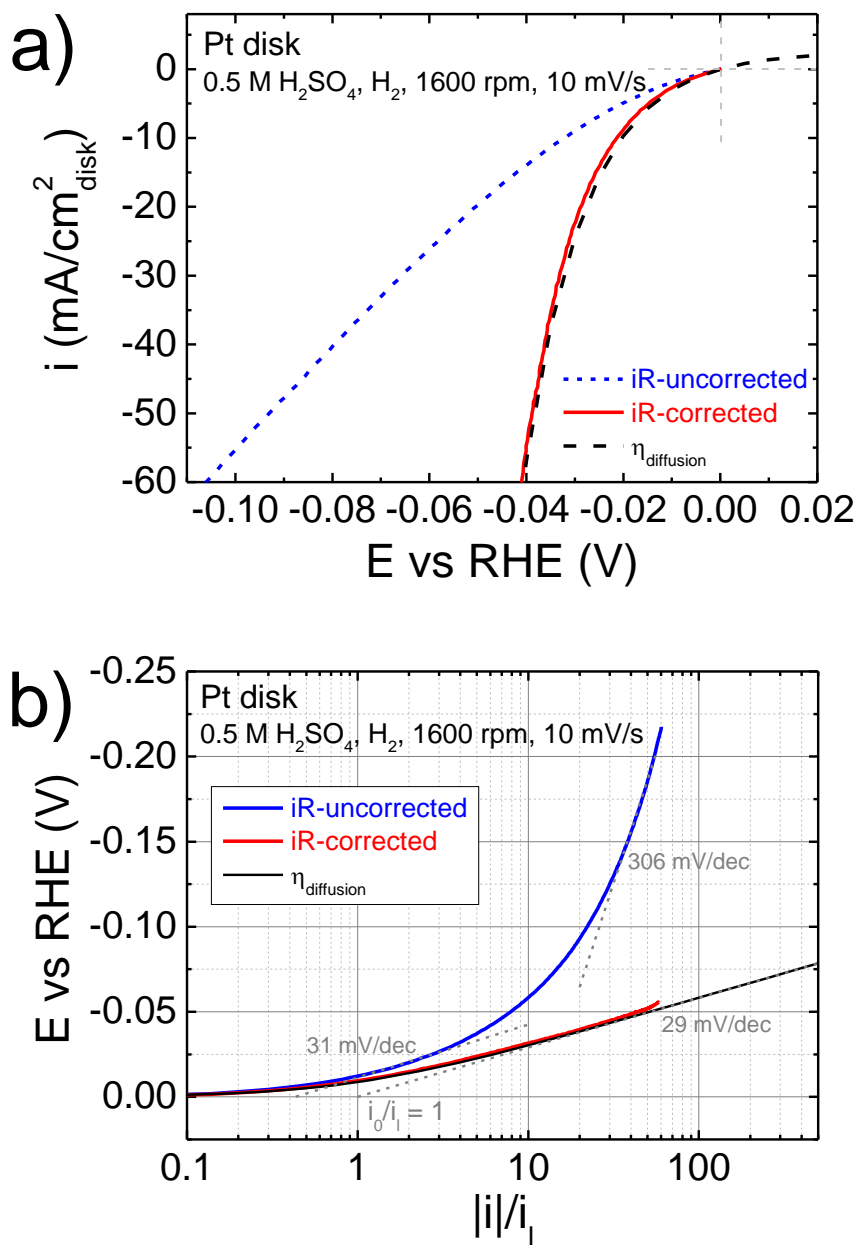


Figure 2.6 (a) HER polarization curves on Pt disk in H<sub>2</sub> – saturated 0.5 M H<sub>2</sub>SO<sub>4</sub> at a scanning rate of 10 mV/s, and a rotating speed of 1600 rpm before (blue dash line), after (red line) iR correction and concentration overpotential curve (black dash line), (b) Tafel plot of HER before (blue line) and after (red line) iR correction, black line represents concentration overpotential curve.

slope at high enough overpotential because the contribution of the pure HOR current is less than 1 % to the total current only when the overpotential is greater than 59 mV at 298 K ( $e \frac{2F\eta}{RT} < 0.01$ ). Tafel slopes determined at overpotentials less than 59 mV (solid black line in Figure 2.6b) are not accurate measures of Tafel slopes since the contribution from the reverse reaction to the overall reaction rate is still significant.

### 2.3.4 Correction of Diffusion Limitation for Both HOR and HER Branches

The contribution of the diffusion current to the net-HOR and net-HER currents must be removed to obtain the kinetic current, based on which true kinetic parameters such as exchange current density and transfer coefficient can be extracted. In this section, we show that the kinetic current can be obtained by the two methods: 1) Extraction of  $i_k$  from Koutecky-Levich equation for reversible reactions (referred as reversible Koutecky-Levich equation hereafter); and 2) Correction of overpotential and current with the diffusion overpotential and the modified Koutecky-Levich equation, respectively.

#### ***Method 1. Reversible Koutecky-Levich equation***

Since HOR/HER is highly reversible, a reversible Koutecky-Levich equation should be used to calculate kinetic current. For a one-electron transfer, one-step *reversible* reaction,  $R \leftrightarrow O + e$ , a Koutecky-Levich equation for reversible reactions can be written in the form of Eq. 2.11,

$$\frac{1}{i} = \frac{1}{i_k} + \frac{1}{i_d} \quad (2.11)$$

where  $i_d$  is the diffusion limited current defined in Eq. 2.5 instead of the maximum limiting current  $i_l$ . [25,78,82] The derivation of the Koutecky-Levich equation for reversible reactions is as follows.

The Butler-Volmer equation with mass transport is in the form of Eq. 2.12 (also see ref. [81]).

$$\frac{i}{i_0} = \left(1 - \frac{i}{i_{l,a}}\right) e^{\alpha F\eta/RT} - \left(1 - \frac{i}{i_{l,c}}\right) e^{-(1-\alpha)F\eta/RT} \quad (2.12)$$

Solving for  $i$ , we get

$$i = (e^{\alpha F\eta/RT} - e^{-(1-\alpha)F\eta/RT}) / \left(\frac{1}{i_0} + \frac{e^{\alpha F\eta/RT}}{i_{l,a}} - \frac{e^{-(1-\alpha)F\eta/RT}}{i_{l,c}}\right) \quad (2.13)$$

The kinetic current  $i_k$  is the current in the absence of mass transport, i.e.,  $i_{l,a}, i_{l,c} \rightarrow \infty$ , thus:

$$i_k = i_0(e^{\alpha F\eta/RT} - e^{-(1-\alpha)F\eta/RT}) \quad (2.14)$$

When  $i_0$  approaches infinity, the measured current is completely controlled by diffusion, i.e.,  $i = i_d$ , and the left hand side of Eq. 2.12 vanishes:

$$0 = \left(1 - \frac{i_d}{i_{l,a}}\right) e^{\alpha F\eta/RT} - \left(1 - \frac{i_d}{i_{l,c}}\right) e^{-(1-\alpha)F\eta/RT} \quad (2.15)$$

Solving Eq. 2.15, we obtain:

$$i_d = (1 - e^{-F\eta/RT}) / \left(\frac{1}{i_{l,a}} - \frac{e^{-F\eta/RT}}{i_{l,c}}\right) \quad (2.16)$$

From Eqs. 2.14 and 2.16, we get:

$$\frac{1}{i_k} + \frac{1}{i_d} = \frac{1}{i_0(e^{\alpha F\eta/RT} - e^{-(1-\alpha)F\eta/RT})} + \left(\frac{1}{i_{l,a}} - \frac{e^{-F\eta/RT}}{i_{l,c}}\right) / (1 - e^{-F\eta/RT}) \quad (2.17)$$

Eq. 2.18 can be obtained by taking the reciprocal of the both sides of Eq. 2.13:

$$\frac{1}{i} = \frac{\frac{1}{i_0} + \frac{e^{\alpha F\eta/RT}}{i_{l,a}} - \frac{e^{-(1-\alpha)F\eta/RT}}{i_{l,c}}}{e^{\alpha F\eta/RT} - e^{-(1-\alpha)F\eta/RT}} = \frac{1}{i_0(e^{\alpha F\eta/RT} - e^{-(1-\alpha)F\eta/RT})} + \left(\frac{1}{i_{l,a}} - \frac{e^{-F\eta/RT}}{i_{l,c}}\right) / (1 - e^{-F\eta/RT}) \quad (2.18)$$

By noting that the right hand sides of Eqs. 2.17 and 2.18 are identical, we arrive at Eq. 2.11.

For a one step, one electron transfer irreversible reaction ( $R \rightarrow O + ne$ ), we have

$$\frac{i}{i_0} = \left(1 - \frac{i}{i_{l,a}}\right) ne^{\alpha F\eta/RT} \quad (2.19)$$

$$i_k = i_0 ne^{\alpha F\eta/RT} \quad (2.20)$$

$$i_d = i_{l,a} \quad (2.21)$$

Similar manipulations lead to a Koutecky-Levich equation in the form of Eq. 2.2, which is widely used to extract kinetic currents from the HOR branch.[2,60,61,67] Alternatively, Eq. 2.2 can be derived by explicitly considering the concentrations of R at the electrode surface ( $c_{R,surf}$ ) and in the bulk ( $c_{R,bulk}$ ). At steady state, the rate of mass transport of R should match that of the electrode reaction:

$$i = nFm_R(c_{R,bulk} - c_{R,surf}) \quad (2.22)$$

When  $c_{R,surf}$  becomes 0, the limiting current ( $i_l$ ) is reached:

$$i_l = nFm_R c_{R,bulk} \quad (2.23)$$

where  $m_R$  is the mass transfer coefficient of R. Hence,

$$\frac{c_{R,surf}}{c_{R,bulk}} = 1 - \frac{i}{i_l} \quad (2.24)$$

Since  $i = kc_{R,surf}$  and  $i_k = kc_{R,bulk}$ ,

$$\frac{i}{i_k} = \frac{c_{R,surf}}{c_{R,bulk}} = 1 - \frac{i}{i_l} \quad (2.25)$$

which is identical to Eq. 2.2.

It is critical to recognize that Eqs. 2.2 and 2.25 only apply to irreversible reactions (referred to as irreversible Koutecky-Levich equation hereafter), and thus unsuitable for the highly reversible HOR/HER, especially at low overpotentials.[22]

The reversible Koutecky-Levich equation should be employed in extracting kinetic currents of HOR/HER.

If we consider HOR/HER as  $\frac{1}{2} H_2 \leftrightarrow H^+ + e$  as a one-electron transfer process (not an elementary step), with the apparent reaction orders of  $\gamma$  and  $\varepsilon$  with respect to  $H_2$  and  $H^+$ , respectively, then

$$i = F A k^0 c_{H_2}^\gamma \exp(\alpha F (E - E^{0'}) / RT) - F A k^0 c_{H^+}^\varepsilon \exp((\alpha - 1) F (E - E^{0'}) / RT) \quad (2.26)$$

$$i_0 = F A k^0 c_{H_2}^\gamma \exp(\alpha F (E_{eq} - E^{0'}) / RT) = F A k^0 c_{H^+}^\varepsilon \exp((\alpha - 1) F (E_{eq} - E^{0'}) / RT) \quad (2.27)$$

where  $E$  is the electrode potential,  $E^{0'}$  is the formal potential, and  $E_{eq}$  is the equilibrium potential of the electrode.

Since

$$E_{eq} = E^{0'} + \frac{RT}{F} \ln\left(\frac{c_{H^+}^\varepsilon}{c_{H_2}^\gamma}\right) \quad (2.28)$$

$$i_0 = F A k^0 c_{H_2}^\gamma \left(\frac{c_{H^+}^\varepsilon}{c_{H_2}^\gamma}\right)^\alpha = F A k^0 c_{H_2}^{(1-\alpha)\gamma} c_{H^+}^{\alpha\varepsilon} \quad (2.29)$$

From Eq. 2.29, it is clear that the reaction order for  $H_2$  is  $(1-\alpha)\gamma$  (with respect to  $i_0$ ), which has been determined by Rheinländer et al.[67] to be 0.5. Multiple studies have shown that the  $\alpha$  value for HOR/HER on Pt is about 0.5,[2,3,25,67,82] which will lead to the conclusion of  $\gamma = 1$ . Therefore, at any given potential, and in turn constant  $k_{HOR}$  and  $k_{HER}$ , the reaction order of  $H_2$  is 1, consistent with the assumed reaction order value in previous reports.[2,3,22]

### **Method 2. Diffusion overpotential ( $\eta_d$ ) correction together with current correction**

A recent detailed analysis by Durst et al. points out the importance of correcting the RDE potential by  $\eta_d$  for HOR branch to obtain the correct kinetic information.[38]

Rheinländer et al. proposed that after  $iR$  and  $\eta_d$  corrections for overpotential, a modified Koutecky-Levich equation should be used to calculate kinetic current for the HOR branch based on their observation that the reaction order of hydrogen with respect to the exchange current density is  $1/2$ , while the HER branch only need to be compensated with  $iR$ . [67] Here we re-derive the method of Rheinländer et al. rigorously for a one-electron transfer, one-step reaction below using a different approach. We will show Method 2 is equivalent to Method 1, i.e., using the reversible Koutecky-Levich equation to extract the kinetic current.

For one-electron transfer, one-step reversible reactions, the  $i - \eta$ , and  $i - \eta_d$  relations can be described by Eq. 2.12 and Eq. 2.30 (similar to Eq. 2.16), respectively.

$$i = (1 - e^{-F\eta_d/RT}) / \left( \frac{1}{i_{l,a}} - \frac{e^{-F\eta_d/RT}}{i_{l,c}} \right) \quad (2.30)$$

Eq. 2.30 can be rearranged to  $1 - \frac{i}{i_{l,a}} = \left(1 - \frac{i}{i_{l,c}}\right) e^{-F\eta_d/RT}$  and substituted into Eq. 2.12 to obtain Eq. 2.31,

$$\frac{i}{i_0} = \left(1 - \frac{i}{i_{l,c}}\right) (e^{-F\eta_d/RT} e^{\alpha F\eta/RT} - e^{-(1-\alpha)F\eta/RT}) \quad (2.31)$$

Multiply both sides of Eq. 2.31 by a factor of  $e^{(1-\alpha)F\eta_d/RT} / \left(1 - \frac{i}{i_{l,c}}\right)$ ,

$$\frac{i}{i_0} e^{(1-\alpha)F\eta_d/RT} / \left(1 - \frac{i}{i_{l,c}}\right) = e^{\alpha F(\eta - \eta_d)/RT} - e^{-(1-\alpha)F(\eta - \eta_d)/RT} \quad (2.32)$$

According to Eq. 2.30,  $e^{-F\eta_d/RT} = \frac{1 - \frac{i}{i_{l,a}}}{1 - \frac{i}{i_{l,c}}}$ , therefore,  $e^{(1-\alpha)F\eta_d/RT} = \left(\frac{1 - \frac{i}{i_{l,a}}}{1 - \frac{i}{i_{l,c}}}\right)^{\alpha-1}$ ,

which can be substituted into Eq. 2.32 to obtain Eq. 2.33,

$$i \left(1 - \frac{i}{i_{l,a}}\right)^{\alpha-1} \left(1 - \frac{i}{i_{l,c}}\right)^{-\alpha} = i_0 (e^{\alpha F(\eta - \eta_d)/RT} - e^{-(1-\alpha)F(\eta - \eta_d)/RT}) = i_0 (e^{\alpha F\eta_k/RT} - e^{-(1-\alpha)F\eta_k/RT}) = i_k \quad (2.33)$$

The last equality of Eq. 2.33 indicates an  $i_k - \eta_k$  relation in the form of a Butler-Volmer Equation. The kinetic current ( $i_k$ ) can be obtained by correcting the measured

current ( $i$ ) via Eq. 2.34, and kinetic overpotential can be obtained correcting the measured overpotential according to  $\eta_k = \eta - \eta_d$ .

$$i_k = i \left(1 - \frac{i}{i_{l,a}}\right)^{\alpha-1} \left(1 - \frac{i}{i_{l,c}}\right)^{-\alpha} \quad (2.34)$$

For HOR/HER,  $i_{l,c} = \infty$  and  $\alpha = 0.5$ , Eq. 2.34 becomes

$$\frac{i}{i_k} = \left(1 - \frac{i}{i_{l,a}}\right)^{0.5} \quad (2.35)$$

which is the modified Koutecky-Levich equation proposed by Rheinländer et al. to calculate the kinetic current for HOR branch after  $\eta_d$  correction.[67]

It is important to stress that corrections for both the measured current and the overpotential are necessary to obtain the correct  $i_k - \eta_k$  relation in the form of the Butler-Volmer Equation. If we assume that the uncorrected current ( $i$ ) relates with the kinetic overpotential ( $\eta_k$ ) in the form of the Butler-Volmer Equation,

$$i = i_0(e^{\alpha f \eta_k} - e^{-(1-\alpha) f \eta_k}) \quad (2.36)$$

By combining Eqs. 2.31 and 2.36, at any given  $i$ ,  $\eta$ ,  $\eta_k$  and  $\eta_d$  are related through Eq. 2.37,

$$e^{\alpha f \eta_k} - e^{-(1-\alpha) f \eta_k} = \left(1 - \frac{i}{i_{l,c}}\right)(e^{f(\alpha \eta - \eta_d)} - e^{-(1-\alpha) f \eta}) \quad (2.37)$$

rather than the simple expression of  $\eta_k = \eta - \eta_d$ , which shows the necessity of the correction of the measured current by Eq. 2.34.

The procedural differences in the two approaches mentioned above have been summarized in Figure 2.7. Method 1 is simpler and more general since it does not require the prior knowledge of the  $\alpha$  value, and only requires correction for the current, rather than both current and potential.

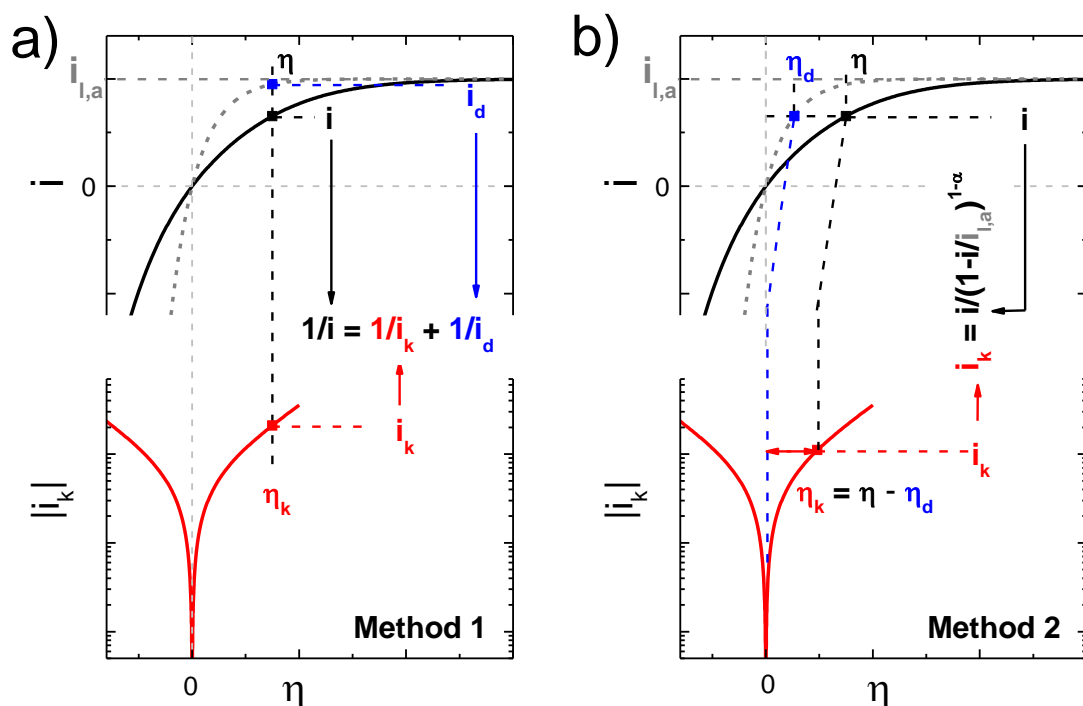


Figure 2.7 Schematic illustration of two methods of converting a measured polarization curve ( $\eta$ ,  $i$ ) to a plot of kinetic overpotential vs. kinetic current ( $\eta_k$ ,  $i_k$ ), based on which electrokinetic parameters can be extracted by fitting with the Butler-Volmer equation. (a) Method 1:  $i_k$  is obtained according to the reversible Koutecky-Levich equation ( $1/i = 1/i_k + 1/i_d$ ), and the measured overpotential  $\eta$  is the kinetic overpotential  $\eta_k$ ; (b)  $i_k$  and  $\eta_k$  are obtained according to  $i_k = i / (1 - i/i_{l,a})^{1-\alpha}$  and  $\eta_k = \eta - \eta_d$ , respectively. The two methods are largely equivalent, except that Method 1 does not require the prior knowledge of the  $\alpha$ .

### 2.3.5 Diffusion Limitation Correction for HER Branch Using Different Approaches

To illustrate the validity of correcting diffusion limitation in HER using the two methods described in the previous section, HOR/HER polarization curves were obtained on a Pt disk in phosphoric acid/phosphate buffer solution at pH = 2.4. These HER curves are close to the concentration overpotential curves and exhibit rotating-speed

dependence (Figure 2.8a). The net-HER currents, if not corrected by diffusion, increase as rotating speed increases (solid lines in Figure 2.8a and dash lines in Figure 2.8b, c). Moreover, the kinetic currents calculated using irreversible Koutecky-Levich equation (Eq. 2.2) from polarization curves at different rotating speeds in the HOR branch do not overlap (Figure 2.8b), which confirms that the correction with the irreversible Koutecky-Levich equation is not sufficient. In contrast, both HOR and HER kinetic currents calculated using the reversible Koutecky-Levich equation (Eq. 2.11) at different rotating speeds overlap, and they are larger than the measured currents (Figure 2.8c). Furthermore, the overpotential and current corrections by  $\eta_k = \eta - \eta_d$  and Eq. 2.35, respectively, generate almost identical  $|i_k| - E - \eta_d$  plots at different rotating speeds (Figure 2.8d), which also match the  $|i_k| - E$  plot constructed with the reversible Koutecky-Levich equation (gray dashed line in Figure 2.8d).

As mentioned before, HER on Pt in base is more sluggish than in acid and therefore diffusion limitation correction is less important. Here we show that diffusion correction is still necessary for obtaining accurate kinetics data. In a recent study, Rheinländer et al. argue that the HER branch only needs to be ohmically compensated to obtain kinetic HER currents on Pt in alkaline media, based on the observation that HER kinetic currents at different rotating speeds do not overlap when calculated using the irreversible Koutecky-Levich equation (Eq. 2.2), but do overlap when using the measured currents as the kinetic currents.[67] In our analysis, we confirm that net-HER kinetic currents obtained by the irreversible Koutecky-Levich equation for different rotating speeds do not overlap (Figure 2.9a), however, net-HER kinetic currents extracted with the reversible Koutecky-Levich equation do overlap (Figure 2.9b).

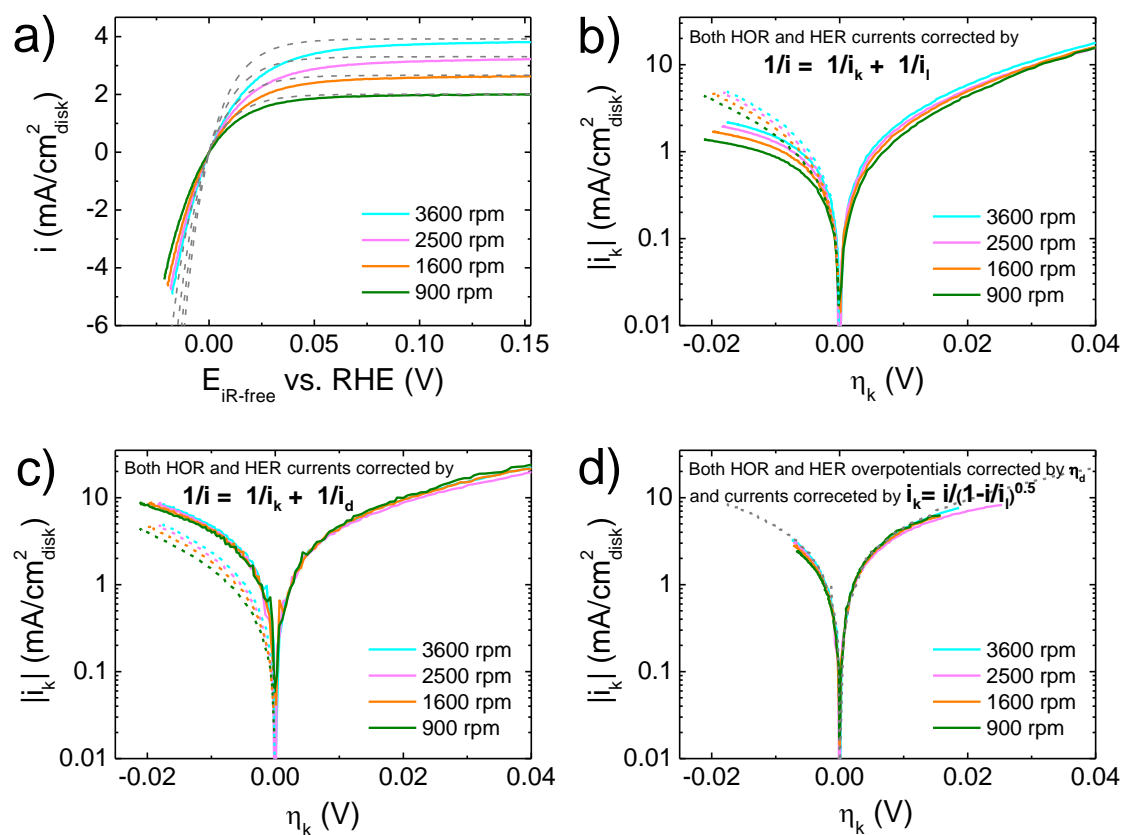


Figure 2.8 (a) HOR/HER polarization curves on a Pt disk in  $\text{H}_2$ -saturated phosphoric acid/phosphate buffer solution ( $\text{pH} = 2.4$ ) at  $10 \text{ mV/s}$  and rotating speeds from  $900$  to  $3600 \text{ rpm}$ . Dash lines represent the concentration overpotential curves. (b) Tafel plots of HOR/HER when both HOR and HER kinetic currents were calculated with the irreversible Koutecky-Levich equation (Eq. 2.2), and the dashed lines represent the experimental net-HER currents, the kinetic overpotential  $\eta_k$  is the  $iR$ -corrected overpotential ( $E_{iR\text{-free}}$  vs. RHE), (c) Tafel plots of HOR/HER when both HOR and HER kinetic currents were calculated with the reversible Koutecky-Levich equation (Eq. 2.11), and the dashed lines represent the experimental net-HER currents, and  $\eta_k = E_{iR\text{-free}}$  vs. RHE, (d) Tafel plots of HOR/HER when both HOR and HER overpotentials are corrected by diffusion overpotential ( $\eta_d$ ) ( $\eta_k = E_{iR\text{-free}}$  vs. RHE -  $\eta_d$ ) and the HOR and HER currents were converted to kinetic current by Eq. 2.35, the gray dashed line represents the  $|i_k|$  vs  $E_{iR\text{-free}}$  curve in (c) at a rotating speed of  $3600 \text{ rpm}$  for comparison.

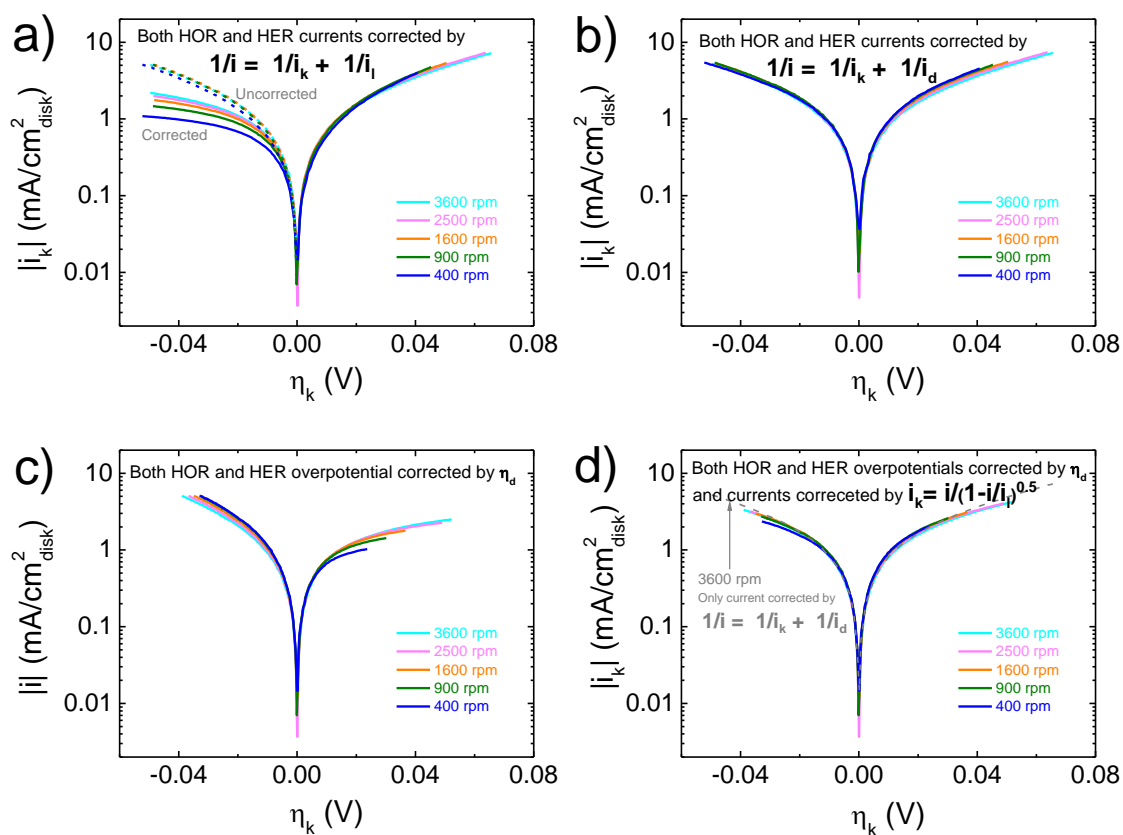
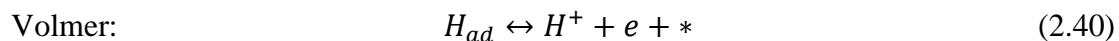
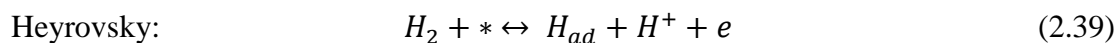


Figure 2.9 Tafel plots for HOR/HER on Pt/C (loading:  $10 \mu\text{g}_{\text{Pt}}/\text{cm}^2_{\text{disk}}$ ) in  $\text{H}_2$  saturated  $0.1 \text{ M KOH}$  at a scanning rate of  $10 \text{ mV/s}$  at different rotating speeds. (a) Both HOR and HER kinetic currents were calculated with the irreversible Koutecky-Levich equation (Eq. 2.2), dashed lines represents experimental net-HER currents, and  $\eta_k = E_{iR\text{-free}}$  vs. RHE, (b) Both HOR and HER kinetic currents were calculated with the reversible Koutecky-Levich equation (Eq. 2.11), and  $\eta_k = E_{iR\text{-free}}$  vs. RHE, and (c) Both HOR and HER currents were uncorrected while the overpotential is corrected by diffusion overpotential ( $\eta_d$ ), so  $\eta_k = E_{iR\text{-free}}$  vs. RHE -  $\eta_d$ . (d) Both HOR and HER overpotentials are corrected by diffusion overpotential ( $\eta_d$ ) and the HOR and HER currents were converted to kinetic current by Eq. 2.35,  $\eta_k = E_{iR\text{-free}}$  vs. RHE -  $\eta_d$ , and gray dashed line represents the  $|i_k|$  vs.  $E_{iR\text{-free}}$  curve in (b) at a rotating speed of  $3600 \text{ rpm}$  for comparison.

Non-overlapping curves were obtained when  $|i|$  was plotted vs.  $E - \eta_d$  at different rotating speed (Figure 2.9c), indicating that a diffusion overpotential correction using  $\eta_k = \eta - \eta_d$  without a current correction is inadequate, as discussed in the previous section. Plots of  $|i_k|$  (calculated with the modified Koutecky-Levich Eq. 2.35) vs.  $E - \eta_d$  at different rotating speeds overlap completely for both HOR and HER branches (Figure 2.9d), demonstrating that this double correction method (both  $\eta$  and  $i$  are corrected) is reliable in extracting kinetic information. Importantly,  $|i_k| - E$  plot obtained by correcting the current with the reversible Koutecky-Levich equation (Method 1, Figure 2.9b) matches those obtained with the double correction method (Method 2), demonstrating the consistency of the two approaches. The gray dashed curve and solid curves in Figure 2.9d are obtained following Methods 1 and 2, respectively, and they match well. The difference in potential range stems from the  $\eta_k = \eta - \eta_d$  correction in Method 2, which modifies the potential range; whereas no potential correction is needed in Method 1.

It should be noted that the reversible Koutecky-Levich equation (Eq. 2.11) is only rigorously derived for one electron transfer elementary reactions. However, HOR/HER is inherently a two electron transfer reaction which consists of at least two elementary steps, e.g., Tafel-Volmer or Heyrovsky –Volmer,[16]



Regardless of the mechanism assumed, the reversible Koutecky-Levich equation (Eq. 2.11) cannot be obtained. Additionally, discrepancy exists between the diffusion current equations derived for a one electron transfer – one step reaction ( $i_d = i_{l,a}(1 -$

$e^{-\frac{F\eta}{RT}}$  from Eq. 2.16 when  $i_{l,c}$  approaches infinity) and derived for HOR/HER ( $i_d = i_{l,\alpha} \left(1 - e^{-\frac{2F\eta}{RT}}\right)$  in Eq. 2.5), which can be solved only if the summation of transfer coefficients for HOR and HER equals to 2. In this case, Eqs. 2.12 and 2.14 become Eqs. 2.41 and 2.42, the diffusion current will have the form of Eq. 2.5, and the reversible Koutecky-Levich equation (Eq. 2.11) remains valid. Similarly, the derivation of Method 2 also assumes the reaction involves only one electron transfer and one step reaction.

$$\frac{i}{i_0} = \left(1 - \frac{i}{i_{l,\alpha}}\right) e^{\alpha' F\eta/RT} - e^{-(2-\alpha')F\eta/RT} \quad (2.41)$$

$$i_k = i_0(e^{\alpha' F\eta/RT} - e^{-(2-\alpha')F\eta/RT}) \quad (2.42)$$

The interdependence between reaction mechanism and kinetic parameters leads to a dilemma: electrokinetics, a powerful tool in the mechanistic study of multi-electron transfer reactions and the reliable extraction of kinetic information, e.g.,  $i_0$  and  $\alpha$ , predicates on the accurate knowledge of kinetic current. At the same time, the formula needed to deconvolute the kinetic and diffusional contributions to the measured currents is dependent on the knowledge of the same set of kinetic parameters, and in turn the reaction mechanism. One solution is to adopt techniques without mass transport limitation, such as the H<sub>2</sub>-pump method [3,38,68] and the floating electrode method.[70] to avoid the entanglement of kinetic and diffusional contributions. However, those methods typically require more complex setups and are often time-consuming, and cannot evaluate materials in the disk forms. Another option is to derive an expression for an assumed mechanism with mass transport, and then fit experimental data numerically into the derived expression.[22] While it is clearly more rigorous, given the large number of possible mechanisms for multi-electron transfer and multi-step processes, this method is more suitable for reaction systems with considerable existing knowledge and the number of possible mechanisms is limited. RDE method with its

simplicity and reliability will remain a powerful technique in the mechanistic study of multi-electron and multi-step electrochemical processes provided that robust data analysis procedures are developed.

Although the reversible Koutecky-Levich equation cannot be rigorously derived for multi-electron, multi-step electrochemical reactions, such as HER/HOR, the kinetic currents obtained is much more consistent than those obtained from irreversible Koutecky-Levich equation, as shown in Figures 2.6 and 2.7. The fundamental reason for the ability of reversible Koutecky-Levich equation to extract information for electrochemical reaction other than one-electron, one-step processes deserves further investigations. Our HOR/HER results suggest that it is reasonable to consider the reversible Koutecky-Levich equation as a semi-empirical expression to calculate kinetic currents with excellent accuracy.

### **2.3.6 Comparison of the Three Methods of Calculating the Kinetic Current and the Exchange Current ( $i_0$ ) of HOR/HER**

The exchange current ( $i_0$ ) of HOR/HER can be obtained by fitting the kinetic current ( $i_k$ ) into the Butler-Volmer equation (Eq. 2.4) or fitting  $i_k$  within a very small overpotential region into the linearized Butler-Volmer equation as in Eq. 2.43,

$$i_k = i_0 F \eta / RT \quad (2.43)$$

Both approaches are based on sound theoretical ground and lead to similar  $i_0$ . The former method has the added benefit of yielding the transfer coefficient  $\alpha$ , which is related to the Tafel slope (TS) by  $TS = 2.303RT/\alpha F$ .

Experimentally, polarization curves with different exchange currents can be generated by varying the pH of the electrolyte, or the loading of the electrocatalyst: the exchange current increases as pH decreases or the loading increase. The HOR/HER

polarization curve on a Pt disk approaches the concentration overpotential curve as the pH of the electrolyte decreases (Figure 2.10a). The following three methods were used for diffusion correction: 1) both HOR and HER currents are converted to kinetic currents by reversible Koutecky-Levich equation (Eq. 2.11) (Method 1), and 2) the overpotential is corrected by diffusion overpotential ( $\eta_k = \eta - \eta_d$ ) and current is converted to kinetic current by a modified Koutecky-Levich equation (Eq. 2.35) for both HOR and HER branches (Method 2) and 3) the net-HOR current is converted to kinetic currents by irreversible Koutecky-Levich equation (Eq. 2.2) while the HER current is uncorrected (Method 3). All the overpotentials were  $iR$  corrected. Tafel plots of HOR/HER kinetic currents at different pHs and their corresponding fittings with the Butler-Volmer equation were shown in Figure 2.11. The fittings with Method 1 (Figure 2.11a1-a6) and Method 2 (Figure 2.11b1-b6) are excellent in the pH range of 1.5-12.8, while fittings with Method 3 (Figure 2.11c1-c6) become increasingly poor with decreasing pHs, as the reaction is increasingly diffusion limited. The exchange current ( $i_0$ ) determined from the three methods mentioned above increases as the pH of the electrolyte decreases (Table 2.1).  $i_0$  determined from Butler-Volmer fitting and linear fitting are similar for all methods. The  $i_0$  from Methods 1 and 2 are identical within the experimental errors, while the  $i_0$  from Method 3 only agrees with the rest two at high pHs when the electrode kinetics is slow, and is substantially underestimated at lower pHs when the kinetics becomes faster (Table 2.1). Transfer coefficients ( $\alpha$ ) from Method 1 are more meaningful compared with those obtained from Method 2, as an  $\alpha$  value of 0.5 is assumed in the derivation of Method 2 (the negative value at pH = 1.5 is clearly not physical, Table 2.1).

HOR/HER polarization curves on carbon supported Pt nanoparticles approach the concentration overpotential curve as the loading of Pt increases from 4 to 40  $\mu\text{g}_{\text{Pt}}/\text{cm}^2_{\text{disk}}$  (Figure 2.10b), and the Butler-Volmer fittings of the HOR/HER kinetic currents obtained using Method 3 are worse than those obtained using Methods 1 and 2 (Figure 2.12). The  $i_0$  determined from the three methods are similar to each other when the loading is less than 15  $\mu\text{g}_{\text{Pt}}/\text{cm}^2_{\text{disk}}$  or  $i_0/i_1 \approx 1.5$  ( $i_1$  is the limiting current in the HOR branch, its value is about 2.5  $\text{mA}/\text{cm}^2_{\text{disk}}$  at 1600 rpm), however, the  $i_0$  determined from Method 3 are significantly underestimated as the loading of the electrocatalyst grows and the reaction becomes increasingly diffusion limited (Table 2.2), which is consistent with the results obtained on the Pt disk in the previous section. For HOR/HER, using the irreversible Koutecky-Levich equation to determine  $j_k$  yields reasonable results only when the total exchange current is less than  $1.5i_1$  (as in the case of HOR/HER on a Pt disk at different pHs or Pt/C with a relatively low loading in 0.1 M KOH), and substantially underestimated exchange current densities are obtained as the true exchange current becomes larger. Therefore, Methods 1 and 2 are recommended in calculating kinetic currents and exchange current densities for HOR/HER. Method 1 is preferred because it requires less correction and Method 2 requires prior knowledge of  $\alpha$  (assumed to be 0.5 in the derivation) to calculate  $i_k$  at overpotential  $\eta - \eta_d$ .

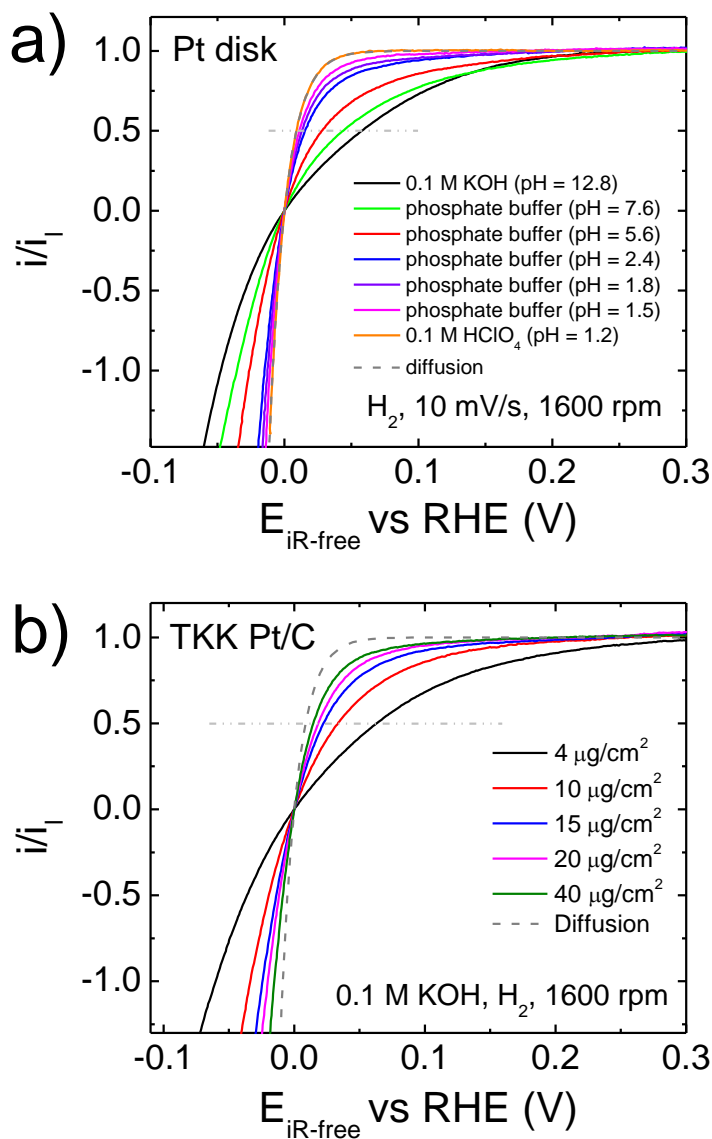


Figure 2.10 (a) HOR/HER polarization curves on Pt(pc) disk in  $H_2$ -saturated 0.1 M KOH, 0.1 M HClO<sub>4</sub> and phosphoric acid/phosphate buffer solutions with different pHs, tested at a scanning rate of 10 mV/s and a rotating speed of 1600 rpm, (b) HOR/HER polarization curves on carbon supported Pt nanoparticles from Tanaka Kikinokoku International, Inc. (TKK Pt/C) with different Pt loadings tested in  $H_2$ -saturated 0.1 M KOH, at 1 mV/s and 1600 rpm.

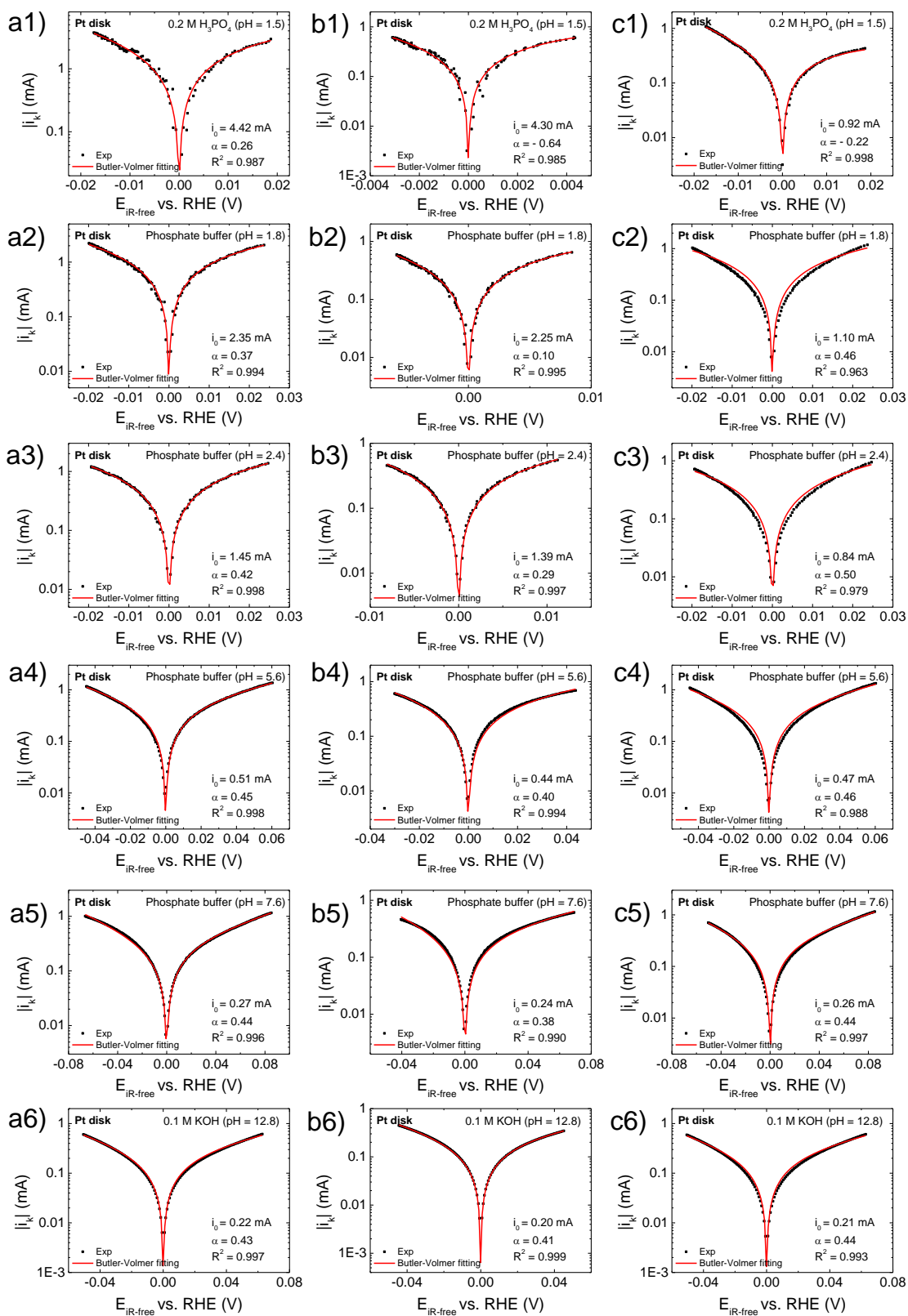


Figure 2.11 Tafel plots of HOR/HER kinetic currents and their corresponding fitting into a Butler-Volmer equation calculated from HOR/HER polarization curves measured on a Pt disk in electrolytes with different pHs at 10 mV/s and 1600 rpm, when (a1 – a6) both HOR and HER kinetic currents were calculated using the reversible Koutecky-Levich equation ( $1/i = 1/i_k + 1/i_d$ ), (b1 – b6) both HOR and HER overpotentials are corrected by diffusion overpotential, and both HOR and HER currents were converted to kinetic currents using  $i/i_k = (1 - i/i_{l,a})^{0.5}$ , and (c1- c6) the HOR kinetic currents were calculated using irreversible Koutecky-Levich equation ( $1/i = 1/i_k + 1/i_l$ ) and the HER kinetic currents were the measured ones corrected for internal resistance ( $iR$ ). All overpotentials were  $iR$ -corrected.

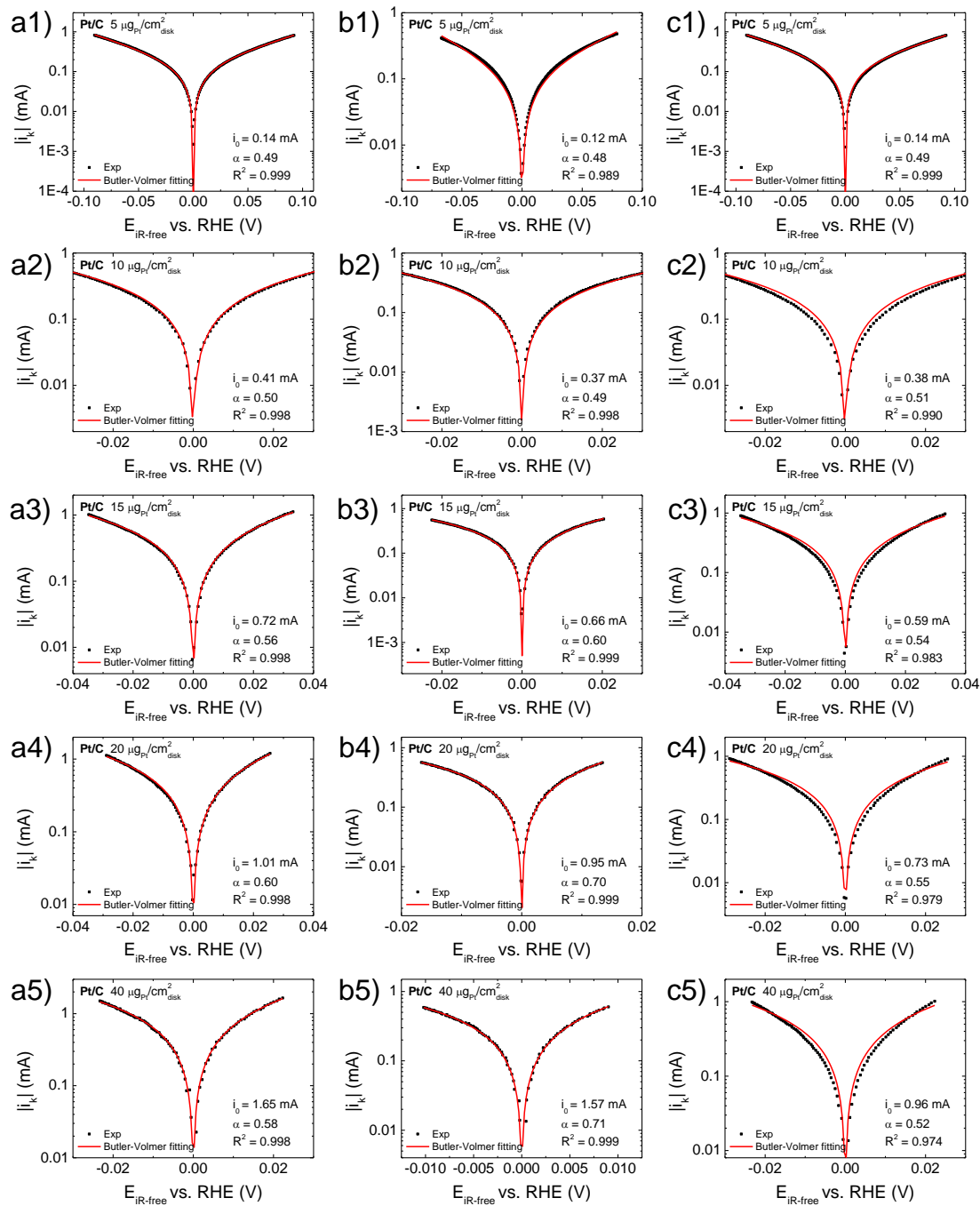


Figure 2.12 Tafel plots of HOR/HER kinetic currents and their corresponding fitting into a Butler-Volmer equation calculated from HOR/HER polarization curves measured on Pt/C in 0.1 M KOH with Pt loadings from 4 to 40  $\mu\text{g}_{\text{Pt}}/\text{cm}^2_{\text{disk}}$  at 1 mV/s and 1600 rpm, when (a1 – a5) both HOR and HER kinetic currents were calculated using the reversible Koutecky-Levich equation ( $1/i = 1/i_k + 1/i_d$ ), (b1 – b5) both HOR and HER overpotentials are corrected by diffusion overpotential, and both HOR and HER currents were converted to kinetic currents using  $i/i_k = (1 - i/i_{l,a})^{0.5}$ , and (c1- c5) the HOR kinetic currents were calculated using irreversible Koutecky-Levich equation ( $1/i = 1/i_k + 1/i_l$ ) and the HER kinetic currents were the measured ones corrected for internal resistance (iR). All overpotentials were iR-corrected.

Table 2.1 Comparison of exchange currents ( $i_0$ ) from three different diffusion-correction methods for HOR/HER on a 5 mm diameter Pt disk in electrolytes with different pHs.

Electrolyte	pH	Method 1 <sup>a</sup>			Method 2 <sup>b</sup>			Method 3 <sup>c</sup>		
		Butler-Volmer		Linear	Butler-Volmer		Linear	Butler-Volmer		Linear
		$i_0$ (mA)	$\alpha$	$i_0$ (mA)	$i_0$ (mA)	$\alpha$	$i_0$ (mA)	$i_0$ (mA)	$\alpha$	$i_0$ (mA)
0.2 M H <sub>3</sub> PO <sub>4</sub>	1.5	4.42	0.26	4.61	4.30	-0.64	4.45	0.92	-0.22	0.90
Phosphoric acid/phosphate buffer	1.8	2.35	0.37	2.38	2.25	0.1	2.33	1.10	0.46	0.91
	2.4	1.45	0.42	1.49	1.39	0.29	1.42	0.84	0.50	0.74
	5.6	0.51	0.45	0.50	0.44	0.40	0.49	0.47	0.46	0.40
	7.6	0.27	0.44	0.28	0.24	0.38	0.27	0.26	0.44	0.24
0.1 M KOH	12.8	0.22	0.43	0.21	0.20	0.41	0.20	0.21	0.44	0.19

- The kinetic current ( $i_k$ ) for both HOR and HER branch is calculated by reversible Koutecky-Levich equation  $\frac{1}{i} = \frac{1}{i_k} + \frac{1}{i_d}$
- The overpotential is corrected by diffusion overpotential  $\eta_k = \eta - \eta_d$ , while the measured current is converted to kinetic current by  $\frac{i}{i_k} = \left(1 - \frac{i}{i_{l,a}}\right)^{0.5}$
- The kinetic current ( $i_k$ ) for HOR branch is calculated by irreversible Koutecky-Levich equation  $\frac{1}{i} = \frac{1}{i_k} + \frac{1}{i_l}$  while the kinetic current ( $i_k$ ) for HER branch remains uncorrected.

Table 2.2 Comparison of exchange current ( $i_0$ ), transfer coefficient ( $\alpha$ ) and exchange current density ( $j_0$ ) from three different diffusion-correction methods for HOR/HER on a 5 mm diameter glassy carbon electrode with different Pt loadings in 0.1 M KOH at 1600 rpm.

Loading ( $\mu\text{g}/\text{cm}^2_{\text{disk}}$ )	Surface area ( $\text{cm}^2$ )	ECSA ( $\text{m}^2/\text{g}$ )	Method 1 <sup>a</sup>			Method 2 <sup>b</sup>			Method 3 <sup>c</sup>		
			$i_0$ (mA)	$\alpha$	$j_0$ ( $\text{mA}/\text{cm}^2_{\text{Pt}}$ )	$i_0$ (mA)	$\alpha$	$j_0$ ( $\text{mA}/\text{cm}^2_{\text{Pt}}$ )	$i_0$ (mA)	$\alpha$	$j_0$ ( $\text{mA}/\text{cm}^2_{\text{Pt}}$ )
4	0.35	45	0.14	0.49	0.40	0.12	0.48	0.34	0.14	0.49	0.39
10	1.03	53	0.41	0.50	0.40	0.37	0.49	0.35	0.38	0.51	0.37
15	1.60	54	0.72	0.56	0.45	0.66	0.60	0.41	0.59	0.54	0.37
20	2.20	56	1.01	0.60	0.46	0.95	0.70	0.43	0.73	0.55	0.33
40	4.00	51	1.65	0.58	0.41	1.57	0.70	0.39	0.96	0.52	0.24

- a. The kinetic current ( $i_k$ ) for both HOR and HER branch is calculated by reversible Koutecky-Levich equation  $\frac{1}{i} = \frac{1}{i_k} + \frac{1}{i_d}$
- b. The overpotential is corrected by diffusion overpotential  $\eta_k = \eta - \eta_d$ , while the measured current is converted to kinetic current by  $\frac{i}{i_k} = \left(1 - \frac{i}{i_{l,a}}\right)^{0.5}$
- c. The kinetic current ( $i_k$ ) for HOR branch is calculated by irreversible Koutecky-Levich equation  $\frac{1}{i} = \frac{1}{i_k} + \frac{1}{i_l}$  while the kinetic current ( $i_k$ ) for HER branch remains uncorrected.

## 2.4 Conclusion

Our study shows that HER is diffusion limited when the electrode kinetics is facile. The diffusion limitation behavior of HER originates from the slow mass transport of produced  $H_2$  on the electrode to the bulk electrolyte and the reversible nature of HOR/HER. Although the diffusion overpotential for HER is typically small, it could have a significant impact on the kinetic analysis especially in the low overpotential region, leading to underestimated activities and inaccurate mechanistic interpretations. The reversible nature of HOR/HER dictates that the reversible Koutecky-Levich equation should be used to calculate kinetic current while the use of the irreversible Koutecky-Levich equation to obtain kinetic currents can lead to significant errors when the electrode kinetics is facile and the process is partially diffusion controlled. In order to obtain accurate kinetic information from polarization curves using RDE method, we recommend: 1) perform  $iR$  correction to compensate the solution resistance; and 2) correct the measured current with the reversible Koutecky-Levich equation to obtain the kinetic current.

### Chapter 3

## CORRELATING HYDROGEN OXIDATION/EVOLUTION ACTIVITY WITH THE MINORITY WEAK HYDROGEN BINDING SITES ON IRIDIUM/C CATALYSTS

Fundamental understanding of the active sites mediating hydrogen oxidation/evolution reaction (HOR/HER) is critical to the design of an efficient HOR/HER electrocatalyst for affordable hydrogen exchange membrane fuel cells and electrolyzers. Here we report the existence of the most active sites on carbon supported iridium nanoparticles (Ir/C) for HOR/HER in alkaline electrolyte by investigating activities of Ir/C with varying particle sizes in the range of 3 – 12 nm. The distribution of surface sites is quantified by deconvoluting the underpotential deposited hydrogen ( $H_{\text{upd}}$ ) desorption peak in cyclic voltammograms. The portion of the sites with the lowest hydrogen binding energy (HBE) increases with the increase of the particle size or the decrease of the total electrochemical active surface area (t-ECSA). The HOR/HER activity normalized to t-ECSA decreases as t-ECSA increases while remains constant when normalized to the surface area of the sites with an average HBE of  $-0.33$  eV, indicating that those sites, accounting, and point out the major conclusions.

This chapter is reprinted with permission from Zheng, J.; Zhuang, Z.; Xu, B.; Yan, Y. Correlating Hydrogen Oxidation/Evolution Reaction Activity with the Minority Weak Hydrogen-Binding Sites on Ir/C Catalysts, *ACS Catalysis* **2015**, 4449. Copyright 2015 American Chemical Society.

### 3.1 Introduction

Fundamental understanding for the sluggish kinetics of HOR/HER in the alkaline environment, the cornerstone for the rational design of efficient HOR/HER catalysts, remains a topic of considerable debate despite intense recent efforts.[2,3,32,52,83,84] A systematic study of HOR/HER activity on transition metals (Ag, Au, Cu, Pt, Pd, Co, Ni, Fe and W) in base reveals a volcano shaped curve when plotting the HOR/HER exchange current density vs. the hydrogen binding energy (HBE) with Pt located at the optimal position, indicating that HBE is a key descriptor for catalytic activity for HOR/HER.[32] Meanwhile, Strmcnik et al. argued that the ability of metals to adsorb OH plays an important role in determining the HOR/HER activity, based on the excellent match between experimentally measured and simulated HOR/HER activity on Au, Pt and Ir in the pH range of 1-13.[83] Later on, Durst et al. correlated the HBE inferred from cyclic voltammetry measurements with HOR activities, and the effect of pH on HOR/HER activity manifests itself by modifying the HBE of electrocatalysts, based on which HBE was proposed to be the “unique and sole” predictor for the performance of HOR/HER electrocatalysts.[3] Wang et al. showed the HOR/HER activity on PtRu/C is more than twice that of Pt/C, which is attributed to the lower HBE on PtRu as revealed by both cyclic voltammetry measurements and density functional theory (DFT)-based calculations.[52] More recently, Sheng et al. correlated the HOR/HER activity on polycrystalline Pt to experimental measured HBE in electrolytes with pH from 0 to 13, and suggested HBE is the unique descriptor for HOR/HER.[85]

Considering that not all surface sites of a catalyst possess the same activity – for example, single crystal electrode studies show that different crystallographic facets of Pt exhibit drastically different HOR/HER activities[39,86] – identifying the most active

sites is a key task for the rational design of better catalysts. Varying the size of metal nanoparticles offers a convenient approach to systematically tune the composition of sites with different local environments, e.g., terrace, edge and corner sites.[87-90] In addition, surface sites with a variety of local environments can be sampled simultaneously with different particle sizes, which is not possible in the studies of single crystal surfaces. Active sites of HOR/HER can then be identified by correlating activities with their key properties, e.g., amount of sites with similar HBE. Strmcnik et al. reported that the HOR polarization curve on polycrystalline Ir in 0.1 M NaOH is essentially overlapping with the concentration overpotential curve, indicating a facile HOR/HER kinetics on polycrystalline Ir.[83] Thus, mechanistic understanding of the HOR/HER activity on Ir is of keen interest not only because it is a more cost effective alternative to Pt (the average price for Pt and Ir during November 2013 to November 2014 is \$1413.53/oz and \$542.16/oz, respectively), but more importantly it could shed light on the guiding principles for the design of efficient non-precious metal-based HOR/HER catalysts. Unlike the extensive research effort on Pt, HOR/HER kinetics studies on Ir are few: most works were carried out in acidic electrolytes with potentially underestimated activity,[29,40,91] and only two in the alkaline environment.[3,83]

In this chapter, we present a detailed kinetic study of HOR/HER on Ir/C catalysts with varying Ir particle sizes (3-12 nm), which establishes the direct correlation of the HOR/HER activity with the lowest HBE minority sites on Ir/C. We first prove that the position of the under potential deposited H ( $H_{\text{upd}}$ ) desorption peak is directly related to the HBE of the corresponding sites, followed by correlating the HOR/HER activity with the amount of sites with different HBEs. Exchange current density normalized by the electrochemical surface area (ECSA) corresponding to sites with  $H_{\text{upd}}$  desorption peak

centered at 0.13 V vs. RHE (or an HBE of  $-0.33$  eV) was found to be independent of total electrochemical active surface area (t-ECSA) or particle size, indicating weak H-binding sites are likely the true active sites for HOR/HER. This finding suggests the design of efficient HOR/HER catalysts should aim at maximizing the density of weakly H-binding sites, rather than the total surface sites.

## **3.2 Materials and Methods**

### **3.2.1 Preparation and Characterization of Ir Nanoparticle with Different Sizes**

Ir/C samples with varying particle sizes were obtained by treating commercial 20 wt.% Iridium on Vulcan XC-72 (Premetek Co.) in Ar at 300 °C, 500 °C, 600 °C, 800 °C for 2 hr. The samples are referred to as Ir/C (untreated), Ir/C-300C, Ir/C-500C, Ir/C-600C, Ir/C-800C, respectively. Their particle sizes and distributions were examined by a combination of high-resolution transmission electron microscopy (HRTEM), powder X-ray diffraction (XRD) and cyclic voltammetry. TEM samples were prepared on TEM grid (Lacey carbon coated copper grids, Electron Microscopy Sciences) by adding a drop of sample suspended in isopropanol after being ultrasonicated for five minutes. The diameters of at least 300 Ir NPs of each sample were measured from TEM images (JEOL 2010F, 200 kV), and the number-averaged diameters were calculated. XRD patterns of each sample were recorded on a Philips X'Pert X-ray diffractometer using Cu K $\alpha$  radiation.

### **3.2.2 Electrochemical Measurements**

The electrochemical measurements were conducted using a three-electrode cell configuration, with a silver-silver chloride (Ag/AgCl) as the reference electrode, a Pt wire as the counter electrode and a 5 mm diameter glassy carbon as the working

electrode (PINE instruments) controlled by a multichannel potentiostat (Princeton Applied Research). All the potentials used in this work were converted to the reversible hydrogen electrode (RHE) calibrated from rotating disk electrode (RDE) measurement of hydrogen oxidation and evolution reactions. The Ir/C ink solutions were prepared by dispersing Ir/C in 0.05 wt % Nafion isopropanol solution to achieve an Ir weight concentration to be 0.2 mg/mL. Isopropanol was chosen as solution for better dispersion of the Ir/C catalysts and Nafion was added as a binder. The thin-film electrodes were prepared by pipetting 5  $\mu\text{L}$  of the catalysts ink twice onto glassy carbon electrodes which has been pre-polished to mirror finish with a final metal loading of 10  $\mu\text{g}_{\text{Ir}}/\text{cm}^2_{\text{disk}}$ .

Cyclic voltammetry experiments were performed in Ar-saturated 0.1 M KOH solution (prepared from KOH pellet, 99.99 % metal trace, Sigma Aldrich) at a scanning rate of 50 mV/s from  $\sim 0.01$  to 1.0 V vs. RHE without rotating. The electrochemical surface areas of Ir/C samples were determined from the hydrogen adsorption/desorption region with subtraction of double layer. The surface charge density of 218  $\mu\text{C}/\text{cm}^2_{\text{Ir}}$  was assumed for a monolayer adsorption of H on Ir.[92]

The HOR/HER activity measurements of all samples were performed in 0.1 M KOH solution saturated with  $\text{H}_2$  at a scanning rate of 50 mV/s and a rotation speed of 1600 rpm for several cycles until a stable polarization curve was obtained. The scanning rate was then change to 1 mV/s, and this curve was reported in this paper. The  $i_{\text{R-free}}$  potential was obtained after the correction of internal resistance measured by electrochemical impedance spectroscopy (EIS), and the correction equation is as follows,

$$E_{i_{\text{R-free}}} = E - iR \quad (3.1)$$

where E is the original potential, i is the corresponding current, R is the internal resistance, and  $E_{iR-free}$  is the iR-free potential. The electrochemical impedance spectroscopy measurement was performed from 200 kHz to 100 mHz right after the HOR/HER measurement.[2]

The kinetic current ( $i_k$ ) of HOR was corrected using the following equation,

$$\frac{1}{i} = \frac{1}{i_k} + \frac{1}{i_d} \quad (3.2)$$

where i is the measured current,  $i_k$  is the kinetic current and  $i_d$  is the diffusion limited current defined as

$$\eta_{diffusion} = -\frac{RT}{2F} \ln\left(1 - \frac{i_d}{i}\right) \quad (3.3)$$

The exchange current density ( $i_0$ ) of HOR/HER was obtained by fitting the kinetic current density into Butler-Volmer equation, which is

$$i_k = i_0 \left[ \exp\left(\frac{\alpha F \eta}{RT}\right) - \exp\left(\frac{(\alpha-1)F \eta}{RT}\right) \right] \quad (3.4)$$

where  $\alpha$  is the transfer coefficient, F is the Faraday's constant (96,485 A·s/mol),  $\eta$  is the overpotential, R is the universal gas constant (8.314 J/(mol·K)) and T is temperature in Kelvin.

### 3.3 Results and Discussion

#### 3.3.1 Characterization of Ir Particle Size

Carbon supported Ir catalysts with varying particle sizes were prepared by annealing commercial Ir/C at 300-800 °C in Ar. TEM images and the corresponding histograms (counted over 300 particles) of the Ir/C, Ir/C-300C, Ir/C-500C, Ir/C-600C and Ir/C-800C samples show increasing average size of Ir particles as the heat treatment temperature rises (Figure 3.1). In addition, the standard deviation from the average

particle size also increases as the average particle size grows, e.g., the number average particle size and distribution of the untreated Ir/C and Ir/C-800C are  $2.86 \pm 0.83$  and  $7.04 \pm 3.60$ , respectively, which are calculated using Eq. 3.5

$$d_n = \frac{\sum_{i=1}^n d_i}{n} \quad (3.5)$$

in which  $d_n$  is the number average particle diameter in nm,  $d_i$  is the individual particle diameter, and  $n$  is the number of particle measured.

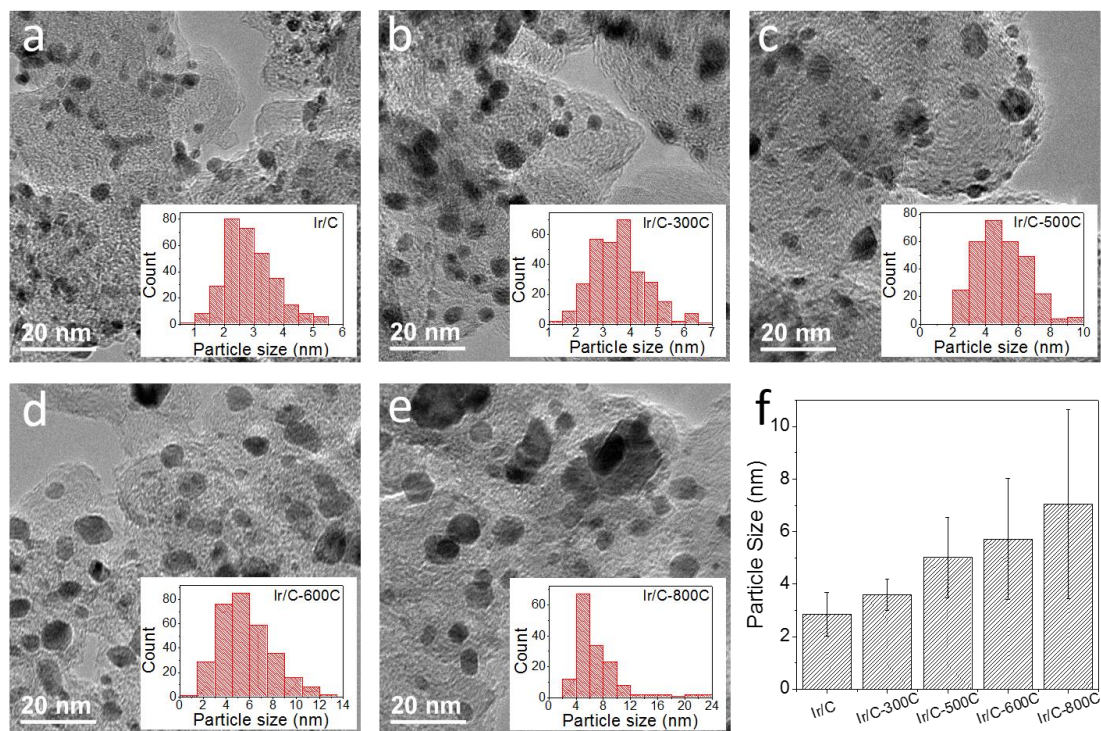


Figure 3.1 TEM images of (a) 20 wt. % Ir/C, (b) Ir/C-300C, (c) Ir/C-500C, (d) Ir/C-600C, and (e) Ir/C-800C. (f) Average particle size determined from TEM images for all Ir/C samples. Insets of (a-e) are the histograms of particle size for the corresponding sample counted over 300 particles.

The volume/area averaged diameter of iridium particles ( $d_{v/a}$ ), which can be calculated by Eq.3.6, is more accurate to represent the specific surface area than the number averaged diameter ( $d_n$ ).[93]

$$d_{v/a} = \frac{\sum_{i=1}^n d_i^3}{\sum_{i=1}^n d_i^2} \quad (3.6)$$

The volume/area averaged particle sizes of all the Ir/C samples are larger than number averaged particle sizes (Table 3.1). The TEM results show that the thermal treatment is a reliable method to obtain Ir particles in the range of 2 – 7 nm (number averaged) or 3 – 12 nm (volume/surface averaged).

XRD patterns of all Ir/C samples (Figure 3.2) show peaks at 40.7 °, 47.3 ° and 69.1 ° corresponding to Ir(111), Ir(200) and Ir(220), respectively. The peaks become narrower from Ir/C to Ir/C-800C, indicating the increase in particle sizes, which is consistent with the observation by TEM. The particle size of each sample is calculated using the Scherrer equation based on the Ir(111) peak, which is the volume averaged particle size ( $d_v^{XRD}$ ),

$$d_v^{XRD} = \frac{0.9\lambda}{\Delta(2\theta)\cos\theta} \quad (3.7)$$

where  $d_v^{XRD}$  is the mean size of the ordered primary crystalline domains,  $\lambda$  is the X-ray wavelength,  $\Delta(2\theta)$  is the full width at half maximum intensity (FWHM) and  $\theta$  is the Bragg angle.  $d_{v/a}^{TEM}$  is in good agreement with  $d_v^{XRD}$  (Table 3.1) indicating that the thermal treatment is a reliable method to obtain Ir particles in the range of 3 – 12 nm.

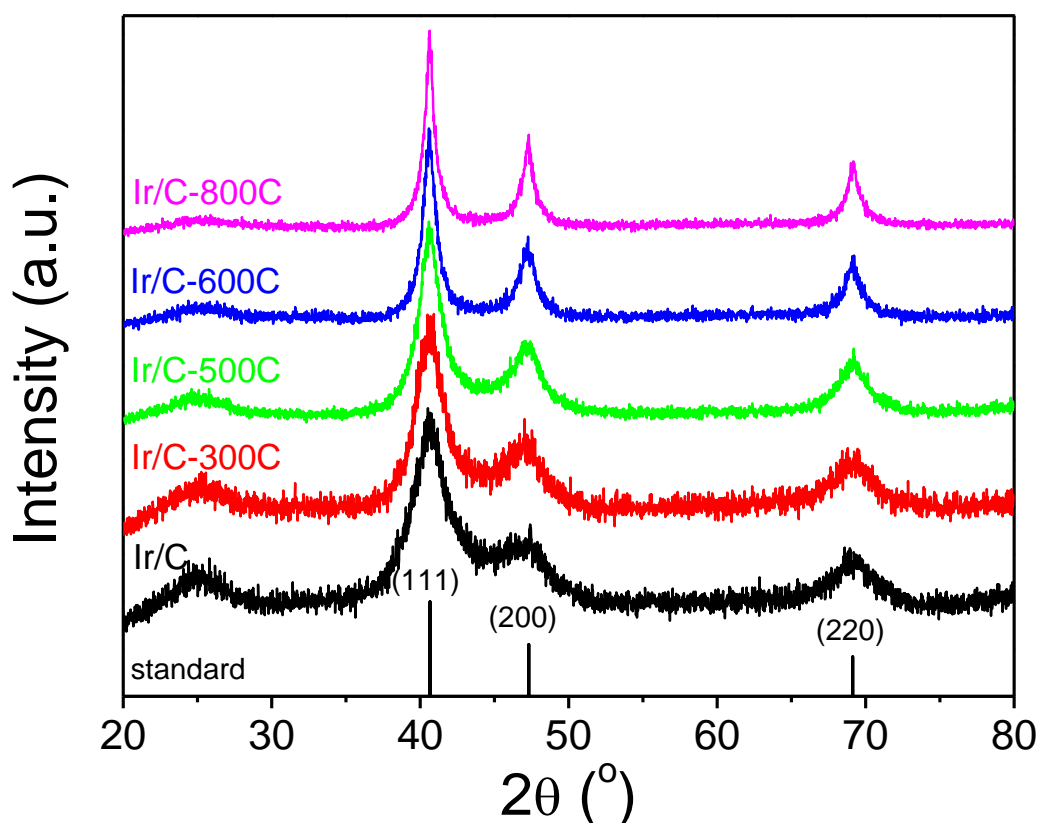


Figure 3.2 X-ray diffraction (XRD) patterns of 20 wt. % Ir/C, Ir/C-300C, Ir/C-500C, Ir/C-600C and Ir/C-800C.

The particle sizes of supported Ir catalysts estimated from total electrochemical surface area (t-ECSA) measurements also agree well with those from TEM and XRD (Table 3.1). Cyclic voltammograms of all Ir/C samples (Figure 3.3) were recorded at 50 mV/s from 0.01 – 1.0 V vs. RHE in Ar-saturated 0.1 M KOH. In a typical Ir-H underpotential deposition ( $H_{\text{upd}}$ ) region (0.05 – 0.5 V), we observed peaks at around 0.16 V, 0.24 V and 0.32 V, potentially attributed to different Ir facets with different hydrogen adsorption energy. The hydrogen adsorption/desorption peak areas, corrected for the contribution from the double layer, were integrated with a cathodic potential

limit of 0.05 V and used to calculate the t-ECSAs of all samples (Table 3.1). t-ECSA decreases as particle size increases at similar Ir loadings, which is expected as a result of the decreasing surface to volume ratio.

The specific surface areas of all the samples area also calculated from  $d_{v/a}^{TEM}$  from TEM ( $S_{v/a}^{TEM}$ ) and  $d_v^{XRD}$  from XRD ( $S_v^{XRD}$ ) using Eq. 3.8, and were listed in Table 3.1,

$$S = \frac{6}{\rho \cdot d} \cdot 10^3 \quad (3.8)$$

where d is particle size in nm (either  $d_{v/a}^{TEM}$  or  $d_v^{XRD}$ ), ECSA is in  $m^2/g_{Ir}$ , and  $\rho$  is the density of iridium ( $22.56 \text{ g/cm}^3$ ). The ECSA measured electrochemically by CV ( $S^{EC}$ ) is smaller than that estimated from TEM ( $S_{v/a}^{TEM}$ ), e.g., for Ir/C sample,  $S^{EC}$  is about 78 % of  $S_{v/a}^{TEM}$ , indicating only 78 % of the surface is electrochemically active largely due to contact of the particle with the carbon support, which is not accessible to cyclic voltammetry measurements.

Table 3.1 Number averaged ( $d_n^{TEM}$ ) and volume/area averaged ( $d_{v/a}^{TEM}$ ) particle size from TEM, volume averaged particle size from XRD ( $d_v^{XRD}$ ), surface areas calculated from  $d_{v/a}^{TEM}$  ( $S_{v/a}^{TEM}$ ),  $d_v^{XRD}$  ( $S_v^{XRD}$ ) and measured electrochemically ( $S_v^{XRD}$ )

	$d_n^{TEM}$ (nm)	$d_{v/a}^{TEM}$ (nm)	$d_v^{XRD}$ (nm)	$S_{v/a}^{TEM}$ ( $m^2/g_{Ir}$ )	$S_v^{XRD}$ ( $m^2/g_{Ir}$ )	$S^{EC}$ ( $m^2/g_{Ir}$ )
Ir/C	$2.86 \pm 0.83$	3.34	3.20	79.6	83.1	$62.2 \pm 8.0$
Ir/C-300C	$3.60 \pm 0.60$	4.24	3.94	62.7	67.5	$52.7 \pm 8.5$
Ir/C-500C	$5.01 \pm 1.53$	5.92	4.99	44.9	53.3	$42.0 \pm 15.4$
Ir/C-600C	$5.72 \pm 2.30$	7.62	8.06	34.9	33.0	$32.0 \pm 2.8$
Ir/C-800C	$7.04 \pm 3.60$	11.57	12.3	23.0	21.6	$13.8 \pm 1.7$

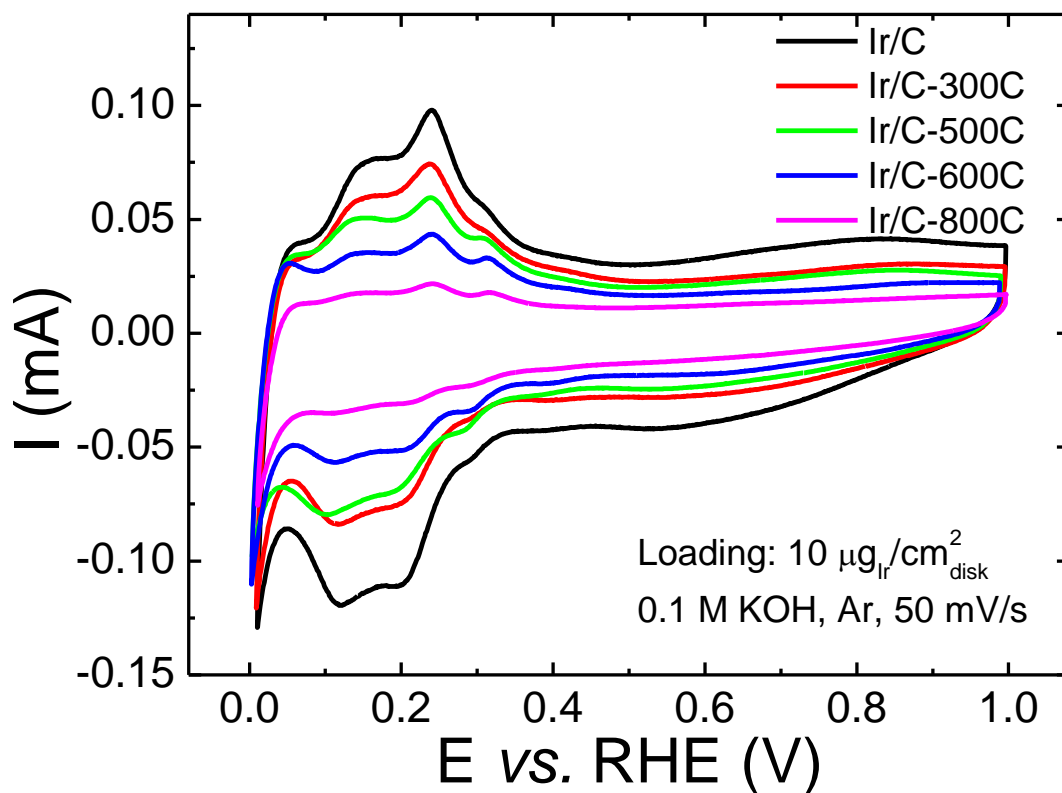


Figure 3.3 Cyclic voltammograms of Ir/C, Ir/C-300C, Ir/C-500C, Ir/C-600C and Ir/C-800C conducted in Ar saturated 0.1 M KOH at a scan rate of 50 mV/s. The Ir loading for all samples is  $10 \mu\text{g}/\text{cm}^2_{\text{disk}}$ .

Supported Ir catalysts with different particle sizes have different composition of surface sites. There are three general features in the anodic branch of  $H_{\text{upd}}$  region in the CV, indicating the Ir sites for the oxidation of  $H_{\text{upd}}$  are not uniform (Figure 3.3). This observation is reminiscent of the well-defined  $H_{\text{upd}}$  peaks assigned to the low-index crystallographic facets of Pt. However, the local environments of sites on supported Ir nanoparticles are much more diverse than single crystal surfaces, and the observed broad features should be interpreted as the manifestation of multiple groups of Ir sites sharing common properties key to HOR.

### 3.3.2 HOR/HER Activity of Supported Ir Catalysts with Varying Particle Sizes

Key kinetic parameters of HOR/HER on Ir/C in alkaline electrolyte were obtained with a series of rotating disk electrode (RDE) measurements (Figure 3.4a-c). The HOR/HER polarization curve on Ir/C in 0.1 M KOH at 293 K (Figure 3.4a) reaches the max hydrogen mass transport limiting current density ( $i_l$ ) at potentials above 0.2 V. Even after iR correction, the curve (red trace, Figure 3.4a) deviates significantly from concentration overpotential curve (blue dashed trace) which enables the quantification of its HOR/HER activity.[2,94] The kinetic current density ( $i_k$ ) was obtained as described in experimental section and fitted with the Butler-Volmer equation to determine the exchange current density ( $i_0$ ) and transfer coefficient ( $\alpha$ ).

The fitted curve matches well with experimental data (Figure 3.4b), with  $i_0$  and  $\alpha$  being  $0.21 \pm 0.02 \text{ mA/cm}^2_{\text{Ir}}$  and  $0.56 \pm 0.03$ , respectively. The  $i_l$  on the HOR/HER polarization curve increases as the rotation speed increases from 400 rpm to 2500 rpm (Figure 3.4c). The  $i_l$  is proportional to the square root of rotating speed ( $\omega$ , in radians per second), as indicated by the Levich equation,  $i_l = 0.62nFD^{2/3}\nu^{-1/6}c_0\omega^{1/2} = Bc_0\omega^{1/2}$ , where  $D$  is the diffusivity of hydrogen in 0.1 M KOH ( $3.7 \times 10^{-5} \text{ cm}^2/\text{s}$ ),  $n$  is the number of electrons transferred in  $\text{H}_2$  oxidation reaction ( $n = 2$ ),  $\nu$  is the kinematic viscosity of the electrolyte ( $1.01 \times 10^{-2} \text{ cm}^2/\text{s}$  (CRC handbook)) and  $c_0$  is the solubility of  $\text{H}_2$  in 0.1 M KOH ( $7.33 \times 10^{-4} \text{ M}$ ). The inverse of  $i_l$  at 0.25 V was plotted as a function of the inverse of  $\omega^{1/2}$  (Inset of Figure 3.4c), which was linearly fitted to generate a line passing through the origin and a  $Bc_0$  value of  $0.0687 \text{ mA}/(\text{cm}^2_{\text{diskrpm}}^{1/2})$ , in good agreement with calculated  $Bc_0$  value ( $0.0678 \text{ mA}/(\text{cm}^2_{\text{diskrpm}}^{1/2})$ ). The HOR/HER polarization curves were measured at temperatures ranging from 275 K to 313 K at 1600 rpm (Figure 3.4d). The  $i_l$  increases with temperature (Figure 3.4d), which is consistent with the report by Sheng et al. in the case of polycrystalline Pt (Pt(pc)).[2] The slope of

the polarization curve becomes steeper with the increase of temperature, and the potential at which the limiting current was reached shifted negatively as temperature increases, indicating a faster kinetics of HOR/HER. The  $i_0$  at different temperatures were extracted via the curve fitting to the Butler-Volmer equation, and an activation energy of  $32.9 \pm 1.5$  kJ/mol was obtained by plotting  $\ln(i_0)$  vs.  $T^{-1}$  (Inset of Figure 3.4d), which is slightly higher than that on both Pt(pc) ( $28.9 \pm 4.3$  kJ/mol) and Pt/C ( $29.5 \pm 4.0$  kJ/mol).[2] Note that the  $i_0$  we obtained at 313 K is  $0.44 \pm 0.03$  mA/cm<sup>2</sup><sub>Ir</sub>, in reasonable agreement with Durst et al.'s result on Ir.[3]

Table 3.2 Summary of average specific exchange current densities based on t-ECSA and mass exchange current densities of HOR/HER on all Ir samples and their corresponding transfer coefficients ( $\alpha$ )

Samples	$i_{0,s}$ (mA/cm <sup>2</sup> <sub>Ir</sub> )	$i_{0,m}$ (A/g <sub>Ir</sub> )	$\alpha$
Ir/C	$0.21 \pm 0.02$	$128.6 \pm 18.8$	$0.56 \pm 0.03$
Ir/C-300C	$0.22 \pm 0.07$	$110.3 \pm 13.1$	$0.55 \pm 0.02$
Ir/C-500C	$0.30 \pm 0.06$	$118.4 \pm 20.0$	$0.53 \pm 0.03$
Ir/C-600C	$0.31 \pm 0.05$	$97.8 \pm 7.6$	$0.54 \pm 0.02$
Ir/C-800C	$0.53 \pm 0.01$	$73.0 \pm 9.0$	$0.50 \pm 0.01$

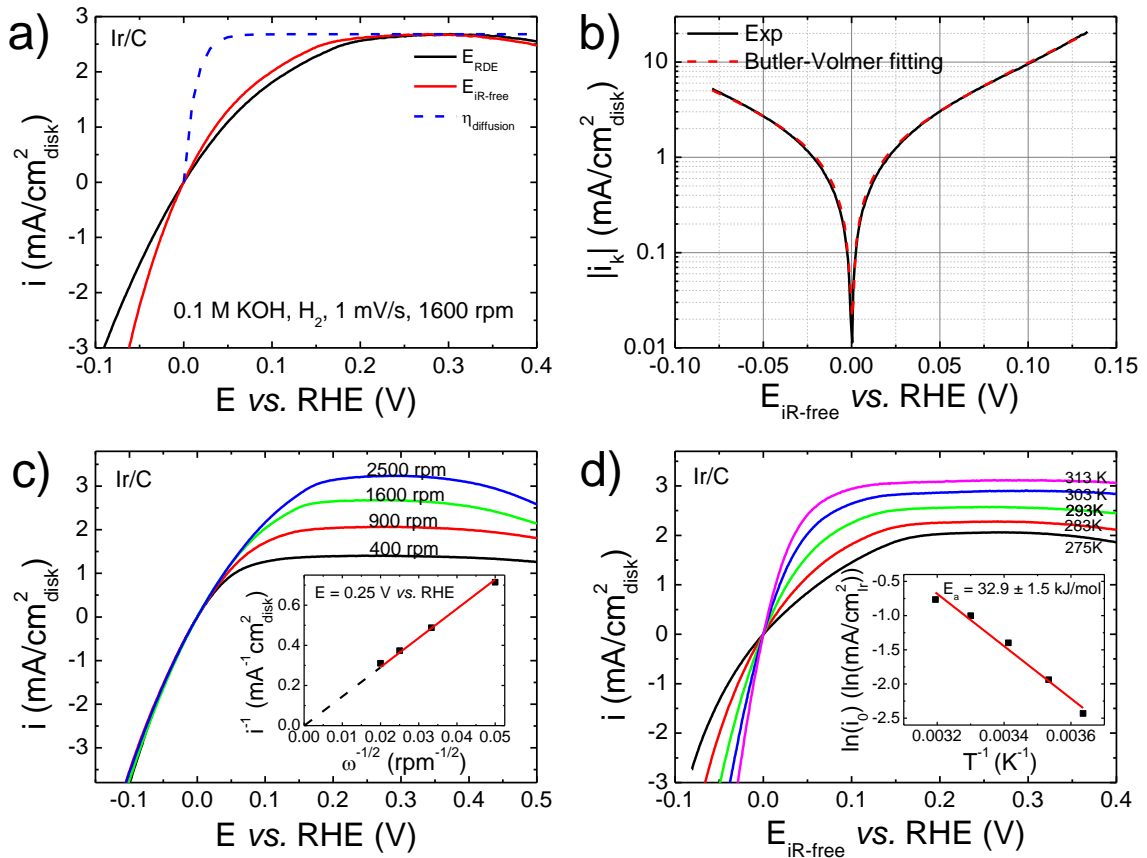


Figure 3.4 (a) HOR/HER polarization curve (positive scan) on Ir/C in 0.1 M KOH saturated with H<sub>2</sub> (1 atm) at a scan rate of 1 mV/s with a rotation speed of 1600 rpm at r.t. (293K) before (black line) and after (red line) iR correction. The blue dashed line is the concentration overpotential curve. The loading of Ir was 10  $\mu\text{g}/\text{cm}^2_{\text{disk}}$ . (b) The measured HOR/HER kinetic current density (black solid line) and the corresponding Butler-Volmer equation (Eq. 3.4) fitting (red dashed line) with  $\alpha = 0.47$ . (c) HOR/HER polarization curves on Ir/C in 0.1 M KOH saturated with H<sub>2</sub> (1 atm) at scan rate of 1 mV/s at r.t. with rotation speeds ranging from 400 rpm to 2500 rpm. The inset shows a Koutecky-Levich plot at 0.25 V vs. RHE. (d) HOR/HER polarization curves on Ir/C in 0.1 M KOH saturated with H<sub>2</sub> (1 atm) at a scan rate of 1 mV/s with a rotation speed of 1600 rpm at temperatures ranging from 275 K to 313 K. The inset shows the Arrhenius plot with the slope corresponding to  $-E_a/R$ , giving an activation energy of  $32.9 \pm 1.5$  kJ/mol.

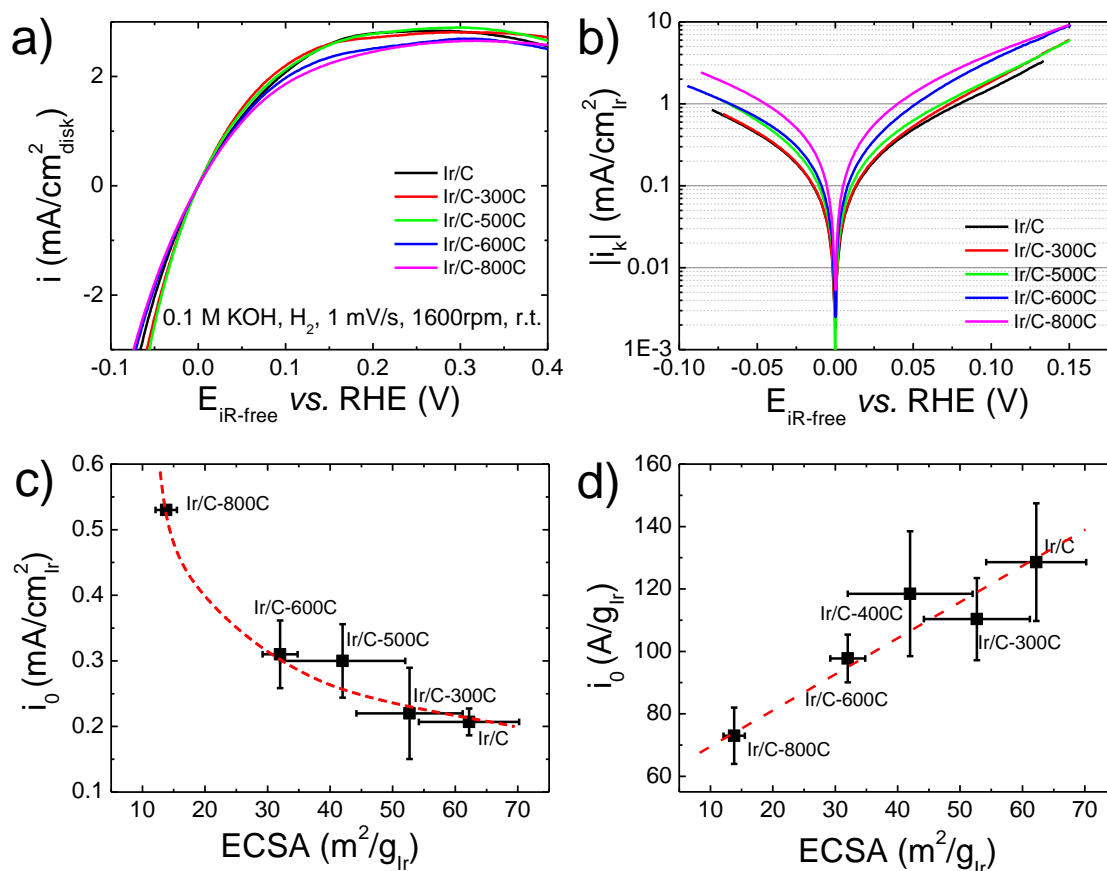


Figure 3.5 (a) iR-corrected HOR/HER polarization curves (positive scan) and (b) measured kinetic current on Ir/C samples with different sizes. All measurements were performed in 0.1 M KOH saturated with H<sub>2</sub> (1 atm) at a scan rate of 1 mV/s with a rotation speed of 1600 rpm at r.t. (293 K). Specific (c) and mass (d) exchange current densities of HOR/HER on Ir/C samples normalized to t-ECSA as a function of t-ECSA. The red dashed lines serve as eye guiding lines for the trends.

Kinetic studies of HOR/HER on Ir/C with varying particle sizes were performed (Figure 3.5a, b). The specific exchange current density of supported Ir catalysts for HOR/HER increases with the decrease of t-ECSA (or the increase of particle size), (Figure 3.5c and Table 3.2) suggesting that not all sites contributing to t-ECSA are equally active. Contrarily, the mass exchange current density decreases as t-ECSA

decreases (or particle size increases) (Figure 3.5d), attributing to decreased t-ECSA of larger particles as mass exchange current density is the product of specific exchange current density and t-ECSA. All Ir/C samples have a similar transfer coefficient value (about 0.5), and in turn a Tafel slope of 116 mV/dec at 293K, illustrating that their HOR/HER share the same mechanism. Strmcnik et al. obtained a polarization curve for HOR/HER that is essentially overlapped with the concentration overpotential curve of polycrystalline Ir (Ir(pc)) under similar conditions.[83] An analysis of the polarization curves as a function of exchange current density reveals that when the exchange current density is a factor of 10 or higher than  $i_1$  – assuming a roughness factor of 1 – significant overlap between the polarization and concentration overpotential curves exists. Based on this analysis, it can be inferred that the exchange current density of Ir(pc) should be at least 15 mA/cm<sup>2</sup> (for a roughness factor of 2) or 30 mA/cm<sup>2</sup> (for a roughness factor of 1), which agrees with our observed trend that the exchange current density increases with the particle size of Ir.

### 3.3.3 Correlating $H_{\text{upd}}$ Peaks in Cyclic Voltammogram with HBE of Active Sites

The position of  $H_{\text{upd}}$  desorption peaks in a cyclic voltammogram can be correlated with the HBE of the corresponding sites, as suggested by Durst et al.[3] Assuming a Langmuir isotherm, we show that the potential at the peak of  $H_{\text{upd}}$  desorption features is related to the HBE of the corresponding sites (Appendix B.1):

$$E_{M-H} = -E_{\text{peak}}F - \frac{1}{2}TS_{H_2}^0 \quad (3.9)$$

in which  $E_{M-H}$ ,  $E_{\text{peak}}$ ,  $F$ ,  $T$ , and  $S_{H_2}^0$  are HBE of the metal sites,  $H_{\text{upd}}$  desorption peak potential vs. RHE, Faraday's constant, temperature, and entropy of  $H_2$  at standard conditions, respectively.

The assumption that an equilibrium state is reached at each potential in CV testing used for the derivation is reasonable considering that  $H_{\text{upd}}$  adsorption and desorption is a fast process compared with the scanning rate, which can be verified by the minimal shift of peak potentials as the scanning rate decreases from 50 mV/s to 5 mV/s (Figure 3.6a). The shape of  $H_{\text{upd}}$  desorption peaks remains essentially unchanged within the range of scanning rate tested (Figure 3.6b) while the relative peak height of  $H_{\text{upd}}$  adsorption peak centered at  $\sim 0.13$  V decreases as scanning rate decrease (Figure 3.6c). We hypothesized that the  $H_{\text{upd}}$  adsorption process is likely influenced by pre-adsorbed species while the  $H_{\text{upd}}$  desorption process is not. Therefore, the  $H_{\text{upd}}$  desorption regions are used for analysis. An  $E_{\text{peak}}$  value of 0.15 V for Pt(110) in 0.1 M HClO<sub>4</sub> yields the HBE of  $-33.6$  kJ/mol, which is consistent with the reported value based on temperature-dependent cyclic voltammograms.[95] Studies also showed good agreements between the hydrogen adsorption energy in solution and in gas-phase.[96] The correlation between  $H_{\text{upd}}$  desorption peak position and HBE of the corresponding sites offers an easy and powerful approach to obtain structure-activity relation for HOR/HER. No detectable shift of  $H_{\text{upd}}$  desorption peak potentials (or HBE) of the different types of sites on Ir nanoparticles with varying particle sizes was observed. However, there is significant redistribution among those sites as particle size grows, as evidenced by the change in the cyclic voltammogram profile in the  $H_{\text{upd}}$  region on the anodic branch (Figure 3.3). It could be a key element in rationalizing the decreasing specific exchange current density for HOR/HER as t-ECSA increases (particle size decreases), since many reactions including HOR/HER are strongly structure sensitive.[39,86,97,98] For example, Marković et al. reported the HOR/HER exchange current densities on three Pt single crystals in the order of (110) > (100) > (111) in both acidic[39] and alkaline[86]

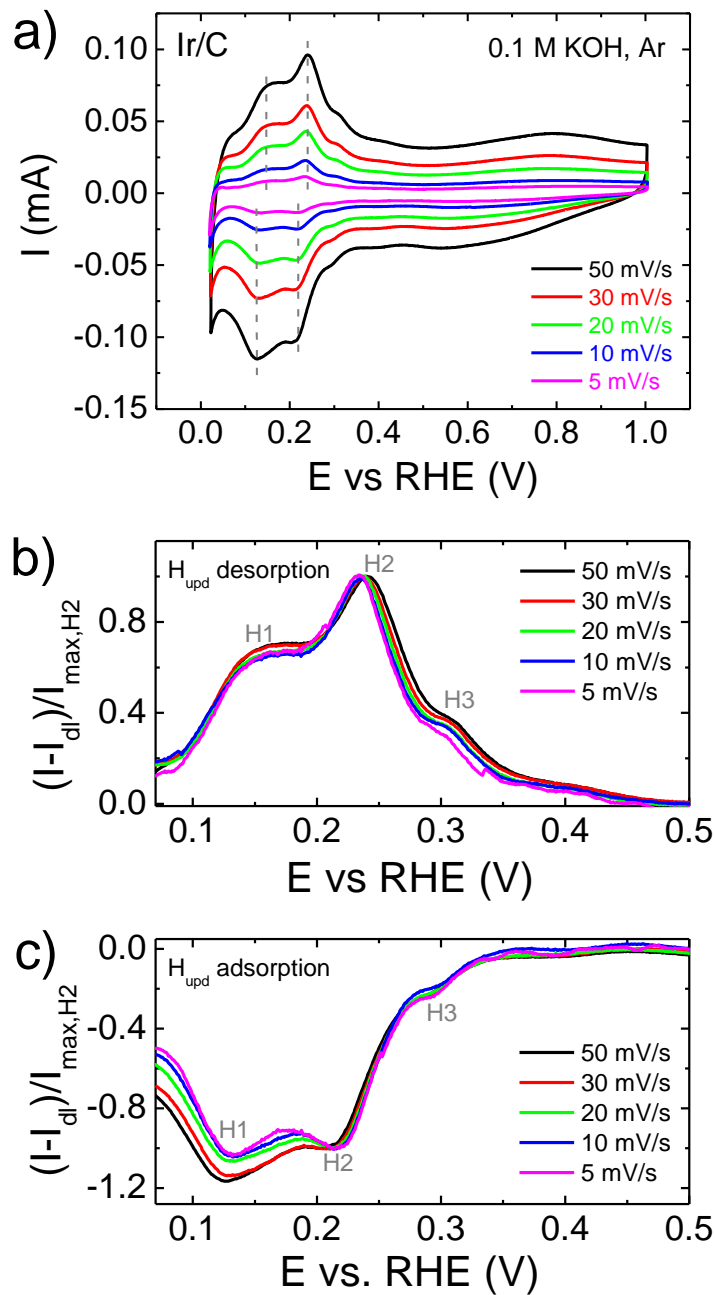


Figure 3.6 (a) Cyclic voltammograms of Ir/C (loading:  $10 \mu\text{g}/\text{cm}^2_{\text{disk}}$ ) measured in Ar-saturated 0.1 M KOH at various scanning rates from 5 to 50 mV/s, 0 rpm, (b)  $H_{\text{upd}}$  desorption profiles from CV in (a) normalized to peak current of  $H_2$  after double-layer correction, and (c)  $H_{\text{upd}}$  adsorption profiles from CV in (a) normalized to peak current of  $H_2$  after double-layer correction.

electrolytes. In addition, Kinoshita et al. observed an increased ratio between the amount of “strongly” adsorbed hydrogen and “weakly” adsorbed hydrogen as Pt particle size increases in both H<sub>2</sub>SO<sub>4</sub>[99,100] and NaOH[100] electrolytes, which was attributed to the change in fractions of different facets as particle size varies.

### 3.3.4 Identifying True Active Sites for HOR/HER via Peak Deconvolution

To gain a more quantitative understanding of the effect of Ir particle size on HOR/HER activity in an alkaline electrolyte, the H<sub>upd</sub> desorption profiles were deconvoluted into multiple peaks to quantify the site distribution followed by correlating the measured HOR/HER activities to the amount of each sites. Initially, the H<sub>upd</sub> desorption profiles were deconvoluted into three naturally existed peaks centered at 0.16 V (H1), 0.24 V (H2) and 0.32 V (H3), respectively (Figure 3.7). However, we were unable to obtain good peak fitting with identical peak widths (FWHM) for each species (H1, H2 and H3), indicating the heterogeneous nature of the sites within each species (Table 3.3). In addition, sites corresponding to H1 have lower H<sub>upd</sub> desorption peak potential for HOR than H2 and H3 by 0.08 and 0.16 V, respectively. Then, the HOR rate constant mediated by H1 should be a factor of 24 and 565 faster than that of H2 and H3, respectively, assuming identical preexponential factors in the Arrhenius equation. It follows that the exchange current density normalized by the fraction of H1 ( $i_{0,H1}$ ) in all sites should be independent of particle size or t-ECSA if sites corresponding to H1 are true active sites for HOR/HER. The  $i_0$  vs. fraction of H1 shows a linear correlation, but does not go through origin (Figure 3.8a). Additionally, Figure 3.8b shows that  $i_{0,H1}$  decreases with increasing t-ECSA (decreasing particle size), suggesting H1 is not a truthful representation of active sites. We attribute the poor correlation

between H1 and HOR/HER activity to the heterogeneity of sites corresponding to H1, and hypothesize that a fraction of sites in H1 with lower HBE are the true active sites.

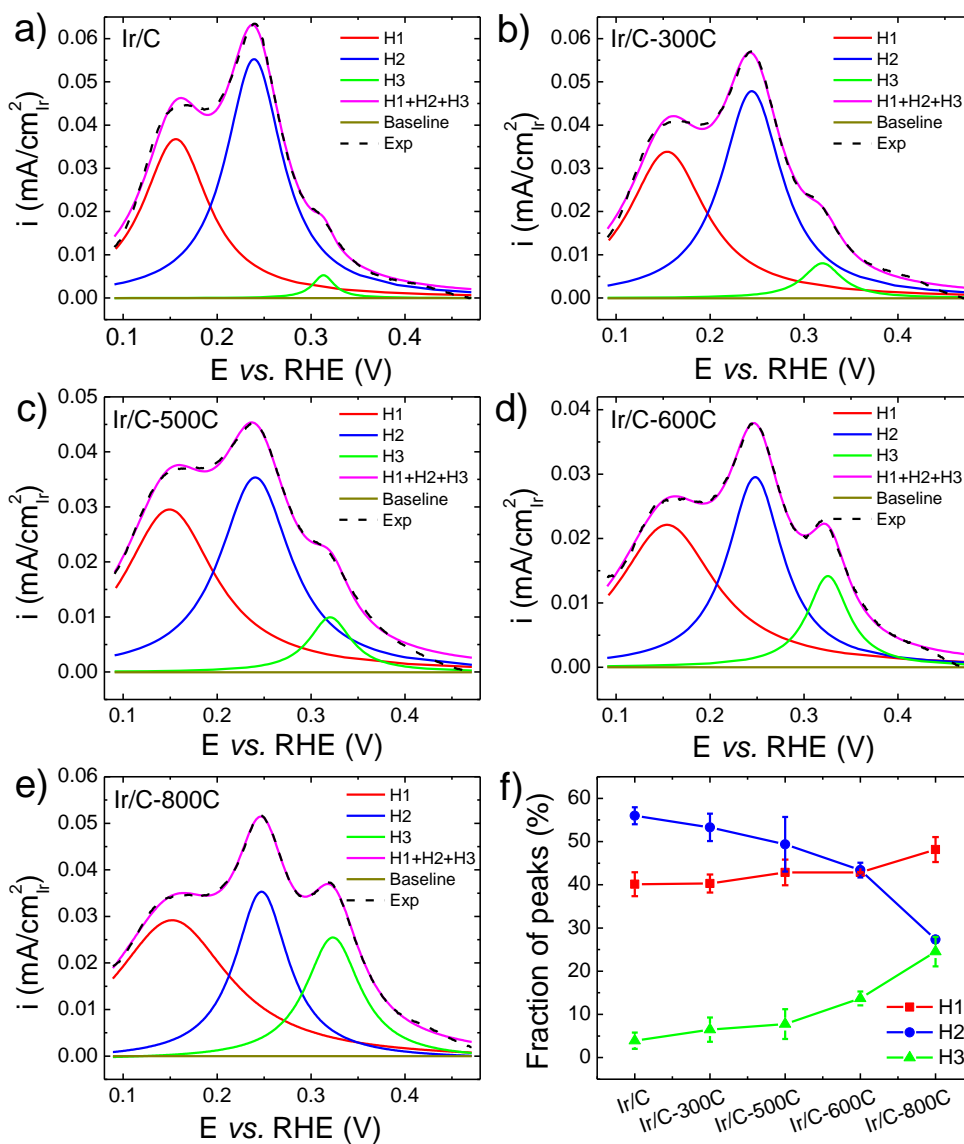


Figure 3.7 Deconvolution of hydrogen desorption peaks into three peaks centered at 0.16 V (H1), 0.24 V (H2) and 0.32 V (H3) for (a) Ir/C, (b) Ir/C-300C, (c) Ir/C-500C, (d) Ir/C-600C, and (e) Ir/C-800C. (f) Fractions of deconvoluted peak H1, H2 and H3 defined by the ratio of deconvoluted peak area and total area.

Table 3.3 FWHM and peak position of deconvoluted peak H1, H2 and H3 for all samples

Samples	FWHM/V		
	Peak H1	Peak H2	Peak H3
Ir/C	0.088 ±0.002	0.076 ±0.002	0.035 ±0.007
Ir/C-300C	0.102 ±0.004	0.080 ±0.006	0.023 ±0.022
Ir/C-500C	0.111 ±0.013	0.080 ±0.008	0.037 ±0.019
Ir/C-600C	0.123 ±0.004	0.074 ±0.002	0.052 ±0.003
Ir/C-800C	0.133 ±0.012	0.072 ±0.002	0.062 ±0.007
Samples	Peak position/V		
	Peak H1	Peak H2	Peak H3
Ir/C	0.156 ±0.001	0.242 ±0.002	0.313 ±0.003
Ir/C-300C	0.153 ±0.002	0.242 ±0.002	0.316 ±0.003
Ir/C-500C	0.152 ±0.005	0.244 ±0.006	0.319 ±0.004
Ir/C-600C	0.153 ±0.002	0.247 ±0.001	0.325 ±0.001
Ir/C-800C	0.151 ±0.001	0.247 ±0.001	0.323 ±0.001

Table 3.4 FWHM and peak positions of deconvoluted peak H1a, H1b, H2 and H3 for all samples

Samples	FWHM/V			
	Peak H1a	Peak H1b	Peak H2	Peak H3
Ir/C	0.069 ±0.001	0.089	0.074	0.054
Ir/C-300C	0.071 ±0.010	0.089	0.074	0.054
Ir/C-500C	0.091 ±0.004	0.089	0.074	0.054
Ir/C-600C	0.094 ±0.004	0.089	0.074	0.054
Ir/C-800C	0.101 ±0.001	0.089	0.074	0.054
Samples	Peak position/V			
	Peak H1a	Peak H1b	Peak H2	Peak H3
Ir/C	0.137 ±0.001	0.172 ±0.002	0.241 ±0.001	0.311 ±0.002
Ir/C-300C	0.135 ±0.001	0.172 ±0.002	0.242 ±0.002	0.317 ±0.003
Ir/C-500C	0.133 ±0.006	0.175 ±0.001	0.241 ±0.001	0.314 ±0.004
Ir/C-600C	0.133 ±0.001	0.175 ±0.001	0.241 ±0.001	0.318 ±0.001
Ir/C-800C	0.137 ±0.001	0.179 ±0.001	0.241 ±0.001	0.317 ±0.001

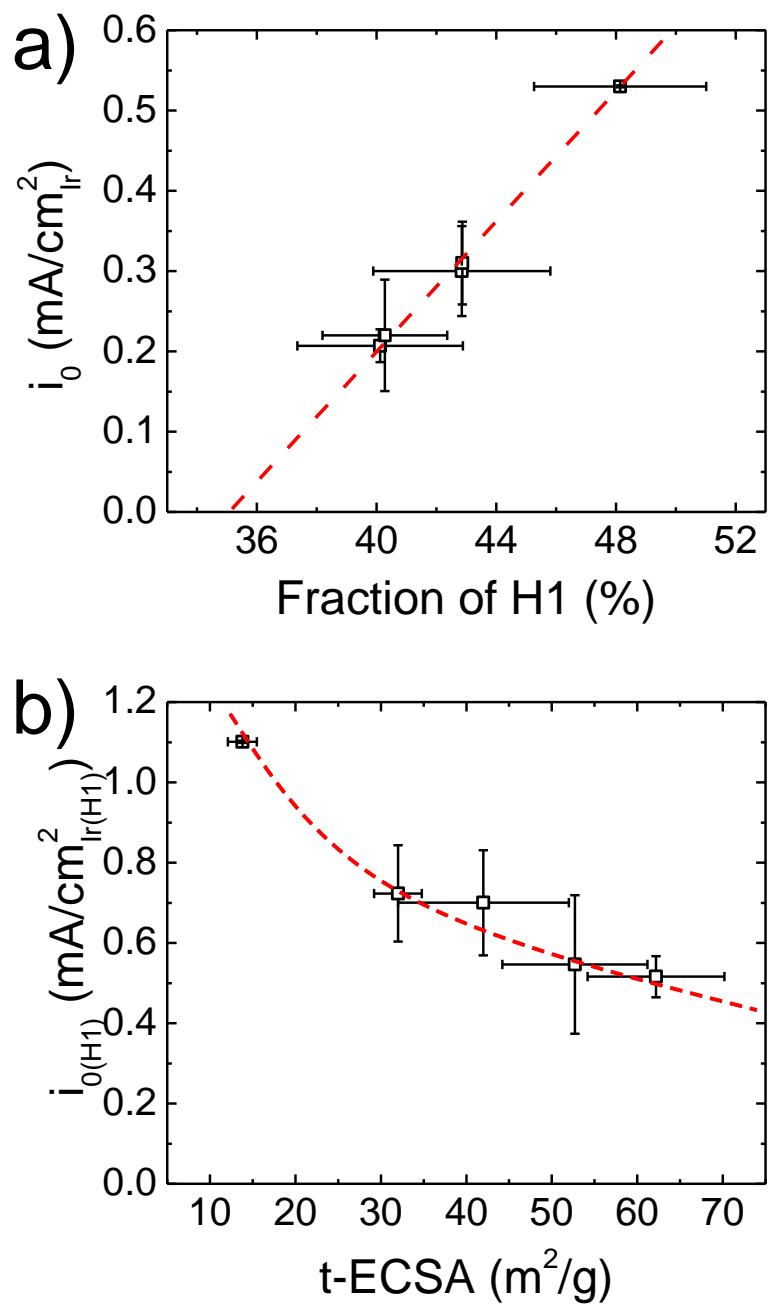


Figure 3.8 (a)  $i_0$  as a function of fraction of peak H1 with three peak deconvolution, and (b)  $i_0$  normalized to surface area of site H1 (peak potential at 0.16 V) ( $i_{0(H1)}$ ) as a function of t-ECSA.

We further deconvoluted H1 into H1a and H1b centered at 0.13 and 0.18 V, respectively (Figure 3.9), and for all samples, the measured HOR/HER activities correlates well with sites corresponding to H1a (Figure 3.10). We fixed the peak width of H1b, H2 and H3 in the fitting, and best fitting was achieved when the peak width of H1a grows slightly with particle size, reflecting a small degree of heterogeneity of H1a sites (Figure 3.9 and Table 3.4). No further deconvolution of H1a peak was attempted because reasonable structure-activity correlation can be extracted with H1a and H1b. The fractions of H1a and H3 sites increase as particle size grows, while the opposite is true for H1b and H2, indicating that H1a and H3 sites are likely terrace sites. Among the four types of sites, H1a site has the lowest HBE, and hence corresponds to most weakly bound  $H_{\text{upd}}$ . When the exchange current densities were normalized to the surface area of H1a, H1b, H2 and H3, respectively (denoted as  $i_{0,H1a}$ ,  $i_{0,H1b}$ ,  $i_{0,H2}$  and  $i_{0,H3}$ ),  $i_{0,H1a}$  becomes independent of t-ECSA while  $i_{0,H1b}$ ,  $i_{0,H2}$  and  $i_{0,H3}$  either increase or decrease with t-ECSA (Figure 3.11), which provides the following key mechanistic insights: 1) Only Ir sites corresponding to H1a contribute significantly to HOR/HER activity. 2) A small fraction (15-30%) of active Ir sites shoulder most of the HOR activity, suggesting that increasing the density of those sites rather than total Ir sites should be the strategy in the design of future Ir-based HOR catalysts. It is consistent with the estimation that the HOR rate constant for H1a sites will be a factor of 7.2 higher than that of sites corresponding to H1b.

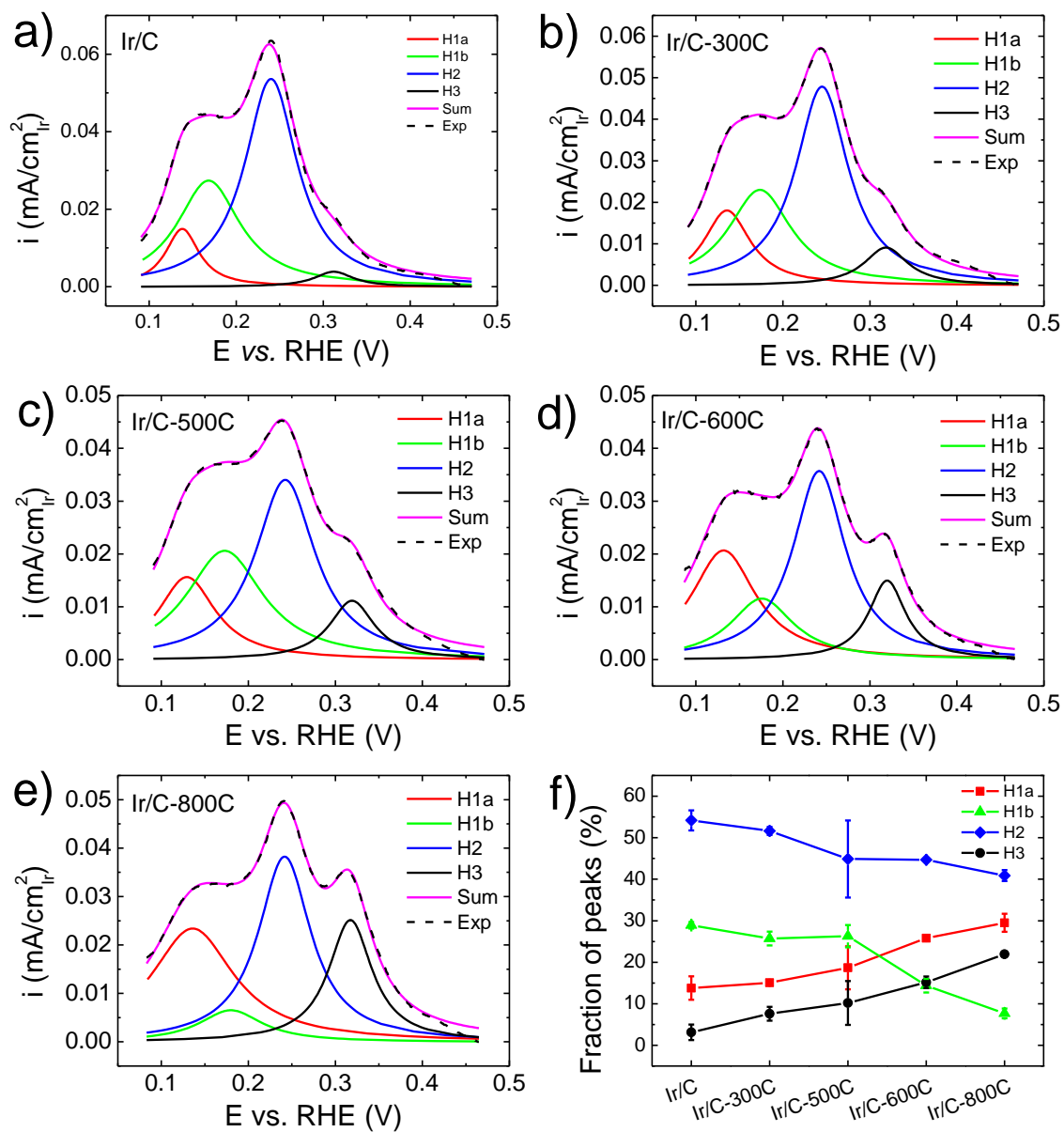


Figure 3.9 Deconvolution of hydrogen desorption peaks into four peaks centered at 0.13 V (H1a), 0.18 V (H1b), 0.24 V (H2) and 0.32 V (H3) for (a) Ir/C, (b) Ir/C-300C, (c) Ir/C-500C, (d) Ir/C-600C and (e) Ir/C-800C. (f) Fraction of peaks H1a, H1b, H2 and H3 among different samples.

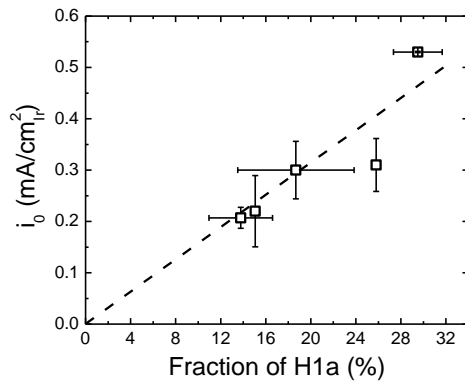


Figure 3.10 Correlation between the exchange current density ( $i_0$ ) normalized to t-ECSA and the fraction of peak H1a.

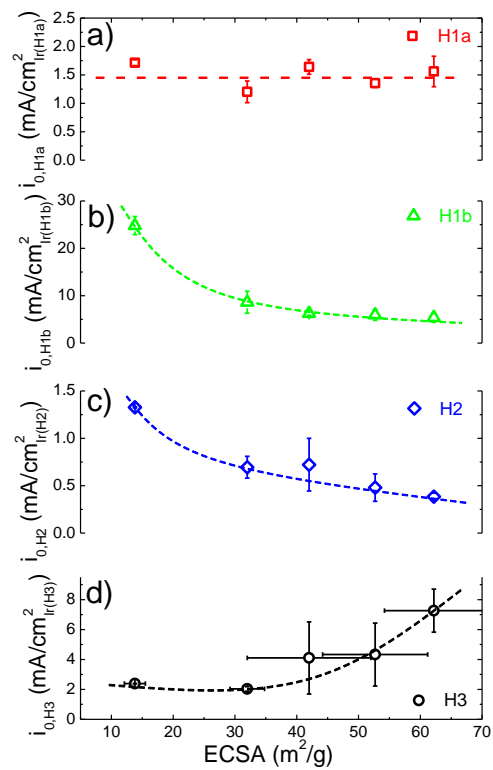


Figure 3.11  $i_0$  normalized to surface area of H1a (peak potential 0.13 V), H1b (peak potential 0.18 V), H2 (peak potential 0.24 V) and H3 (peak potential 0.32 V) as a function of t-ECSA.

We also simulated the exchange current density based on weighed addition of the four peaks: the simulated exchange current densities agree well the experimental ones, with the majority of the activity contributed from sites associated with peak H1a (Figure 3.12), indicating peak H1a sites are the most active ones. 3) Ir sites on low index planes are more likely to be the active sites for HOR (H1a) since the fraction of low index planes typically increases as particle size grows. This can be inferred by comparing the plot of peak H1a, H1b, H2 and H3 fractions for different-sized Ir/C samples (Figure 3.9f) and the simulated surface distribution of a cubo-octahedron structure (Figure 3.13). The hydrogen adsorption and desorption on single crystal Ir were studied by Motoo et al. where different hydrogen desorption peak potentials were observed for the three low index facets in the order of  $(110) < (111) < (100)$  in 0.1 M HClO<sub>4</sub>. [101] More positive hydrogen desorption peak potentials were observed on high index Ir facets as compared with Ir(110) and Ir(111) by Furuya et al. [102], indicating a higher hydrogen binding energy on high index Ir facets. In addition, it is also consistent with the report by Strmcnik et al. that polycrystalline Ir disk exhibits very high HOR activity, [83] in that Ir disk contains higher density of low index planes than nanoparticles. Furthermore, the coordination number for Ir atoms on low index planes is higher than that of defective surfaces, which typically leads to lower binding to adsorbates. The increasing trend of peak H3 with particle size seems to suggest the sites associated with peak H3 might also be certain type of low-coordinate site with a high HBE. Similar phenomenon has been observed on Pt/C that the H<sub>upd</sub> desorption peak with highest HBE arises as particle size increases. [103] However, more detailed investigations on single crystalline Ir surfaces for accurate peak assignments will be the subject of future studies.

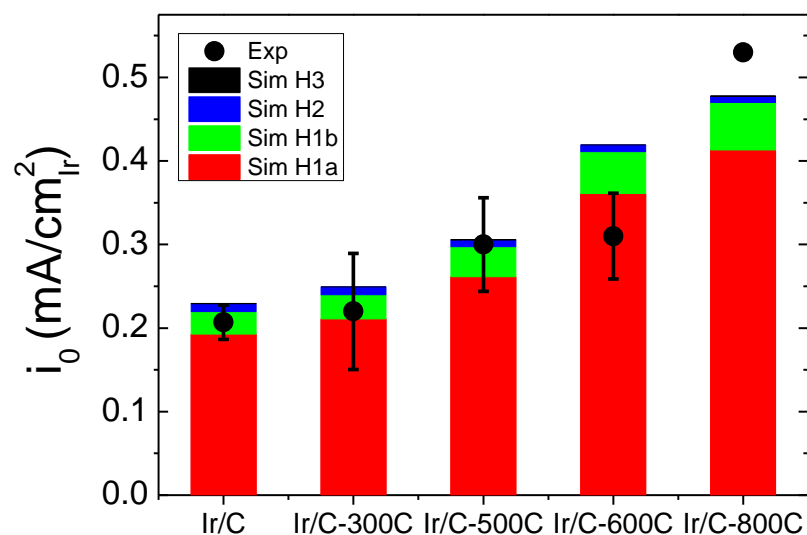


Figure 3.12 Experimental exchange current densities (black circle dots) and simulated exchange current densities (bars) with contribution from H1a (red bars), H1b (green bars), H2 (blue bars) and H3 (black bars) of all the samples.

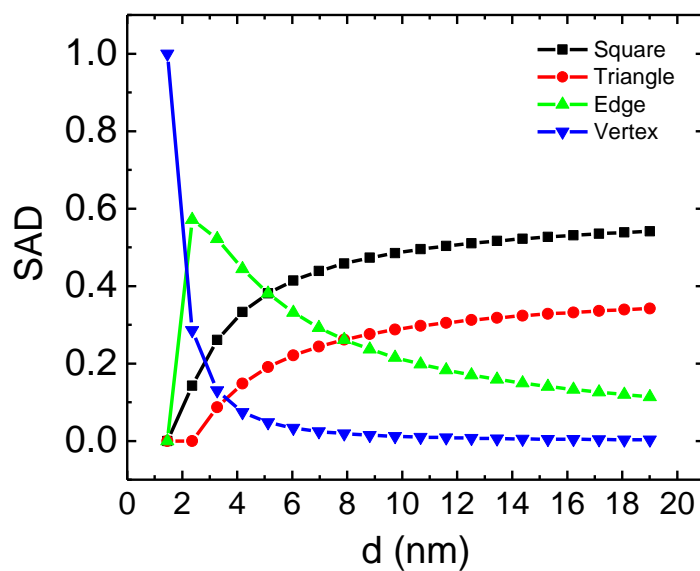


Figure 3.13 Surface averaged distribution (SAD) of square, triangle, edge and vertex sites of particles with a cubo-octahedron structure as a function of particle size. The method for calculating the site distribution can be found in the supporting information of ref.[90]

The excellent correlation between sites with lowest HBE and the HOR/HER activity supports the hypothesis that HBE is the key descriptor for HOR/HER catalysts, as argued by Durst et al.[3], Sheng et al.[85] and Wang et al.[52]. It was hypothesized that Pt showed much lower HOR/HER activity in alkaline electrolyte than that in acid mainly due to its higher HBE in the alkaline environment. Similarly, it has been shown by Durst et al.[3] that Ir have more positive  $H_{\text{upd}}$  desorption peak potential in alkaline than in acid electrolyte, revealing the HBE of Ir is also higher in alkaline than in acidic media. Iridium has been grouped in the weak hydrogen binding branch in the volcano plot for acidic electrolyte.[31] If we consider that Ir has an inferior HOR/HER activity than Pt simply due to its weaker HBE than Pt in acid, then one would expect an increase of HOR/HER activity on Ir in alkaline electrolyte due to the stronger HBE in alkaline electrolyte. The HOR/HER activity of Ir/C at 313 K measured using  $H_2$ -pump with proton exchange membrane (which mimics the acidic environment) is 120 times of that in 0.1 M NaOH.[3] This experimental observation suggest that Ir also belongs to the branch with too strong HBE, and it follows that sites with lower HBE will have higher HOR/HER activity.

### **3.4 Conclusion**

In conclusion, we studied the HOR/HER kinetics on Ir/C in alkaline electrolyte systematically using a thin-film RDE method. By tuning the Ir particle size from 3 to 12 nm, we were able to vary the surface site distribution quantified by deconvolution analysis on the  $H_{\text{upd}}$  desorption region of CVs: the population of the sites with smallest HBE (higher HOR/HER activity) increases as particle size increase. Particle size effect of HOR/HER on Ir/C was observed: the specific HOR/HER activities (activity normalized to t-ECSA) decrease as t-ECSA increases (or particle size decreases).

HOR/HER activities normalized to the surface area of the lowest hydrogen binding site are independent of t-ECSA, indicating that those sites with low HBE (most likely low-index facets) are the most active sites for HOR/HER. Therefore, our study suggests that extended Ir nanostructure with high fraction of low-index facets such as Ir nanotubes or nanowires may have higher HOR/HER activities compared with small Ir nanoparticles.

## Chapter 4

### SIZE-DEPENDENT HYDROGEN OXIDATION AND EVOLUTION REACTION ACTIVITY ON PALLADIUM NANOPARTICLES IN ACID AND BASE

The study of particle size effect provides fundamental understanding of the active sites, bridges the activity difference on materials in the form of bulk or nanoparticles, and offers guidance for design and development of better catalysts. Here we report a systematic investigation of particle size effect of hydrogen oxidation and evolution reaction (HOR/HER) on carbon supported Pd nanoparticles with sizes ranging from 3 to 42 nm in both acidic and alkaline electrolytes using rotating disk electrode (RDE) method. Similar particle size effect was obtained in both acid and base: the HOR/HER activity in terms of specific exchange current density increases as Pd particle size increases from 3 to 20 nm, and then reaches a plateau with activity similar to that of bulk Pd. The enhanced activity with rising particle size could be attributed to the increased ratio of the sites with smaller hydrogen adsorption energy revealed in cyclic voltammograms. Pd/C samples with different sizes all showed much higher HOR/HER activity in acid than in base, which is largely attributed to their smaller Pd-H binding energy in acid evidenced by the more negatively located  $H_{\text{upd}}$  peak in cyclic voltammograms as well as the smaller activation energy in acid.

## 4.1 Introduction

The development of affordable and active HOR catalysts is highly desirable for the development of hydroxide exchange membrane fuel cells (HEMFCs). Pd, a member of the Pt-group-metals, is not only much cheaper than Pt (\$724/oz for Pd vs. \$1449/oz for Pt for 2010 – 2015 averaged price) but also about fifty times more abundant in the known natural reserves. Although Pd and Pd-based catalysts have been studied as HOR catalysts in fuel cells,[104,105] fundamental understanding of HOR/HER kinetics on Pd is largely missing. Lower HOR/HER activities were observed on Pd/C than bulk Pd,[32,106,107] suggesting a particle size effect, but a systematic study of the particle size effect on the HOR/HER activity changes over Pd/C is still lacking.

Particle size effect on Pd/C has been investigated for various reactions including oxygen reduction reaction (ORR)[108,109] and formic acid oxidation reaction.[110] For HOR/HER, studies are mainly focused on Pt. Antoine et al. reported an increase of specific and mass HOR activity for smallest Pt particles;[111] whereas Sheng et al. reported no particle size effect for HOR/HER on Pt in alkaline media as they obtained similar exchange current densities on both 2 nm Pt nanoparticle supported on carbon and polycrystalline Pt.[2] Sun et al. reported increased activity with increased particle size for HOR/HER on 2-7 nm Pt nanoparticles in acid,[103] and Ohyama et al. reported the same trend for HOR/HER on 2-4 nm Pt nanoparticles in base.[51] The RDE method cannot be used to measure HOR/HER activity on Pt in acid due to the overlapping polarization and concentration overpotential curves,[49,78] and thus the results from Sun et al.[103] via RDE measurements might not be reliable. Using the H<sub>2</sub>-pump method in a proton exchange membrane configuration, Durst et al. characterized the exchange current densities of HOR/HER on 2 – 9 nm Pt/C and reported no particle size effect.[33] However, the discrepancy of the difference in particle size effect on Pt is

uncertain. Ohyama et al. explored the particle size effect of HOR/HER on Ru nanoparticles in 0.1 M NaOH, and their results indicated an optimum exchange current density at particle size of 3 nm due to the optimum ratio of amorphous-like Ru on the surface at 3 nm.[51] Zheng et al. reported that the exchange current density on Ir/C in 0.1 M KOH increases as particle size increases from 3 to 12 nm.[49]

In this chapter, we investigated the particle size effect for HOR/HER in both acidic and alkaline electrolytes on carbon supported Pd catalysts with the Pd particle size ranging from 3 to 42 nm via RDE measurements. The HOR/HER activity in terms of specific exchange current density ( $i_0$ ) increases with rising particle size on Pd/C in both acid and base.

## **4.2 Materials and Methods**

### **4.2.1 Preparation and Physical Characterization of Palladium Nanoparticles with Different Size**

Carbon-supported palladium nanoparticles with varying particle sizes were prepared by annealing the commercial 20 wt. % Pd on Vulcan XC-72 (Pd/C, Premetek Co.) at different temperatures in an Ar/H<sub>2</sub> atmosphere in a tube furnace: the quartz tube was first purged with Ar for 30 min at room temperature to remove air. Furnace temperature was then raised to 100 °C at a rate of 10 °C/min in Ar and maintained at 100 °C for 30 min to remove adsorbed H<sub>2</sub>O on the catalyst. Finally H<sub>2</sub> was introduced into Ar (5 vol. % H<sub>2</sub>) and the temperature was increased to 300 °C, 400 °C, 500 °C and 600 °C at a rate of 10 °C/min and maintained for 2 h.[108] The obtained catalysts are denoted as Pd/C-300C, Pd/C-400C, Pd/C-500C and Pd/C-600C, respectively. Diameters of Pd nanoparticles were measured from transmission electron microscopy (TEM) images obtained on a JEOL JEM-2010F TEM. X-ray diffraction (XRD) patterns

of Pd samples were measured using a Philips X'Pert X-ray diffractometer with Cu K $\alpha$  radiation.

#### 4.2.2 Electrochemical Measurements

The electrochemical measurements were conducted in a three-electrode glass cell with a double-junction silver/silver chloride (Ag/AgCl) electrode as the reference electrode, a Pt wire as the counter electrode and a glassy carbon (5 mm diameter, PINE Ins.) as the working electrode. The ink dispersions of Pd/C samples were prepared by dispersing Pd/C (20 wt.%) in 0.05 wt.% Nafion isopropanol solution to a final concentration of 2 mg<sub>Pd/C</sub>/mL with ultrasonication for 1 h. The thin-film electrodes were prepared by pipetting 2.5  $\mu$ L of the ink (2 mg<sub>Pd/C</sub>/mL) once, four times or six times to achieve a final loading of 5, 20 or 30  $\mu$ g<sub>Pd</sub>/cm<sup>2</sup><sub>disk</sub>. The Pd loading on the electrodes were 20  $\mu$ g<sub>Pd</sub>/cm<sup>2</sup><sub>disk</sub> for all the five Pd samples measured in 0.1 M KOH prepared from KOH tablet (85 wt.%, 99.99 % metal trace, Sigma Aldrich). The final loadings were 5  $\mu$ g<sub>Pd</sub>/cm<sup>2</sup><sub>disk</sub> for Pd/C, Pd/C-300C, Pd/C-400C, 20  $\mu$ g<sub>Pd</sub>/cm<sup>2</sup><sub>disk</sub> for Pd/C-500C, and 30  $\mu$ g<sub>Pd</sub>/cm<sup>2</sup><sub>disk</sub> for Pd/C-600C measured in 0.1 M HClO<sub>4</sub> prepared by diluting 70 wt.% HClO<sub>4</sub> (EMD) with DI water.

Cyclic voltammetry experiments were performed in both Ar-saturated 0.1 M KOH and 0.1 M HClO<sub>4</sub> electrolytes at a scanning rate of 50 mV/s in the potential range of 0.07 to 1.25 V vs. reversible hydrogen electrode (RHE). All the potentials reported were converted to a RHE scale. The electrochemical surface areas of all the Pd/C samples were determined from PdO reduction peak from cyclic voltammograms based on a charge density of 424  $\mu$ C/cm<sup>2</sup><sub>Pd</sub>. [112,113]

Activity measurements for hydrogen oxidation and evolution reactions (HOR/HER) on Pd catalysts were carried out in H<sub>2</sub>-saturated 0.1 M KOH or 0.1 M

HClO<sub>4</sub> at a scanning rate of 50 mV/s and a rotating speed of 1600 rpm by cycling the potential several times until a stable polarization curve was obtained. The scanning rate was then switched to 1 mV/ to minimize the contribution of capacitance current, and the positive scan of the first cycle at 1 mV/s was reported as the HOR/HER polarization curve. The internal resistance was determined by electrochemical impedance spectroscopy (EIS) measured from 300 kHz to 100 mHz at open circuit voltage right after the HOR/HER measurement, which was then used to correct the measured potential to iR-free potential based on the Eq. 3.1.

### 4.3 Results and Discussion

#### 4.3.1 Characterization of the Particle Size of All Pd/C Samples

**TEM images.** – The Pd nanoparticle size increases as the annealing temperature rises: the number-averaged particle diameter grows from 3.2 nm for Pd/C to 33.6 nm for Pd/C-600C as shown by the TEM images and the corresponding histograms (Figure 4.1). The volume/area averaged particle diameters ( $d_{v/a}^{TEM}$ ) calculated by  $d_{v/a}^{TEM} = \sum_{i=1}^n d_i^3 / \sum_{i=1}^n d_i^2$  are larger than the number averaged particle diameters ( $d_n^{TEM}$ ) calculated by  $d_n^{TEM} = \sum_{i=1}^n d_i / n$  (Table 4.1). The  $d_{v/a}^{TEM}$  is considered a better measure of average particle diameter than  $d_n^{TEM}$  for calculating the specific surface area ( $S_{v/a}^{TEM}$ ) [93] (Table 4.1), according to Eq. 3.8.

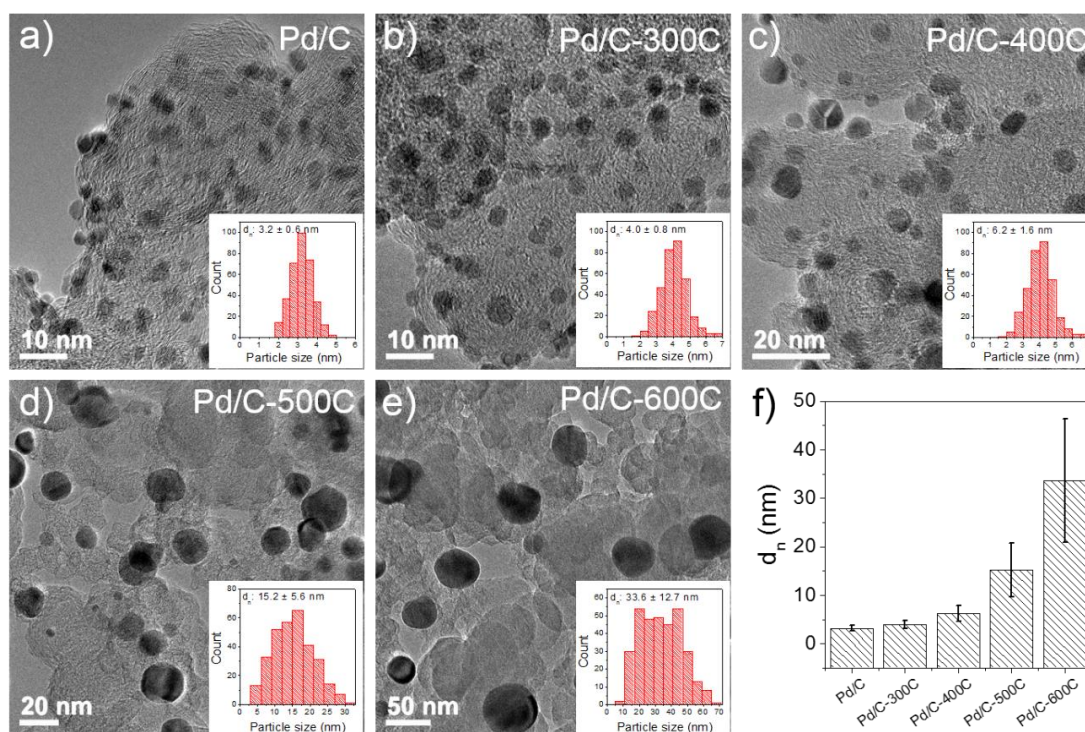


Figure 4.1 Transmission electron microscopy (TEM) images of (a) Pd/C, (b) Pd/C-300C, (c) Pd/C-400C, (d) Pd/C-500C, (e) Pd/C-600C and (f) number averaged particle size determined from TEM images for all Pd/C samples. Insets of (a-e) are the histograms of the particle size for each sample counted over 300 particles.

**X-ray diffraction patterns.** – X-ray diffraction (XRD) patterns of all samples (Figure 4.2) exhibit characteristic peaks at  $40.1^\circ$ ,  $46.6^\circ$ ,  $68.1^\circ$  and  $82.1^\circ$  corresponding to (111), (200), (220) and (311) facets of Pd (JCPDS card no. 46-1043), respectively. The width of diffraction peaks width becomes narrower as the annealing temperature increases, suggesting an increase in the particle size, which is consistent with the TEM observations. The particle diameter determined from XRD, denoted as the volume-averaged particle diameter ( $d_v^{\text{XRD}}$ ), [93] can be calculated using the Scherrer equation (Eq. 3.7). The Pd(111) peaks were used for the particle size calculation. The  $d_{v/a}^{\text{TEM}}$  and

$d_v^{XRD}$  agree well for Pd/C, Pd/C-300C, Pd/C-400C and Pd/C-500C. However, the average particle diameter determined by TEM is significantly larger than that determined by XRD for Pd/C-600C (Table 4.1), which can be caused by: 1) the width of XRD patterns reflects the primary crystalline size, while particles in TEM images could be polycrystalline, i.e., agglomerates of several primary crystals. The larger the particles are, the more likely the particles are polycrystalline. 2) The particle size distribution of Pd/C-600C is broad (Figure 4.1f), which could introduce errors in calculating the average particle size with by counting a finite number of particles. Specific surface areas of different Pd samples calculated from  $d_v^{XRD}$  using Eq. 3.8, denoted as  $S_v^{XRD}$ , are comparable with  $S_{v/a}^{TEM}$  (Table 4.1).

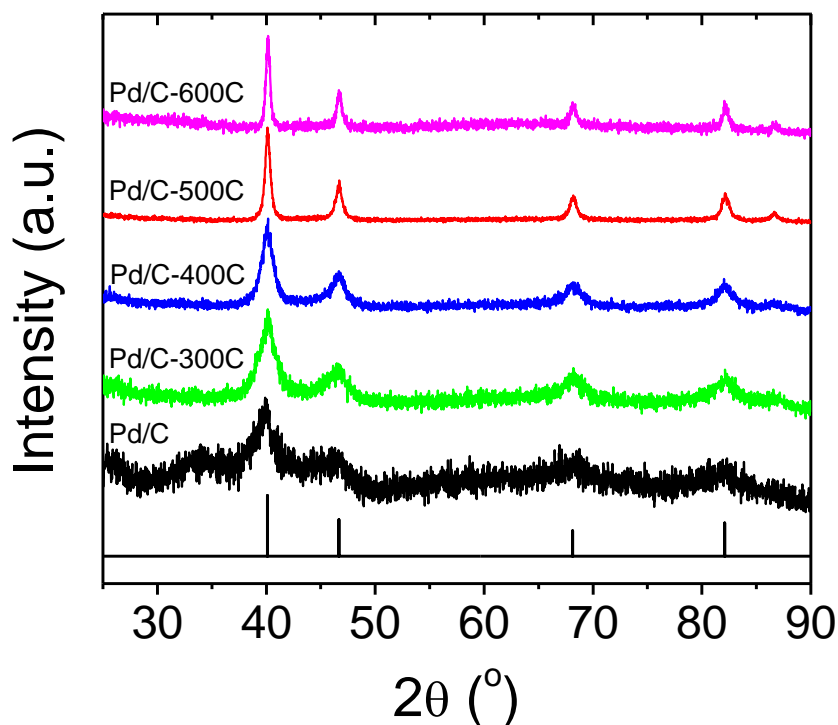


Figure 4.2 X ray diffraction (XRD) patterns of Pd/C, Pd/C-300C, Pd/C-400C, Pd/C-500C and Pd/C-600C.

**Electrochemical active surface area (ECSA) measurement from cyclic voltammograms.** – Specific surface areas of the supported Pd catalysts can also be measured from cyclic voltammograms (CVs) (Figure 4.3). The lower limit was chosen to be 0.07 V to avoid the diffusion of H atoms into Pd lattice. In 0.1 M KOH, the underpotential deposited hydrogen ( $H_{\text{upd}}$ ) adsorption and desorption peaks in the potential region of 0.07 – 0.45 V are very asymmetric and the double layer regions are not well defined (Figure 4.3a), making it difficult to determine surface areas using the  $H_{\text{upd}}$  adsorption and desorption peaks. Additionally, the  $H_{\text{upd}}$  desorption peaks for all the samples in 0.1 M KOH are located at round 0.35 V (Figure 4.3a). Contrarily, the  $H_{\text{upd}}$  adsorption and desorption peaks are more symmetric in 0.1 M  $\text{HClO}_4$ , with a well-defined  $H_{\text{upd}}$  desorption peak at 0.26 V and a shoulder at around 0.19 V (Figure 4.3b) which could represent different facets of Pd. The PdO reduction peak shifts to a more positive value as Pd particle size increase (from Pd/C to Pd/C-600C sample) in both KOH and  $\text{HClO}_4$  (Figure 4.3a and b), indicating a weaker Pd-O binding as the Pd particle size increases. In this study, we use integrated area of the PdO reduction peak to determine the electrochemical active surface area (ECSA) of supported Pd catalysts, and the ECSAs calculated from CV conducted in KOH ( $S_{\text{Base}}^{\text{EC}}$ ) and in  $\text{HClO}_4$  ( $S_{\text{Acid}}^{\text{EC}}$ ) are comparable (Table 4.1), in agreement with Henning et al.'s earlier observations.[107] Consistent with the surface area determined by TEM and XRD, ECSA decreases with increasing particle size (Table 4.1), however, ECSAs are roughly a factor of two smaller than  $S_{\text{v/a}}^{\text{TEM}}$  and  $S_{\text{v}}^{\text{XRD}}$  (Table 4.1). One potential cause for this discrepancy is that a fraction of every particle is in contact with the support and thus is not electrochemically accessible. Alternative methods such as  $H_{\text{upd}}$  adsorption/desorption peaks and CO-stripping can also be used to determine surface

area, all of which have advantages and drawbacks.[107] Although the ECSAs derived from PdO reduction might not be the most accurate in absolute terms, the general trend is consistent with values obtained with other methods. Thus, it is still meaningful to compare activities normalized by ECSAs obtained with PdO reduction.

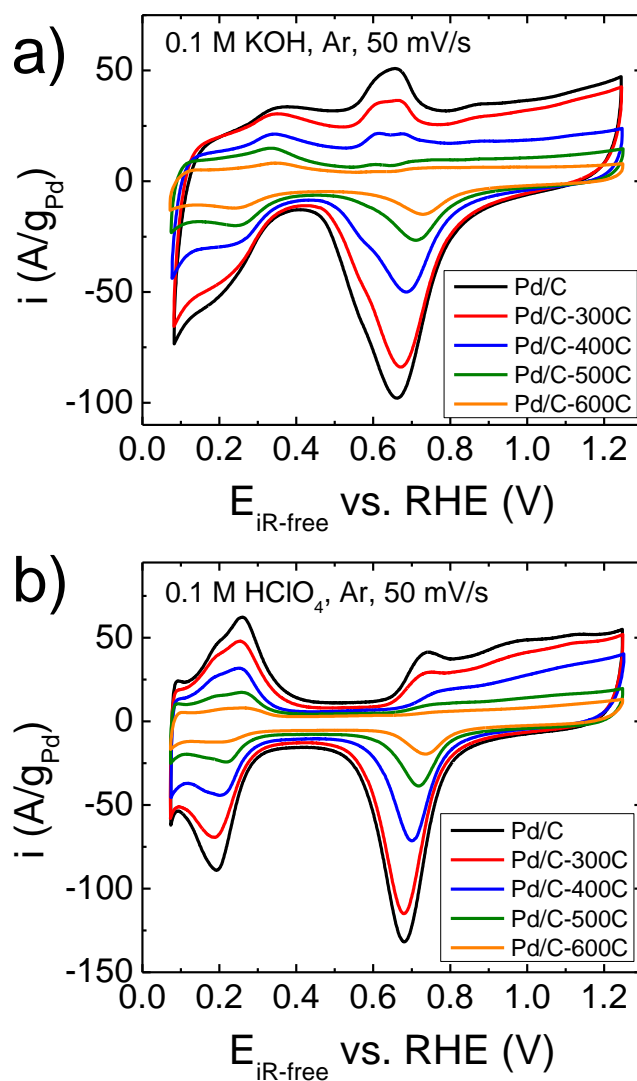


Figure 4.3 Cyclic voltammograms of Pd/C, Pd/C-300C, Pd/C-400C, Pd/C-500C and Pd/C-600C measured at a scanning rate of 50 mV/s in (a) Ar-saturated 0.1 M KOH and (b) Ar-saturated 0.1 M HClO<sub>4</sub>.

Table 4.1 Number averaged ( $d_n^{\text{TEM}}$ ) and volume/area averaged ( $d_{v/a}^{\text{TEM}}$ ) particle size determined from TEM, volume averaged particle size from XRD ( $d_v^{\text{XRD}}$ ), specific surface area calculated from  $d_{v/a}^{\text{TEM}}$  ( $S_{v/a}^{\text{TEM}}$ ),  $d_v^{\text{XRD}}$  ( $S_v^{\text{XRD}}$ ) and electrochemically measured from cyclic voltammograms ( $S^{\text{EC}}$ ).

	$d_n^{\text{TEM}}$ (nm)	$d_{v/a}^{\text{TEM}}$ (nm)	$d_v^{\text{XRD}}$ (nm)	$S_{v/a}^{\text{TEM}}$ (m <sup>2</sup> /gPd)	$S_v^{\text{XRD}}$ (m <sup>2</sup> /gPd)	$S_{\text{Base}}^{\text{EC}}$ (m <sup>2</sup> /gPd)	$S_{\text{Acid}}^{\text{EC}}$ (m <sup>2</sup> /gPd)
Pd/C	3.2 ± 0.6	3.4	3.1	147	161	74.9 ± 4.3	74.0 ± 7.1
Pd/C-300C	4.0 ± 0.8	4.3	5.9	116	85	64.3 ± 4.0	63.2 ± 4.2
Pd/C-400C	6.2 ± 1.6	7.1	6.9	70	72	33.4 ± 1.0	38.1 ± 1.2
Pd/C-500C	15.2 ± 5.6	19.1	15.2	26	33	17.0 ± 0.5	17.7 ± 0.4
Pd/C-600C	33.6 ± 12.7	42.4	19.6	12	25	7.0 ± 2.0	7.9 ± 0.2

### 4.3.2 Measurement of HOR/HER Kinetics

The HOR/HER polarization curves measured in 0.1 M KOH deviate significantly from the concentration overpotential curve (grey-dash line) and reach the HOR limiting current at overpotentials above 0.3 V (Figure 4.4a). The concentration overpotential curve can be calculated using the Eq.2.5. The HOR limiting currents for all the polarization curves are about 2.9 mA/cm<sup>2</sup><sub>disk</sub> (Figure 4.4a) which agrees with the theoretical values within experimental errors. The HOR/HER polarization curves measured in 0.1 M HClO<sub>4</sub> reach the HOR limiting current at overpotentials as low as 0.07 V and are close to the concentration overpotential curve (Figure 4.4b), indicating faster HOR/HER kinetics in acid than in base. Similar HOR limiting currents of about 2.9 mA/cm<sup>2</sup><sub>disk</sub> were observed in acid as in base (Figure 4.4b).

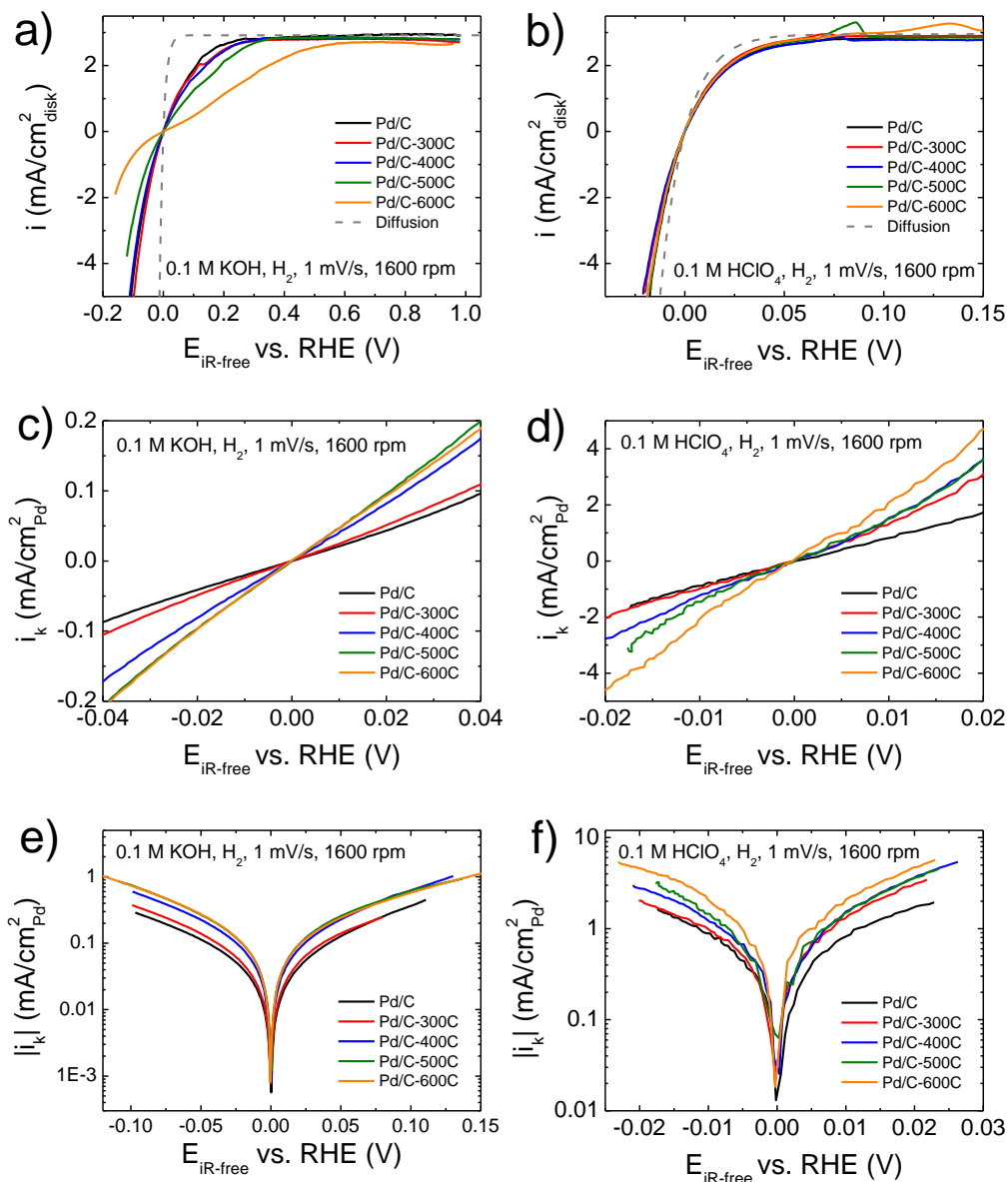
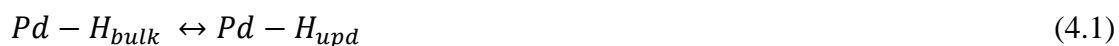


Figure 4.4 Polarization curves of Pd/C, Pd/C-300C, Pd/C-400C, Pd/C-500C and Pd/C-600C measured at r.t. with a scanning rate of 1 mV/s, a rotating speed of 1600 rpm in (a)  $H_2$ -saturated 0.1M KOH with a Pd loading of 20  $\mu\text{g}_{\text{Pd}}/\text{cm}^2_{\text{disk}}$ , and (b)  $H_2$ -saturated 0.1M HClO<sub>4</sub> with the Pd loadings of 5  $\mu\text{g}_{\text{Pd}}/\text{cm}^2_{\text{disk}}$  for Pd/C, Pd/C-300C, Pd/C-400C, 20  $\mu\text{g}_{\text{Pd}}/\text{cm}^2_{\text{disk}}$  for Pd/C-500C, and 30  $\mu\text{g}_{\text{Pd}}/\text{cm}^2_{\text{disk}}$  for Pd/C-600C. The grey-dash lines represent concentration overpotential curve. Representative linear plots of kinetic current densities as a function of overpotential in (c) 0.1 M KOH and (d) 0.1 M HClO<sub>4</sub>. Representative Tafel plots of kinetic current densities in (e) 0.1 M KOH and (f) 0.1 M HClO<sub>4</sub>. All the potentials are  $iR$ -corrected.

Atomic hydrogen is known to be able to diffuse into the Pd lattice ( $H_{bulk}$ ), therefore the HOR/HER process might be accompanied by hydrogen absorption/desorption reaction (Eq, 4.1) which can be revealed as an extra oxidation peak in the polarization curve.[38,107]



However, no extra peaks associated with oxidation of absorbed hydrogen were observed in the polarization curves in 0.1 M KOH (Figure 4.4a), which might be attributed to the slow scanning rate used in the measurement to allow the absorbed hydrogen to diffuse back to the surface to be reacted as  $H_{upd}$ . In 0.1 M HClO<sub>4</sub>, there indeed exists absorbed hydrogen oxidation peaks in the polarization curves for Pd/C-300C, Pd/C-400C, Pd/C-500C and Pd/C-600C at about 0.069 V, 0.079 V, 0.086 V and 0.134 V, respectively (Figure 4.4b).

To determine the exchange current densities of HOR/HER, the kinetic currents ( $I_k$ ) were first calculated according to the Koutecky-Levich (Eq. 2.11).[49,114] The kinetic currents for all Pd/C samples are then normalized by their corresponding Pd surface area (which are referred to as specific kinetic current densities,  $i_k$ ) and plotted as a function of overpotential. A linear relationship was observed between  $i_k$  and  $\eta$  in the micropolarization regions (Figure 4.4c and 4.4d) where  $i_k$  and  $\eta$  can be fitted into the linearized Butler-Volmer equation with the assumption that the summation of anodic and cathodic transfer coefficient equals to 1 ( $\alpha_a + \alpha_c = 1$ ) (Eq. 2.43) to obtain the exchange current density ( $i_0$ ). Alternatively, the kinetic currents can also be fitted into the Butler-Volmer equation (Eq. 2.4) to get the exchange current densities and transfer coefficients.

The specific exchange current density determined using linear fitting for Pd/C in 0.1 M KOH at 293 K is  $0.052 \pm 0.002 \text{ mA/cm}^2_{\text{Pd}}$  (Table 4.2), which is higher than the value obtained on Pd/C reported ( $0.06 \pm 0.02 \text{ mA/cm}^2_{\text{Pd}}$  at 313 K corresponding to  $0.02 \text{ mA/cm}^2_{\text{Pd}}$  at 293 K).[3] The Butler-Volmer fitting with  $\alpha_a + \alpha_c = 1$  yields a very similar exchange current density value of  $0.051 \pm 0.002 \text{ mA/cm}^2_{\text{Pd}}$  and a  $\alpha_a$  value of  $0.54 \pm 0.02$  (Table 4.3) which corresponds to an anodic Tafel slope about 108 mV/dec. This suggests that the Volmer-step ( $H_{ad} \leftrightarrow H^+ + e$ ) to be the rate-determining step, in agreement with Durst et al.'s report.[3] Without constraining  $\alpha_a + \alpha_c = 1$ , the best fitting into the Butler-Volmer equation generates  $\alpha_a$  value of  $0.45 \pm 0.01$  and  $\alpha_c$  value of  $0.38 \pm 0.02$  (Table 4.3), and a slightly higher exchange current density of  $0.060 \pm 0.003 \text{ mA/cm}^2_{\text{Pd}}$ . The HOR/HER activity on Pd/C is much higher in 0.1 M HClO<sub>4</sub> than in 0.1 M KOH – the specific exchange current densities determined from linear fitting and Butler-Volmer fitting with  $\alpha_a + \alpha_c = 1$  on Pd/C are  $2.56 \pm 0.12$  and  $2.70 \pm 0.04 \text{ mA/cm}^2_{\text{disk}}$ , respectively, which represents a 50-fold increase of that in 0.1 M KOH. The exchange current density determined using H<sub>2</sub>-pump in a proton exchange membrane fuel cell configuration (which resemble that in electrolyte with pH = 0) is  $5.2 \pm 1.2 \text{ mA/cm}^2_{\text{Pd}}$  at 313 K,[3] which can be converted to  $2.3 \pm 0.5 \text{ mA/cm}^2_{\text{Pd}}$  at 293 K according to Arrhenius equation with an activation energy of 31 kJ/mol.[38] The excellent agreement in the exchange current densities measured using RDE in this work and H<sub>2</sub>-pump indicates the validity of RDE method to characterize HOR/HER activity on Pd/C in acid.

### 4.3.3 Particle Size Effect for HOR/HER Activity

The specific exchange current density of HOR/HER increases as the Pd particle size increases from 3 to 20 nm and then levels off afterward in both acid and base (Table 4.2 and Figure 4.5a). The specific exchange current density (from linear fitting) reaches about 0.12 mA/cm<sup>2</sup><sub>Pd</sub> as the particle size exceeds 20 nm. Sheng et al. reported an exchange current density value of 0.13 mA/cm<sup>2</sup><sub>Pd</sub> on polycrystalline bulk Pd disk electrode in 0.1 M KOH by extrapolating from the Tafel Plot in the HER region to equilibrium potential (0 V).[32] Alia et al. obtained an exchange current density of 0.18 mA/cm<sup>2</sup><sub>Pd</sub> by fitting the kinetic current from HOR/HER polarization curve into the Butler-Volmer equation.[106] The specific exchange current density on Pd nanoparticles larger than 20 nm approaches that of a bulk Pd electrode. Specific exchange current densities determined from the following three methods show good agreement: 1) linear fitting (black squares in Figure 4.5a), 2) Butler-Volmer fitting with  $\alpha_a + \alpha_c = 1$  (red circles in Figure 4.5a), and 3) Butler-Volmer fitting with unconstrained  $\alpha_a + \alpha_c$  (blue triangles in Figure 4.5a). The mass exchange current density shows a general decreasing trend with the growing particle size (Figure 4.5b), most likely due to the decrease of ECSA.

Transfer coefficient ( $\alpha$ ) and Tafel slope (TS) are related according to  $TS = 2.303 RT/\alpha F$ , which are important parameters to reveal the reaction mechanism. For HOR/HER on different-sized Pd/C in 0.1 M KOH, the  $\alpha_a$  obtained from the Butler-Volmer fitting decreases from 0.54 on Pd/C (3 nm) to 0.45 on Pd/C-600C (42 nm) when constraining  $\alpha_a + \alpha_c = 1$  (Table 4.3), which corresponds to a change of anodic TS from 108 to 129 mV/dec. However, a  $R^2$  value of 0.991 was obtained when the fitting was conducted by fixing  $\alpha_a + \alpha_c = 1$ . In contrast, much better fitting of the Butler-Volmer

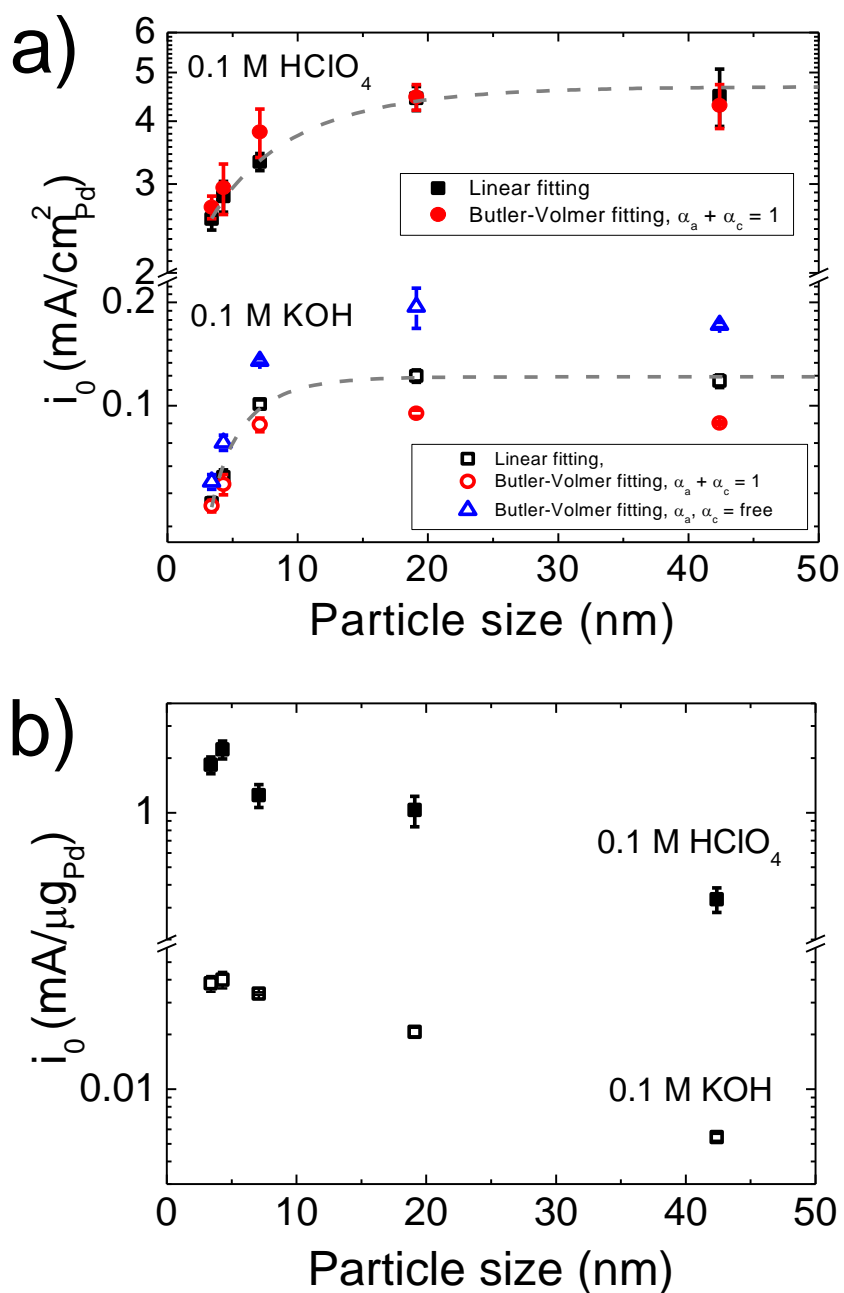


Figure 4.5 HOR/HER (a) specific and (b) mass exchange current densities in terms of as a function of Pd particle size (volume/area averaged particle size) in both 0.1 M KOH and 0.1 M HClO<sub>4</sub>. The specific exchange current densities were determined from different methods including linear fitting in the micropolarization regions, Butler-Volmer fitting with  $\alpha_a + \alpha_c = 1$  and  $\alpha_a, \alpha_c$  unconstrained, and the mass exchange current densities were determined from linear fitting in the micropolarization regions.

equation, a  $R^2$  value of 0.999, can be achieved by removing the condition of  $\alpha_a + \alpha_c = 1$ . Similarly, the  $\alpha_a$  decreases with increase of Pd particle size (from 0.45 to 0.32) which translates to a TS change from 129 to 182 mV/dec, while the  $\alpha_c$ 's are about 0.38 (TS = 153 mV/dec) and barely change with particle size (Table 4.3). In 0.1 M HClO<sub>4</sub>, the  $\alpha_a$  value ranges from 0.57 to 0.71 when the fitting was conducted by fixing  $\alpha_a + \alpha_c = 1$  (Table 4.3). Only currents in the narrow potential regions (-20 mV to 20 mV) can be used for data analysis in acid, and thus introducing a large degree of uncertainty in the curve fitting, we did not calculate  $\alpha_a$  and  $\alpha_c$  without constraining  $\alpha_a + \alpha_c = 1$ . Sheng et al. reported a TS value of 210 mV/dec (or  $\alpha_c = 0.28$ ) for HER on bulk Pd in 0.1 M KOH at 293 K,[32] and Durst et al. reported an  $\alpha_a$  value of  $0.43 \pm 0.07$  in 0.1 M NaOH and  $0.35 \pm 0.1$  in H<sub>2</sub>-pump with PEMFC configuration at 313 K.[3] The discrepancy in the transfer coefficient values between our work and literature might be resulted from the possible diffusion of atomic hydrogen into the Pd lattice, which introduces uncertainty in the transfer coefficient. To mitigate the H absorption into Pd, Henning et al. deposited Pd on polycrystalline Au electrode and measured their HOR/HER activity in 0.1 M NaOH, and Pd surface coverage - dependent TS was obtained: surfaces with low Pd coverage yield HOR TS of about 240 mV/dec while surface with high Pd coverage generates a HOR TS of 150 mV/dec.[107] In 0.1 M HClO<sub>4</sub>, Schmidt et al. obtained a HOR TS of about 210 mV/dec on Pd/Au(111) at 293 K.[115]

Table 4.2 Summary of specific and mass exchange current densities determined from linear fitting in low micropolarization regions for all Pd samples in 0.1 M KOH and 0.1 M HClO<sub>4</sub>

	0.1 M KOH		0.1 M HClO <sub>4</sub>	
	$i_{0,s}$ (mA/cm <sup>2</sup> <sub>Pd</sub> )	$i_{0,m}$ (mA/μg <sub>Pd</sub> )	$i_{0,s}$ (mA/cm <sup>2</sup> <sub>Pd</sub> )	$i_{0,m}$ (mA/μg <sub>Pd</sub> )
Pd/C	0.052 ± 0.002	0.038 ± 0.004	2.56 ± 0.12	1.83 ± 0.20
Pd/C-300C	0.062 ± 0.003	0.040 ± 0.004	2.84 ± 0.20	2.23 ± 0.25
Pd/C-400C	0.101 ± 0.003	0.034 ± 0.001	3.32 ± 0.13	1.25 ± 0.18
Pd/C-500C	0.122 ± 0.005	0.021 ± 0.001	4.44 ± 0.25	1.03 ± 0.20
Pd/C-600C	0.118 ± 0.005	0.005 ± 0.001	4.49 ± 0.33	0.33 ± 0.05

Table 4.3 Summary of transfer coefficients ( $\alpha$ )

	0.1 M KOH			0.1 M HClO <sub>4</sub>
	$\alpha_a + \alpha_c = 1$	$\alpha_a + \alpha_c$ unconstrained		$\alpha_a + \alpha_c = 1$
	$\alpha_a$	$\alpha_a$	$\alpha_c$	$\alpha_a$
Pd/C	0.54 ± 0.02	0.45 ± 0.01	0.38 ± 0.02	0.65 ± 0.11
Pd/C-300C	0.52 ± 0.01	0.43 ± 0.03	0.41 ± 0.01	0.71 ± 0.03
Pd/C-400C	0.49 ± 0.01	0.39 ± 0.01	0.39 ± 0.01	0.64 ± 0.05
Pd/C-500C	0.46 ± 0.01	0.31 ± 0.03	0.36 ± 0.02	0.57 ± 0.10
Pd/C-600C	0.45	0.32	0.38	0.57 ± 0.06

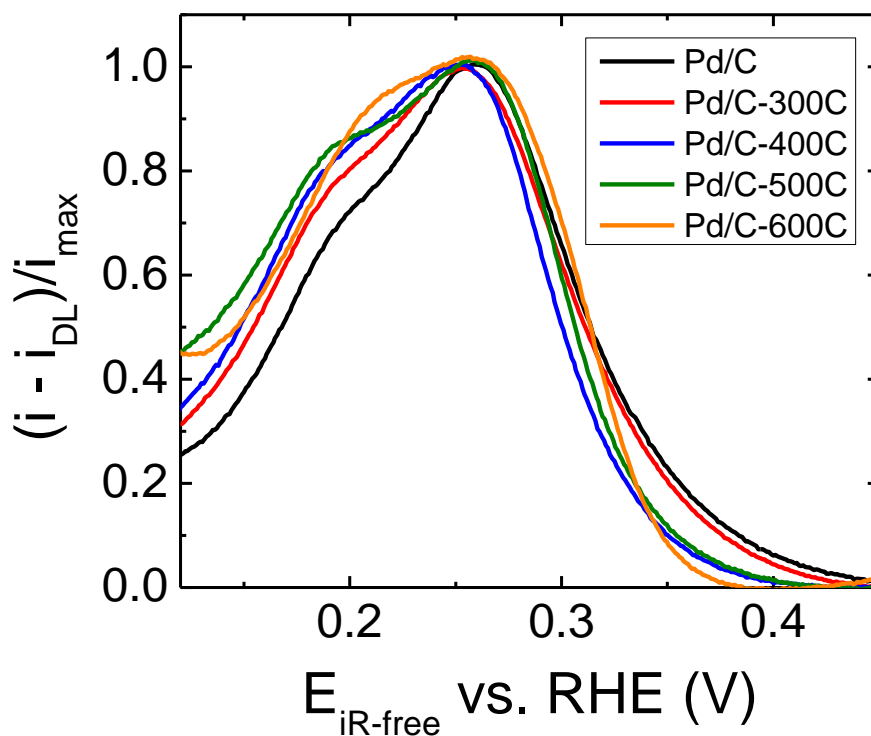


Figure 4.6  $H_{\text{upd}}$  desorption profiles for all the Pd samples from cyclic voltammograms measured in 0.1 M  $\text{HClO}_4$  where the current is normalized to the peak current after double layer current deduction.

The particle size effect of HOR/HER activity on Pd/C could be attributed to the redistribution of surface facets among different-sized Pd nanoparticles (known as geometric effect), as revealed by the change in peak ratios in the  $H_{\text{upd}}$  desorption peak profiles (Figure 4.6), together with the structure sensitivity of the reaction activity on different facets. When the current is normalized to the peak current after double layer current deduction, the height of the peak at about 0.26 V is fixed while that of the peak at about 0.19 V increases with increases of particle size (Figure 4.6). The change of lineshape of the  $H_{\text{upd}}$  desorption peak suggests a redistribution of facets in different Pd samples, which is consistent with a previous report on Pd/C.[109]. Studies on single

crystalline Pt showed that the exchange current density of HOR/HER increases in the order of Pt(111) < Pt(100) < Pt(110) in both acidic[45] and alkaline[116] electrolytes. HOR/HER activities on single crystalline Pd surfaces have not been reported, which is likely also due to the diffusion of hydrogen atoms into the bulk of single crystal samples. It is reasonable to conclude that HOR/HER on Pd is structure sensitive based on the particle size dependence of HOR/HER activities in this study. The particle size effect of HOR/HER on carbon supported Ir nanoparticle in alkaline electrolyte also suggest the possibility of structure sensitivity of HOR/HER on Ir.[49] Additionally, the  $H_{\text{upd}}$  desorption peak potential is related to hydrogen binding energy (HBE) which has been proposed to be a dominating descriptor for HOR/HER activities according to  $HBE = -FE_{\text{peak}} - \frac{1}{2}TS_{H_2}^0$  (Eq. 3.9).[49] Since Pd belongs to the strongly-binding branch in the “volcano plot” (HOR/HER exchange current densities vs. HBE),[32,117] sites with weaker HBE will possess higher HOR/HER activity. It is reasonable to assume that the  $H_{\text{upd}}$  desorption peaks with different peak potentials are associated with sites with different HBE. Zhou et al. deconvoluted the  $H_{\text{upd}}$  desorption in the cyclic voltammograms of Pd/C they obtained in 0.1 M HClO<sub>4</sub>, and attributed them to low-index Pd facets (111), (100) and (110).[109] Sites associated with the  $H_{\text{upd}}$  desorption peak centered at around 0.19 V on Pd samples in 0.1 M HClO<sub>4</sub> bind to hydrogen more weakly than those associated with peak centered at around 0.24 V, and thus should have higher HOR/HER activity. The increased ratio of the sites with lower HBE with rising particle size is responsible for the improved HOR/HER activity from untreated Pd/C (about 3 nm) to Pd/C-500C (about 20 nm). Similar result has been observed on Ir/C where the exchange current density and the fraction of sites with lowest HBE increase with particle size and a good correlation between exchange current density and the

fraction of sites with lowest HBE is obtained.[49] Meanwhile, it is generally accepted that larger particles contain less defect sites compared with smaller particles. The higher ratio of the defect sites with low coordination number and a stronger binding strength to adsorbates (Pd-H binding in this case) in smaller nanoparticles could lead to a lower HOR/HER activity. Therefore, extended Pd structure with less defect sites such as Pd nanowires (PdNWs) or Pd nanotubes (PdNTs) will have higher activity towards HOR/HER than Pd nanoparticles. Indeed, a much higher exchange current density of  $0.96 \text{ mA/cm}^2_{\text{Pd}}$  was obtained on PdNTs synthesized via galvanic displacement reaction using copper nanowires (CuNWs) as templates, which is even about 5 times of bulk Pd possibly attributed to the small amount of Cu left in Pd lattice.[106]

#### **4.3.4 HOR/HER Activities: Acid vs. Base**

The HOR/HER activities in  $0.1 \text{ M HClO}_4$  are approximately a factor of 50 higher than those in  $0.1 \text{ M KOH}$  on all Pd samples with different particle size (Table 4.2 and Figure 4.5a). Durst et al. reported that the exchange current density on Pd/C (about 3 nm) measured using  $\text{H}_2$  pump in a PEMFC configuration (equivalent to  $\text{pH} = 0$ ) is about 90 times of that obtained in  $0.1 \text{ M NaOH}$  using RDE method at 313 K,[3] which is consistent with our results. Consensus has not been reached regarding the root cause for the higher HOR/HER activity in acid than in base on Pt or Pt group metals so far: whether HBE is the sole and unique descriptor for HOR/HER[3,25,49,52] or there is a change in reaction mechanism from acid to base and adsorption OH will facilitate HOR/HER in base.[53,118] The  $\text{H}_{\text{upd}}$  adsorption/desorption peaks on Pd samples in CVs measured in  $0.1 \text{ M HClO}_4$  are located at more negative potentials compared with those measured in  $0.1 \text{ M KOH}$  (Figure 4.3), suggesting a weaker Pd-H binding energy in acid than in base. Therefore, HOR/HER should have a smaller activation energy in acid

according to the Brønsted-Evans-Polanyi (BEP) principle. In this regard, we measured HOR/HER polarization curves on Pd/C in both 0.1 M HClO<sub>4</sub> and 0.1 M KOH at temperatures from 275 to 313 K, and determined the exchange current densities at each temperature to generate the Arrhenius plots (Figure 4.7).

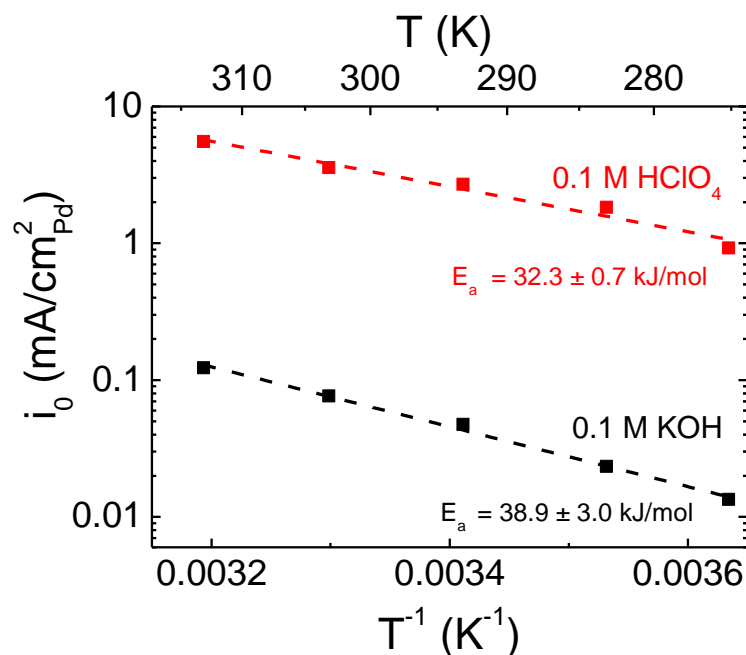


Figure 4.7 Arrhenius plots of HOR/HER activities on Pd/C (about 3 nm diameter) measured in 0.1 M HClO<sub>4</sub> and 0.1 M KOH.

The activation energy of HOR/HER on Pd/C in 0.1 M HClO<sub>4</sub> is  $32.3 \pm 0.7$  kJ/mol, which is similar to that reported when the exchange current densities were determined using H<sub>2</sub>-pump ( $31 \pm 2$  kJ/mol).[38] A higher activation energy is obtained in 0.1 M KOH ( $38.9 \pm 3.0$  kJ/mol) than in 0.1 M HClO<sub>4</sub>, which confirms our prediction. In addition, the activation energies of HOR/HER on Pt/C, Pd/C and Ir/C in 0.1 M KOH

are in the sequence of Pt/C ( $29.5 \pm 4.0$  kJ/mol)[2] < Ir/C ( $32.9 \pm 1.5$  kJ/mol)[49] < Pd/C ( $38.9 \pm 3.0$  kJ/mol, this work), which correlates well to the sequence of HOR/HER activity in base in the order of Pt/C ( $0.57 \pm 0.07$  mA/cm<sup>2</sup><sub>Pt</sub>)[2] > Ir/C ( $0.21 \pm 0.02$  mA/cm<sup>2</sup><sub>Ir</sub>)[49] > Pd/C ( $0.052 \pm 0.002$  mA/cm<sup>2</sup><sub>Pd</sub>, this work). Similar correlation between the activation energy and the exchange current density on Pt/C, Pd/C and Ir/C is also valid in acid.[38] Therefore, the stronger Pd-H binding energy in base is likely responsible for the lower HOR/HER activity.

#### 4.4 Conclusion

In summary, we studied the kinetics of HOR/HER on Pd catalysts with different particle sizes ranging from 3 to 42 nm in both acidic and alkaline electrolytes using RDE measurement. Similar particle size effects were observed on Pd in acid and base: the HOR/HER specific exchange current density increases as Pd particle size increases and then levels off at about 20 nm while the mass exchange current density increases slightly initially, and then decreases with the increase of particle size in both acidic and alkaline electrolytes. This particle size effect suggests that HOR/HER activity on Pd is structure sensitive with the sites of lower HBE (possibility low-index facets) being more active. The HOR/HER activities on Pd in acid are about 50 times of those in base, which is highly possible to be attributed to the lower Pd-H binding energy in acid revealed from the negative shift of H<sub>upd</sub> peak from base to acid as well as the smaller activation energy obtained in acid ( $32.3 \pm 0.7$  kJ/mol) than in base ( $38.9 \pm 3.0$  kJ/mol).

## Chapter 5

### **UNIVERSAL DEPENDENCE OF HYDROGEN OXIDATION AND EVOLUTION REACTION ACTIVITY OF PLATINUM-GROUP-METALS ON PH AND HYDROGEN BINDING ENERGY**

Understanding how pH affects the activity of hydrogen oxidation reaction (HOR) and hydrogen evolution reaction (HER) is key to developing active, stable and affordable HOR/HER catalysts for hydroxide exchange membrane fuel cells and electrolyzers. A common linear correlation between hydrogen binding energy (HBE) and pH is observed for four supported platinum-group-metal catalysts (Pt/C, Ir/C, Pd/C and Rh/C) over a broad pH range (0-13), suggesting that the influence of pH to HBE is independent of the nature of the metals. A universal correlation between exchange current density and HBE is also observed on the four metals, indicating that they may share the same elementary steps and rate determining steps, and that the HBE is the dominant descriptor for HOR/HER activities. The onset potential of CO-stripping on the four metals decreases with pH, indicating a stronger OH adsorption, which provides evidence against the pro-motional effect of adsorbed OH on HOR/HER.

## 5.1 Introduction

The alkaline environment of hydroxide exchange membrane fuel cells (HEMFCs) and electrolyzers (HEMELs) opens up the possibility of employing non-precious metals as catalysts, and in turn an affordable alternative to the precious metal-reliant proton exchange membrane fuel cells (PEMFCs) and electrolyzers (PEMELs).[82,84,88,119-123] Only a negligible fraction of precious metal, as well as cost, in PEMFCs and PEMELs is on the negative electrode, due to the extremely fast HOR/HER kinetics in the acid environment. However, the sluggish kinetics of HOR/HER in alkaline media – two orders of magnitude slower than that in acid on Pt[2,3,68], Ir[3] and Pd[3] – necessitates higher precious metal loadings on the negative electrode at equivalent overpotential and could offset the reduced cost from the use of non-precious metal-based catalysts on the positive electrode.

Despite recent discussion in the literature on the potential role of adsorbed OH for HOR in base,[83,118] hydrogen binding energy (HBE) has been shown to be the dominant descriptor for HER/HOR activity.[3,25,32,52] Volcano-shaped curves were obtained when plotting HER activity vs. HBE on various mono-metallic metals in base[32] (as well as in acid[29,33,117]) suggesting that an optimal HBE exists (Sabatier's principle). Recent studies on HOR/HER activity of Pt at different pHs suggests that the pH of electrolytes affects HOR activity by modifying the HBE of catalysts. For example, lower HOR/HER kinetics in base coincides with higher HBE calculated from cyclic voltammograms (CVs).[25] Wang et al. showed that PtRu alloy was twice as active as Pt for HOR in alkaline media in spite of the lower onset potential for adsorbed OH on the latter, indicating that the oxophilicity of catalysts does not play a major role in facilitating HOR.[52] Despite the growing evidence on specific systems, general correlation between HOR activity and HBE, and between HBE and pH among

different metals remains to be studied. Establishing such correlations on precious metals, which are stable over a broad pH range and hence ideal model systems, will set the stage for the rational search of non-precious metal based HOR catalysts.

In this chapter, we demonstrate the generality of the impact of pH (0-13) on HBE and HBE on HOR/HER activities, in terms of exchange current densities ( $i_0$ ), on supported platinum-group metal Pt, Ir, Pd and Rh nanoparticles (Ru is not studied because it is susceptible to oxidation in the hydrogen adsorption/desorption potential region). We show that the HBE of each metal increases linearly with pH with a similar slope, indicating that the effect of pH on HBE is independent of metal. We also show that the  $\log(i_0)$  of each metal decreases linearly with HBE with a similar slope, which indicates a universal correlation of  $i_0$  with HBE and provides convincing evidence that HBE is the dominant descriptor for HOR/HER activities. Furthermore, the onset potential for adsorbed OH, as indicated by CO-stripping experiments, decreases linearly with pH, indicating that the role of adsorbed OH in promoting HOR is minimal.

## **5.2 Materials and Methods**

### **5.2.1 Materials and Characterization**

Pt/C (5 wt.% Pt supported on Vulcan XC-72, Premetek Co.), Ir/C (20 wt.% Ir supported on Vulcan XC-72, Premetek Co.), Pd/C (20 wt.% Pd supported on Vulcan XC-72, Premetek Co.) and Rh/C (20 wt.% Rh supported on Vulcan XC-72, Premetek Co.) are obtained commercially and used as received. Their particle sizes and distributions were examined from transmission electron microscopy (TEM, JEOL 2010F, 200 kV) images. To prepare TEM samples, Pt/C, Ir/C, Pd/C and Rh/C were first added into water, and ultrasonicated for 30 min to form uniform suspensions; a drop of

the suspensions were then added onto Cu grids (Lacy carbon coated copper grids, Electron Microscopy Sciences) to obtain TEM samples.

### 5.2.2 Preparation of Electrolytes

0.1 M and 1 M Perchloric acid ( $\text{HClO}_4$ ), 0.1 M and 0.2 M sulfuric acid ( $\text{H}_2\text{SO}_4$ ), 0.2 M phosphoric acid ( $\text{H}_3\text{PO}_4$ ) and 0.2 M acetic acid ( $\text{CH}_3\text{COOH}$ ) were prepared by diluting 70 wt.%  $\text{HClO}_4$  (EMD), 95 wt.%  $\text{H}_2\text{SO}_4$  (EMD), 80 wt.%  $\text{H}_3\text{PO}_4$  (Sigma Aldrich) and 99.9%  $\text{CH}_3\text{COOH}$  (Sigma Aldrich) with de-ionized (DI) water ( $18.2 \text{ M}\Omega\cdot\text{cm}$ ). 0.1 M and 4 M potassium hydroxide (KOH), 0.2 M citric acid ( $\text{C}_6\text{H}_8\text{O}_7$ ), 0.2 M potassium bicarbonate ( $\text{KHCO}_3$ ), 0.2 M boric acid ( $\text{H}_3\text{BO}_3$ ) were prepared from KOH tablet (85 wt.%, 99.99 % metal trace, Sigma Aldrich),  $\text{C}_6\text{H}_8\text{O}_7$  powder (99 wt.%, Sigma Aldrich),  $\text{KHCO}_3$  powder (99.7 wt.%, Sigma Aldrich) and  $\text{H}_3\text{BO}_3$  powder (99 wt.%, Sigma Aldrich). Buffer solutions were prepared by adding different amounts (1 to 14 ml) of 4 M KOH into 100 mL 0.2 M  $\text{C}_6\text{H}_8\text{O}_7$ , 0.2 M  $\text{CH}_3\text{COOH}$ , 0.2 M  $\text{H}_3\text{PO}_4$ , 0.2 M  $\text{KHCO}_3$  and 0.2 M  $\text{H}_3\text{BO}_3$ .

### 5.2.3 Electrochemical Measurements

The electrochemical measurements were performed in a three-electrode cell with saturated calomel electrode (SCE, Princeton Applied Research) immersed in a Luggin Capillary (Princeton Applied Research) filled with 2 M potassium nitrate ( $\text{KNO}_3$ , Sigma Aldrich) as the reference electrode, a Pt wire (PINE Ins.) as the counter electrode and a glassy carbon (5 mm diameter, PINE Ins.) as the working electrode. Ink solutions of Pt/C (4  $\text{mg}_{\text{Pt}}/\text{mL}$ ), Ir/C (1  $\text{mg}_{\text{Ir}}/\text{mL}$ ), Pd/C (2  $\text{mg}_{\text{Pd}}/\text{mL}$ ) and Rh/C (1  $\text{mg}_{\text{Rh}}/\text{mL}$ ) were prepared by dispersing Pt/C, Ir/C, Pd/C and Rh/C in 0.05 wt.% Nafion isopropanol solution followed by ultrasonication for 1 h. The thin-film electrodes were

made by pipetting 2  $\mu\text{L}$  of the ink solutions once, twice or four times onto pre-polished glassy carbon electrodes with final metal loadings of 2 to 20  $\mu\text{g}_{\text{metal}}/\text{cm}^2_{\text{disk}}$ . All potentials reported were converted to a reversible hydrogen electrode (RHE) scale.

Cyclic voltammetry (CV) measurements for all samples were first carried out in Ar-saturated 0.1 M KOH solution and followed by measurements in electrolytes with different pHs at a scanning rate of 50 mV/s. The electrochemical surface areas of the Pt/C, Ir/C, Pd/C and Rh/C electrodes were obtained from CVs in both 0.1 M KOH (ex-situ) and the buffered electrolytes (in-situ). The electrochemical surface areas of Pt, Ir and Rh were determined from the hydrogen adsorption/desorption peaks with subtraction of double layer corresponding to charge densities of 210  $\mu\text{C}/\text{cm}^2_{\text{Pt}}$ , [113,124] 218  $\mu\text{C}/\text{cm}^2_{\text{Ir}}$ , [92,113] and 221  $\mu\text{C}/\text{cm}^2_{\text{Rh}}$ , [112,113] respectively, while the surface area of Pd was determined from PdO reduction peak at about 0.7 V vs. RHE from CV recorded in the range of 0.07 – 1.25 V vs. RHE corresponding to a charge density of 424  $\mu\text{C}/\text{cm}^2_{\text{Pd}}$ . [112,113]

HOR/HER activity measurements of all samples were performed in  $\text{H}_2$ -saturated electrolytes with different pHs at a rotation speed of 1600 rpm. The scanning rate was set to 50 mV/s initially for about 5 cycles to achieve a stable polarization curve and then changed to 1 mV/s to minimize the influence of capacitance charge. The polarization curves at 1 mV/s were reported and used for calculation of exchange current densities ( $i_0$ ). The internal resistance ( $R_s$ ) was measured by electrochemical impedance spectroscopy (EIS) from 200 kHz to 100 mHz at open circuit voltage (OCV), which was used to obtain  $iR$ -free potential ( $E_{iR\text{-free}}$ ) according to the following equation,

$$E_{iR\text{-free}} = E - IR_s \quad (5.1)$$

where E is the measured potential, I is the corresponding current.

The pH values of the electrolytes were calculated from HOR/HER equilibrium potential (potential at current equals to zero,  $E_{H_2/H^+ \text{ vs. SCE}}$ ) as follows based on Nernst equation,

$$\text{pH} = \frac{-E_{H_2/H^+ \text{ vs. SCE}} - E_{SCE}}{2.303RT/F} \quad (5.2)$$

where  $E_{SCE}$  is the standard potential for SCE (0.241 V), R is the universal gas constant (8,314 J/(mol·K)), T is the temperature in Kelvin and F is the Faraday's constant (96,485 A·s/mol)).

The HOR/HER activity is represented using exchange current density ( $i_0$ ), which is obtained by fitting kinetic current ( $I_k$ ) with the Butler-Volmer equation,

$$I_k = i_0 A_s \left[ \exp\left(\frac{\alpha_a F \eta}{RT}\right) - \exp\left(\frac{-\alpha_c F \eta}{RT}\right) \right] \quad (5.3)$$

in which  $\alpha_a$  and  $\alpha_c$  are the transfer coefficients for HOR and HER, respectively, with  $\alpha_a + \alpha_c = 1$ ,  $\eta$  is the overpotential,  $A_s$  is the electrochemical surface area of the samples.

$I_k$  is calculated using equations 5.4 and 5.5,[114]

$$\frac{1}{I} = \frac{1}{I_k} + \frac{1}{I_d} \quad (5.4)$$

$$\eta_{diffusion} = -\frac{RT}{2F} \ln\left(1 - \frac{I_d}{I_l}\right) \quad (5.5)$$

where I is the measured current (in mA),  $I_d$  is the diffusion limited current defined in Eq. 5.5,  $I_l$  is the maximum current from polarization curves (in mA).

CO stripping was performed by holding the electrode potential at 0.1 V vs. RHE for 10 min in the flowing CO to reach a full monolayer of adsorbed CO on the metal surface, then switching to flow Ar for another 10 min to remove dissolved CO in the electrolyte, and followed by cycling in the potential region similar to a normal CV scan at a scan rate of 20 mV/s, and the first forward scan represent the stripping of a

monolayer of CO. The CO-stripping peak can also be used to determine surface area corresponding to a charge density of 420  $\mu\text{C}/\text{cm}^2$ . [58]

### 5.3 Results and Discussion

#### 5.3.1 Particle Size Characterization of Pt, Ir, Pd and Rh Nanoparticles

TEM images of Pt/C, Ir/C, Pd/C and Rh/C are shown in Figure 5.1. The diameters of over 300 Pt, Ir, Pd and Rh nanoparticles were measured, and plotted as the histograms (inset of Figure 5.1). The number averaged particle size ( $d_n$ ) was calculated by  $d_n = \frac{\sum_{i=1}^n d_i}{n}$  (listed in Table 5.1), where  $d_i$  is the individual particle diameter, and  $n$  is the number of particles measured. The volume/area averaged particle size ( $d_{v/a}$ ) is more accurate to represent the specific surface area than the number averaged particle size, which can be calculated by  $d_{v/a} = \frac{\sum_{i=1}^n d_i^3}{\sum_{i=1}^n d_i^2}$  (listed in Table 5.1). The surface area determined from  $d_{v/a}^{TEM}$  ( $S_{v/a}^{TEM}$ ) was calculated by  $S_{v/a}^{TEM} = \frac{6}{\rho d} \times 10^3$  (listed in Table 5.1), where  $\rho$  is the density of the metal (21.45  $\text{g}/\text{cm}^3$  for Pt, 22.56  $\text{g}/\text{cm}^3$  for Ir, 12.02  $\text{g}/\text{cm}^3$  for Pd, and 12.41  $\text{g}/\text{cm}^3$  for Rh),  $d$  is the particle size in nm,  $S_{v/a}^{TEM}$  is in unit of  $\text{m}^2/\text{g}$ .

The electrochemical surface areas of Pt/C, Ir/C and Rh/C in this work were determined from the  $\text{H}_{\text{upd}}$  adsorption and desorption peaks while that of Pd/C was determined from PdO reduction peak from their corresponding CV in 0.1 M KOH (Figure 5.2), and are listed in Table 5.1 as  $\text{ECSA}_{\text{CV}}$ . The surface areas can also be determined from CO-stripping peak (Figure 5.3) corresponding to a charge density of 420  $\mu\text{C}/\text{cm}^2$ , [58] which were listed in Table 5.1 as  $\text{ECSA}_{\text{CO-stripping}}$ .

$\text{ECSA}_{\text{CV}}$  and  $\text{ECSA}_{\text{CO-stripping}}$  of Pt/C, Ir/C, Pd/C and Rh/C (except  $\text{ECSA}_{\text{CO-stripping}}$  of Rh/C) are smaller than their corresponding volume/surface averaged surface

area ( $S_{v/a}^{TEM}$ ), probably due to the partial covering of the particles' surface by the carbon support. The  $ECSA_{CO-stripping}$  is larger than  $ECSA_{CV}$  for all four supported metals (Table 5.1). Similar results were obtained by Durst et al., and they suggested to normalize the HOR/HER kinetic currents by surface area determined from CO-stripping.[38] However, since we are studying the trends of activities vs pH or HBE, normalizing the activities by  $ECSA_{CV}$  will not alter our conclusion as long as we follow the same protocol for all experiments. In addition, the difference between  $ECSA_{CO-stripping}$  and  $ECSA_{CV}$  is less than a factor of 2, which is not significant compared with the two-orders of magnitude difference of HOR/HER activity in acid and base.

Table 5.1 Number averaged ( $d_n^{TEM}$ ) and volume/area averaged ( $d_{v/a}^{TEM}$ ) particle size from TEM, surface area calculated from  $d_{v/a}^{TEM}$  ( $S_{v/a}^{TEM}$ ) and electrochemical surface area determined from CV in 0.1 M KOH ( $ECSA_{CV}$ ) and CO stripping in 0.1 M KOH ( $ECSA_{CO-stripping}$ ) of Pt/C, Ir/C, Pd/C and Rh/C.

	$d_n^{TEM}$ (nm)	$d_{v/a}^{TEM}$ (nm)	$S_{v/a}^{TEM}$ (m <sup>2</sup> /g)	$ECSA_{CV}$ (m <sup>2</sup> /g)	$ECSA_{CO-stripping}$ (m <sup>2</sup> /g)
5 wt % Pt/C	1.9 ± 0.4	2.12	132	64 ± 9	103 ± 6
20 wt.% Ir/C	2.9 ± 0.8	3.34	80	64 ± 9	71
20 wt.% Pd/C	3.2 ± 0.6	3.38	148	78 ± 8	96
20 wt.% Rh/C	3.4 ± 0.7	3.73	130	80 ± 12	143 ± 18

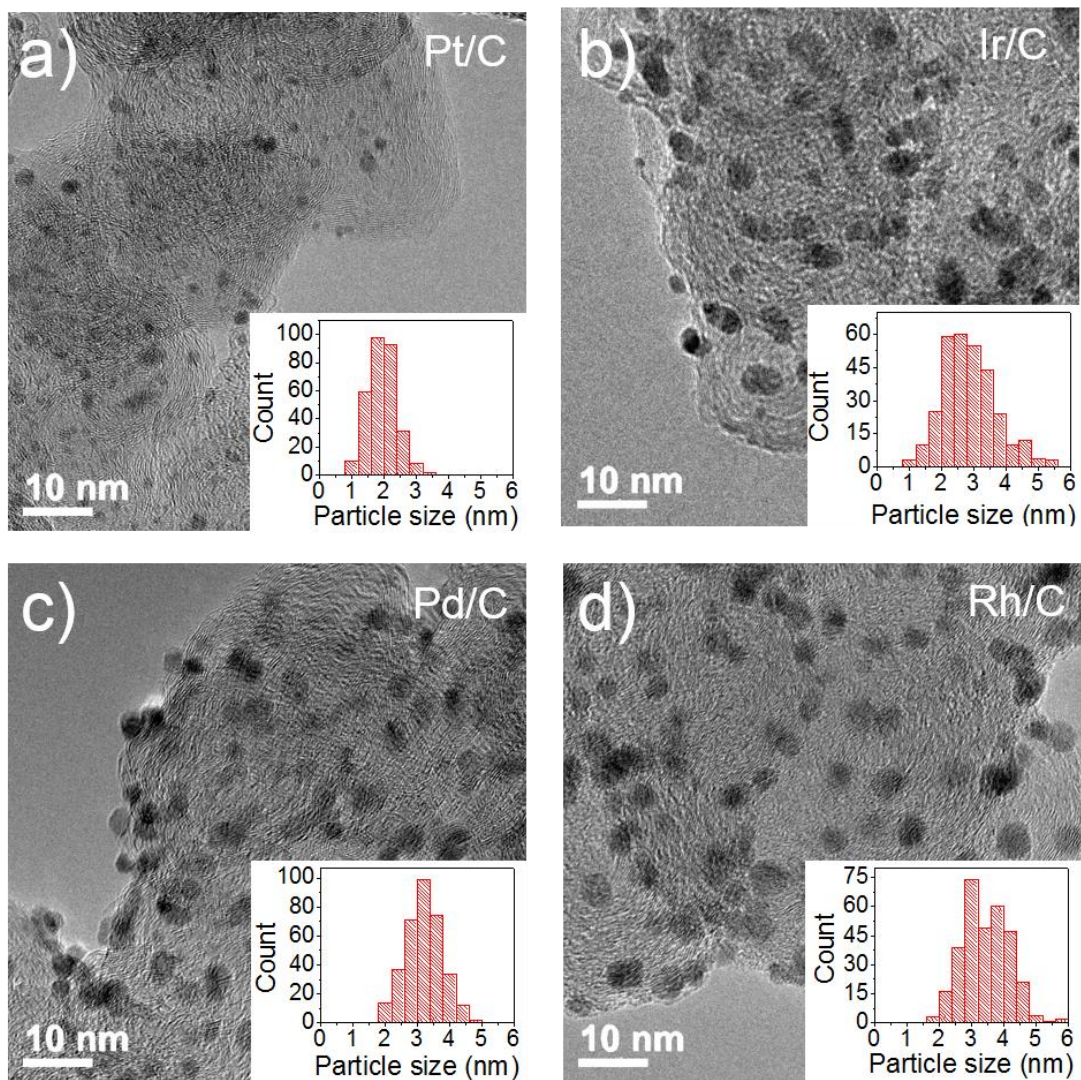


Figure 5.1 TEM image and the corresponding histograms of particles size (inset) of (a) Pt/C, (b) Ir/C, (c) Pd/C and (d) Rh/C. The number average particle size is  $1.9 \pm 0.4$  nm for Pt/C,  $2.9 \pm 0.8$  nm for Ir/C,  $3.2 \pm 0.6$  nm for Pd/C and  $3.4 \pm 0.7$  nm for Rh/C.

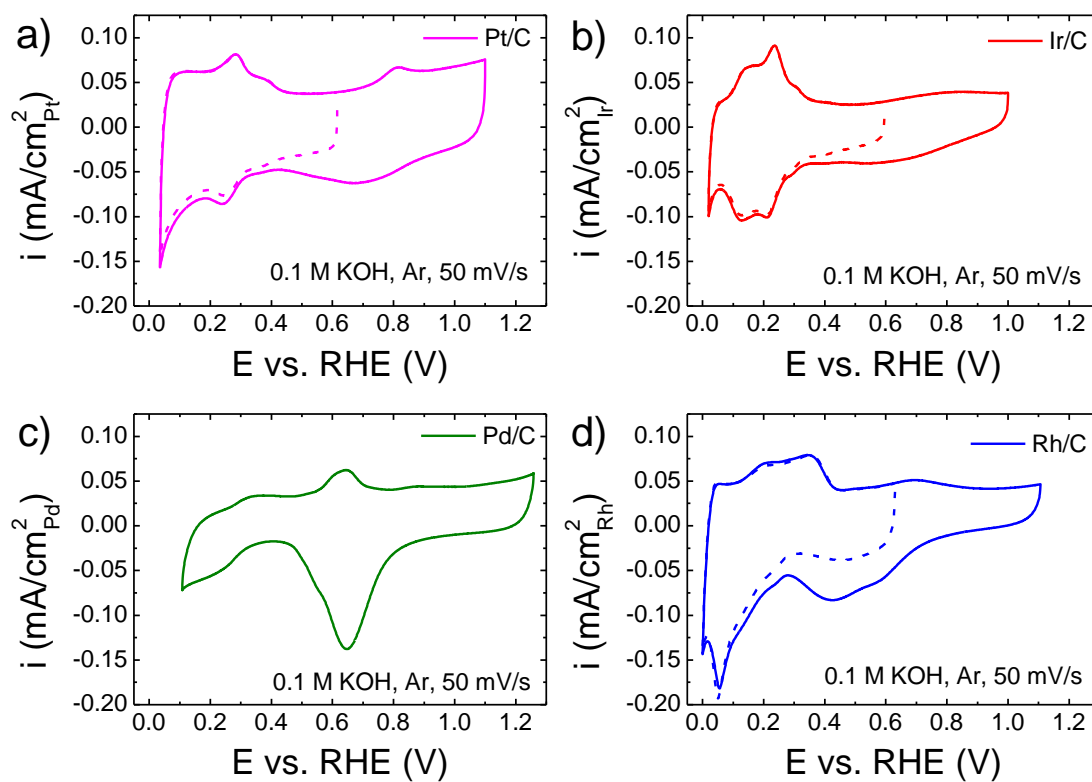


Figure 5.2 Cyclic voltammograms (CVs) of a) Pt/C, b) Ir/C, c) Pd/C and d) Rh/C measured in Ar-saturated 0.1 M KOH with a scanning rate of 50 mV/s. The dash line represents CV scans in a small potential range to avoid the contribution of oxide reduction current to the  $H_{upd}$  adsorption current. Currents were normalized to the surface area determined from CV.

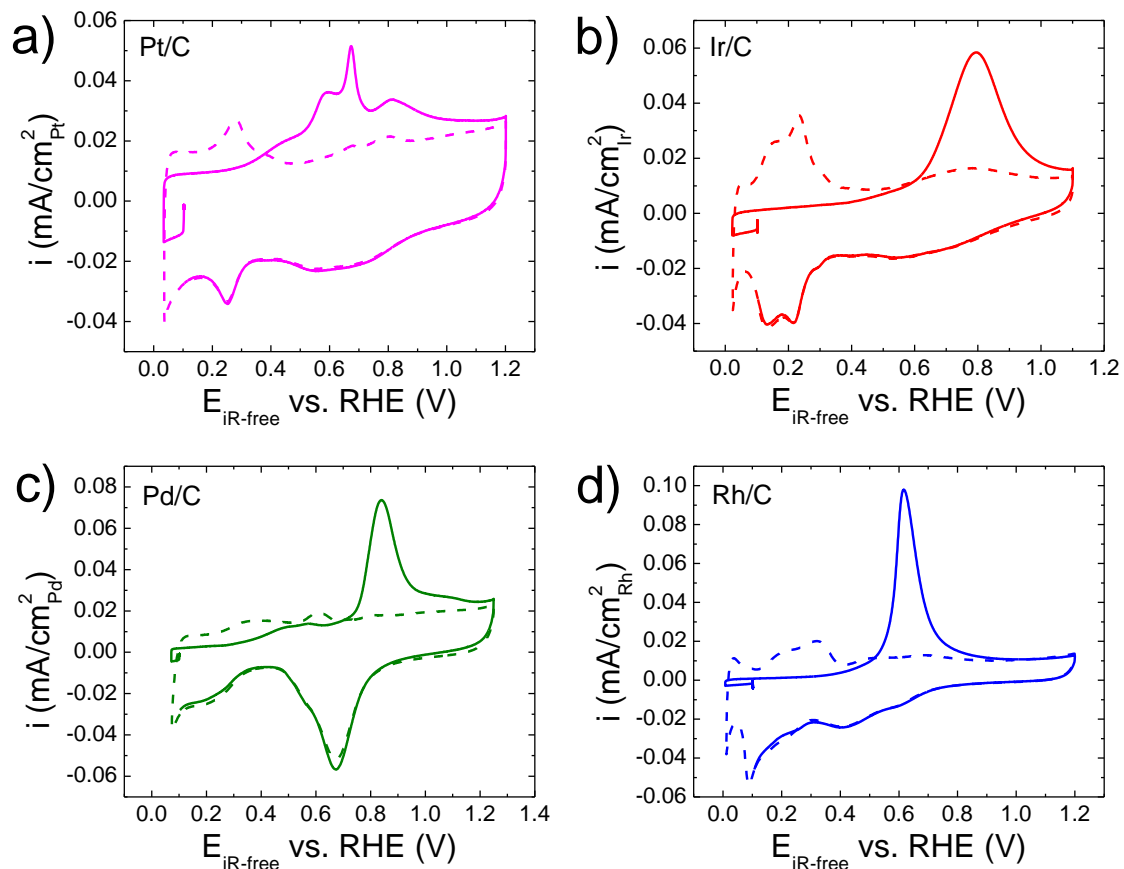


Figure 5.3 CO-stripping on (a) Pt/C, (b) Ir/C, (c) Pd/C and (d) Rh/C in 0.1 M KOH. Currents were normalized to the surface area determined from CO-stripping.

### 5.3.2 pH-Dependent HBE of Carbon Supported Pt, Ir, Pd and Ir Nanoparticles Determined from Cyclic Voltammograms

Desorption peaks for underpotential deposited hydrogen ( $H_{\text{upd}}$ ) on carbon supported Pt, Ir, Pd and Rh nanoparticles (Pt/C, Ir/C, Pd/C and Rh/C) are obtained from the respective CVs recorded in buffered electrolytes with pH ranging from 0 to 13 (Figure 5.4). The desorption peak potentials ( $E_{\text{peakS}}$ ) all shift to more positive potentials as the pH of the electrolyte increases, indicating that the increase of HBE with pH is a general trend (Figure 5.5). Two distinctive  $H_{\text{upd}}$  adsorption/desorption peaks

corresponding to Pt(110) (lower overpotential) and Pt(100) (higher overpotential) are clearly visible in CVs of Pt/C (Figure 5.4a) over the entire pH range tested. Both peaks rise almost linearly with the pH (0 to 13) (0.12 to 0.27 V and 0.22 to 0.37 V for the 110 and 100 facets, respectively), with a slope of 13 mV/pH for Pt(110) and 12 mV/pH for Pt(100) (Figure 5.5a), in reasonable agreement with reported values for polycrystalline Pt (10 mV/pH for Pt(110) and 8 mV/pH for Pt(100)[25] or ~ 11 mV/pH for both facets[125]) and high-index single crystalline Pt (10 mV/pH for Pt(553) and Pt(533)).[126] Similar correlations between the  $E_{\text{peak}}$  and pH are observed on Ir/C, Pd/C and Rh/C (Figure 5.5b, c, d), with a slope of 9, 11 mV/pH, and 10 mV/pH for Ir/C, Pd/C and Rh/C, respectively. The similar linear correlation and slope observed for all four metals suggests the generality of the effect of pH on the  $E_{\text{peak}}$ . The positive shift of  $E_{\text{peak}}$  represents an increase in HBE from acid to base. Given the prominent role HBE plays in determining the HOR/HER activities on monometallic Pt-group-metal catalysts,[25] it is likely that pH affects the HOR/HER activity mainly via the tuning of HBE, as shown for Pt/C, Ir/C, Pd/C and Rh/C below.

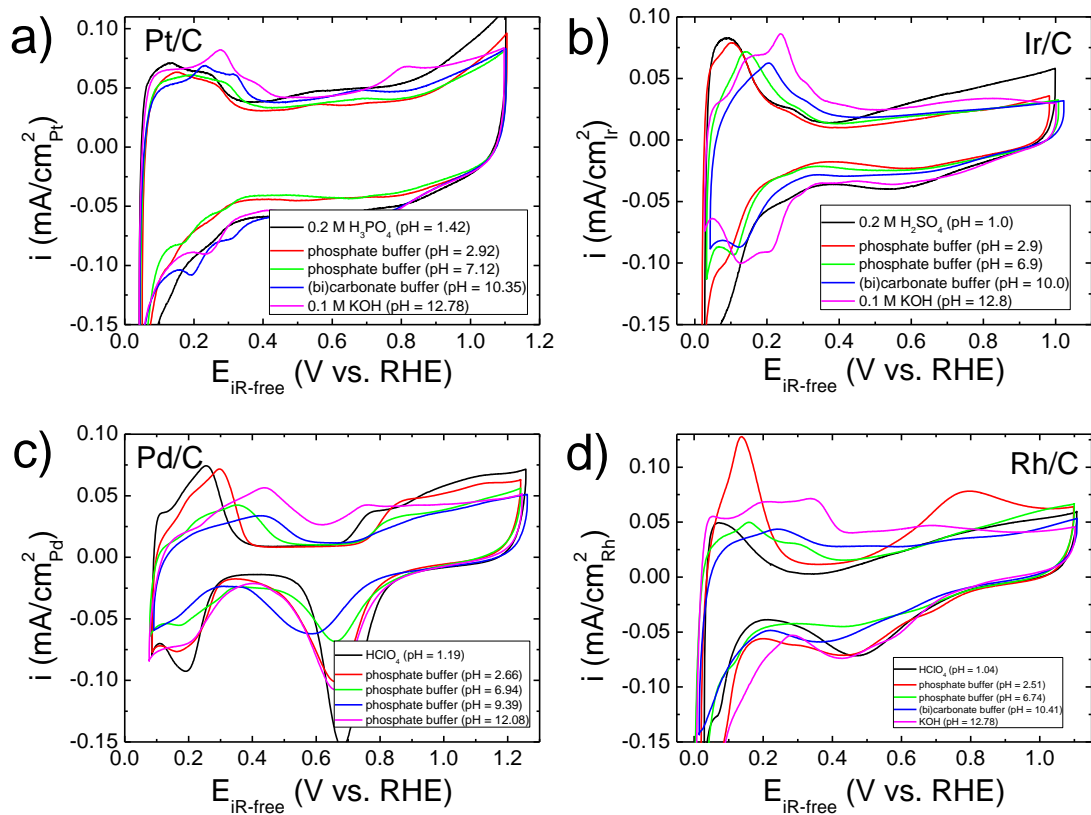


Figure 5.4 Representative cyclic voltammograms (CVs) of (a) Pt/C, (b) Ir/C, (c) Pd/C and (d) Rh/C in electrolytes with different pHs (currents were normalized to ECSA<sub>CV</sub> measured in 0.1 M KOH).

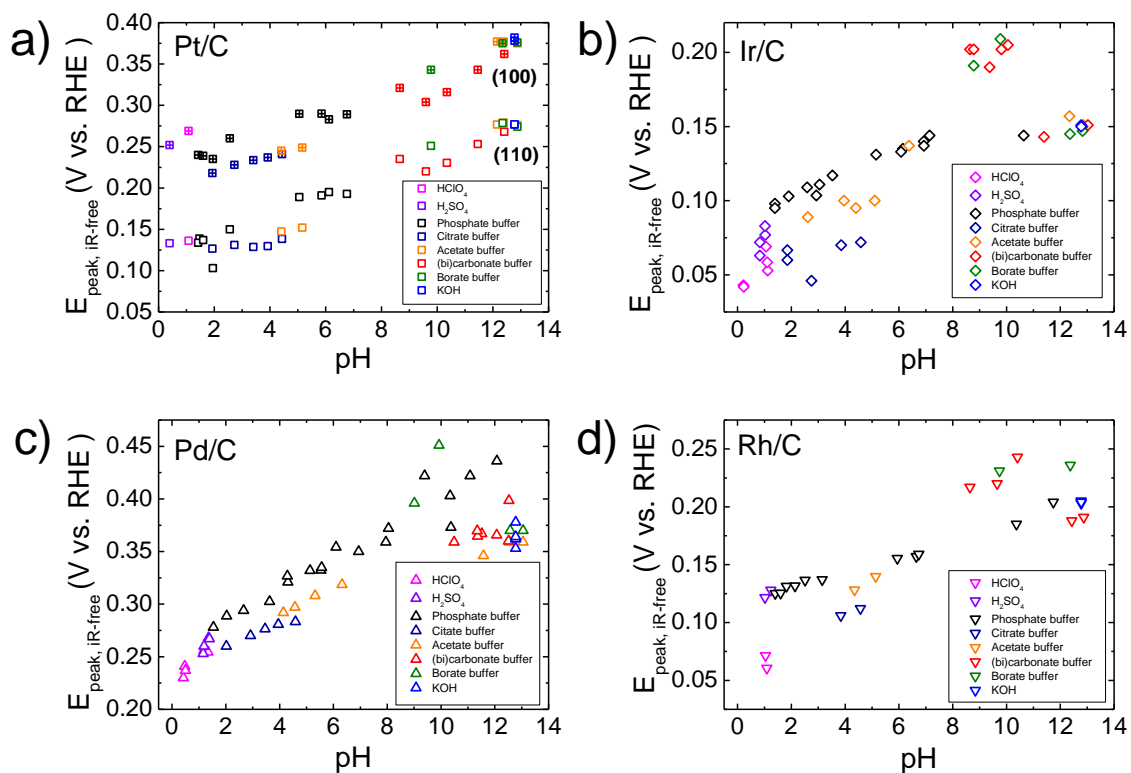


Figure 5.5 Underpotential deposited hydrogen (H<sub>upd</sub>) desorption peak potentials from cyclic voltammograms of (a) Pt/C, (b) Ir/C, (c) Pd/C and (d) Rh/C from CVs as a function of pH.

### 5.3.3 pH-Dependent HOR/HER Activity on Carbon Supported Pt, Ir, Pd and Ir Nanoparticles

HOR/HER activities were measured on Pt/C (Figure 5.6), Ir/C (Figure 5.7), Pd/C (Figure 5.8) and Rh/C (Figure 5.9) in various electrolyte with different pHs. Buffer solutions were employed to avoid the deviation of pH at the electrode surface from the bulk[127] so that reliable kinetic data can be obtained.[25] Multiple buffer solutions, i.e., phosphoric acid/phosphate, citric acid/citrate, acetic acid/acetate, carbonate/bicarbonate, boric acid/borate were used and their effectiveness in eliminating local concentration was confirmed by the lack of plateau in the HER portion

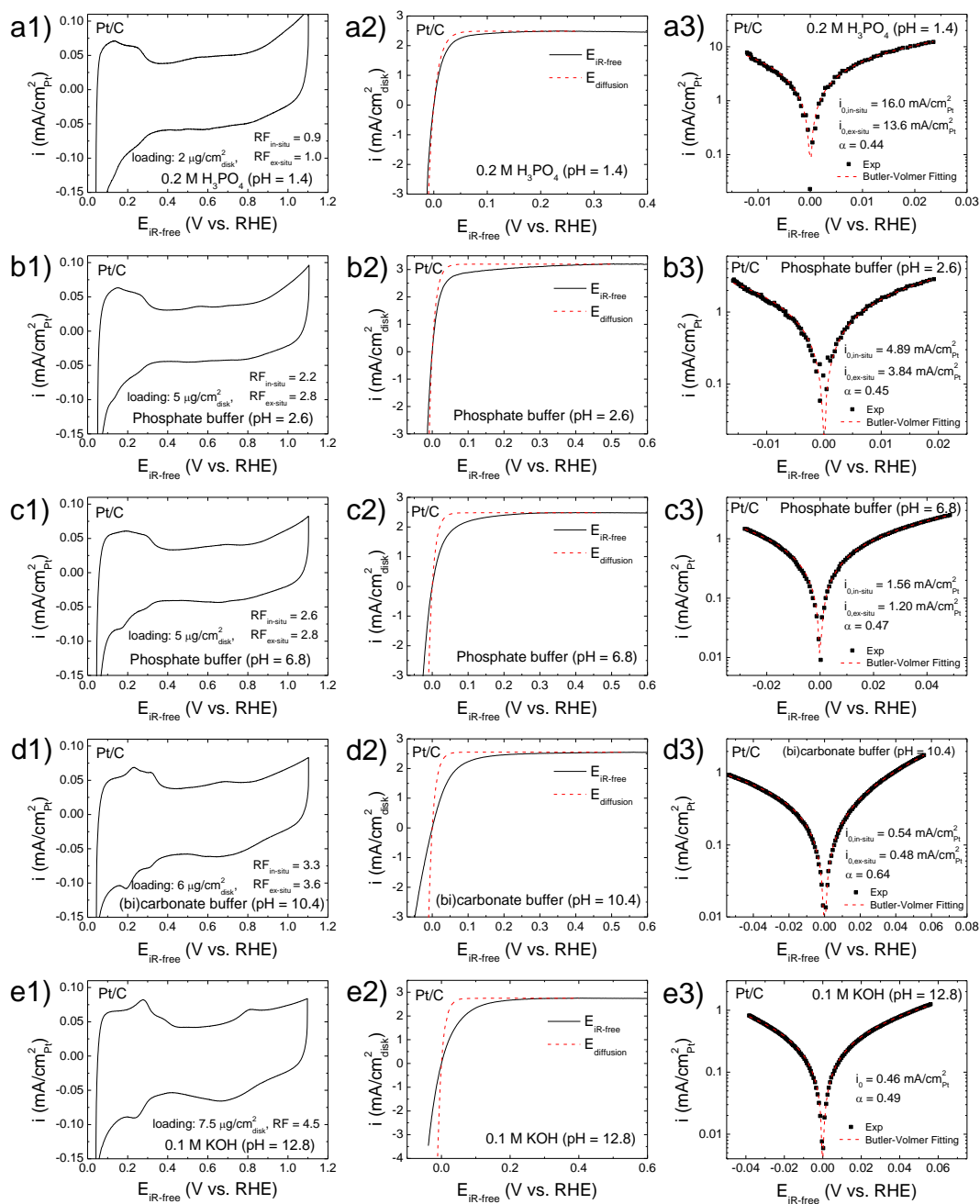


Figure 5.6 CVs (a1-e1), HOR/HER polarization curves (a2-e2), and kinetic current densities with fittings based on the Butler-Volmer equation with  $\alpha_a + \alpha_c = 1$  (a3-e3) on Pt/C in electrolytes at different pHs. CVs were measured in Ar at a scanning rate of 50 mV/s. HOR/HER polarization curves were collected in H<sub>2</sub>-saturated electrolytes at a scanning rate of 1 mV/s and a rotating speed of 1600 rpm.

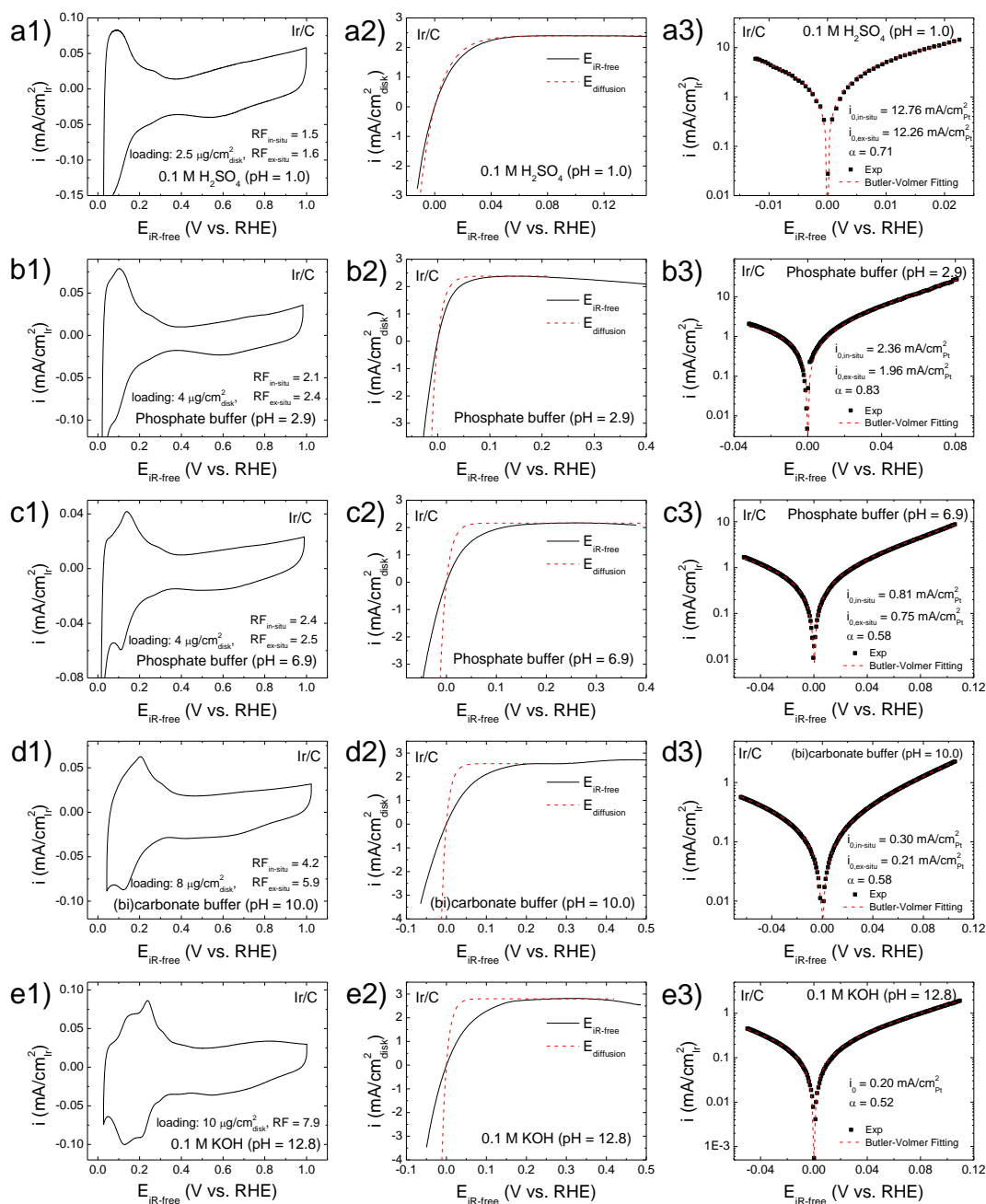


Figure 5.7 CVs (a1-e1), HOR/HER polarization curves (a2-e2), kinetic current density with their fitting into the Butler-Volmer equation with  $\alpha_a + \alpha_c = 1$  (a3-e3) on Ir/C in electrolytes with different pH. CVs were measured in Ar at a scanning rate of 50 mV/s, HOR/HER polarization curves were collected in H<sub>2</sub>-saturated electrolytes at a scanning rate of 1 mV/s and a rotating speed of 1600 rpm.

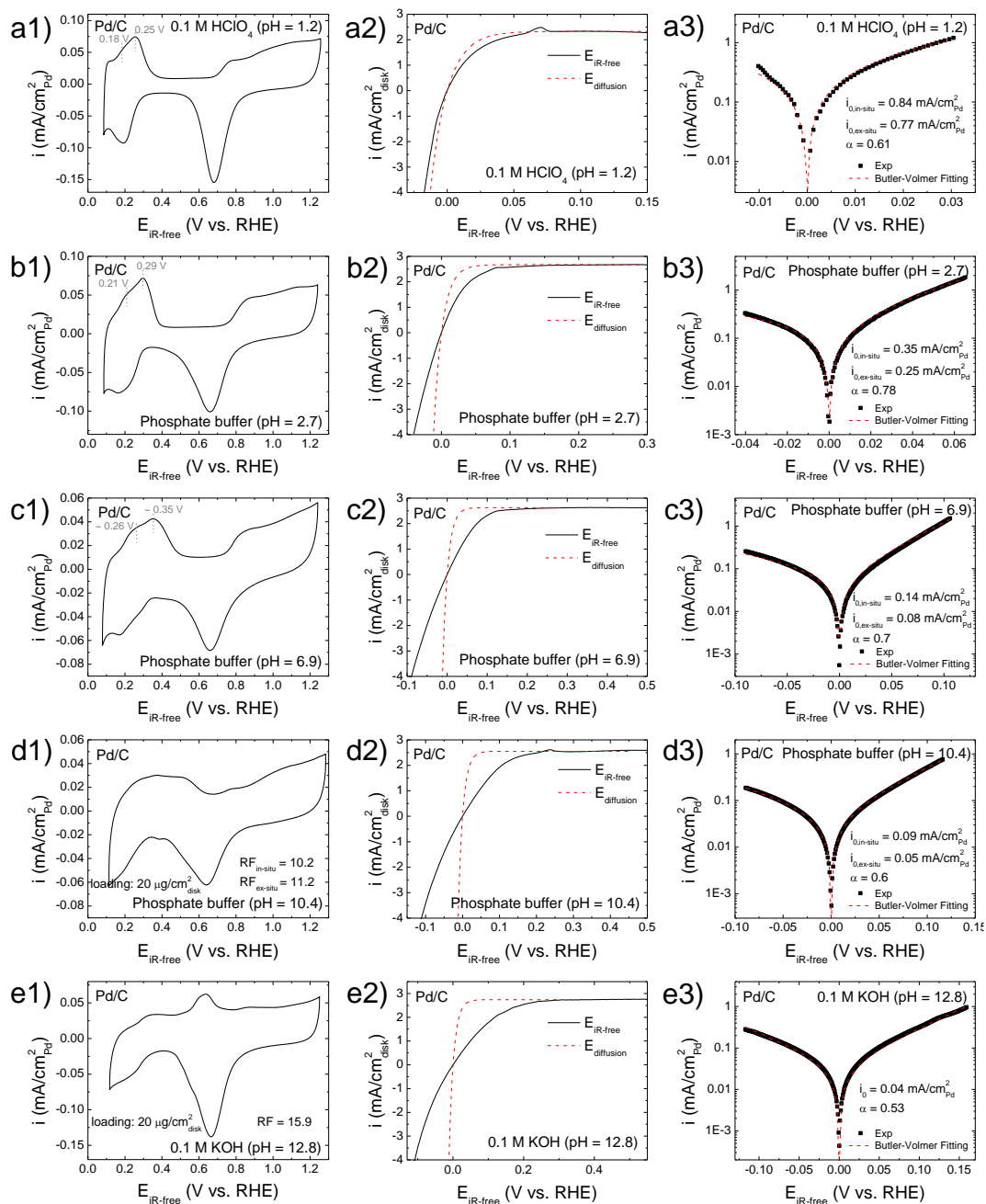


Figure 5.8 CVs (a1-e1), HOR/HER polarization curves (a2-e2), kinetic current density with their fitting into the Butler-Volmer equation with  $\alpha_a + \alpha_c = 1$  (a3-e3) on Pd/C in electrolytes with different pH. CVs were measured in Ar at a scanning rate of 50 mV/s, HOR/HER polarization curves were collected in H<sub>2</sub>-saturated electrolytes at a scanning rate of 1 mV/s and a rotating speed of 1600 rpm.

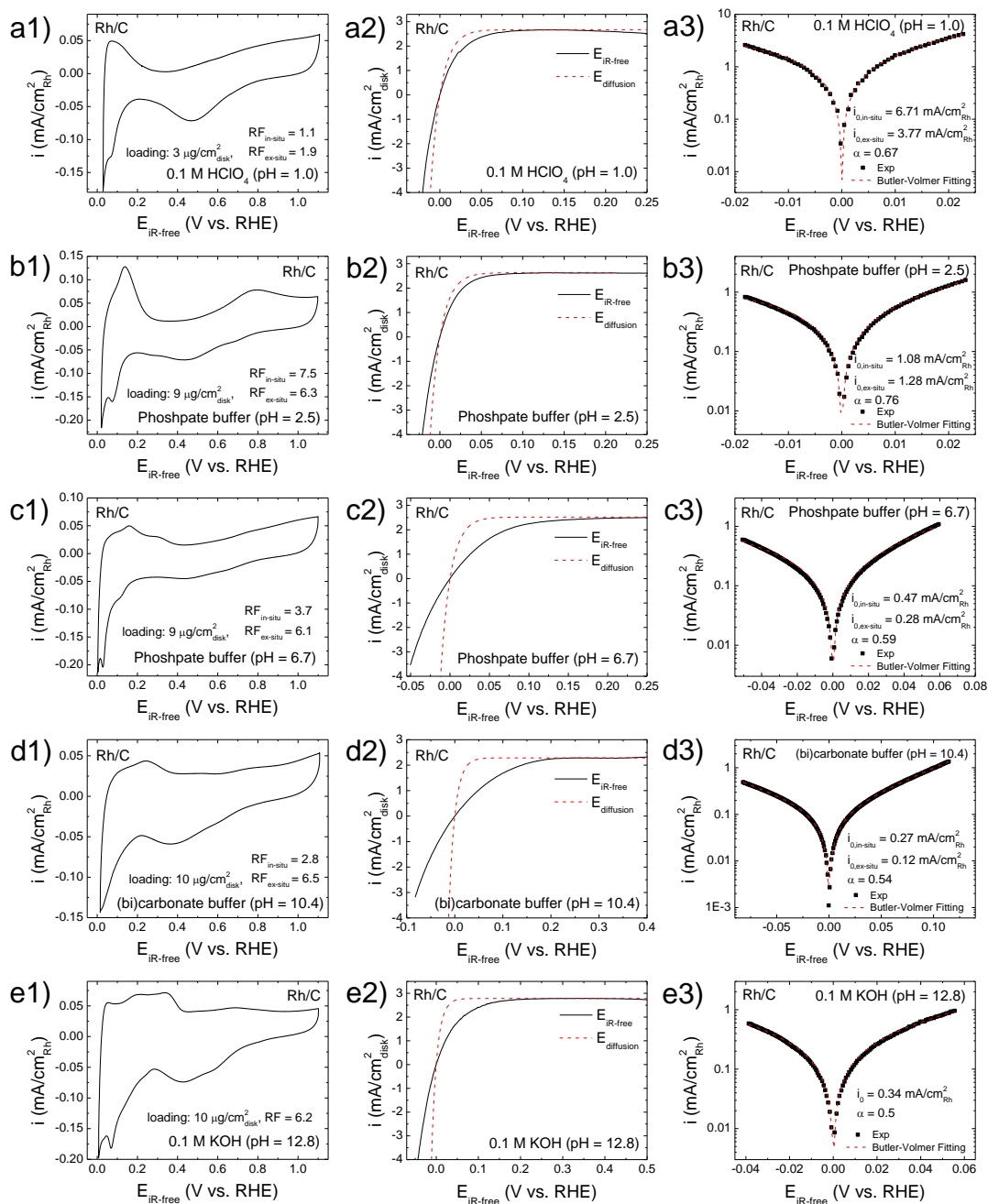


Figure 5.9 CVs (a1-e1), HOR/HER polarization curves (a2-e2), kinetic current density with their fitting into the Butler-Volmer equation with  $\alpha_a + \alpha_c = 1$  (a3-e3) on Rh/C in electrolytes with different pH. CVs were measured in Ar at a scanning rate of 50 mV/s, HOR/HER polarization curves were collected in H<sub>2</sub>-saturated electrolytes at a scanning rate of 1 mV/s and a rotating speed of 1600 rpm.

of the HOR/HER polarization curves (Figure 5.6 – 5.9). Exchange current densities ( $i_0$ ), which represent the intrinsic HOR/HER activities, are obtained by normalization to the electrochemical surface area of the catalysts (Figure 5.6 – 5.9) in the same electrolyte used for activity measurements. HOR/HER activities of Pt/C, Ir/C, Pd/C and Rh/C, determined using the rotating disk electrode (RDE) method, decrease monotonically with pH (from 0 to 13, Figure. 5.10), consistent with the theory that higher HBE suppresses catalytic performance.

Since HBE of the four metals increases with pH, our results confirm that higher HBE leads to lower HOR/HER activities, and thus provide convincing evidence supporting HBE as the dominant performance descriptor for HOR/HER catalysts. In addition, only small variations were observed for both  $E_{\text{peak}}$  and HOR/HER activity measured in different buffer solutions at similar pHs (Figure 5.5 and 5.10), indicating that the nature and adsorption of anions do not affect the results in any significant way. This is reasonable because anion adsorption typically occurs above the potential of zero-charge (PZC),  $\sim 0.57$  V vs. RHE for Pt[128], while HOR/HER proceeds below the PZC. Our  $i_0$  values of Pt/C, Ir/C, Pd/C and Rh/C at 293 K at low pH are in excellent agreement with those measured with a H<sub>2</sub>-pump method in a PEMFC configuration, where pH is presumed to be zero and reactions are in principle free of H<sub>2</sub> transport limitation (grey stars in Figure 5.10).[38] This agreement confirms the reliability of our activity measurements, especially for those in the acidic environment.

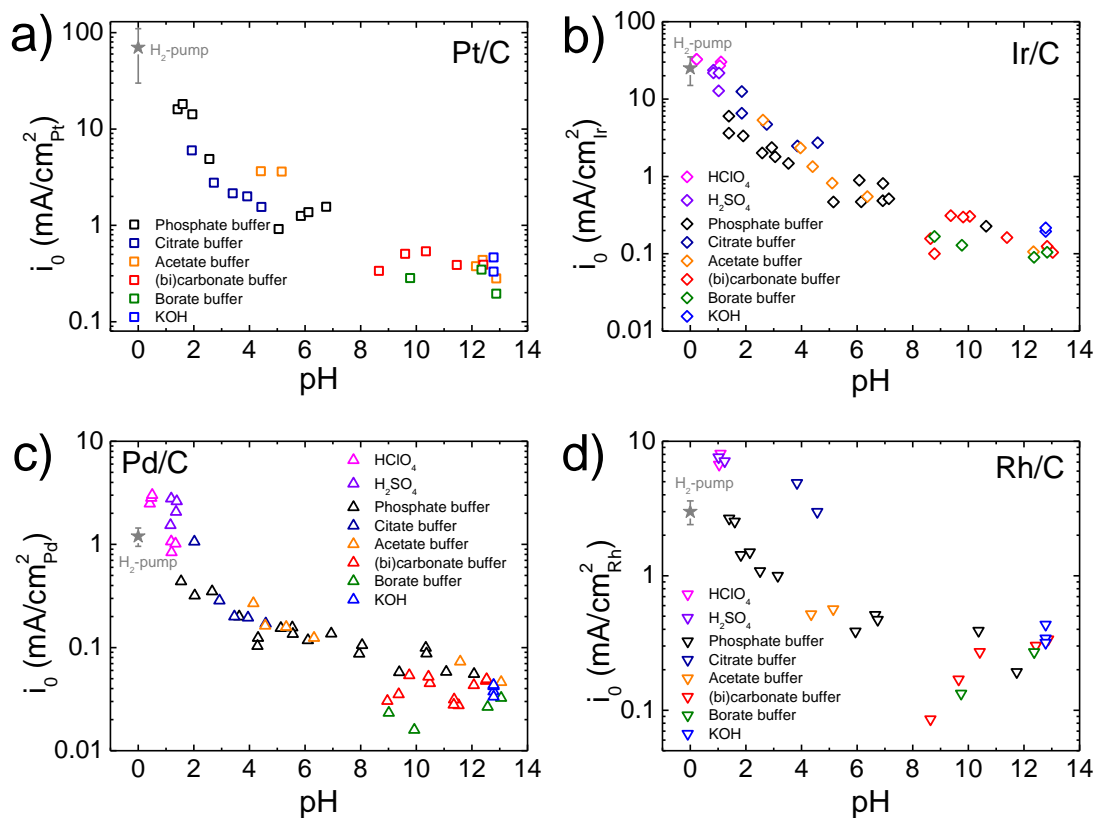


Figure 5.10 Exchange current densities ( $i_0$ ) of HOR/HER on (a) Pt/C, (b) Ir/C, (c) Pd/C and (d) Rh/C as a function of pH of electrolyte. HOR/HER polarization curves were measured using rotating disk electrode (RDE) method in  $H_2$ -saturated electrolytes at a scanning rate of 1 mV/s and a rotation speed of 1600 rpm at 293 K. Grey stars represent HOR/HER exchange current densities at 293 K estimated from the Arrhenius plot in ref.[38], in which all the activities were measured using an  $H_2$ -pump configuration.

### 5.3.4 Correlation of HOR/HER Activity with HBE

Linear correlations between  $\log(i_0)$  and  $E_{\text{peak}}$  (i.e., HBE) are obtained for Pt/C, Ir/C, Pd/C and Rh/C, respectively (Figure 5.11). From the Arrhenius equation and Brønsted-Evans-Polanyi (BEP) relation we can derive the following equation (see Appendix B.2):

$$i_0 = A \exp\left(-\frac{\beta F E_{peak}}{RT}\right) \quad (5.6)$$

where  $A$  is the pre-exponential coefficients,  $\beta$  characterizes the position of transition state along the reaction coordinate ( $0 \leq \beta \leq 1$ ),  $F$  is the faraday constant (96485 C/mol),  $R$  is the gas constant (8.31447 J/(mol·K)), and  $T$  is the temperature in Kelvin. This equation is used to fit the  $\log(i_0)$  vs.  $E_{peak}$  data (Figure 5.12) to obtain  $A$  and  $\beta$  (Table 5.2). Similar  $\beta$  values (0.5 - 0.8) support that a similar HOR/HER mechanism is at play on all four metals. The pre-exponential coefficients ( $A$ ) of Pt/C, Ir/C, Pd/C and Rh/C are also on the same order of magnitude (36-59) (Table 5.2). A universal  $i_0$  and HBE correlation is revealed when we plot  $i_0$  vs.  $E_{peak}$  for the four metals together (Figure 5.12). Note that the  $E_{peak}$  for Pd/C in Figure 5.4 is derived from the second peak since the first peak is not well defined from CVs in majority of the electrolytes. Our previous work showed that the sites with weakest HBE were the most active sites for HOR/HER,[129] therefore, the lowest  $E_{peak}$  is the best descriptor to correlate with activity and should be used for the universal correlation. Based on the observation that the peak potential difference between the first and second  $H_{upd}$  desorption peak on Pd/C in certain electrolytes is around 0.08 V (Figure 5.8) and the assumption the peak potential difference remains roughly the same in all pHs, as demonstrated in the case of for Pt(110) and Pt(100), the potential of the first  $E_{peak}$  of Pd/C (Figure 5.12) is estimated using:  $E_{peak, first} \approx E_{peak, second} - 0.08$  V.

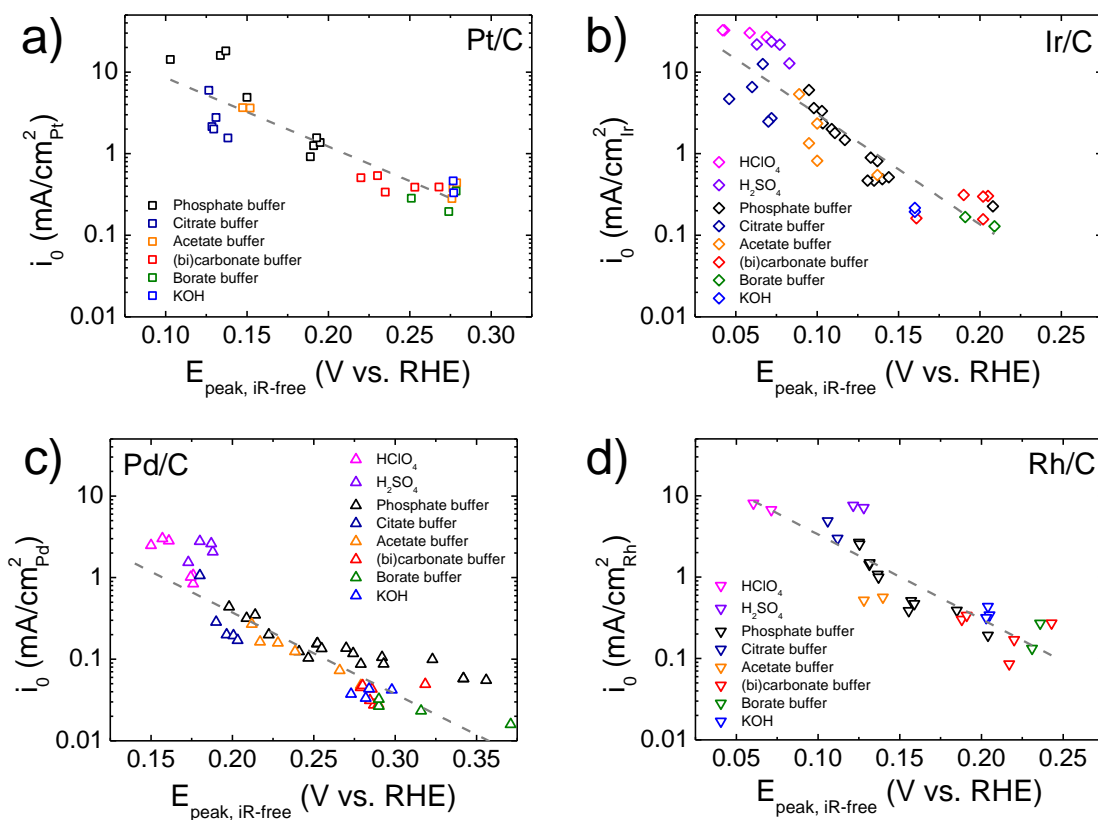


Figure 5.11: Exchange current densities of HOR/HER on (a) Pt/C, (b) Ir/C, (c) Pd/C and (d) Rh/C as a function of underpotential deposited hydrogen ( $H_{\text{upd}}$ ) desorption peak potential ( $E_{\text{peak}}$ ) from CVs. Gray dash lines in the four figures are linear fittings of the data.

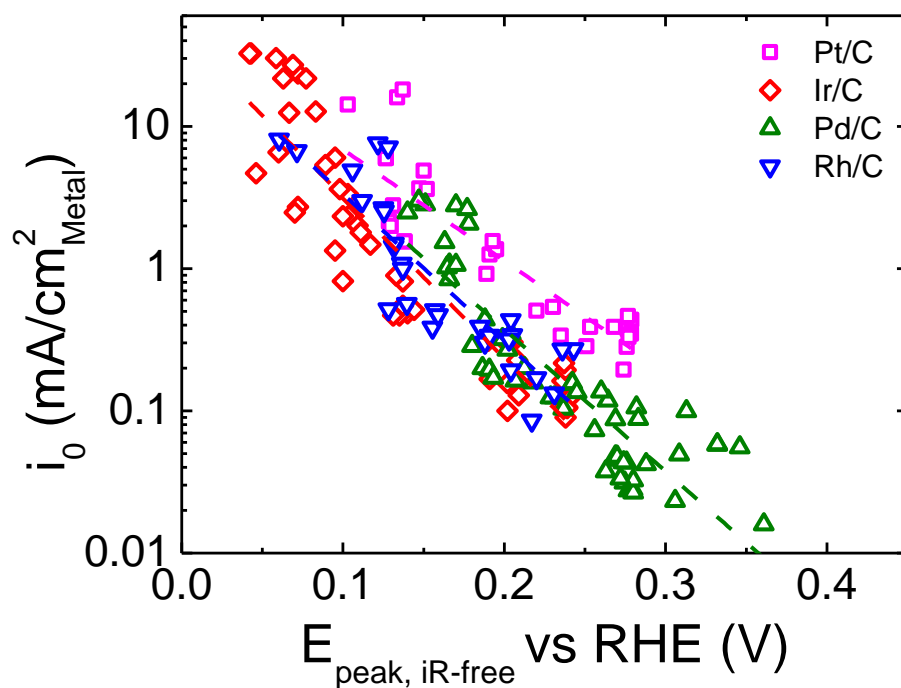


Figure 5.12: Exchange current densities of HOR/HER ( $i_0$ ) on Pt/C, Ir/C, Pd/C and Rh/C as a function of the lowest underpotential deposited hydrogen ( $H_{\text{upd}}$ ) desorption peak potential ( $E_{\text{peak}}$ ) from CVs. Dash line represents linear fitting of all data points.

Activation energies ( $E_a$ ) of HOR/HER on Pt/C, Ir/C and Pd/C in 0.1 M KOH are determined using RDE method in this work (Figure 5.13) and they are greater than those measured in  $H_2$ -pumps presumed to be at  $\text{pH} = 0$  [38] (Table 5.2). Rh/C does not follow this trend, with similar  $E_a$  observed in 0.1 M KOH and  $H_2$ -pumps. Our activation value of  $29.6 \pm 0.4$  kJ/mole on Pt/C in base is in good agreement with reported values on polycrystalline Pt ( $28.9 \pm 4.3$  kJ/mol) and Pt/C ( $29.5 \pm 4.0$  kJ/mol.[2] An alternative and independent method to obtain  $\beta$  stems from the definition of the BEP relation, from which Eq. 5.7 can be derived (Appendix B.3):

$$\Delta E_a = \beta F \Delta E_{\text{peak}} \quad (5.7)$$

where  $\Delta E_a$  is the activation energy difference between base and acid ( $(E_a(0.1\text{ M KOH}) - E_a(\text{H}_2\text{ pump}))$ ),  $\Delta E_{peak}$  is the difference of  $E_{peak}$  between base and acid ( $E_{peak}$  for H<sub>2</sub>-pump measurement (pH = 0) are estimated from CV in liquid electrolytes with similar pH. The  $\beta$  values calculated via Eq. 5.7, denoted  $\beta_{Ea}$  (Table 5.2), agree well with those obtained from  $\log(i_0)$  vs.  $E_{peak}$  fitting, which validates the activity –  $E_{peak}$  correlation. Moreover, this correlation is consistent with the previous report that Pt(100) has higher HBE and activation energy for HOR/HER than Pt(110).[39] Hence, it is reasonable to conclude that the higher activation barrier originates from its stronger HBE and is responsible for the slow HOR/HER kinetics in base.

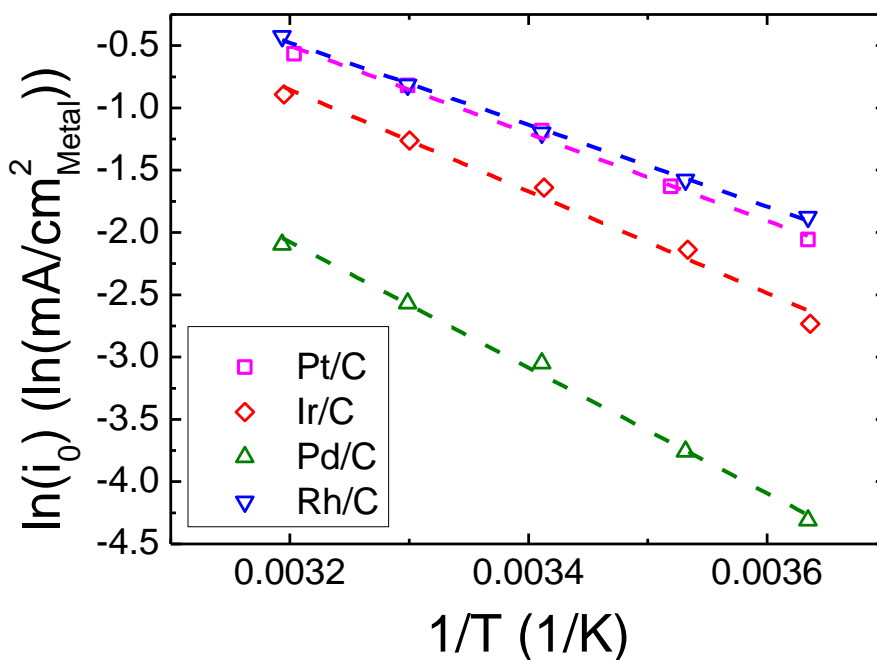


Figure 5.13: Arrhenius plot of HOR/HER activities on Pt/C (a), Ir/C (b), Pd/C (c) and Rh/C (d) in 0.1 M KOH.

Table 5.2  $\beta$  and A from fitting  $i_0$  to  $E_{peak}$  using expression  $i_0 = A \exp(-\beta FE_{peak}/RT)$ , activation energy ( $E_a$ ) measured by RDE in 0.1 M KOH from this work and by H<sub>2</sub>-pump from ref[38], difference in H<sub>upd</sub> desorption peak potentials ( $\Delta E_{peak}$ ) in 0.1 M KOH and acid with pH  $\approx$  0, and  $\beta_{Ea}$  calculated by  $(E_a(0.1 \text{ M KOH}) - E_a(\text{H}_2 \text{ pump}))/F\Delta E_{peak}$

	$i_0 = A \exp(-\frac{\beta FE_{peak}}{RT})$		$E_a$ (kJ/mol)		$\Delta E_{peak}$ (V)	$\beta_{Ea}$
	$\beta$	A	0.1 M KOH	H <sub>2</sub> -pump (pH=0) [38]		
Pt/C	0.5	59	29.6 $\pm$ 0.4	16 $\pm$ 2	0.17	0.8
Ir/C	0.8	68	32.8 $\pm$ 0.4	19 $\pm$ 3	0.20	0.7
Pd/C	0.6	37	38.9 $\pm$ 3.0	31 $\pm$ 2	0.14	0.6
Rh/C	0.6	36	26.6 $\pm$ 0.7	28 $\pm$ 1	-	-

### 5.3.5 pH-Dependent CO-Stripping Onset Potential

The CO-stripping profiles were obtained on Pt/C (Figure 5.14), Ir/C (Figure 5.15), Pd/C (Figure 5.16) and Rh/C (Figure 5.17) in electrolytes with different pHs. The onset potential of CO-stripping on all four metals (Pt/C, Ir/C, Pd/C and Rh/C) decreases monotonically with pH (Figure 5.18), suggesting co-adsorbed OH is unlikely to play a major role in promoting HOR. There is an extensive debate regarding whether adsorbed OH enhances HOR/HER activity.[2,3,25,52,83,118] The onset potential of CO-stripping provides a sensitive measure of lowest potential at which OH<sub>ad</sub> is present on the surface, and in turn the binding energy of OH<sub>ad</sub>, since it is well established that OH<sub>ad</sub> facilitates the removal of CO<sub>ad</sub>. [52,130] The onset potential of CO-stripping on the four metals decreases with pH (Figure 5.14 – 5.18), indicating that OH tends to adsorb at a lower potential when the pH become higher. Therefore, if the presence of OH<sub>ad</sub> promotes HOR, higher HOR activity would have been observed at higher pH. However, the opposite trend is observed in Figure 5.10. Note that our CO-stripping data are in agreement with Gisbert et al.'s results that CO-stripping on poly-oriented and single-

crystal Pt over a wide range of pH from 2 to 13 in phosphoric acid/phosphate buffer solution.[131] It is interesting to observe that both the HOR/HER activities and oxophilicity of low-index single-crystal Pt facets follow the same sequence of Pt(111) < Pt(100) < Pt(110),[132] which seems to suggest that more oxophilic surface processes higher activity. However, an alternative explanation exists in that Pt(110) is more active than Pt(100) because it has lower HBE (Figure 5.4a). Similarly, the enhanced HOR/HER activity on PtRu as compared to Pt, which has been attributed to the higher oxophilicity of Ru,[83] is likely induced by the weakened Pt-H bonding in the presence of neighboring Ru.[52] The contradictory trend of HOR/HER activity vs. the oxophilicity discussed above points to the possibility of no inherent correlation between these two variables.

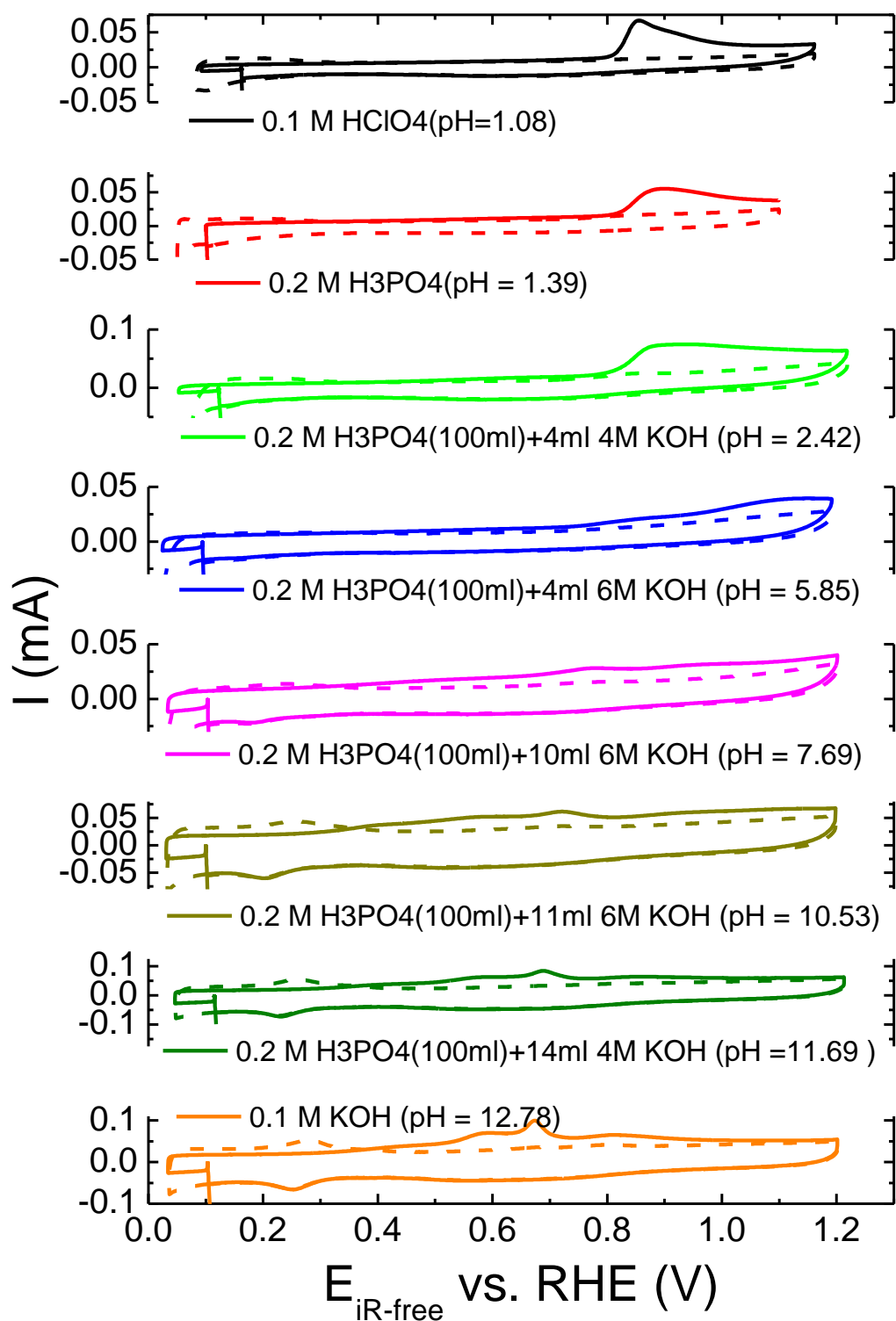


Figure 5.14 CO stripping profiles on Pt/C in various electrolytes with different pHs.

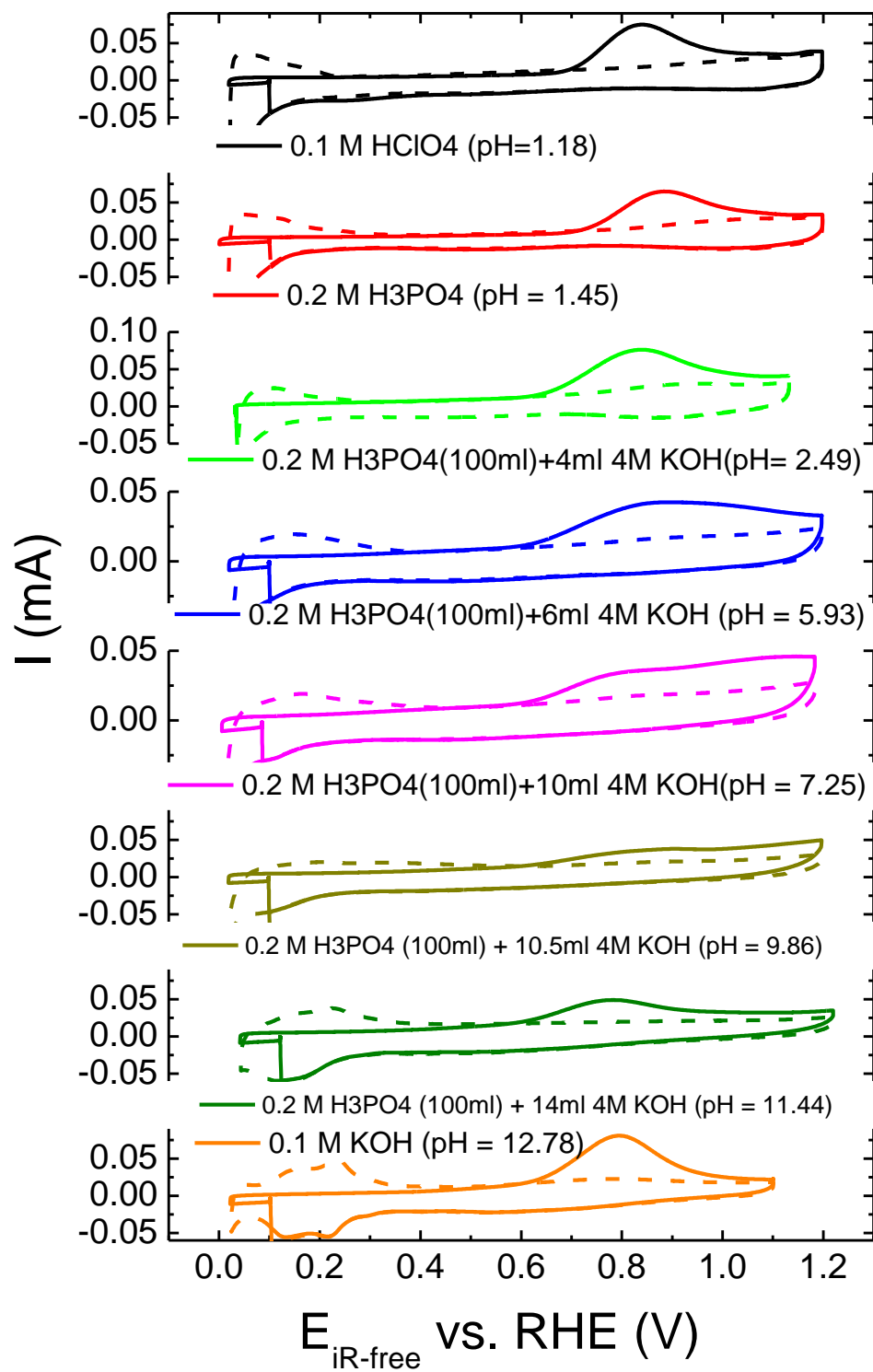


Figure 5.15 CO stripping profiles on Ir/C in various electrolytes with different pHs.

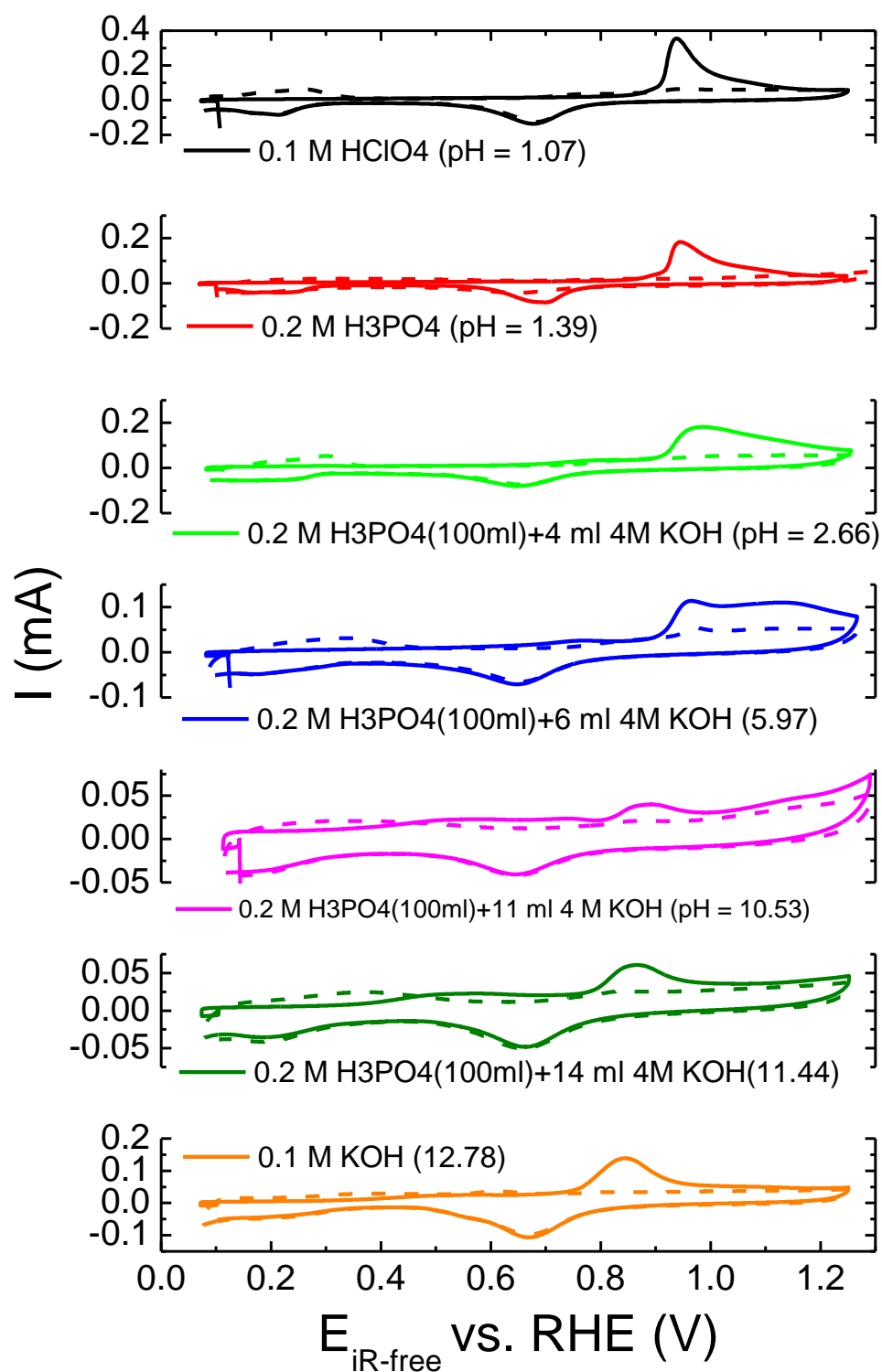


Figure 5.16 CO stripping profiles on Pd/C in various electrolytes with different pHs.

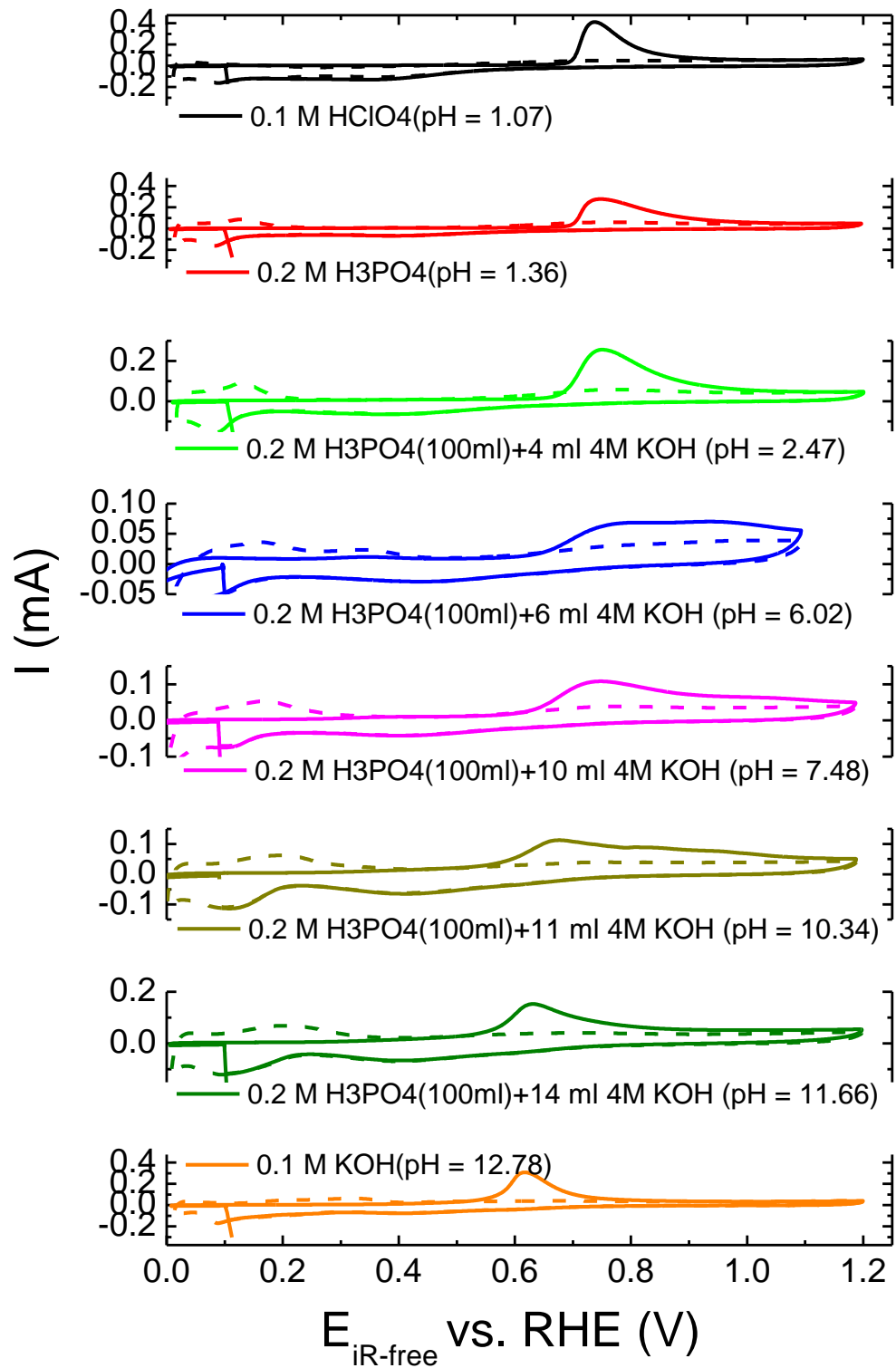


Figure 5.17 CO stripping profiles on Rh/C in various electrolytes with different pHs.

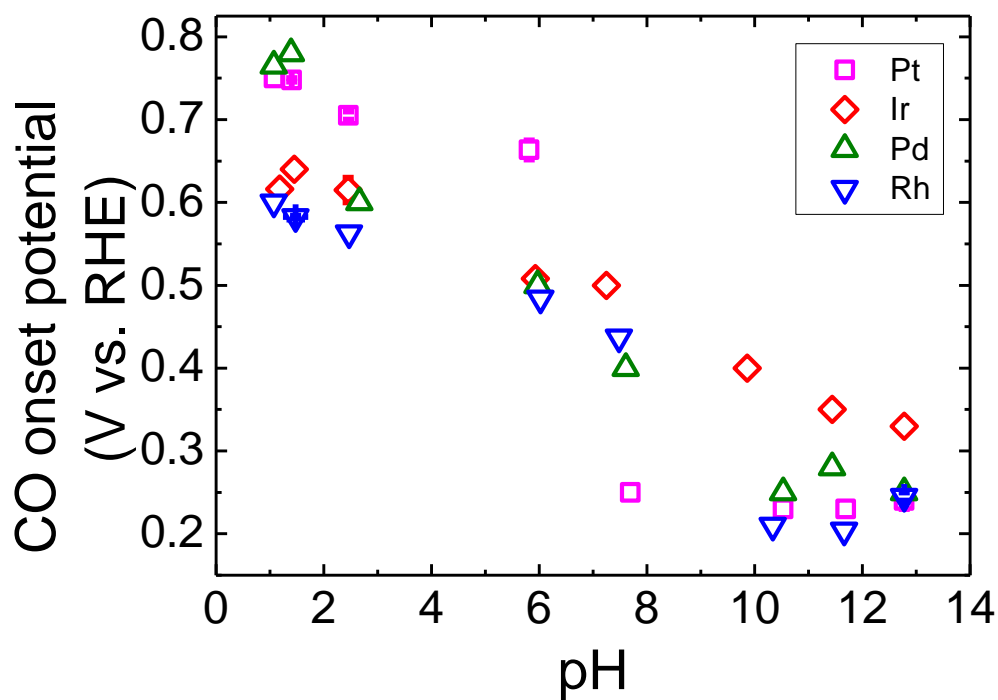


Figure 5.18 CO stripping onset potentials as a function of pH on Pt/C (magenta squares), Ir/C (red diamonds), Pd/C (olive up-triangles) and Rh/C (blue down-triangles).

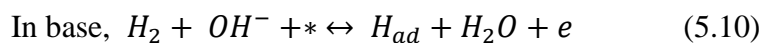
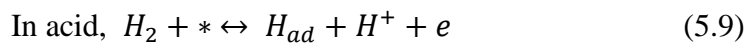
### 5.3.6 Discussion about pH-Dependent HBE and HOR/HER Activity

HOR/HER ( $H_2 \leftrightarrow 2H^+ + 2e$  in acid and  $H_2 + 2OH^- \leftrightarrow 2H_2O + 2e$  in base) is believed to proceed via either a Tafel-Volmer (Eqs. 5.8, 5.11, and 5.12) or a Heyrovsky-Volmer (Eqs. 5.9-5.12) pathway:[16]

Tafel:



Heyrovsky:



Volmer:



The universal correlation between  $i_0$  and HBE on the four metals indicates that HOR/HER on those metals may share the same reaction mechanism, i.e., same elementary steps and rate determining step (RDS). The good fitting of the data into Butler-Volmer equation with  $\alpha_a + \alpha_c = 1$  (Figure 5.6- 5.9) suggests that Tafel-Volmer with Volmer being the RDS is likely the reaction mechanism because a Heyrovsky-Volmer mechanism would have resulted  $\alpha_a + \alpha_c = 2$ .<sup>[67]</sup> Additional evidence for the Volmer step being RDS includes 1) the excellent correlation between HOR/HER activity and HBE<sup>[3,25]</sup> and 2) the identical activities determined from HOR/HER measurements and  $H_{upd}$  charge transfer resistance.<sup>[3]</sup>

A number of theories have been proposed to explain the slower kinetics of HOR/HER in alkaline than in acidic electrolytes. In early studies, Osetrova and Bagotsky suggested that HOR/HER followed a different path in alkaline solutions through the formation of an  $H_2^+$  intermediate rather than dissociative adsorption of  $H_2$ .<sup>[132,133]</sup> An alternative theory suggested that the formation of  $H_{ad}$  is more difficult from  $H_2O$  than from  $H^+$ , which led to the sluggish kinetics for the reverse reaction of Eq. 5.12, as compared to that of Eq. 5.11.<sup>[26,134]</sup> However, this hypothesis cannot be applied to HOR as H is abstracted from  $H_2$  instead of  $H^+$  or  $H_2O$ . The potential effects of  $OH_{ad}$  on HOR in the potential region where  $OH_{ad}$  is present based on CO stripping (above 0.4 V vs. RHE) are: 1) site blocking; 2) modifying HBE through  $H_{upd}/OH_{ad}$  interaction;<sup>[132]</sup> and 3) modifying HBE through  $H_{upd}/OH^-$  interaction.<sup>[25]</sup> Considering the two orders of magnitude higher activity in acid than base, it is unlikely that site blocking effect of  $OH_{ad}$  plays any major role in affecting HOR/HER activity with less

than two fold decrease in ECSA from acid to base. The tuning of HBE is more plausible as a ~150 mV difference in  $H_{\text{upd}}$  desorption peak potentials has been observed between acid and base electrolytes. Sheng et al. proposed that HBE was tuned by  $\text{OH}^-$  in the solution phase instead of  $\text{OH}_{\text{ad}}$  based on the barely existence of  $\text{OH}_{\text{ad}}$  at reversible HOR/HER potential.[25]

Specific adsorption of anions was also found to affect the H adsorption, e.g., addition of  $\text{Cl}^-$  will affect the CV of Pt in sulfuric acid by inhibiting the strongly bonded H and shifting the overall curve to cathodic potentials.[113] Similarly, Kinoshita et al. attributed the stronger H adsorption on Pt in alkaline than acidic electrolytes to the less extent specific adsorption of  $\text{OH}^-$  than  $\text{HSO}_4^-$ . [100] However, this hypothesis cannot explain the HBE difference of Pt in  $\text{HClO}_4$  and KOH. The  $\text{ClO}_4^-$  adsorption is known to weaker than  $\text{OH}^-$ , however, the HBE of Pt in  $\text{HClO}_4$  is still lower than that in KOH. Addition of KCl,  $\text{K}_2\text{SO}_4$  and  $\text{NaClO}_4$  (the adsorption strength in the order of  $\text{Cl}^- > \text{SO}_4^{2-} > \text{ClO}_4^-$ )[132] to 0.1 M KOH while keeping the pH constant leads to only a slight change to the  $E_{\text{peak}}$  (or HBE) (Figure 5.19a, c, e, and Table 5.3) and the exchange current densities (Figure 5.19b, d, f), which is consistent with the hypothesis that HBE is the dominant descriptor for HOR/HER activity. The similar dependence of HBE on pH for all four metals indicates that the mechanism through which pH affects HBE is likely to be metal independent. In this regard, the presence of cations in the immediate vicinity of the electrode surface and their potential interaction with adsorbed H in alkaline electrolytes could be a possible mechanism.[132,135,136]

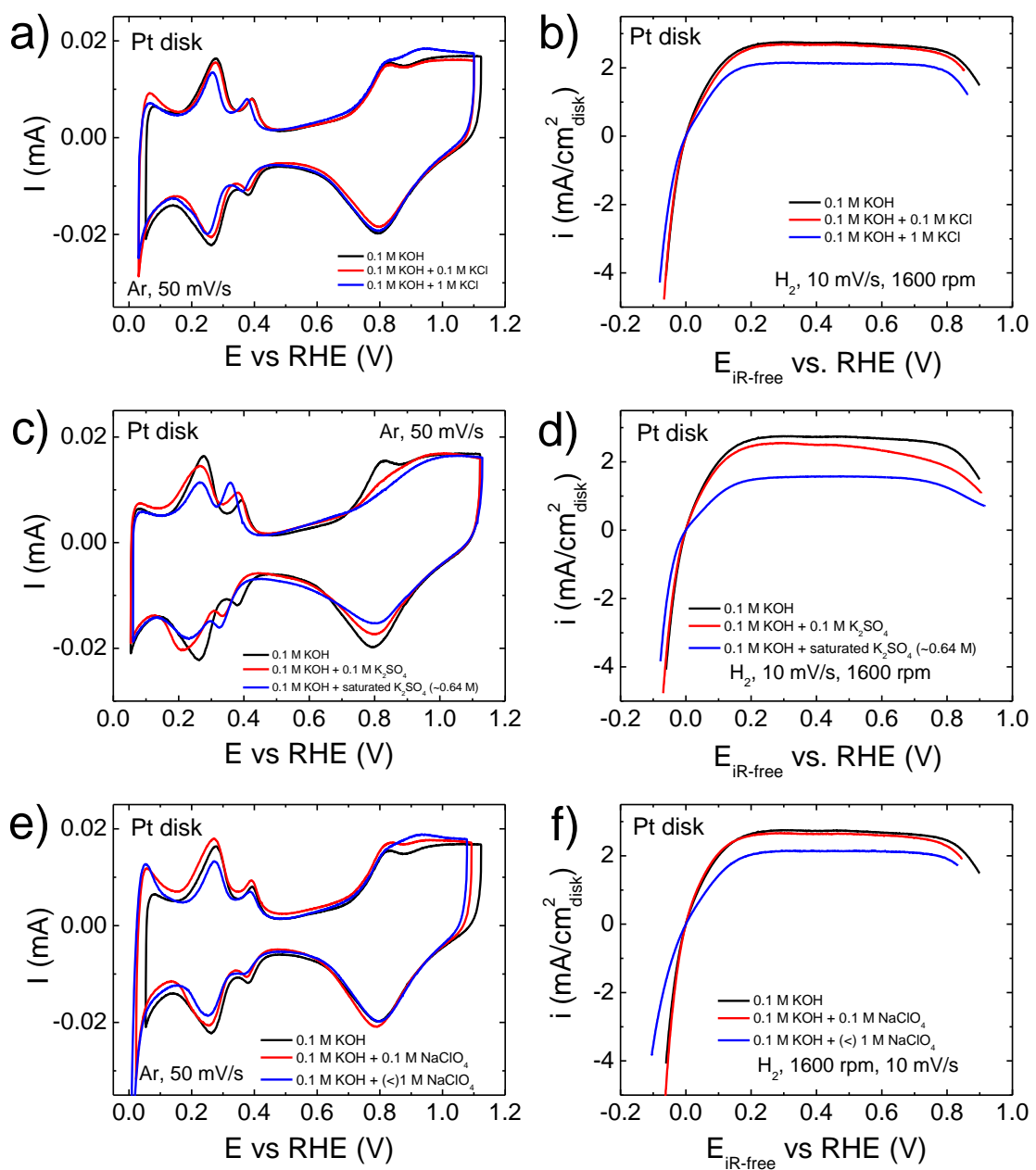


Figure 5.19 CVs and the HOR/HER polarization curves on a Pt disk in 0.1 M KOH with additional salts of (a, b) KCl, (c, d)  $K_2SO_4$ , and (e, f)  $NaClO_4$ .

Table 5.3 Surface area measured from  $H_{\text{upd}}$  adsorption and desorption peaks, potentials for Pt(110) and Pt(100) and the corresponding exchange current densities ( $i_0$ ) in 0.1 M KOH with addition of various salts

Electrolyte	Surface area (cm <sup>2</sup> )	Peak(110) (V)	Peak(100) (V)	$i_0$ (mA/cm <sup>2</sup> <sub>Pt</sub> )
0.1 M KOH	0.303	0.276	0.393	0.805
0.1 M KOH + 0.1 M KCl	0.280	0.276	0.392	0.679
0.1 M KOH + 1 M KCl	0.244	0.266	0.377	0.590
0.1 M KOH + 0.1 M K <sub>2</sub> SO <sub>4</sub>	0.293	0.265	0.381	0.763
0.1 M KOH + saturated (~0.64 M) K <sub>2</sub> SO <sub>4</sub>	0.230	0.261	0.359	0.483
0.1 M KOH + 0.1 M NaClO <sub>4</sub>	0.310	0.271	0.391	0.893
0.1 M KOH + (<) 1 M NaClO <sub>4</sub>	0.244	0.271	0.385	0.428

Water, as the most abundant species in the electrolyte, is known to be ubiquitously adsorbed on the electrode interface,[35] which could potentially affect the HOR/HER kinetics or metal-HBE. The presence of water was considered to have little impact on the Pt-H binding energy based on the similar HBE determined electrochemically from temperature-dependent cyclic voltammograms in acid and measured from gas-phase in ultrahigh vacuum.[35,96,137] However, stronger HBE is obtained in alkaline electrolyte than in acid, which breaks the similarity between HBE measured electrochemically and from gas-phase, therefore, the influence of water may not be excluded. Different orientation of adsorbed water, which is electrode potential or surface charge dependent, was mentioned by Trasatti, with the oxygen atom in the water molecule points towards the metal on a positively charged surface and an opposite orientation on a negatively charged surface.[29] In electrolytes with different pH, the electrode surface potential differs in the SHE scale, which might leads to different extents in water dipole orientation or water dipole moments and consequently influence

water adsorption/desorption energy. If we consider the hydrogen adsorption/desorption process in electrolyte is accompanied by displacing/re-adsorption of water molecules, then the apparent HBE might be altered by the adsorption/desorption of water in electrolytes with different pHs. However, it is a tentative hypothesis which requires further efforts.

#### **5.4 Conclusion**

The pH dependence of HBE and HOR/HER activities on Pt/C, Ir/C, Pd/C and Rh/C have been mapped out with cyclic voltammetry and rotating disk electrode methods in multiple buffer solutions with pH ranging from 0 to 13. Linear correlations between pH and HBE with a similar slope on all four catalysts suggest that the pH dependence of HBE is likely metal independent.  $\text{Log}(i_0)$  decreases linearly with pH, and in turn HBE, which is consistent with the hypothesis that HBE is the dominant descriptor for HOR/HER catalysts. Low onset potentials of adsorbed OH, characterized by CO stripping experiments, correlate with low HOR/HER activities, indicating that the oxophilicity of metals does not play a significant role in determining HOR/HER activities.

## Chapter 6

### PLATINUM-RUTHENIUM NANOTUBES AND PLATINUM-RUTHENIUM COATED COPPER NANOWIRES AS EFFICIENT CATALYSTS FOR ELECTRO-OXIDATION OF METHANOL

The sluggish kinetics of methanol oxidation reaction (MOR) is a major barrier to the commercialization of direct methanol fuel cells (DMFCs). In this chapter, we report a facile synthesis of platinum-ruthenium nanotubes (PtRuNTs) and platinum-ruthenium coated copper nanowires (PtRu/CuNWs) by galvanic displacement reaction using copper nanowires as a template. The PtRu compositional effect on MOR is investigated; the optimum Pt/Ru bulk atomic ratio is about 4 and surface atomic ratio about 1 for both PtRuNTs and PtRu/CuNWs. Enhanced specific MOR activities are observed on both PtRuNTs and PtRu/CuNWs compared with the benchmark commercial carbon supported PtRu catalyst (PtRu/C, Hispec 12100). X-ray photoelectron spectroscopy (XPS) reveals a larger extent of electron transfer from Ru to Pt on PtRu/CuNWs, which may lead to a modification of the d-band center of Pt and consequently a weaker bonding of CO (the poisoning intermediate) on Pt and a higher MOR activity on PtRu/CuNWs.

This chapter is reprinted with permission from Zheng, J.; Cullen, D. A.; Forest, R. V.; Wittkopf, J. A.; Zhuang, Z.; Sheng, W.; Chen, J. G.; Yan, Y., Platinum–Ruthenium Nanotubes and Platinum–Ruthenium Coated Copper Nanowires As Efficient Catalysts for Electro-Oxidation of Methanol, *ACS Catalysis* **2015**, *5*, 1468.. Copyright 2015 American Chemical Society.

## 6.1 Introduction

Direct methanol fuel cells (DMFCs) are an attractive alternative to hydrogen-fueled proton exchange membrane fuel cells (PEMFCs) for powering portable devices because of their high energy density (4.8 kWh/L) and ease of fuel transportation and storage.[14,15] However, in practice, DMFCs exhibit low energy density and efficiency due to the sluggish methanol oxidation reaction (MOR) (which leads to a large overpotential) and the crossover of methanol from anode to cathode.[138] Tremendous efforts have been devoted to the development of novel MOR catalysts in the past few decades to lower the anode overpotential, and PtRu alloys are recognized as the most active catalyst so far.[139,140] However, even with the state-of-art PtRu catalysts (carbon supported PtRu nanoparticles or PtRu/C), the MOR activity is still not high enough: an anode overpotential of about 350 mV exists which needs to be reduced.

One-dimensional (1D) nanostructures with extended surfaces such as nanowires, nanotubes and nanorods usually have a preferential exposure of certain facets which may enhance their catalytic MOR activities since MOR is well known to be structure sensitive.[97] Koenigsmann et al. gave a detailed review on 1D noble metal catalysts as a promising structure paradigm for both MOR and oxygen reduction reaction in DMFCs.[59] Studies have shown that Pt nanotubes (PtNTs),[141] porous Pt nanotubes (porous-PtNTs)[142] and ultrathin Pt nanowires (PtNWs)[143] all exhibited improved MOR activity over supported Pt nanoparticles (Pt/C). 1D Pt alloy nanostructures, such as PtNi nanotubes,[144] PtNiP composite nanotubes,[145] PtPd nanotubes and nanorods,[146] PtFe and PtPdFe nanowires,[147] PtRu nanowires,[148,149] PtPdTe nanowires[150] and Au/Pt and Au/PtCu nanowires,[151] have also been demonstrated to be better MOR catalysts, attributed to bifunctional mechanisms[152,153] or electronic effects[154] of the Pt alloy systems. In addition to the improved MOR

activity, 1D nanostructures are believed to have the potential to enhance mass transport in the electrode during fuel cell operation.[148] Among various alloying elements, Ru is still the best choice in improving the MOR kinetics. Benefiting from the advantages of 1D structure and the promotional effect of Ru, 1D PtRu nanostructures are of great interest but work in this area has been limited. 1D PtRu nanostructures reported were synthesized by template-assisted electrodeposition using AAO[155] or SBA-15[148] as hard template followed by template removal or by electrodeposition of PtRu on Au-coated ZnO-NTs.[156] Their MOR activities are similar or slightly higher than that of PtRu/C. Additionally, these methods usually are only suitable for small scale synthesis and the yield is low. Alternatively, galvanic displacement reactions were widely used for synthesizing noble metal materials using less noble metal as template, such as Ag,[157-159] Cu[160-163] and Te.[150,164,165]

In this chapter, we report a simple galvanic displacement method to generate PtRuNTs and PtRu/CuNWs as efficient MOR catalysts. CuNWs were used as template and were synthesized by reduction of copper nitrate with hydrazine and ethylenediamine.[166] PtRuNTs and PtRu/CuNWs were prepared by complete and partial galvanic displacing Cu with Pt and Ru, respectively. By varying the Pt and Ru precursor ratio, PtRuNTs and PtRu/CuNWs with different Pt/Ru ratios were obtained. PtRuNTs and PtRu/CuNWs showed higher MOR activities than the benchmark commercial PtRu/C catalyst (Johnson Matthey Hispec 12100, 50 wt. % Pt, 25 wt. % Ru on high surface area advanced carbon support).

## **6.2 Materials and Methods**

### **6.2.1 Preparation of CuNWs, PtRuNTs and PtRu/CuNWs**

#### **6.2.1.1 Synthesis of CuNWs**

CuNWs were synthesized by reduction of copper nitrate trihydrate ( $\text{Cu}(\text{NO}_3)_2 \cdot 3\text{H}_2\text{O}$ , Sigma-Aldrich) with hydrazine ( $\text{N}_2\text{H}_4$ , 35 wt. % solution in water, Aldrich) in an aqueous sodium hydroxide ( $\text{NaOH}$ , Fisher Chemical) solution in the presence of ethylenediamine (EDA,  $\geq 99.5\%$ , Fluka). In a typical CuNW synthesis, 200 mg  $\text{Cu}(\text{NO}_3)_2$  in 10 mL DI  $\text{H}_2\text{O}$  was added to 200 mL 10 M  $\text{NaOH}$  in a 500 mL glass bottle. EDA (1.5 mL) and  $\text{N}_2\text{H}_4$  (0.25 mL) were subsequently added to the solution. The glass bottle was capped after the addition of all the components and shaken vigorously to ensure well mixing. Then the bottle was heated in a 65 °C water bath for one hour. The product was collected by filtration and washed with DI water until the pH of filtrate reached seven. The filter cake was stored in a desiccator, dried overnight and collected for future use.

#### **6.2.1.2 Synthesis of PtRuNTs and PtRu/CuNWs**

PtRuNTs and PtRu/CuNWs were synthesized by complete and partial galvanic displacement of CuNWs. In a typical synthesis, CuNWs (20 mg) were dispersed in 400 mL water and added into a 1 L three neck round bottom flask with a stir bar inside. Various amounts of chloroplatinic acid ( $\text{H}_2\text{PtCl}_6 \cdot x\text{H}_2\text{O}$ , Aldrich) and ruthenium chloride ( $\text{RuCl}_3 \cdot x\text{H}_2\text{O}$ , Aldrich) in 100 mL water were prepared in a dropping funnel and added dropwise in a dropping rate of about 2 seconds per drop to the CuNWs suspension after flowing Ar for 15 min. The reaction continued for 1 hour at room temperature to ensure a complete reaction. After the synthesis, the products were collected by filtration and

washed with copious of DI water. The products were stored in a desiccator under vacuum, dried overnight and collected for characterization. All the PtRuNTs samples were annealed at 250 °C in a tube furnace for 2 hr in Ar while all the PtRu/CuNWs were not.

## **6.2.2 Characterization**

### **6.2.2.1 Electron Microscopy Characterization**

The morphology of synthesized CuNWs, PtRuNTs and PtRu/CuNWs were characterized by scanning electron microscopy (SEM, JSM-7400F) and transmission electron microscopy (TEM, JEM-2010F). TEM samples were prepared on a lacey carbon copper grid by adding a drop of sample water suspension on top. The compositional ratio was studied by electron dispersive X-ray spectroscopy (EDS) on SEM. The elemental mappings of PtRuNTs and PtRu/CuNWs were obtained by scanning transmission electron microscopy (STEM), specimens were prepared by sonicating the nanowires in methanol, then drop casting the solution onto lacey carbon-coated Au grids. Energy dispersive X-ray spectroscopy (EDS) spectrum imaging was performed in a Hitachi 3300 equipped with a 60 mm<sup>2</sup> Bruker X-flash detector, as well as secondary electron (SE) and high-angle annular dark-field (HAADF) detectors for image capture. Higher-resolution STEM images were recorded in an aberration-corrected JEOL 2200FS.

### **6.2.2.2 X-ray Diffraction and X-ray Photoelectron Spectroscopy**

X-ray diffraction (XRD) patterns were recorded on a Philips X'Pert X-ray diffractometer using Cu K<sub>α</sub> radiation. X-ray photoelectron spectroscopy (XPS) measurements were performed using a Physical Electronics 5600 series XPS system

equipped with a multi-channel hemispherical analyzer and Mg anode X-ray source. The binding energy scale was calibrated by comparing the primary photoelectron peaks of Au, Ag, and Cu reference foils to values published in literature. Sample charging was corrected by setting the binding energy of the C1s peak to 284.8 eV.

### 6.2.2.3 Electrochemical Measurements

The electrochemical measurements were conducted using a three-electrode cell configuration, with silver/silver chloride electrode (Ag/AgCl) as the reference electrode, Pt wire as the counter electrode and 5 mm diameter glassy carbon (PINE instruments) as working electrode on a multichannel potentiostat (Princeton Applied Research). All the potentials used in this work were referred to that of the reversible hydrogen electrode (RHE).

The thin-film electrodes were prepared by pipetting 20  $\mu\text{L}$  catalyst ink (catalyst ultrasonically dispersed in water) onto glassy carbon electrodes which had been pre-polished to mirror finish. The final precious metal loading for PtRuNTs is 100  $\mu\text{g}_{\text{PtRu}}/\text{cm}^2_{\text{disk}}$ , and that for PtRu/CuNWs about 25 – 30  $\mu\text{g}_{\text{PtRu}}/\text{cm}^2_{\text{disk}}$ . Cyclic voltammetry experiments were performed in 0.1 M  $\text{HClO}_4$  solution with 1 M  $\text{CH}_3\text{OH}$  at a scanning rate of 5 mV/s in an Ar atmosphere. A small scanning rate of 5 mV/s was used in order to minimize the contribution of current from cyclic voltammetry without methanol as well as to give the system enough time to achieve steady state during the sweeping of potential. The cyclic voltammograms (CVs) were recorded in the potential region of 0.02 to 0.9 V vs. RHE.

CO-stripping was used to determine the surface areas as well as the CO tolerance properties of Pt and PtRu catalysts. In a CO-stripping test, the electrode potential was held at 0.1V vs. RHE for 10 min for a fully adsorption of CO on the catalyst surface

followed by flowing Ar for another 10 min to remove the CO in the electrolyte. The first positive scan shows the stripping of a monolayer of CO while a second scan will be used to judge whether the adsorbed CO has been completely oxidized in the first scan. The oxidation charge of CO stripping ( $Q_{CO}$ ) was calculated by integrating the area under CO stripping curve with subtraction of CV curve in the second scan, and the electrochemical surface areas (ECSAs) were calculated using Eq.6.1. The oxidation charge for removing one monolayer of CO was assumed to be  $420 \mu\text{C}/\text{cm}^2$  on PtRu surfaces.

$$ECSA = \frac{Q_{CO}}{420 \mu\text{C}/\text{cm}^2} \quad (6.1)$$

### 6.3 Results and Discussion

#### 6.3.1 Electron Microscopy and Elemental Characterization of Synthesized Catalysts

CuNWs with diameters in the range of 80 – 110 nm and lengths in the range of 20 - 40  $\mu\text{m}$  were synthesized (see SEM image in Figure 6.1a and TEM image in Figure 6.1b) and used as template to generate PtRuNTs and PtRu/CuNWs.

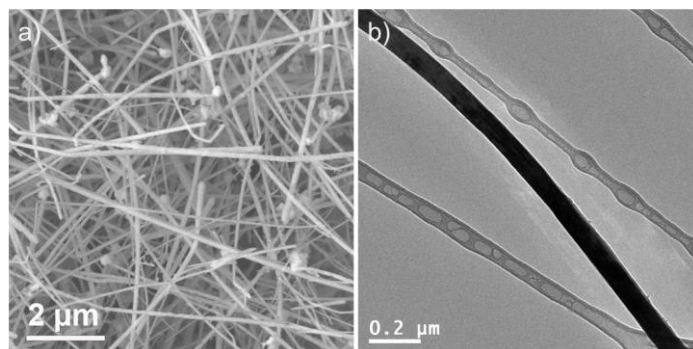


Figure 6.1 (a) Scanning electron microscopy (SEM) image and (b) transmission microscopy image of CuNWs.

### 6.3.1.1 PtRu Nanotubes (PtRuNTs)

PtRuNTs were synthesized via complete galvanic displacement reaction using CuNWs as template. By varying the amount of Pt and Ru precursors, PtRuNTs with Pt/Ru atomic ratio of 1, 3, 6 and 9 were obtained, denoted as PtRu(1-1)NTs, PtRu(3-1)NTs, PtRu(6-1)NTs and PtRu(9-1)NTs, respectively. (The number in the parentheses indicates the bulk Pt/Ru atomic ratio.) PtRuNTs with different Pt/Ru atomic ratios show similar 1D tubular structure with length in the range of 6 – 10  $\mu\text{m}$  due to cracking during the galvanic displacement reaction, as shown in their SEM images (Figure 6.2a, c, e, g). The elemental compositions of all the PtRuNTs samples were measured by energy dispersive X-ray spectroscopy (EDX) (Figure 6.2b, d, f, h), and the results were listed in Table 6.1, where we observed a residual copper content of about 5 – 9 wt% for all PtRuNTs samples. In addition, the bulk Pt/Ru atomic ratio determined from EDX agrees well with that in the Pt and Ru precursors, which indicates a complete reduction of both Pt and Ru by Cu.

The TEM images of a PtRu(6-1)NT in the side view (Figure 6.3a-c) and cross-sectional view (Figure 6.3d) show clear hollow tube structures caused by the so-called “Kirkendall Effect”.[167,168] The diameter of PtRuNTs is about 80 – 120 nm and the nanotube wall thickness is about 30 nm. The nanotube is composed with small metallic PtRu nanoparticle grains as revealed by the HRTEM images taken at the surface the nanotube (Figure 6.3e and f). Amorphous  $\text{RuO}_x$  were also observed occasionally on the nanotube surfaces (TEM images in Figure 6.3c, d and HRTEM image in Figure 6.3e) probably due to the oxidation of surface Ru.

The high angle angular dark-field scanning transmission electron microscopy (HAADF-STEM) images of a typical PtRu(6-1)NT and the corresponding elemental spectrum images in side view and cross-sectional view are shown in Figure 6.4a-d and

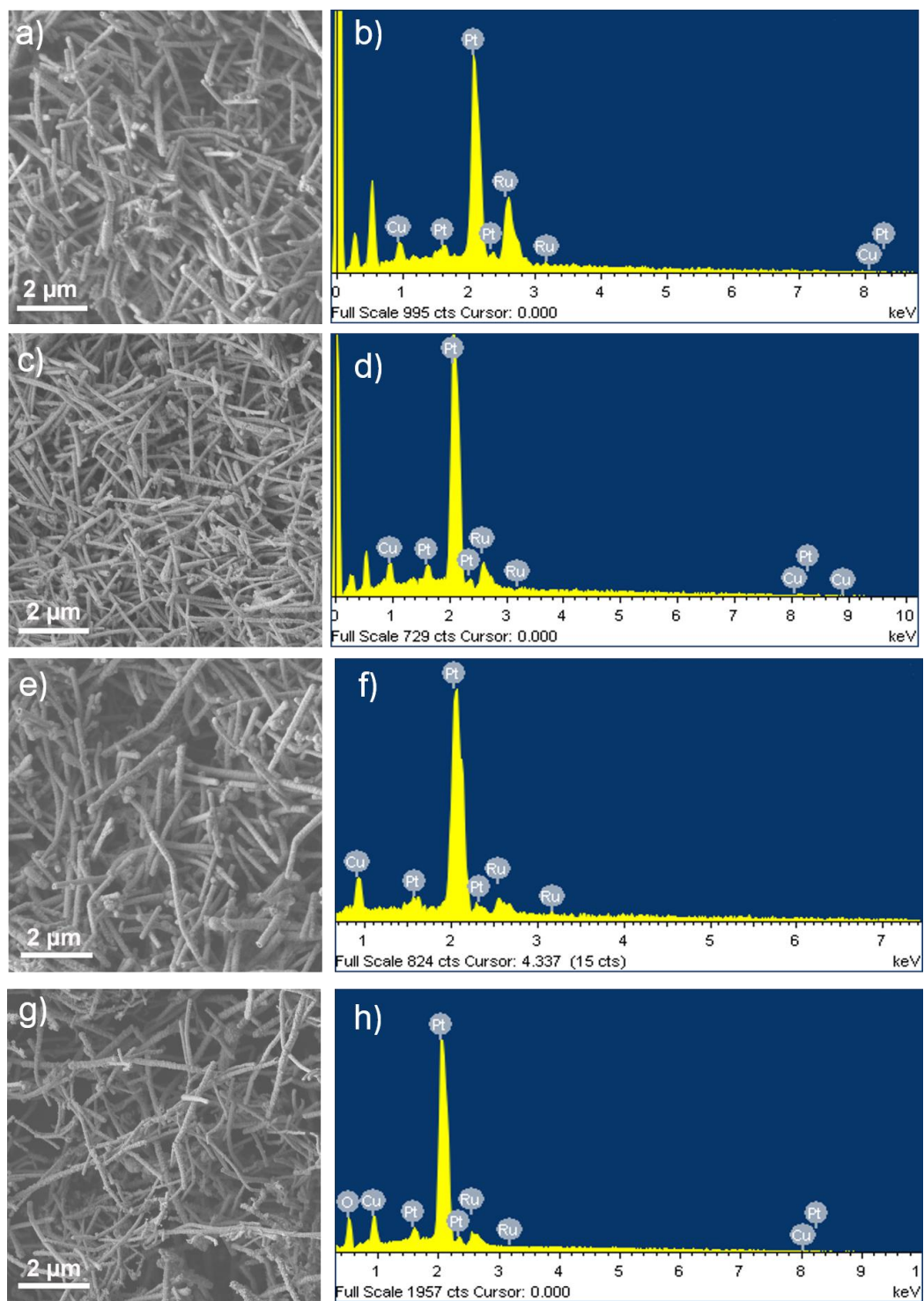


Figure 6.2 SEM images and corresponding EDX spectra of (a,b) PtRu(1-1)NTs, (c,d) PtRu(3-1)NTs, (e,f) PtRu(6-1)NTs and (g, h) PtRu(9-1)NTs.

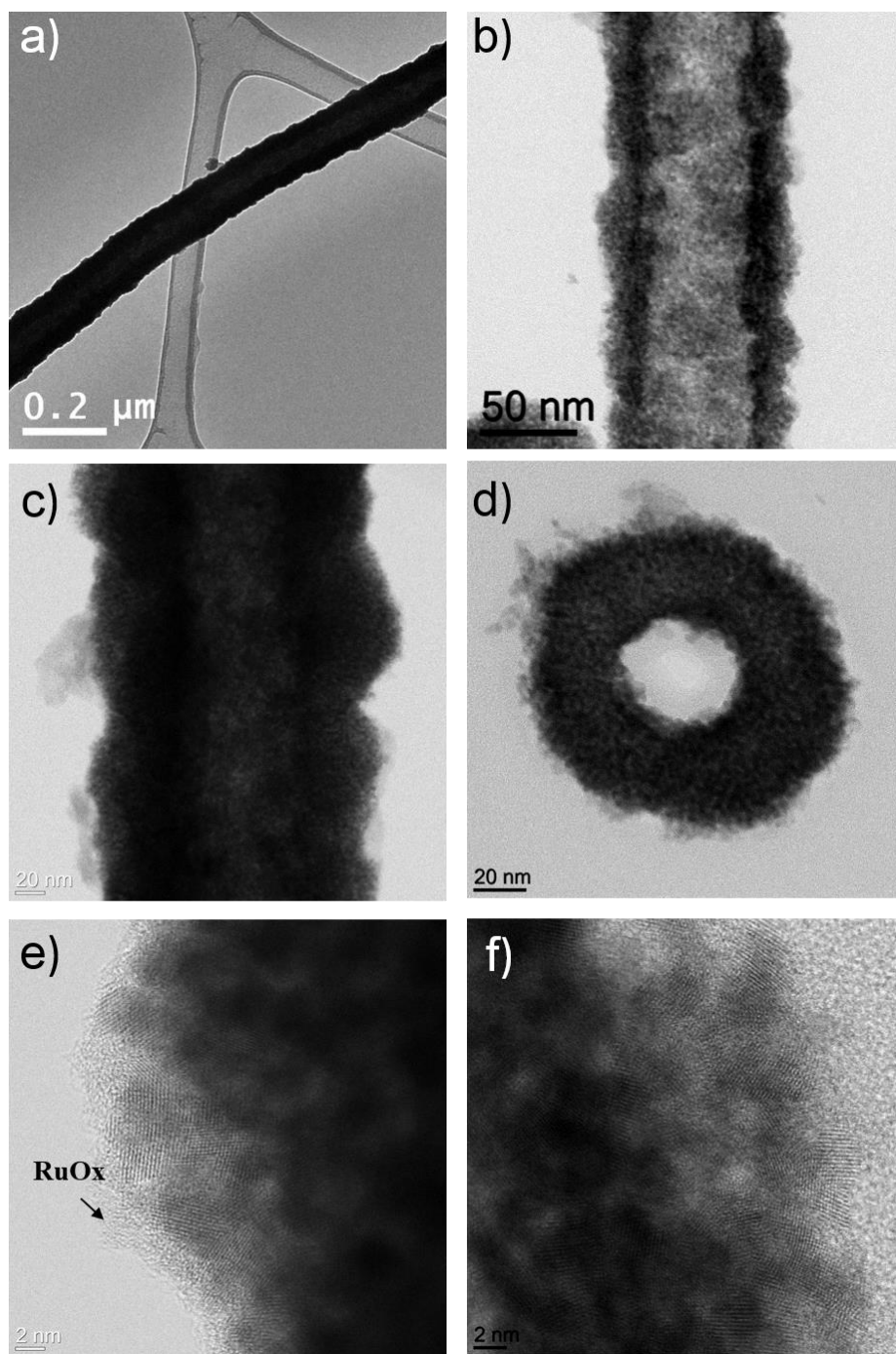


Figure 6.3 (a, b, c) TEM images of a PtRu(6-1)NT in size view with different magnifications. (d) TEM image of a PtRu(6-1)NT in a cross-sectional view. HRTEM image of a PtRu(6-1)NT surface from (e) side view and (f) cross-sectional view.

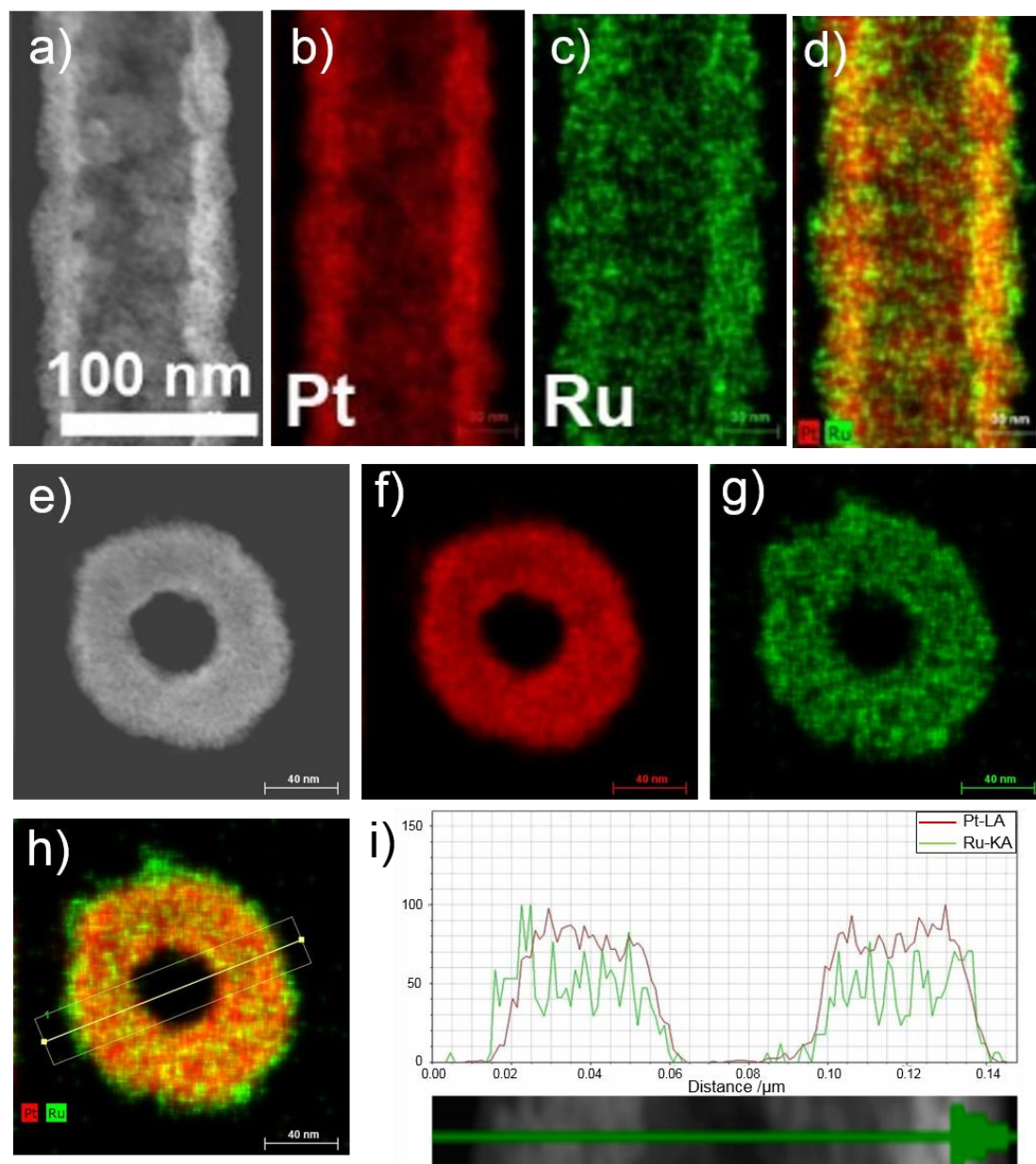


Figure 6.4 HAADF-STEM image (a, e) and corresponding elemental Pt (b,f), Ru (c, g), overlapping of Pt and Ru (d, h) spectrum images of a PtRu(6-1)NTs in side and cross-sectional view, (i) line scan along the direction shown in (h) of Pt(red) and Ru(green).

6.4e-h, respectively. A hollow structure of the PtRu(6-1)NT can be obviously seen, with Pt (shown as red in Figure 6.3b and f) and Ru (shown as green in Figure 6.3 c and g) being homogeneously distributed inside the tube and a rich in Ru on the nanotube surface revealed by the thin green layer on the surface when the signals from Pt and Ru are overlaid (Figure 6.3d and h). The line scan along the tube also clearly demonstrates the existence of a hollow structure in a PtRu(6-1)NT as well as the homogeneous distribution of Pt and Ru in the tube (Figure 6.4i).

### **6.3.1.2 PtRu Coated Copper Nanowires (PtRu/CuNWs)**

PtRu/CuNWs were prepared by partial galvanic displacement reaction by only displacing the surface portion of the CuNWs. PtRu/CuNWs with different Pt/Ru atomic ratios were obtained by varying the amount of Pt and Ru precursors from 1 to 9, and the synthesized samples were denoted as PtRu(1-1)/CuNWs, PtRu(3-1)/CuNWs, PtRu(4-1)/CuNWs, PtRu(6-1)/CuNWs and PtRu(9-1)/CuNWs, respectively. The SEM images and corresponding EDX spectra of all the PtRu/CuNWs samples are shown in Figure 6.5, from which we observed the remaining of the 1D nanowire structure in PtRu/CuNWs as well as the elemental compositions which were also listed in Table 6.1. Similar to PtRuNTs, the Pt/Ru atomic ratios determined from EDX are similar to those in the precursors, indicating a complete reduction of both Pt and Ru during the reaction. The PtRu/CuNWs samples had a copper content of about 70 – 75 wt% (Table 6.1). The weight percentages of the precious metals (Pt and Ru) in PtRu/CuNWs were about 25 – 30 wt%, which are about 1/3 of those in PtRuNTs samples (around 90 wt%) (Table 6.1). Therefore, the shell thickness of PtRu/CuNWs can be roughly estimated to be about 10 nm, assuming the thickness is also 1/3 of that of PtRuNTs (about 30 nm).

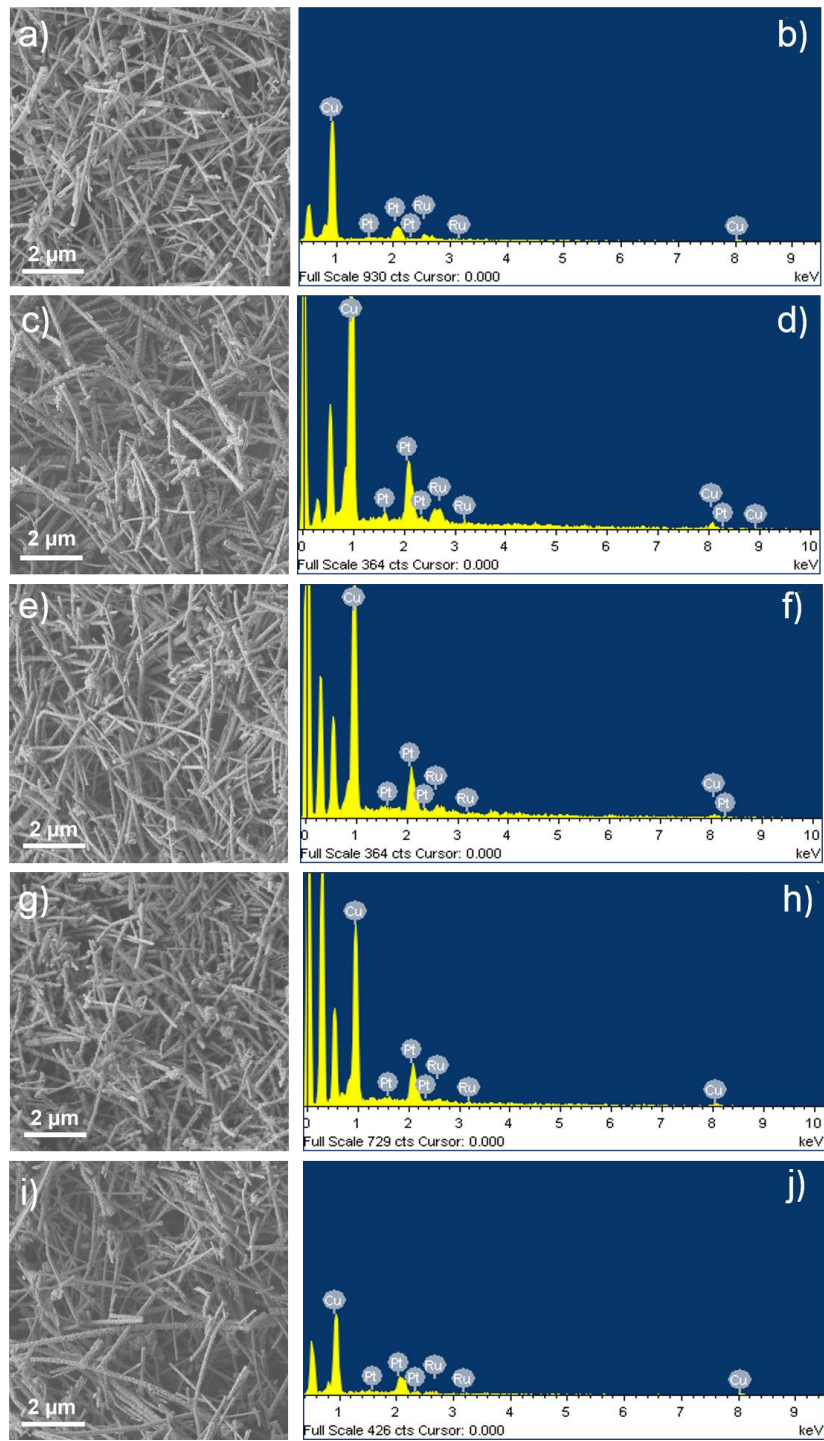


Figure 6.5 SEM images and EDX spectra of (a) PtRu(1-1)/CuNWs, (b) PtRu(3-1)/CuNWs, (c) PtRu(4-1)/CuNWs, (d) PtRu(6-1)/CuNWs and (e) PtRu(9-1)/CuNWs.

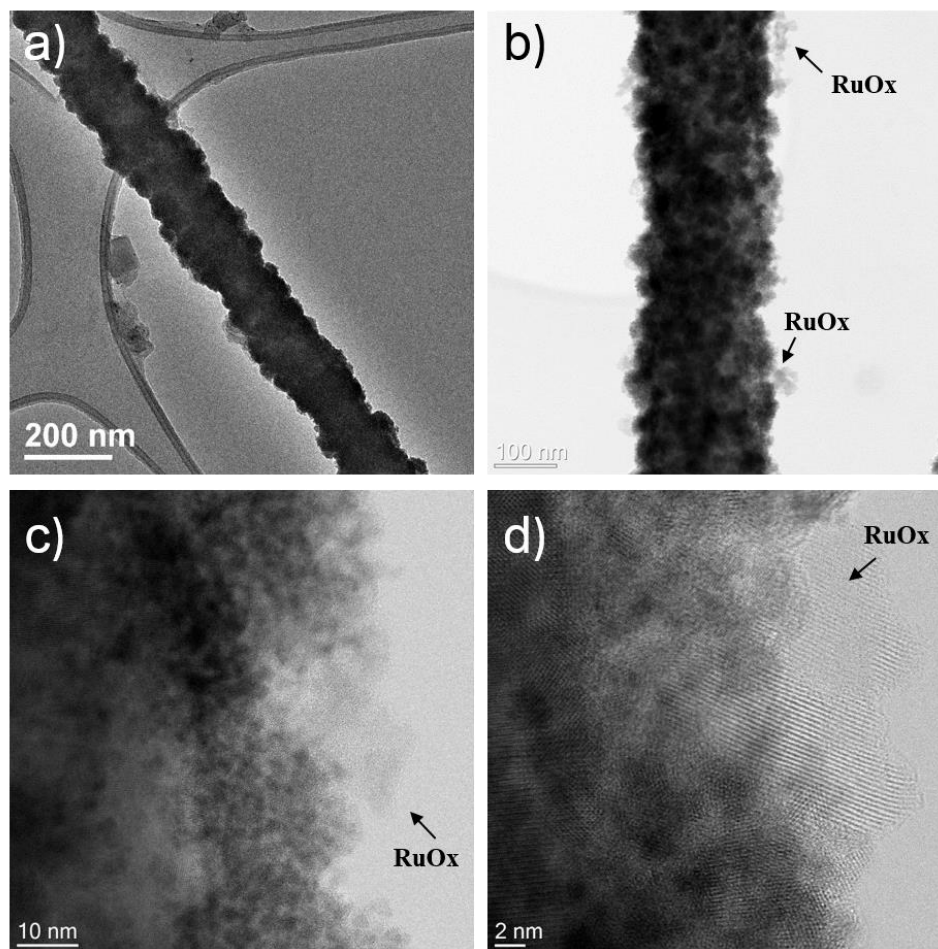


Figure 6.6 (a, b) TEM images of a PtRu(4-1)/CuNW, (c) TEM image of a PtRu(4-1)/CuNW surface, (d) HRTEM image of a PtRu(4-1)/CuNW.

The TEM images of a PtRu(4-1)/CuNWs show 1D nanowire structure with roughened surfaces (Figure 6.6a and b). The PtRu/CuNW surface is consisted of small nanoparticles, as revealed by the TEM and HRTEM images (Figure 6.6c and d). Similar to PtRuNTs, amorphous RuO<sub>x</sub> was also observed occasionally on the surface of the PtRu/CuNWs, probably due to the oxidation of surface Ru (Figure 6.6b, c and d).

The HAADF-STEM image of a PtRu(4-1)/CuNWs (Figure 6.7a) and the corresponding elemental spectrum images for Pt, Ru and Cu as well as the overlaid image for the three elements (Figure 6.7b-e) confirms that PtRu/CuNWs have a Cu-rich core, PtRu-rich shell structure, which can also be verified by elemental profiles of Pt, Ru and Cu in the line scan along the diameter of the PtRu(4-1)/CuNWs (Figure 6.7f).

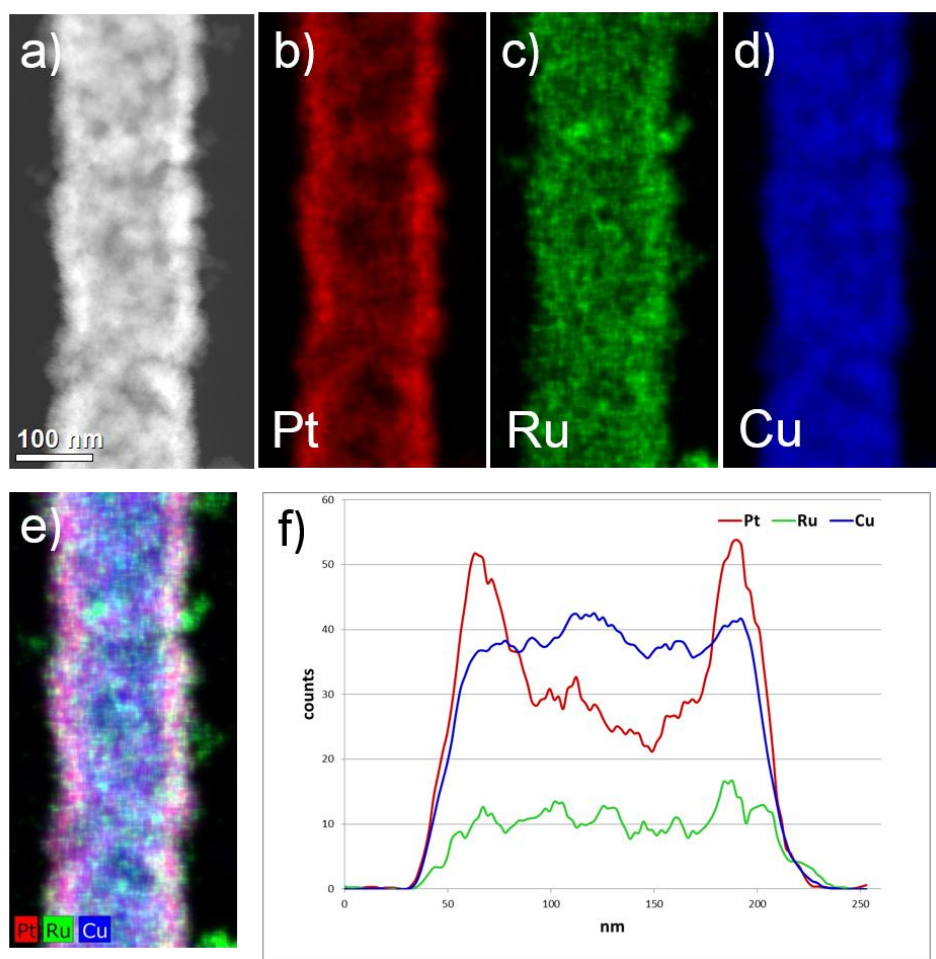


Figure 6.7 HAADF-STEM image (a) of a PtRu/(4-1)CuNW and the corresponding elemental Pt (b), Ru (c), Cu (d) and overlapping of Pt, Ru and Cu (e) spectrum images in side view. (f) Line scan along the diameter direction of a PtRu(4-1)/CuNW in (e).

Table 6.1 Elemental composition of PtRuNTs, PtRu/CuNWs by EDX or XPS

	Weight %			Atomic % (EDX)			Atomic % (XPS)			Pt:Ru at. ratio	
	Pt	Ru	Cu	Pt	Ru	Cu	Pt	Ru	Cu	EDX	XPS
PtRu(1-1)NTs	68	27	5	50	38	12	-	-	-	1.31	-
PtRu(3-1)NTs	79	13	9	60	19	21	-	-	-	3.26	-
PtRu(6-1)NTs	84	13	9	68	11	21	43	39	18	6.19	1.10
PtRu(9-1)NTs	87	5	8	72	8	20	-	-	-	8.58	-
PtRu(1-1)CuNWs	18	7	75	7	5	88	11	24	64	1.31	0.46
PtRu(3-1)CuNWs	24	4	72	9	3	87	10	13	77	3.01	0.77
PtRu(4-1)CuNWs	25	3	72	10	2	88	27	20	53	4.12	1.35
PtRu(6-1)CuNWs	23	2	75	9	2	89	21	11	68	5.65	1.91
PtRu(9-1)CuNWs	30	2	68	12	1	86	21	8	71	8.95	2.63
	Pt	Ru	C	Pt	Ru	C	Pt	Ru	C		
PtRu/C*	50	25	25	10	10	81	64	36	-	1.04	1.78

\* PtRu/C refers to HiSPEC® 12100 from Johnson Matthey, its elemental composition is from manufacturer data.

### 6.3.2 X-ray Spectroscopy Analysis

#### 6.3.2.1 X-ray Diffraction Pattern

The X-ray diffraction (XRD) patterns show that the CuNWs (Figure 6.8a) have a face-centered cubic (fcc) structure (SG: Fm-3m; JCPDS card no. 04-0836) and the PtRuNTs (Figure 6.8b) also possess a fcc structure with diffraction peaks of Pt(111), Pt(200) and Pt(220). The Pt peaks shift to higher  $2\theta$  angles than pure Pt, reflecting a lattice contraction due to the partial substitution of Pt by Ru to form a PtRu alloy. In the case of PtRu/CuNWs (Figure 6.8c), the three narrow Cu peaks at  $2\theta$  angles of  $43.4^\circ$ ,

50.4 ° and 74.1 ° are due to the presence of pure copper core. The broad peak at 42.3 ° is from PtRuCu alloys formed on the surface. The formation of surface alloy during galvanic displacement reaction was also reported in literature to be essential for maintaining the original template structures.[169] The two peaks at 36.4 ° and 61.4 ° can be attributed to Cu<sub>2</sub>O(111) and Cu<sub>2</sub>O(220) largely due to the oxidation of surface copper during sample handling and storage. Upon increasing the amount of Pt and Ru precursors, as in the case of PtRuNTs, the Cu<sub>2</sub>O peaks disappeared. This phenomenon was also observed in the synthesis of CuPd and CuPt nanotubes using galvanic displacement reaction.[161] The XRD patterns of PtRuNTs and PtRu/CuNWs with other Pt/Ru ratios were very similar to the ones shown here.

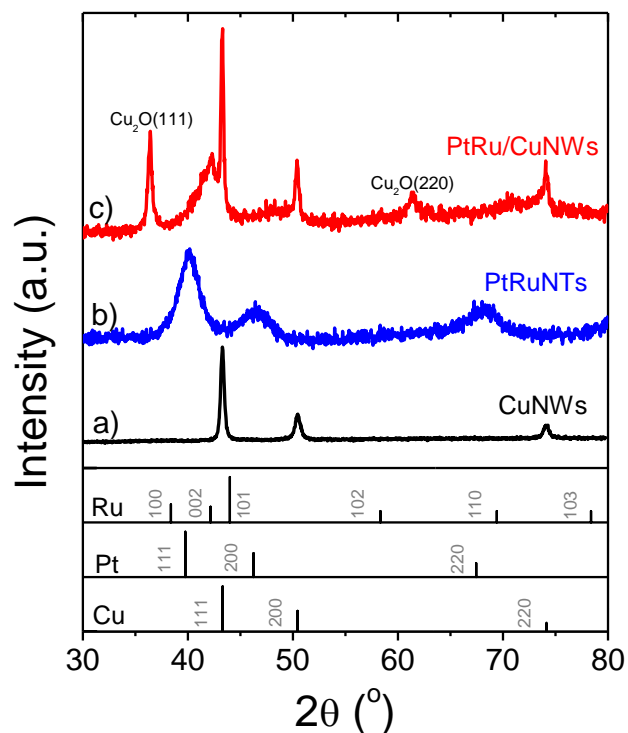


Figure 6.8 X-ray diffraction (XRD) patterns of (a) CuNWs, (b) PtRu(6-1)NTs and (c) PtRu(4-1)/CuNWs.

### 6.3.2.2 X-ray Photoelectron Spectroscopy

X-ray photoemission spectroscopy (XPS) was used to determine the surface compositions as well as the electronic states of PtRuNTs, PtRu/CuNWs and PtRu/C. The surface compositions of Pt, Ru and Cu measured from XPS are listed in Table 6.1. Smaller PtRu surface atomic ratio was obtained than PtRu bulk atomic ratio on PtRu(6-1)NTs and all PtRu/CuNWs, indicating the surface enrichment of Ru during galvanic displacement reaction. Since  $\text{PtCl}_6^{2-}$  has a higher redox potential (0.742 V) than  $\text{Ru}^{3+}$  (0.616 V), the larger driving force between Pt and Cu will lead to a more preferential displacement of Cu with Pt. Therefore, CuNWs will be displaced by Pt and Ru in a PtRu ratio higher than the stoichiometric PtRu ratio in the precursor initially and lower than the stoichiometric value in the final stage, resulting in a higher Ru content in the surface. The enrichment of Ru on the surface can also be validated from the elemental mapping of Ru in PtRu(6-1)NTs (Figure 6.4 d,h) and PtRu(4-1)/CuNWs (Figure 6.7e).

Figure 6.9 represents the Pt 4f XPS spectra for PtRu/C, PtRu(6-1)NTs, PtRu(1-1)/CuNWs, PtRu(3-1)/CuNWs, PtRu(4-1)/CuNWs, PtRu(6-1)/CuNWs and PtRu(9-1)/CuNWs. The Pt 4f spectra forms doublet peaks Pt 4f<sub>7/2</sub> and Pt 4f<sub>5/2</sub> due to spin orbit coupling, and the intensity ratio between 7/2 and 5/2 peaks are 4:3. All PtRu samples have Pt 4f peaks at binding energy (BE) values of about 71 eV and 74 eV assigned to Pt(0) species and peaks with BE values of 73 eV and 76 eV attributed to Pt(II) species (Figure 6.9). For PtRu/CuNWs, there exist Cu 3p<sub>3/2</sub> and Cu 3p<sub>1/2</sub> peaks in the Pt 4f region, causing the broadening of the peak at BE of about 74 eV (Figure 6.9c-g).

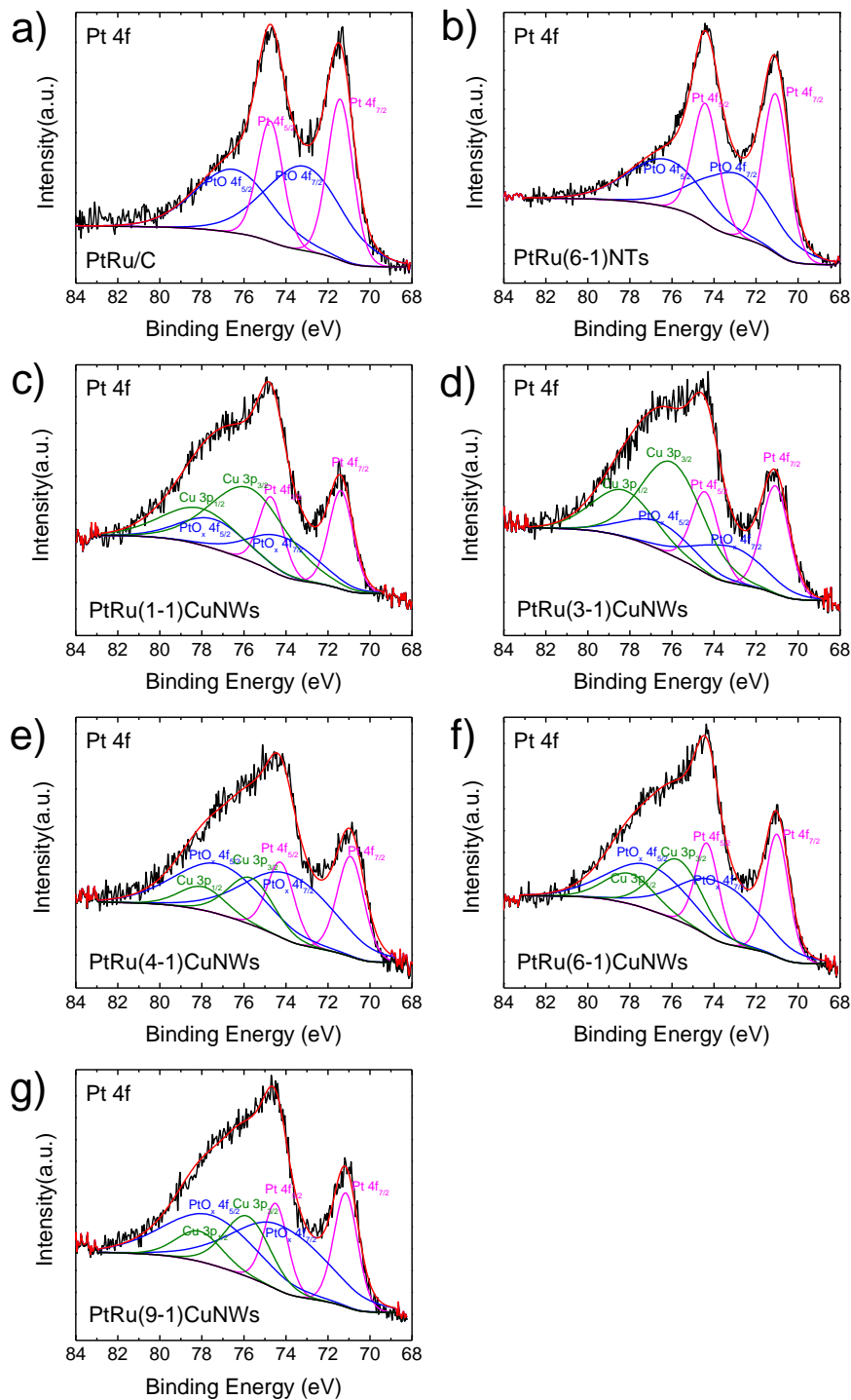


Figure 6.9 XPS of Pt 4f of (a) PtRu(6-1)NTs, (b) PtRu/C, (c) PtRu(1-1)/CuNWs, (d) PtRu(3-1)/CuNWs, (e) PtRu(4-1)/CuNWs, (f) PtRu(6-1)/CuNWs and (g) PtRu(9-1)/CuNWs.

### 6.3.3 Cyclic Voltammograms and CO-Stripping of PtRuNTs and PtRu/CuNWs

The cyclic voltammograms (CVs) of PtRuNTs and PtRu/CuNWs with different Pt/Ru atomic ratios (Figure 6.10a and c) were recorded in the potential range of 0.02 – 0.9 V vs. RHE after about 20 cycles until a stable CV was obtained at a scanning rate of 50 mV/s, with the  $H_{\text{upd}}$  adsorption and desorption peaks showing up in the potential regions of 0 to 0.35 V. The upper potential was chosen to be 0.9 V in order to prevent Ru dissolution.[170] The large capacitive current in the “double-layer region” in the potential range of 0.3-0.7 V vs. RHE is due to the presence of Ru. PtRuNTs showed a similar CV curve as that of PtRu/C while PtRu/CuNWs exhibited a higher peak at about 0.7 V (Figure 6.10e). This peak is suspected to be resulted from the existence of remnant copper on the surface.

Since Ru oxidation occurs at about 0.25 V vs. NHE which overlaps with the hydrogen oxidation region (0 – 0.3 V),[171] it is not suitable to use hydrogen adsorption and desorption peaks to determine the electrochemical active surface area (ECSA) of a PtRu sample. Hence, CO stripping voltammetry[172] is adopted to obtain the ECSA of all PtRu samples in this work. Figure 6.10b and d show the CO-stripping profiles of PtRuNTs and PtRu/CuNWs with different Pt/Ru atomic ratio, where the Pt/Ru composition dependent CO-stripping peak potentials are observed. The ECSAs determined from CO stripping of PtRu(4-1)/CuNWs, PtRu(6-1)NTs and PtRu/C (Figure 6.10f) are  $29.0 \pm 2.4 \text{ m}^2/\text{g}_{\text{PtRu}}$ ,  $9.4 \pm 0.9 \text{ m}^2/\text{g}_{\text{PtRu}}$  and  $73.6 \pm 5.1 \text{ m}^2/\text{g}_{\text{PtRu}}$ , respectively. PtRu(4-1)/CuNWs have an ECSA about three times that of PtRu(6-1)NTs. CO stripping voltammograms also reveal the relative anti-CO poisoning properties of PtRu/CuNWs, PtRuNTs and PtRu/C. Although PtRu(4-1)/CuNWs have a CO stripping peak potential at about 0.56 V, which is higher than those of PtRu(6-1)NTs (0.54 V) and PtRu/C (0.54 V), PtRu(4-1)/CuNWs exhibit a lower onset potential (0.28 V) for CO monolayer

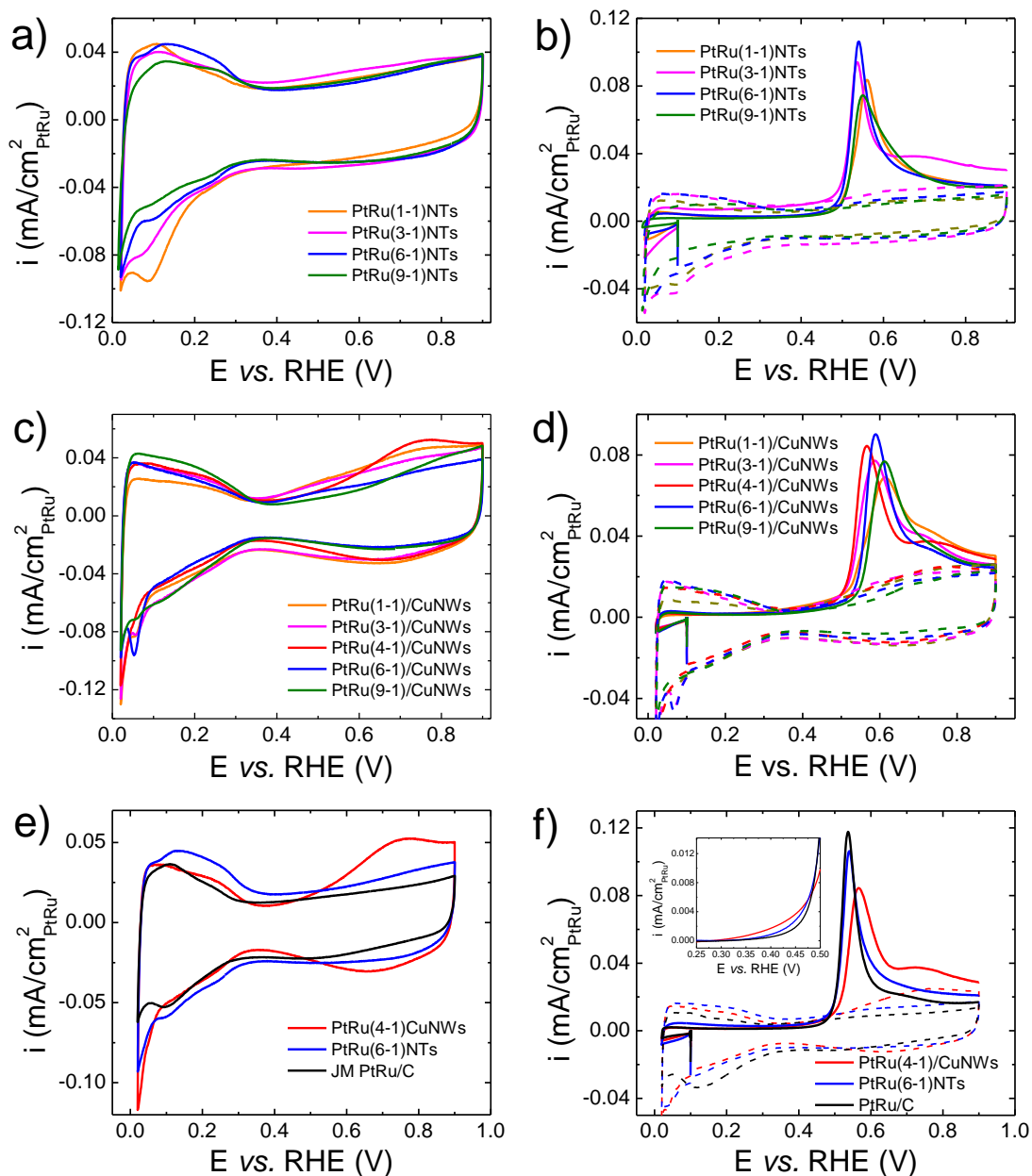


Figure 6.10 Cyclic voltammograms of (a) PtRuNTs and (c) PtRu/CuNWs with various PtRu ratios tested in Ar-saturated 0.1 M HClO<sub>4</sub> at a scanning rate of 50 mV/s. CO stripping curves (Solid curves) and cyclic voltammograms directly after CO stripping (dash curves) of (b) PtRuNTs and (d) PtRu/CuNWs with various PtRu ratios. Comparison of (d) cyclic voltammograms and (e) CO-stripping curves of PtRu(4-1)/CuNWs, PtRu(6-1)NTs and PtRu/C. Inset of (e): zoom in of CO stripping curves in 0.25 - 0.5 V vs. RHE.

oxidation than PtRu(6-1)NTs (0.30 V) and PtRu/C (0.32 V). (The onset potentials are determined at the potential when the specific current is  $0.03 \mu\text{A}/\text{cm}^2_{\text{PtRu}}$ .) The higher CO stripping peak potential of PtRu/CuNWs might be caused by the presence of surface copper. When we compare the CO stripping peak potential of Pt/CuNWs and PtNTs (Figure 6.15d), Pt/CuNWs showed a higher peak potential than PtNTs.

### **6.3.4 Performance of PtRuNTs and PtRu/CuNWs Towards Methanol Oxidation Reaction**

#### **6.3.4.1 Activity of Methanol Oxidation Reaction of PtRuNTs and PtRu/CuNWs**

The performance of PtRuNTs and PtRu/CuNWs with different Pt/Ru atomic ratios towards MOR were evaluated from their CVs recorded in 0.1 M HClO<sub>4</sub> with 1 M CH<sub>3</sub>OH, and compared with that of the benchmark MOR catalyst PtRu/C (Figure 6.11a-d). The PtRu compositional effect was clearly observed on PtRu/CuNWs and PtRuNTs. The specific MOR activities at 0.5 V and 0.6 V vs. RHE of PtRuNTs and PtRu/CuNWs with various Pt/Ru ratios were obtained from their cyclic voltammograms (Figure 6.11a and c) and were plotted as a function of PtRu atomic ratio measured from EDX (Figure 6.11e and f). Similar trends were obtained on both PtRuNTs and PtRu/CuNWs: a PtRu atomic ratio of about 4 gave the highest specific activity. In particular, if we compare the activity of PtRu(6-1)NTs, PtRu(4-1)/CuNWs (which are the performers of PtRuNTs and PtRu/CuNWs) and PtRu/C, PtRu(6-1)NTs have a peak MOR specific current density ( $0.5 \text{ mA}/\text{cm}^2_{\text{PtRu}}$ ) 1.7 times that of PtRu/C ( $0.29 \text{ mA}/\text{cm}^2_{\text{PtRu}}$ ) while PtRu(4-1)/CuNWs exhibit much higher specific activity: its peak current density ( $1.6 \text{ mA}/\text{cm}^2_{\text{PtRu}}$ ) is 3.2 times that of PtRu(6-1)NTs and 5.5 times that of PtRu/C (Figure 6.11a and c). PtRuNTs show much smaller mass activity than PtRu/C (Figure 6.11b),

attributed to their small ECSAs. Owing to enhanced specific activity and increased ECSA, PtRu(4-1)/CuNWs show a mass activity comparable to PtRu/C in the potential region of 0.4 – 0.6 V, and 2.5 times that of PtRu/C at peak potential (Figure 6.11d).

While the optimum PtRu atomic ratio range from 1 to 3 in bulk composition has been reported,[152,173-178] the work from Gasteiger et al. showed that PtRu alloys with a surface composition of 10 at. % Ru has the highest activity.[170]The discrepancy in the optimal PtRu ratio may be attributed to the difference between the surface PtRu composition and the bulk composition, as well as the difference in preparation methods of each catalyst. The optimal surface PtRu atomic ratios of PtRuNTs and PtRu/CuNWs, which are around 1.10 and 1.35 (determined by XPS and listed in Table 6.1), are quite different from that reported by Gasteiger et al. which is 9.[170] Since adsorption of methanol on Pt require three adjacent Pt sites, according to a model based on bifunctional mechanism, a surface structure having one Ru atom neighboring three Pt sites represents optimum geometry, and it was calculated that 10 at. % Ru maximizes this configuration, supporting Gasteiger's report. However, this model fails to capture the electronic effect on Pt induced by Ru. The presence of Cu in PtRuNTs and PtRu/CuNWs might also alter the optimum PtRu ratio due to the electronic effect to Pt induced by Cu. Additionally, the preparation methods of the catalysts will influence the optimum PtRu atomic ratio, considering different preparation methods could lead to catalysts with various degrees of alloying, morphologies etc. Watanabe et al. reported an optimal surface PtRu atomic ratio of 1 for PtRu alloy and Ru decorated Pt disk,[152] which is similar to that in our case.

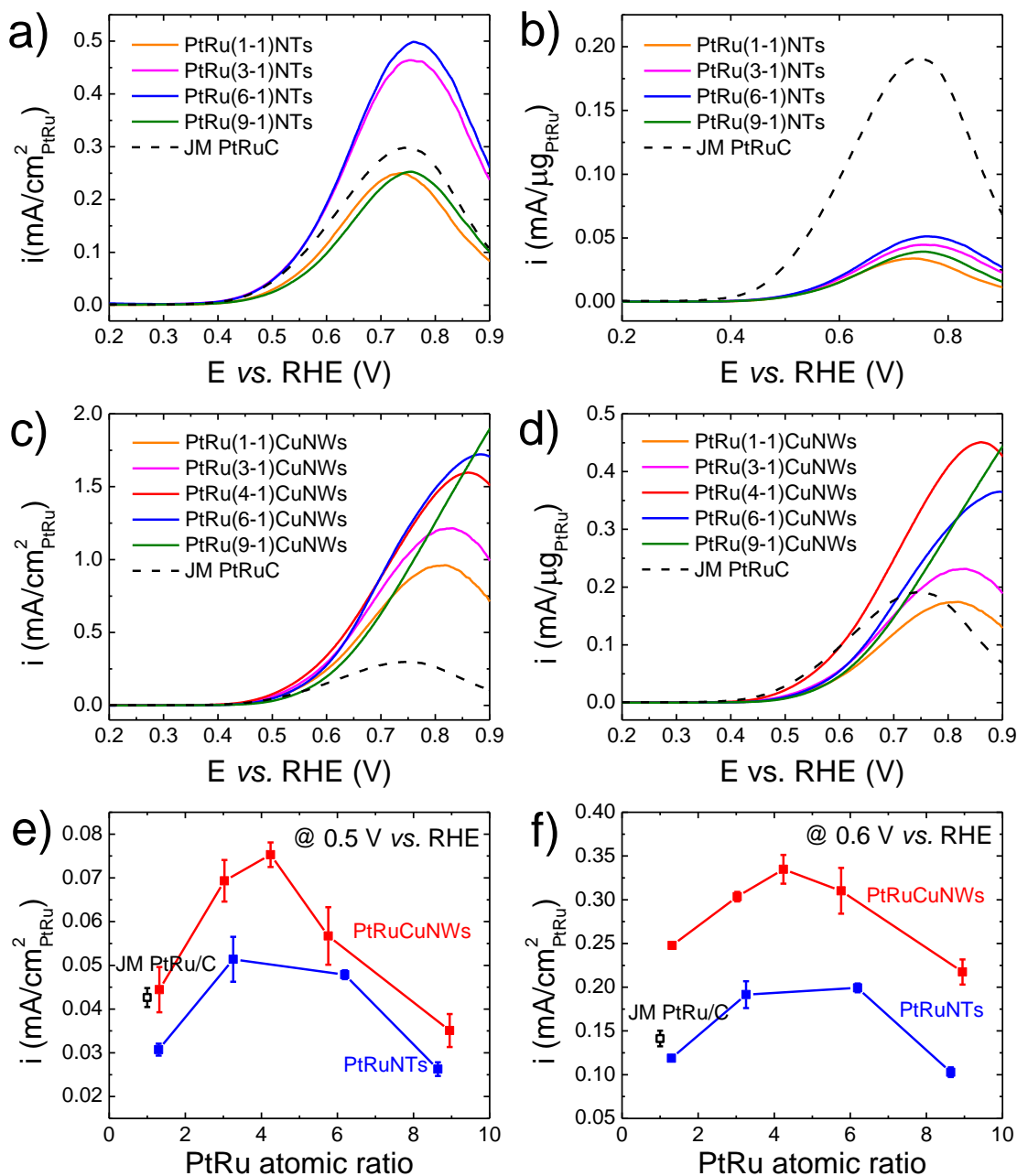


Figure 6.11 Cyclic voltammogram (forward scan) of PtRuNTs and PtRu/CuNWs with various PtRu ratios and PtRu/C in terms of (a, c) specific activity and (b, d) mass activity in Ar-saturated 0.1 M  $\text{HClO}_4$  with 1 M  $\text{CH}_3\text{OH}$  at a scanning rate of 5 mV/s. Plot of specific MOR activities at (e) 0.5 V vs. RHE and (f) 0.6 V vs. RHE as a function of PtRu atomic ratio on PtRu/CuNWs, PtRuNTs and PtRu/C. Error bars represents three independent measurements of each sample.

### 6.3.4.2 Durability of Methanol Oxidation Reaction on PtRuNTs and PtRu/CuNWs

Chronoamperometry curves of PtRu(6-1)NTs, PtRu(4-1)/CuNWs and PtRu/C were recorded at 0.6 V vs. RHE for 1800 s to evaluate the stability of the catalysts (Figure 6.12). The currents decayed rapidly initially due to the poisoning of the surface by strongly adsorbed intermediates. In the initial 200 s, PtRu(4-1)/CuNWs showed the lowest decaying rate, followed by PtRu(6-1)NTs and PtRu/C. Over longer period of time, a relatively higher current was observed on PtRu(6-1)NTs and PtRu(4-1)/CuNWs than PtRu/C, indicating their better stability. The stability of core Cu is important for the application of PtRu/CuNWs in fuel cells since dissolution of Cu is detrimental to the stability of proton exchange membrane, e.g. Nafion. Our previous study on a similar structure Pt coated CuNWs annealed at 250 °C (PtCu-250) showed minimal Cu dissolution after accelerated durability test via cycling between 0.6 to 1.1 V vs. RHE at 50 mV/s in 0.1 M HClO<sub>4</sub> for 30,000 cycles once the sample was pre-dealloyed,[179] indicating that the core Cu is well protected.

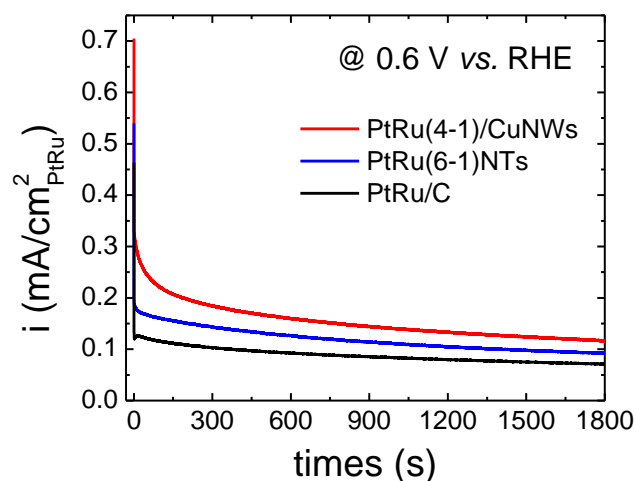


Figure 6.12 Chronoamperometry of PtRu(4-1)/CuNWs, PtRu(6-1)NTs and PtRu/C measured at 0.6 V vs. RHE for 1800 s.

### 6.3.4.3 Activation Energy of Methanol Oxidation Reaction on PtR/CuNWs and PtRu/C

The MOR activity increases with the increase of temperature, as revealed from the CVs of PtRu/CuNWs with different Pt/Ru atomic ratio and PtRu/C in 0.1 M HClO<sub>4</sub> with 1M CH<sub>3</sub>OH measured at various temperatures from 20 to 80 °C at a scanning rate of 5 mV/s (Figure 6.13). The apparent MOR activation energies ( $E_a$ ) at 0.5 V and 0.6 V vs. RHE on PtRu/CuNWs samples and PtRu/C were determined from their corresponding Arrhenius plots (Insets of Figure 6.13) and listed in Table 6.2., The obtained  $E_a$  values are potential-dependent with  $E_a$  at 0.6 V being smaller than that at 0.5 V for all the samples: the  $E_a$  values at 0.5 V are ranging from about 29 to 40 kJ/mol while those at 0.6 V are from 24 to 27 kJ/mol (Table 6.2). The apparent  $E_a$  values were found to be dependent on potential, the path taken to reach that potential, the nature of the electrolytes (e.g. pH and anion adsorption), resulted in a wide range of activation energies reported in literatures,[180] therefore, the  $E_a$  values can only be compared fairly at the same overpotential and with same test conditions. The similar activation energies on PtRu/CuNWs samples (although small variations were observed with PtRu compositions) and PtRu/C at either 0.5 or 0.6 V suggests that MOR on those samples probably follows the same reaction mechanism.

Table 6.2 Summary of MOR activation energies ( $E_a$ ) at 0.5 V and 0.6 V vs. RHE on PtRu/CuNWs with different Pt/Ru atomic ratio and PtRu/C

Samples	$E_a$ (0.5 V) (kJ/mol)	$E_a$ (0.6 V) (kJ/mol)
PtRu(1-1)/CuNWs	40.0	27.1
PtRu(3-1)/CuNWs	29.3	24.3
PtRu(4-1)/CuNWs	33.5	25.3
PtRu(6-1)/CuNWs	32.3	24.2
PtRu(9-1)/CuNWs	32.2	26.0
PtRu/C	33.9	26.4

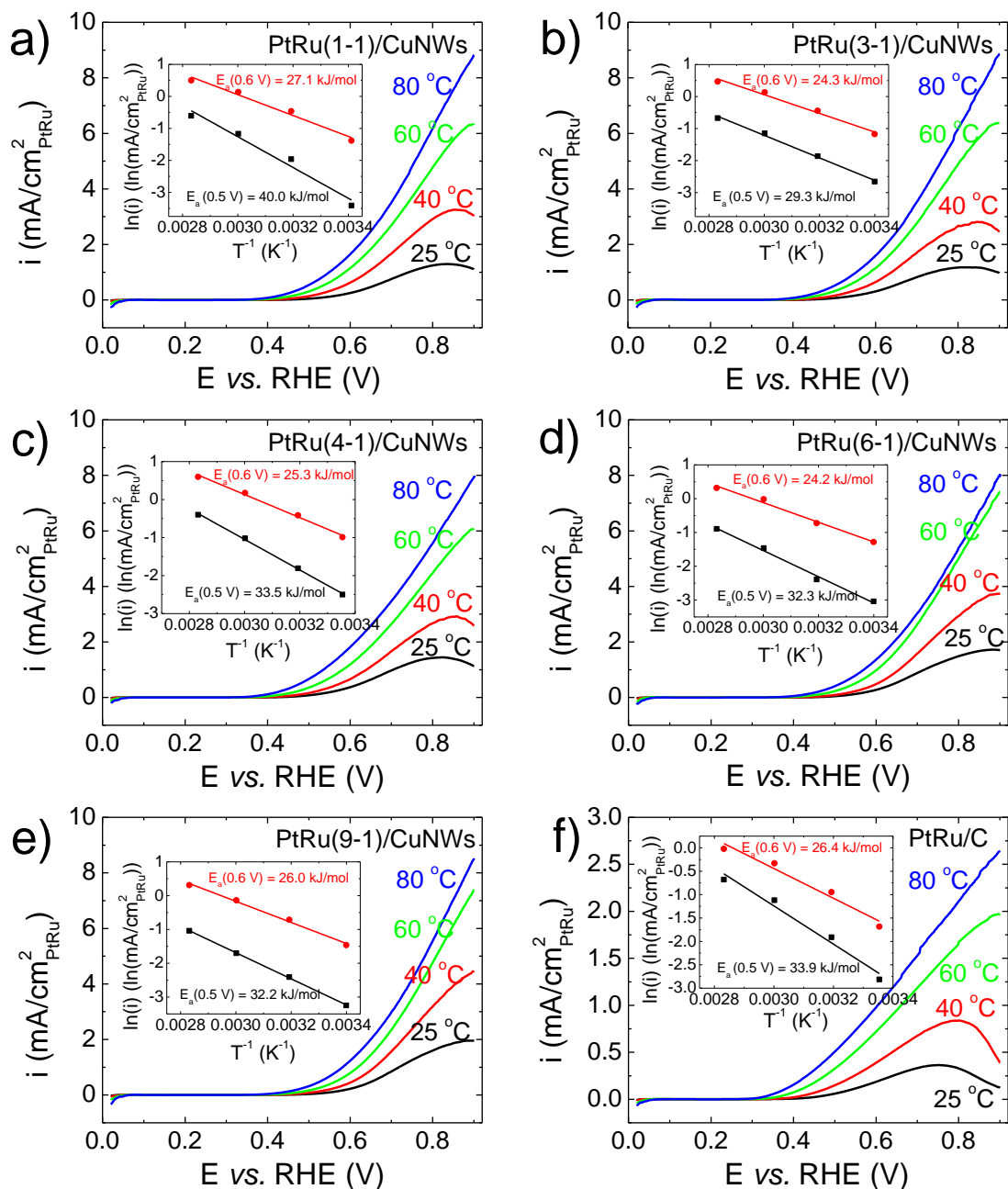


Figure 6.13 Cyclic voltammogram (forward scan) and Arrhenius plots of MOR activities at 0.5 and 0.6 V vs. RHE in the inset of (a) PtRu(1-1)/Cu NWs, (b) PtRu(3-1)/CuNWs, (c) PtRu(4-1)/CuNWs, (d) PtRu(6-1)/CuNWs, (e) PtRu(9-1)/CuNWs and (f)PtRu/C measured in Ar-saturated 0.1 M HClO<sub>4</sub> with 1 M CH<sub>3</sub>OH at a scanning rate of 5 mV/s

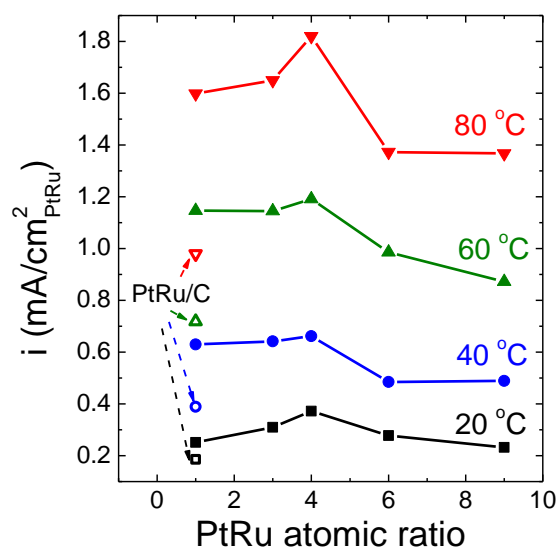


Figure 6.14 Plot of specific MOR activities at 0.6 V vs. RHE as a function of PtRu atomic ratio on PtRu/CuNW at 20 °C (black), 40 °C (blue), 60 °C (green) and 80 °C (red). Hollow dots represents MOR activity of PtRu/C for comparison.

Considering the similar activation energies on all the PtRu samples, the PtRu compositional effects on MOR activities of PtRu/CuNWs remains when the temperature is raised from 20 to 80 °C: with PtRu(4-1)/CuNWs showing the highest specific MOR activity (Figure 6.14).

### 6.3.5 Originality of the Enhanced MOR Activity of PtRuNTs and PtRu/CuNWs

To understand the enhanced MOR activity of PtRuNTa and PtRu/CuNWs, we looked into the role of the one-dimensional structure by synthesizing PtNTs and Pt/CuNWs using the same methods as in the synthesis of PtRuNTs and PtRu/CuNWs without adding Ru precursors (see SEM images in Figure 6.15a and b). Their MOR activities were investigated and compared with that of Pt disk and TKK Pt/C (Figure 6.15c). PtNTs show a specific MOR activity similar to Pt disk, but much higher than

Pt/C, which agrees with the results reported by Alia et al.[142] From CO stripping experiments (Figure 6.15d), similar CO stripping peak potentials are observed for PtNTs and Pt disk at about 0.70 V, while Pt/C exhibited a peak at a much higher potential (about 0.83 V). Particle size effects on MOR for Pt has been investigated by various groups,[154,181-184] and the MOR specific activity was found to decrease as Pt nanoparticle size decreases.

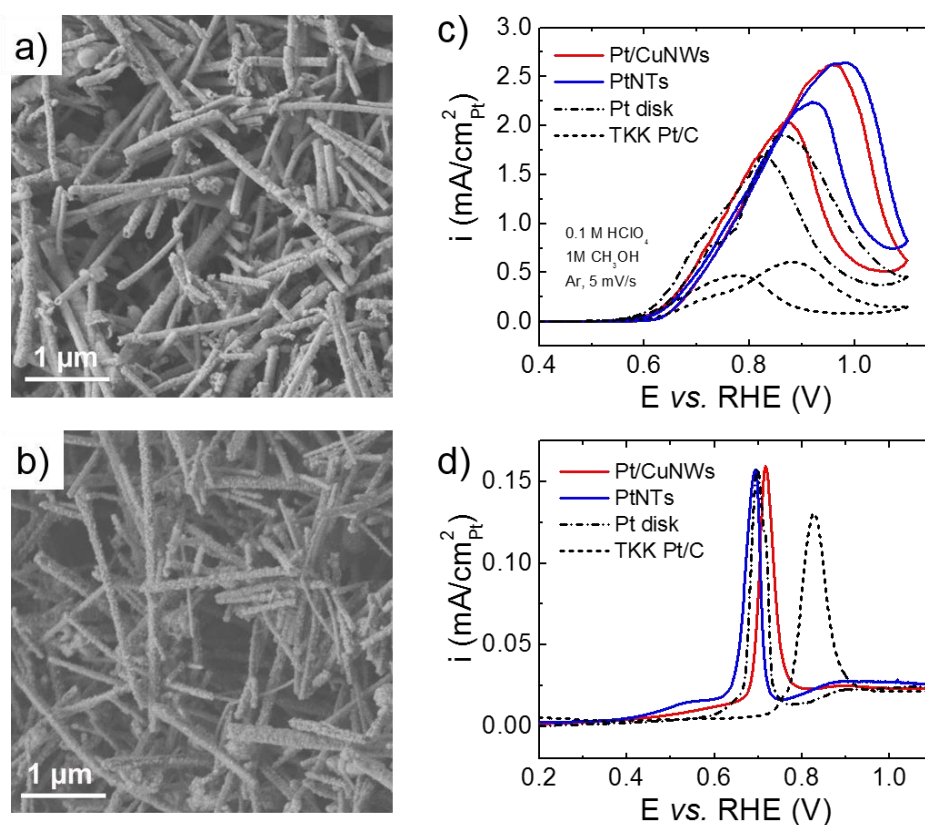


Figure 6.15 SEM images of (a) PtNTs and (b) Pt/CuNWs. (c) Cyclic voltammograms of Pt/CuNWs(Pt 25 wt.%) , PtNTs, Pt disk and TKK Pt/C tested in 0.1 M HClO<sub>4</sub>, 1 M CH<sub>3</sub>OH, Ar, 5 mV/s, activities were normalized to surface area of Pt calculated from H<sub>ads</sub> and H<sub>des</sub> peaks, (d) CO stripping of Pt/CuNWs(Pt 25 wt.%) , PtNTs, Pt disk and TKK Pt/C tested in 0.1 M HClO<sub>4</sub>, 20 mV/s, CO was pre-adsorbed at 0.1 V vs. RHE for 10 min followed by another 10 min Ar-purging.

With this trend, we expect that bulk platinum will have the highest MOR activity, which explains why PtNTs with extended surfaces show MOR activity similar to Pt disk, and much higher than Pt nanoparticles. Meanwhile, the CO stripping peak position is strongly dependent on surface facets: for low index Pt facets, the CO stripping peak occurs at 0.87 V for Pt(111),[185] 0.7 V for Pt(110)[186] and 0.79 V for Pt(100).[187] PtNTs show the same CO stripping peak potential as Pt(110), indicating PtNTs might preferentially expose Pt(110) facets on their surface, which is known to possess the highest MOR activity among the three low index facets.[97] Although step or defect sites are beneficial for enhancing MOR activity on Pt,[188] their promotional effect may not be as effective as exposing the most active surface. Analogously, we hypothesize that PtRuNTs achieved a higher activity than PtRu/C due to their extended surfaces.

Figure 6.16 represents the Pt 4f and Ru 3p<sub>3/2</sub> XPS spectra for PtRu/C, PtRu(6-1)NTs and PtRu(4-1)/CuNWs. The Pt 4f binding energy decreased in order of PtRu/C > PtRu(6-1)NTs > PtRu(4-1)/CuNWs (Figure 6.16a) while the Ru 3p binding energy followed the exact opposite trend (Figure 6.16b), indicating that Pt obtains more electrons from Ru from PtRu(4-1)/CuNWs to PtRu(6-1)NTs to PtRu/C. This is consistent with the fact that Pt has a larger electronegativity than Ru (2.28 vs. 2.20). Additionally, the surface copper in PtRuNTs and PtRu/CuNWs could also contribute electrons to Pt due to its even lower electronegativity (1.90). The core-level shifts in XPS are usually correlated with changes in the d-band center. However, while some conclude that an upshift of binding energy corresponds to a lower d-band center, i.e., with d-band center further away from the Fermi level,[150,189] others report the opposite correlation that a downshift of binding energy is indicative of a lower d-band center.[176,178,190] This discrepancy is discussed by Poh et al. that the XPS core level

shift is affected by several factors and both correlations are possible.[189] They finally explained the trend of the d-band center shift based on the existence of charge transfer from metals with low work function to metals with higher work function, leading to the rise of Fermi level of the metal with higher work function, which corresponds to the downshift of d-band center. In our case, we observed more electron transfer from Ru or Cu to Pt in PtRu/CuNWs than PtRuNTs and PtRu/C, hence the d-band center of PtRu/CuNWs will be the lowest among the three samples. The lower d-band center is usually related with a weaker binding of the adsorbate to the metal,[191] and in this case, the poisoning intermediate CO to Pt. The early onset of CO monolayer oxidation in CO stripping measurements on PtRu/CuNWs (0.28 V) compared with that of PtRuNTs (0.3 V) and PtRu/C (0.32 V) (inset of Figure 6.10f), is another strong evidence of weaker Pt-CO binding in PtRu/CuNWs.

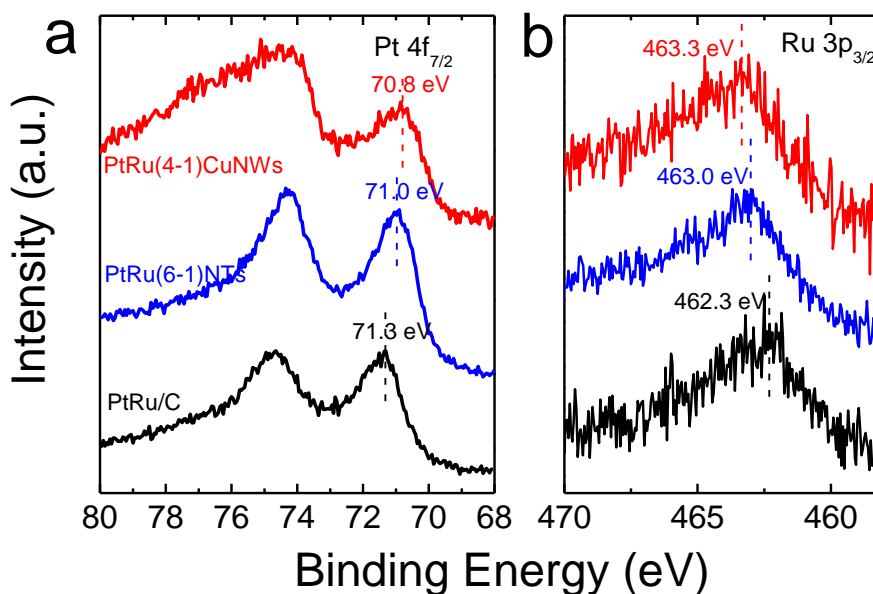


Figure 6.16 XPS spectra of PtRu/C, PtRu(6-1)NTs and PtRu(4-1)/CuNWs: (a) Pt 4f, (b) Ru 3p<sub>3/2</sub>.

## 6.4 Conclusion

In conclusion, we have synthesized PtRuNTs and PtRu/CuNWs via galvanic displacement reaction using CuNWs as template and presented their efficient catalytic activities of electro-oxidation of methanol. The compositional effect study show an optimal PtRu bulk ratio of about 4 and surface ratio of about 1 for both PtRuNTs and PtRu/CuNWs. Enhanced specific MOR activities were observed on PtRuNTs and PtRu/CuNWs compared with the benchmark PtRu/C, with specific activity in the order of PtRu/CuNWs > PtRuNTs > PtRu/C. The improvement of specific activity of PtRuNTs might be partially attributed from the extended surface of their intrinsic nanotube structure. The XPS measurement of PtRu(4-1)/CuNWs, PtRu(6-1)NTs and PtRu/C revealed a stronger electron transfer from Ru to Pt in PtRu(4-1)/CuNWs than PtRu(6-1)NTs followed by PtRu/C which corresponds to its lower d-band center. Meanwhile, the modification of the d-band center can lead to a weaker bonding of Pt to the poisoning intermediate CO, resulting in improved specific MOR activity of PtRu(4-1)/CuNWs. However, a smaller mass MOR activity was obtained on PtRuNTs compared with PtRu/C caused by their small ECSA. PtRu(4-1)/CuNWs achieved a comparable mass activity at lower potential range (< 0.6 V vs. RHE) and a much higher mass activity at potential larger than 0.6 V vs. RHE, ascribed to their improved specific activity as well as increased ECSA. We believe that PtRu/CuNWs with 1D morphology will be a promising anode catalyst for DMFCs due to their good mass activity and their potential benefit in improving mass transport.

## Chapter 7

### CONCLUSIONS AND PERSPECTIVES

#### 7.1 Conclusions

Fundamental understating of HOR is important for design and development of efficient catalysts for HOR in alkaline electrolyte. Performing the kinetic studies correctly is the perquisite for obtaining reliable activity and mechanistic information on the catalysts being evaluated. We demonstrated that HER could also be limited by diffusion when its kinetics is facile in RDE measurement, and established a protocol for correcting the diffusion limitation for both HOR and HER based on a reversible Koutecky-Levich equation. While the HOR diffusion limitation comes from the insufficient mass transport of H<sub>2</sub> in the bulk electrolyte to the electrode surface, the HER diffusion limitation originates from the insufficient mass transport of the produced H<sub>2</sub> from the electrode surface to the bulk electrolyte and the highly reversible nature of HOR/HER. Correlating with irreversible Koutecky-Levich equation would lead to underestimated HOR/HER activity when the kinetics is facile. Therefore, to obtain reliable kinetic information using RDE method, it is recommended to correct the measured current with the reversible Koutecky-Levich equation together with internal resistance (*iR*) compensation.

The particle size effect study provides information about active sites and bridges the gap between bulk material and nanoparticles. The HOR/HER activities were investigated on carbon supported Ir nanoparticles with size ranging from 3 to 12 nm and Pd nanoparticles from 3 to 42 nm. For both Ir/C and Pd/C, we found that the HOR/HER

specific activities increase with increasing particle size. The HOR/HER activities of Ir/C normalized to the surface area of lowest hydrogen binding sites (determined from the  $H_{\text{upd}}$  profiles in cyclic voltammograms) are particle size - independent, suggesting that those sites with lowest HBE are the most active sites for HOR/HER. Similarly, the increased HOR/HER activity on larger Pd nanoparticles correlates with an increased ratio of the sites with lower HBE revealed in cyclic voltammograms. These findings suggest that HOR/HER on Ir and Pd could be structure sensitive, and extended structures with more low-index facets might have higher activities compared with nanoparticles.

To understand the HOR/HER activity difference between acid and base, the pH-dependent HBE and HOR/HER activities on monometallic PGMs (Pt/C, Ir/C, Pd/C and Rh/C) were investigated in electrolytes over a broad range of pHs using CV and RDE methods. Linear correlations between  $\text{Log}(i_0)$  and HBE were quantitatively determined and similar slopes were obtained, indicating that HBE is the dominant descriptor for HOR/HER. The CO stripping onset potentials decrease as pH increases, which suggests an earlier adsorption of  $\text{OH}_{\text{ad}}$  with increasing pH, and provides evidence against the promotional role of  $\text{OH}_{\text{ad}}$  on HOR/HER activity.

Finally, extended PtRu nanostructures, PtRuNTs and PtRu/CuNWs, were synthesized via galvanic displacement reaction, which showed higher specific activities towards MOR compared with benchmark PtRu/C catalysts and thus are promising for application in DMFCs. The improved activities of PtRuNTs and PtRu/CuNWs were attributed to weakened Pt-CO binding revealed by XPS analysis as well as the earlier CO-stripping onset potentials.

## 7.2 Perspectives

### 7.2.1 Fundamental Studies of Hydrogen Oxidation Reaction

Great progress has been made on the fundamental understanding of HOR/HER in terms of the reaction mechanism, kinetic studies, activity descriptor as well as the pH-dependent HBE and activity. However, there is still unsolved issues which deserve further investigation.

For the mechanism of HOR/HER, discrepancy exists on whether Tafel or Volmer step is the RDS for HOR on Pt in acid.[3,21] Tafel-Volmer is most likely to be the reaction pathway as least in the low overpotential region, with Volmer step widely accepted as the RDS in base.[3,25,52] This leads to the question whether there is a change of rate-determining step for HOR from acid to base. On the other hand, there might be no RDS for HOR/HER on Pt in acid since its kinetic is so fast that the rate of Tafel and Volmer step might be comparable.

The particle size effect studies suggest that HOR/HER on Ir and Pd might be structure sensitive. Multiple  $H_{\text{upd}}$  adsorption/desorption peaks were observed on the cyclic voltammograms of Ir and Pd, which could be attributed to facets with different HBE. Studies on single crystalline Ir and Pd will be beneficial in order to probe the structure sensitivity, as well as to assign the  $H_{\text{upd}}$  peaks to certain facets.

Although HBE is the dominant descriptors for HOR/HER activities on monometallic PGMs, it remains unclear whether HBE is still the unique and sole descriptor for HOR/HER activity in base or  $\text{OH}_{\text{ad}}$  plays a role in promoting HOR/HER activity through a bifunctional mechanism due to the change in reaction mechanism for HOR from acid to base if possible, which will influence the catalyst design and development. It was observed that HBE increases as the pH of the electrolyte increases,

however, through what mechanism does pH influences HBE remains uncertain. Development on the theoretical calculation (e.g., DFT) to incorporate the effect of solvent on the binding energy is demand to give an insight on the cause of the pH-dependent HBE. In addition, majority of HOR/HER studies are focused on monometallic metals currently, it will be interesting to extend the studies to bimetallic catalysts such as Pt-alloys.

### **7.2.2 Catalysts Development for Hydrogen Oxidation Reaction in Base**

Considering that the HOR activity on Pt in alkaline electrolyte is two orders of magnitude lower than that in acid, searching for alternative efficient catalysts with high activity and low cost is essential for the development and commercialization of HEMFCs. While the ultimate goal is to design and develop non-precious metals or metal-free catalysts to replace the costly and less abundant precious metals, improving the HOR activity of the precious metals so as to reduce the amount of precious metals required would be an option in the short term. Strategies of improving catalytic activity include 1) increasing the amount of active sites, and 2) enhancing the activity of the active sites. Since HBE is recognized to be the dominating descriptor for HOR activity, tuning the HBE of a certain metal to the optimal binding strength as well as increasing the quantity of sites with optimal binding strength are the two approaches for HOR catalysts design which will be demonstrated in the cases of both precious metals and non-precious metals.

The Pt-group metals (Pt, Pd, Ir and Rh) belong to the strongly H bound branch in the volcano plot, reducing the HBE of those metals is the right approach to enhance HOR activity, which can be achieved through alloying them with other transition metals. Ru, when alloyed with Pt, has the ability to lower the d-band center of Pt through

electronic and strain effect, and weaken the Pt-adsorbate binding energy. Indeed, higher HOR/HER activities were obtained on Pt alloys nanostructures including PtRu alloys,[52,53] Ru@Pt nanoparticles,[24] PtRuNTs[192] and Pt/CuNWs.[193] However, the improvements on those catalysts are minimal (up to 4-fold increase) compared with the two-orders of magnitude activity difference between acid and base. The anode catalyst cost gap cannot be bridged unless comparable HOR activities are achieved on novel Pt-based catalysts in base and on Pt in acid.

For non-precious metal catalysts, Raney-Ni as well as Cr or Ti-decorated Raney-Ni have been reported to show HOR activity, though very low, in 6 M KOH at elevated temperature about 60 or 80 °C.[194-196] NiMoCo prepared by electrodeposition exhibits specific HOR activity 20 times of that of pure Ni, resulted from its weakened Ni-HBE induced by Mo and Co.[84] More importantly, the geometric area based HOR activity of NiMoCo exceed that of polycrystalline Pt electrode, demonstrating that NiMoCo is very promising for replacing Pt in HEMFCs. However, for it to be applied in a real fuel cell, dispersed NiMoCo such as carbon supported NiMoCo nanoparticles should be prepared, which might be a challenge. Additionally, the passivation of Ni at a very low over potential (about 0.1 V) could potentially result in a durability issue unless a good control on the HEMFC operation potential is achieved to ensure the anode overpotential will not exceed 0.1 V. Therefore, besides improving the activity of those non-precious metals, it is critical to address their stability issue towards oxidation with application of overpotential. Decorating Ni nanoparticles with CrO<sub>x</sub> has been shown to weaken the Ni-O bond, and stabilize the Ni,[197] which might be a possible approach to improve the stability of Ni-based catalysts. Currently, the HOR activities of the non-precious metals were determined ex-situ using RDE, it will be of great significant if the

non-precious metal catalysts with high HOR activity could be constructed into an operating HEMFC.

### **7.2.3 PtRu Catalysts for Methanol Oxidation Reaction**

PtRu/CuNWs showed higher specific MOR activity and comparable mass activity compared with benchmark PtRu/C. The MOR activity of PtRu/CuNWs was measured ex-situ using CV, it will be interesting to verify its performance in a DMFCs. Trace amount of cationic ions such as  $\text{Cu}^{2+}$  and  $\text{Fe}^{2+}$  will contaminate the membrane and accelerate membrane degradation, thus impacting the durability of the operating fuel cells.[198] Therefore, attentions have to be paid on the potential leaching of Cu from PtRu/CuNWs. No bulk Cu dissolution peaks are observed on the CVs of PtRu/CuNWs in the first scan, indicating the unalloyed Cu are protected by the PtRu-rich shell from leaching. Additionally, since PtRu/CuNWs is used at the anode where the overpotentials are below the Cu dissolution potential (0.34 V), the leaching of Cu would be minimal. A Cu pre-leaching approach is also worth investigating to eliminate the leaching of Cu when applied into a real fuel cell.

To further improve the MOR activity of PtRu/CuNWs, a possible method is to implement heat treatment together with in-situ dealloying of Cu which has been proved to be effective to tune the activity of Pt/CuNWs toward ORR.[179]

## REFERENCES

- [1] Shah, R. K. In *Recent Trends in Fuel Cell Science and Technology*; Basu, S., Ed.; Springer New York: **2007**, 10.1007/978-0-387-68815-2\_1, p 1-9.
- [2] Sheng, W.; Gasteiger, H. A.; Shao-Horn, Y. *Journal of The Electrochemical Society* **2010**, *157*, B1529-B1536.
- [3] Durst, J.; Siebel, A.; Simon, C.; Hasche, F.; Herranz, J.; Gasteiger, H. A. *Energy & Environmental Science* **2014**, *7*, 2255-2260.
- [4] Zhang, J.; Yang, H.; Fang, J.; Zou, S. *Nano Letters* **2010**, *10*, 638-644.
- [5] Chen, C.; Kang, Y.; Huo, Z.; Zhu, Z.; Huang, W.; Xin, H. L.; Snyder, J. D.; Li, D.; Herron, J. A.; Mavrikakis, M.; Chi, M.; More, K. L.; Li, Y.; Markovic, N. M.; Somorjai, G. A.; Yang, P.; Stamenkovic, V. R. *Science* **2014**, *343*, 1339-1343.
- [6] Hernandez-Fernandez, P.; Masini, F.; McCarthy, D. N.; Strebel, C. E.; Friebel, D.; Deiana, D.; Malacrida, P.; Nierhoff, A.; Bodin, A.; Wise, A. M.; Nielsen, J. H.; Hansen, T. W.; Nilsson, A.; StephensIfan, E. L.; Chorkendorff, I. *Nat Chem* **2014**, *6*, 732-738.
- [7] Gu, S.; Cai, R.; Luo, T.; Jensen, K.; Contreras, C.; Yan, Y. *ChemSusChem* **2010**, *3*, 555-558.
- [8] Wang, J.; Gu, S.; Kaspar, R. B.; Zhang, B.; Yan, Y. *ChemSusChem* **2013**, *6*, 2079-2082.
- [9] Varcoe, J. R.; Atanassov, P.; Dekel, D. R.; Herring, A. M.; Hickner, M. A.; Kohl, P. A.; Kucernak, A. R.; Mustain, W. E.; Nijmeijer, K.; Scott, K.; Xu, T.; Zhuang, L. *Energy & Environmental Science* **2014**, *7*, 3135-3191.
- [10] Filpi, A.; Boccia, M.; Gasteiger, H. A. *ECS Transactions* **2008**, *16*, 1835-1845.

- [11] Piana, M.; Catanorchi, S.; Gasteiger, H. A. In *Proton Exchange Membrane Fuel Cells 8, Pts 1 and 2*; Fuller, T., Shinohara, K., Ramani, V., Shirvanian, P., Uchida, H., Cleghorn, S., Inaba, M., Mitsushima, S., Strasser, P., Nakagawa, H., Gasteiger, H. A., Zawodzinski, T., Lamy, C., Eds. **2008**; Vol. 16, p 2045-2055.
- [12] Piana, M.; Boccia, M.; Filpi, A.; Flammia, E.; Miller, H. A.; Orsini, M.; Salusti, F.; Santiccioli, S.; Ciardelli, F.; Pucci, A. *Journal of Power Sources* **2010**, *195*, 5875-5881.
- [13] Chung, H. T.; Won, J. H.; Zelenay, P. *Nature Communications* **2013**, *4*.
- [14] Aricò, A. S.; Baglio, V.; Antonucci, V. In *Electrocatalysis of Direct Methanol Fuel Cells*; Wiley-VCH Verlag GmbH & Co. KGaA: **2009**, 10.1002/9783527627707.ch1, p 1-78.
- [15] Hamnett, A. In *Handbook of Fuel Cells*; John Wiley & Sons, Ltd: **2010**; Vol. 1.
- [16] Breiter, M. W. In *Handbook of Fuel Cells*; John Wiley & Sons, Ltd: **2010**; Vol. 2, p 361-367.
- [17] Breiter, M. W. In *Handbook of Fuel Cells*; John Wiley & Sons, Ltd: **2010**, 10.1002/9780470974001.f204027.
- [18] Krischer, K.; Savinova, E. R. In *Handbook of Heterogeneous Catalysis*; Wiley-VCH Verlag GmbH & Co. KGaA: **2008**, 10.1002/9783527610044.hetc0101.
- [19] Vetter, K. J. *Electrochemical kinetics : theoretical and experimental aspects*; Academic Press, **1967**.
- [20] Conway, B. E.; Tilak, B. V. *Electrochimica Acta* **2002**, *47*, 3571-3594.
- [21] Vogel, W.; Lundquist, L.; Ross, P.; Stonehart, P. *Electrochimica Acta* **1975**, *20*, 79-93.
- [22] Chen, S.; Kucernak, A. *The Journal of Physical Chemistry B* **2004**, *108*, 13984-13994.
- [23] Wang, J. X.; Springer, T. E.; Adzic, R. R. *Journal of The Electrochemical Society* **2006**, *153*, A1732-A1740.
- [24] Elbert, K.; Hu, J.; Ma, Z.; Zhang, Y.; Chen, G.; An, W.; Liu, P.; Isaacs, H. S.; Adzic, R. R.; Wang, J. X. *ACS Catalysis* **2015**, 10.1021/acscatal.5b01670, 6764-6772.

- [25] Sheng, W.; Zhuang, Z.; Gao, M.; Zheng, J.; Chen, J. G.; Yan, Y. *Nat Commun* **2015**, *6*.
- [26] Schouten, K. J. P.; van der Niet, M. J. T. C.; Koper, M. T. M. *Physical Chemistry Chemical Physics* **2010**, *12*, 15217-15224.
- [27] Łosiewicz, B.; Jurczakowski, R.; Lasia, A. *Electrochimica Acta* **2012**, *80*, 292-301.
- [28] Sabatier, P. *Berichte der deutschen chemischen Gesellschaft* **1911**, *44*, 1984-2001.
- [29] Trasatti, S. *Journal of Electroanalytical Chemistry* **1972**, *39*, 163-184.
- [30] Parsons, R. *Transactions of the Faraday Society* **1958**, *54*, 1053-1063.
- [31] Norskov, J. K.; Bligaard, T.; Logadottir, A.; Kitchin, J. R.; Chen, J. G.; Pandalov, S. *Journal of the Electrochemical Society* **2005**, *152*, J23-J26.
- [32] Sheng, W.; Myint, M.; Chen, J. G.; Yan, Y. *Energy & Environmental Science* **2013**, *6*, 1509-1512.
- [33] Durst, J.; Simon, C.; Siebel, A.; Rheinländer, P. J.; Schuler, T.; Hanzlik, M.; Herranz, J.; Hasché F.; Gasteiger, H. A. *ECS Transactions* **2014**, *64*, 1069-1080.
- [34] Krishtalik, L. I. In *Advances in Electrochemistry and Electrochemical Engineering*; Delahay, P., Tobias, C. W., Eds.; Interscience: New York, **1970**; Vol. 7, p 283-339.
- [35] Conway, B. E.; Jerkiewicz, G. *Electrochimica Acta* **2000**, *45*, 4075-4083.
- [36] Gasteiger, H. A.; Panels, J. E.; Yan, S. G. *Journal of Power Sources* **2004**, *127*, 162-171.
- [37] Schmickler, W.; Trasatti, S. *Journal of The Electrochemical Society* **2006**, *153*, L31-L32.
- [38] Durst, J.; Simon, C.; Hasché F.; Gasteiger, H. A. *Journal of The Electrochemical Society* **2015**, *162*, F190-F203.
- [39] Markovic, N. M.; Grgur, B. N.; Ross, P. N. *Journal of Physical Chemistry B* **1997**, *101*, 5405-5413.

- [40] Montero, M. A.; Fernández, J. L.; Gennero de Chialvo, M. R.; Chialvo, A. C. *Journal of Physical Chemistry C* **2013**, *117*, 25269-25275.
- [41] Montero, M. A.; Fernández, J. L.; Gennero de Chialvo, M. R.; Chialvo, A. C. *Journal of Power Sources* **2014**, *254*, 218-223.
- [42] Schmidt, T. J.; Ross Jr, P. N.; Markovic, N. M. *Journal of Electroanalytical Chemistry* **2002**, 524–525, 252-260.
- [43] Rheinländer, P.; Henning, S.; Herranz, J.; Gasteiger, H. A. *ECS Transactions* **2013**, *50*, 2163-2174.
- [44] Woodroof, M. D.; Wittkopf, J. A.; Gu, S.; Yan, Y. S. *Electrochemistry Communications* **2015**, *61*, 57-60.
- [45] Marković, N. M.; Grgur, B. N.; Ross, P. N. *The Journal of Physical Chemistry B* **1997**, *101*, 5405-5413.
- [46] Zhou, J.; Zu, Y.; Bard, A. J. *Journal of Electroanalytical Chemistry* **2000**, *491*, 22-29.
- [47] Zoski, C. G. *The Journal of Physical Chemistry B* **2003**, *107*, 6401-6405.
- [48] Sun, Y.; Lu, J.; Zhuang, L. *Electrochimica Acta* **2010**, *55*, 844-850.
- [49] Zheng, J.; Zhuang, Z.; Xu, B.; Yan, Y. *ACS Catalysis* **2015**, *5*, 4449-4455.
- [50] Montero, M. A.; Fernández, J. L.; Gennero de Chialvo, M. R.; Chialvo, A. C. *The Journal of Physical Chemistry C* **2013**, *117*, 25269-25275.
- [51] Ohyama, J.; Sato, T.; Yamamoto, Y.; Arai, S.; Satsuma, A. *Journal of the American Chemical Society* **2013**, *135*, 8016-8021.
- [52] Wang, Y.; Wang, G.; Li, G.; Huang, B.; Pan, J.; Liu, Q.; Han, J.; Xiao, L.; Lu, J.; Zhuang, L. *Energy & Environmental Science* **2015**, *8*, 177-181.
- [53] Strmcnik, D.; Uchimura, M.; Wang, C.; Subbaraman, R.; Danilovic, N.; van der, V.; Paulikas, A. P.; Stamenkovic, V. R.; Markovic, N. M. *Nat Chem* **2013**, *5*, 300-306.
- [54] Iwasita, T. *Electrochimica Acta* **2002**, *47*, 3663-3674.
- [55] Nagao, R.; Cantane, D. A.; Lima, F. H. B.; Varela, H. *Physical Chemistry Chemical Physics* **2012**, *14*, 8294-8298.

- [56] Ferrin, P.; Nilekar, A. U.; Greeley, J.; Mavrikakis, M.; Rossmeisl, J. *Surface Science* **2008**, *602*, 3424-3431.
- [57] Liu, H.; Song, C.; Zhang, L.; Zhang, J.; Wang, H.; Wilkinson, D. P. *Journal of Power Sources* **2006**, *155*, 95-110.
- [58] Sarma, L. S.; Taufany, F.; Hwang, B.-J. In *Electrocatalysis of Direct Methanol Fuel Cells*; Wiley-VCH Verlag GmbH & Co. KGaA: **2009**, 10.1002/9783527627707.ch3, p 115-163.
- [59] Koenigsmann, C.; Wong, S. S. *Energy & Environmental Science* **2011**, *4*, 1161-1176.
- [60] Gasteiger, H. A.; Markovic, N. M.; Ross, P. N. *The Journal of Physical Chemistry* **1995**, *99*, 8290-8301.
- [61] Schmidt, T. J.; Gasteiger, H. A.; Stäb, G. D.; Urban, P. M.; Kolb, D. M.; Behm, R. J. *J. Electrochem. Soc.* **1998**, *145*, 2354-2358.
- [62] Lawson, D. R.; Whiteley, L. D.; Martin, C. R.; Szentirmay, M. N.; Song, J. I. *Journal of The Electrochemical Society* **1988**, *135*, 2247-2253.
- [63] Gloaguen, F.; Andolfatto, F.; Durand, R.; Ozil, P. *JOURNAL OF APPLIED ELECTROCHEMISTRY* **1994**, *24*, 863-869.
- [64] Galus, Z.; Olson, C.; Lee, H. Y.; Adams, R. N. *Analytical Chemistry* **1962**, *34*, 164-166.
- [65] Gasteiger, H. A.; Kocha, S. S.; Sompalli, B.; Wagner, F. T. *Applied Catalysis B: Environmental* **2005**, *56*, 9-35.
- [66] Mayrhofer, K. J. J.; Strmcnik, D.; Blizanac, B. B.; Stamenkovic, V.; Arenz, M.; Markovic, N. M. *Electrochimica Acta* **2008**, *53*, 3181-3188.
- [67] Rheinländer, P. J.; Herranz, J.; Durst, J.; Gasteiger, H. A. *Journal of The Electrochemical Society* **2014**, *161*, F1448-F1457.
- [68] Neyerlin, K. C.; Gu, W.; Jorne, J.; Gasteiger, H. A. *J. Electrochem. Soc.* **2007**, *154*, B631-B635.
- [69] Bagotzky, V. S.; Osetrova, N. V. *Journal of Electroanalytical Chemistry and Interfacial Electrochemistry* **1973**, *43*, 233-249.
- [70] Zalitis, C. M.; Kramer, D.; Kucernak, A. R. *Physical Chemistry Chemical Physics* **2013**, *15*, 4329-4340.

- [71] Cheng, L.; Huang, W.; Gong, Q.; Liu, C.; Liu, Z.; Li, Y.; Dai, H. *Angewandte Chemie International Edition* **2014**, *53*, 7860-7863.
- [72] Deng, J.; Ren, P.; Deng, D.; Yu, L.; Yang, F.; Bao, X. *Energy & Environmental Science* **2014**, *7*, 1919-1923.
- [73] Faber, M. S.; Dziedzic, R.; Lukowski, M. A.; Kaiser, N. S.; Ding, Q.; Jin, S. *Journal of the American Chemical Society* **2014**, *136*, 10053-10061.
- [74] Gao, M.-R.; Liang, J.-X.; Zheng, Y.-R.; Xu, Y.-F.; Jiang, J.; Gao, Q.; Li, J.; Yu, S.-H. *Nat Commun* **2015**, *6*.
- [75] Tavakkoli, M.; Kallio, T.; Reynaud, O.; Nasibulin, A. G.; Johans, C.; Sainio, J.; Jiang, H.; Kauppinen, E. I.; Laasonen, K. *Angewandte Chemie International Edition* **2015**, *54*, 4535-4538.
- [76] Wang, D.-Y.; Gong, M.; Chou, H.-L.; Pan, C.-J.; Chen, H.-A.; Wu, Y.; Lin, M.-C.; Guan, M.; Yang, J.; Chen, C.-W.; Wang, Y.-L.; Hwang, B.-J.; Chen, C.-C.; Dai, H. *Journal of the American Chemical Society* **2015**, *137*, 1587-1592.
- [77] Maruyama, J.; Inaba, M.; Katakura, K.; Ogumi, Z.; Takehara, Z.-i. *Journal of Electroanalytical Chemistry* **1998**, *447*, 201-209.
- [78] Zheng, J.; Zhuang, Z.; Xu, B.; Yan, Y. *ACS Catalysis* **2015**, 10.1021/acscatal.5b00247, 4449-4455.
- [79] Chen, Q.; Luo, L.; White, H. S. *Langmuir* **2015**, *31*, 4573-4581.
- [80] Chen, Q.; Luo, L.; Faraji, H.; Feldberg, S. W.; White, H. S. *The Journal of Physical Chemistry Letters* **2014**, *5*, 3539-3544.
- [81] Bard, A. J.; Faulkner, L. R. *Electrochemical Methods: Fundamentals and Applications*; 2 ed.; John Wiley & Sons, Inc, **2001**.
- [82] Kong, D.; Wang, H.; Lu, Z.; Cui, Y. *J. Am. Chem. Soc.* **2014**, *136*, 4897-4900.
- [83] Strmcnik, D.; Uchimura, M.; Wang, C.; Subbaraman, R.; Danilovic, N.; van der Vliet, D.; Paulikas, A. P.; Stamenkovic, V. R.; Markovic, N. M. *Nature Chemistry* **2013**, *5*, 300-306.
- [84] Sheng, W.; Bivens, A. P.; Myint, M.; Zhuang, Z.; Forest, R. V.; Fang, Q.; Chen, J. G.; Yan, Y. *Energy & Environmental Science* **2014**, *7*, 1719-1724.

- [85] Sheng, W.; Zhuang, Z.; Gao, M.; Zheng, J.; Chen, J. G.; Yan, Y. *Nature Communications* **2015**, *6*.
- [86] Marković, N. M.; Sarraf, S. T.; Gasteiger, H. A.; Ross, P. N. *Journal of the Chemical Society, Faraday Transactions* **1996**, *92*, 3719-3725.
- [87] Mukerjee, S. *JOURNAL OF APPLIED ELECTROCHEMISTRY* **1990**, *20*, 537-548.
- [88] Jaramillo, T. F.; Jørgensen, K. P.; Bonde, J.; Nielsen, J. H.; Horch, S.; Chorkendorff, I. *Science* **2007**, *317*, 100-102.
- [89] Maillard, F.; Pronkin, S.; Savinova, E. R. In *Handbook of Fuel Cells*; John Wiley & Sons, Ltd: **2010**, 10.1002/9780470974001.f500002a.
- [90] Nesselberger, M.; Ashton, S.; Meier, J. C.; Katsounaros, I.; Mayrhofer, K. J. J.; Arenz, M. *Journal of the American Chemical Society* **2011**, *133*, 17428-17433.
- [91] Zoski, C. G. *Journal of Physical Chemistry B* **2003**, *107*, 6401-6405.
- [92] Woods, R. J. *Electroanal. Chem. Interfac.* **1974**, *49*, 217-226.
- [93] Ferreira, P. J.; la O', G. J.; Shao-Horn, Y.; Morgan, D.; Makharia, R.; Kocha, S.; Gasteiger, H. A. *Journal of The Electrochemical Society* **2005**, *152*, A2256-A2271.
- [94] Gasteiger, H. A.; Markovic, N. M.; Ross, P. N. *Journal of Physical Chemistry* **1995**, *99*, 8290-8301.
- [95] Jerkiewicz, G. *Progress in Surface Science* **1998**, *57*, 137-186.
- [96] Jerkiewicz, G.; Zolfaghari, A. *Journal of The Electrochemical Society* **1996**, *143*, 1240-1248.
- [97] Herrero, E.; Franaszczuk, K.; Wieckowski, A. *J. Phys. Chem.* **1994**, *98*, 5074-5083.
- [98] Perez, J.; Villullas, H. M.; Gonzalez, E. R. *Journal of Electroanalytical Chemistry* **1997**, *435*, 179-187.
- [99] Kinoshita, K.; Lundquist, J.; Stonehart, P. *Journal of Catalysis* **1973**, *31*, 325-334.
- [100] Kinoshita, K.; Ferrier, D. R.; Stonehart, P. *Electrochimica Acta* **1978**, *23*, 45-54.

- [101] Motoo, S.; Furuya, N. *Journal of Electroanalytical Chemistry and Interfacial Electrochemistry* **1984**, *181*, 301-305.
- [102] Furuya, N.; Koide, S. *Surface Science* **1990**, *226*, 221-225.
- [103] Sun, Y.; Dai, Y.; Liu, Y.; Chen, S. *Physical Chemistry Chemical Physics* **2012**, *14*, 2278-2285.
- [104] Antolini, E. *Energy & Environmental Science* **2009**, *2*, 915-931.
- [105] Shao, M. *Journal of Power Sources* **2011**, *196*, 2433-2444.
- [106] Alia, S. M.; Yan, Y. *Journal of The Electrochemical Society* **2015**, *162*, F849-F853.
- [107] Henning, S.; Herranz, J.; Gasteiger, H. A. *Journal of The Electrochemical Society* **2015**, *162*, F178-F189.
- [108] Jiang, L.; Hsu, A.; Chu, D.; Chen, R. *Journal of The Electrochemical Society* **2009**, *156*, B643-B649.
- [109] Zhou, W.; Li, M.; Ding, O. L.; Chan, S. H.; Zhang, L.; Xue, Y. *International Journal of Hydrogen Energy* **2014**, *39*, 6433-6442.
- [110] Zhou, W.; Lee, J. Y. *The Journal of Physical Chemistry C* **2008**, *112*, 3789-3793.
- [111] Antoine, O.; Bultel, Y.; Durand, R.; Ozil, P. *Electrochimica Acta* **1998**, *43*, 3681-3691.
- [112] Rand, D. A. J.; Woods, R. *J. Electroanal. Chem. Interfac.* **1971**, *31*, 29-38.
- [113] Woods, R. In *Electroanalytical chemistry: a series of advances*; Dekker: New York, **1976**; Vol. 9, p 1-162.
- [114] Zheng, J.; Yan, Y.; Xu, B. *Journal of The Electrochemical Society* **2015**, *162*, F1470-F1481.
- [115] Schmidt, T. J.; Stamenkovic, V.; Markovic, N. M.; Ross Jr, P. N. *Electrochimica Acta* **2003**, *48*, 3823-3828.
- [116] Markovica, N. M.; Sarraf, S. T.; Gasteiger, H. A.; Ross, P. N. *Journal of the Chemical Society, Faraday Transactions* **1996**, *92*, 3719-3725.

- [117] Nørskov, J. K.; Bligaard, T.; Logadottir, A.; Kitchin, J. R.; Chen, J. G.; Pandelov, S.; Stimming, U. *Journal of The Electrochemical Society* **2005**, *152*, J23-J26.
- [118] Koper, M. T. M. *Nat Chem* **2013**, *5*, 255-256.
- [119] Popczun, E. J.; McKone, J. R.; Read, C. G.; Biacchi, A. J.; Wiltrout, A. M.; Lewis, N. S.; Schaak, R. E. *J. Am. Chem. Soc.* **2013**, *135*, 9267-9270.
- [120] Kibsgaard, J.; Jaramillo, T. F. *Angew. Chem. Int. Ed.* **2014**, *53*, 14433-14437.
- [121] Liao, L.; Wang, S.; Xiao, J.; Bian, X.; Zhang, Y.; Scanlon, M. D.; Hu, X.; Tang, Y.; Liu, B.; Girault, H. H. *Energy Environ. Sci.* **2014**, *7*, 387-392.
- [122] Popczun, E. J.; Read, C. G.; Roske, C. W.; Lewis, N. S.; Schaak, R. E. *Angew. Chem. Int. Ed.* **2014**, *53*, 5427-5430.
- [123] Zheng, Y.; Jiao, Y.; Zhu, Y.; Li, L. H.; Han, Y.; Chen, Y.; Du, A.; Jaroniec, M.; Qiao, S. Z. *Nat Commun* **2014**, *5*.
- [124] Biegler, T.; Rand, D. A. J.; Woods, R. *Journal of Electroanalytical Chemistry and Interfacial Electrochemistry* **1971**, *29*, 269-277.
- [125] Gisbert, R.; Garc á, G.; Koper, M. T. M. *Electrochimica Acta* **2010**, *55*, 7961-7968.
- [126] van der Niet, M. J. T. C.; Garcia-Araez, N.; Hernández, J.; Feliu, J. M.; Koper, M. T. M. *Catalysis Today* **2013**, *202*, 105-113.
- [127] Auinger, M.; Katsounaros, I.; Meier, J. C.; Klemm, S. O.; Biedermann, P. U.; Topalov, A. A.; Rohwerder, M.; Mayrhofer, K. J. J. *Physical Chemistry Chemical Physics* **2011**, *13*, 16384-16394.
- [128] Gileadi, E.; Argade, S. D.; Bockris, J. O. M. *The Journal of Physical Chemistry* **1966**, *70*, 2044-2046.
- [129] Zheng, J.; Zhuang, Z.; Xu, B.; Yan, Y., Submitted.
- [130] Zhuang, L.; Jin, J.; Abruña, H. D. *Journal of the American Chemical Society* **2007**, *129*, 11033-11035.
- [131] Gisbert, R.; Garc á, G.; Koper, M. T. M. *Electrochimica Acta* **2011**, *56*, 2443-2449.

- [132] Marković, N. M. In *Handbook of Fuel Cells*; John Wiley & Sons, Ltd: **2010**, 10.1002/9780470974001.f204027m.
- [133] Osetrova, N. V.; Bagotzky, V. S. *Electrokhimiya* **1973**, 9, 1527.
- [134] Barber, J. H.; Conway, B. E. *Journal of Electroanalytical Chemistry* **1999**, 461, 80-89.
- [135] Slygin, A.; Frumkin, A. N. *Acta Physicochim. URSS* **1935**, 3, 791.
- [136] Frumkin, A. N. In *Advances in Electrochemistry and Electrochemical Engineering*; P., D., Ed.; Interscience: New York, **1963**; Vol. 3.
- [137] Zolfaghari, A.; Jerkiewicz, G. *Journal of Electroanalytical Chemistry* **1999**, 467, 177-185.
- [138] Iwasita, T. In *Handbook of Fuel Cells*; John Wiley & Sons, Ltd: **2010**; Vol. 2.
- [139] Wasmus, S.; Küver, A. *Journal of Electroanalytical Chemistry* **1999**, 461, 14-31.
- [140] Liu, H. S.; Song, C. J.; Zhang, L.; Zhang, J. J.; Wang, H. J.; Wilkinson, D. P. *Journal of Power Sources* **2006**, 155, 95-110.
- [141] Bi, Y.; Lu, G. *Electrochemistry Communications* **2009**, 11, 45-49.
- [142] Alia, S. M.; Zhang, G.; Kisailus, D.; Li, D.; Gu, S.; Jensen, K.; Yan, Y. *Advanced Functional Materials* **2010**, 20, 3742-3746.
- [143] Ruan, L.; Zhu, E.; Chen, Y.; Lin, Z.; Huang, X.; Duan, X.; Huang, Y. *Angewandte Chemie International Edition* **2013**, 52, 12577-12581.
- [144] Cui, C.-H.; Li, H.-H.; Yu, S.-H. *Chemical Science* **2011**, 2, 1611-1614.
- [145] Ding, L.-X.; Wang, A.-L.; Li, G.-R.; Liu, Z.-Q.; Zhao, W.-X.; Su, C.-Y.; Tong, Y.-X. *Journal of the American Chemical Society* **2012**, 134, 5730-5733.
- [146] Kim, S. M.; Liu, L.; Cho, S. H.; Jang, H. Y.; Park, S. *Journal of Materials Chemistry A* **2013**, 1, 15252-15257.
- [147] Guo, S.; Zhang, S.; Sun, X.; Sun, S. *Journal of the American Chemical Society* **2011**, 133, 15354-15357.
- [148] Choi, W. C.; Woo, S. I. *Journal of Power Sources* **2003**, 124, 420-425.

- [149] Li, B.; Higgins, D. C.; Zhu, S.; Li, H.; Wang, H.; Ma, J.; Chen, Z. *Catalysis Communications* **2012**, *18*, 51-54.
- [150] Li, H.-H.; Zhao, S.; Gong, M.; Cui, C.-H.; He, D.; Liang, H.-W.; Wu, L.; Yu, S.-H. *Angewandte Chemie International Edition* **2013**, *52*, 7472-7476.
- [151] Hong, W.; Wang, J.; Wang, E. *Small* **2014**, *10*, 3262-3265.
- [152] Watanabe, M.; Motoo, S. *Journal of Electroanalytical Chemistry* **1975**, *60*, 267-273.
- [153] Marković, N. M.; Gasteiger, H. A.; Ross Jr, P. N.; Jiang, X.; Villegas, I.; Weaver, M. J. *Electrochimica Acta* **1995**, *40*, 91-98.
- [154] Frelink, T.; Visscher, W.; Vanveen, J. A. R. *Journal of Electroanalytical Chemistry* **1995**, *382*, 65-72.
- [155] Zhao, G.-Y.; Xu, C.-L.; Guo, D.-J.; Li, H.; Li, H.-L. *Journal of Power Sources* **2006**, *162*, 492-496.
- [156] Minch, R.; Es-Souni, M. *Chemical Communications* **2011**, *47*, 6284-6286.
- [157] Chen, Z.; Waje, M.; Li, W.; Yan, Y. *Angewandte Chemie International Edition* **2007**, *46*, 4060-4063.
- [158] Sun, Y. *Nanoscale* **2010**, *2*, 1626-1642.
- [159] Alia, S. M.; Jensen, K. O.; Pivovar, B. S.; Yan, Y. *Acs Catalysis* **2012**, *2*, 858-863.
- [160] Lu, X.; McKiernan, M.; Peng, Z.; Lee, E. P.; Yang, H.; Xia, Y. *Science of Advanced Materials* **2010**, *2*, 413-420.
- [161] Mohl, M.; Dobo, D.; Kukovecz, A.; Konya, Z.; Kordas, K.; Wei, J.; Vajtai, R.; Ajayan, P. M. *Journal of Physical Chemistry C* **2011**, *115*, 9403-9409.
- [162] Li, H.-H.; Cui, C.-H.; Zhao, S.; Yao, H.-B.; Gao, M.-R.; Fan, F.-J.; Yu, S.-H. *Advanced Energy Materials* **2012**, *2*, 1182-1187.
- [163] Alia, S. M.; Jensen, K.; Contreras, C.; Garzon, F.; Pivovar, B.; Yan, Y. *Acs Catalysis* **2013**, *3*, 358-362.
- [164] Zhu, C.; Guo, S.; Dong, S. *Journal of Materials Chemistry* **2012**, *22*, 14851-14855.

- [165] Zhu, C.; Guo, S.; Dong, S. *Advanced Materials* **2012**, *24*, 2326-2331.
- [166] Chang, Y.; Lye, M. L.; Zeng, H. C. *Langmuir* **2005**, *21*, 3746-3748.
- [167] Fan, H. J.; Gösele, U.; Zacharias, M. *Small* **2007**, *3*, 1660-1671.
- [168] Wang, J. X.; Ma, C.; Choi, Y.; Su, D.; Zhu, Y.; Liu, P.; Si, R.; Vukmirovic, M. B.; Zhang, Y.; Adzic, R. R. *Journal of the American Chemical Society* **2011**, *133*, 13551-13557.
- [169] Xia, X.; Wang, Y.; Ruditskiy, A.; Xia, Y. *Advanced Materials* **2013**, *25*, 6313-6333.
- [170] Gasteiger, H. A.; Markovic, N.; Ross, P. N.; Cairns, E. J. *Journal of Physical Chemistry* **1993**, *97*, 12020-12029.
- [171] Kinoshita, K.; Ross, P. N. *Journal of Electroanalytical Chemistry* **1977**, *78*, 313-318.
- [172] Schmidt, T. J.; Noeske, M.; Gasteiger, H. A.; Behm, R. J.; Britz, P.; Brijoux, W.; Bönnemann, H. *Langmuir* **1997**, *13*, 2591-2595.
- [173] Watanabe, M.; Uchida, M.; Motoo, S. *Journal of Electroanalytical Chemistry* **1987**, *229*, 395-406.
- [174] Chu, D.; Gilman, S. *Journal of the Electrochemical Society* **1996**, *143*, 1685-1690.
- [175] Lizcano-Valbuena, W. H.; Paganin, V. A.; Gonzalez, E. R. *Electrochimica Acta* **2002**, *47*, 3715-3722.
- [176] Mao, X.; Yang, L.; Yang, J.; Key, J.; Ji, S.; Wang, H.; Wang, R. *Journal of the Electrochemical Society* **2013**, *160*, H219-H223.
- [177] Taufany, F.; Pan, C.-J.; Lai, F.-J.; Chou, H.-L.; Sarma, L. S.; Rick, J.; Lin, J.-M.; Lee, J.-F.; Tang, M.-T.; Hwang, B.-J. *Chemistry-a European Journal* **2013**, *19*, 905-915.
- [178] Johansson, A.-C.; Larsen, J. V.; Verheijen, M. A.; Haugshøj, K. B.; Clausen, H. F.; Kessels, W. M. M.; Christensen, L. H.; Thomsen, E. V. *Journal of Catalysis* **2014**, *311*, 481-486.
- [179] Wittkopf, J. A.; Zheng, J.; Yan, Y. *ACS Catalysis* **2014**, *4*, 3145-3151.

- [180] Cohen, J. L.; Volpe, D. J.; Abruna, H. D. *Physical Chemistry Chemical Physics* **2007**, *9*, 49-77.
- [181] Takasu, Y.; Fujii, Y.; Matsuda, Y. *Bulletin of the Chemical Society of Japan* **1986**, *59*, 3973-3974.
- [182] Yahikozawa, K.; Fujii, Y.; Matsuda, Y.; Nishimura, K.; Takasu, Y. *Electrochimica Acta* **1991**, *36*, 973-978.
- [183] Kabbabi, A.; Gloaguen, F.; Andolfatto, F.; Durand, R. *Journal of Electroanalytical Chemistry* **1994**, *373*, 251-254.
- [184] Takasu, Y.; Iwazaki, T.; Sugimoto, W.; Murakami, Y. *Electrochemistry Communications* **2000**, *2*, 671-674.
- [185] Gasteiger, H. A.; Markovic, N.; Ross, P. N.; Cairns, E. J. *Journal of Physical Chemistry* **1994**, *98*, 617-625.
- [186] Hayden, B. E.; Murray, A. J.; Parsons, R.; Pegg, D. J. *Journal of Electroanalytical Chemistry* **1996**, *409*, 51-63.
- [187] Herrero, E.; Feliu, J. M.; Aldaz, A. *Journal of Electroanalytical Chemistry* **1994**, *368*, 101-108.
- [188] Lee, S. W.; Chen, S.; Sheng, W.; Yabuuchi, N.; Kim, Y.-T.; Mitani, T.; Vescovo, E.; Shao-Horn, Y. *Journal of the American Chemical Society* **2009**, *131*, 15669-15677.
- [189] Poh, C. K.; Tian, Z.; Gao, J.; Liu, Z.; Lin, J.; Feng, Y. P.; Su, F. *Journal of Materials Chemistry* **2012**, *22*, 13643-13652.
- [190] Wang, S.; Yang, F.; Jiang, S. P.; Chen, S.; Wang, X. *Electrochemistry Communications* **2010**, *12*, 1646-1649.
- [191] Hammer, B.; Nørskov, J. K. In *Advances in Catalysis*; Bruce C. Gates, H. K., Ed.; Academic Press: **2000**; Vol. 45, p 71-129.
- [192] St. John, S.; Atkinson, R. W.; Unocic, K. A.; Unocic, R. R.; Zawodzinski, T. A.; Papandrew, A. B. *ACS Catalysis* **2015**, 10.1021/acscatal.5b01432, 7015-7023.
- [193] Alia, S. M.; Pivovar, B. S.; Yan, Y. *Journal of the American Chemical Society* **2013**, *135*, 13473-13478.

- [194] Mund, K.; Richter, G.; Sturm, F. V. *Journal of The Electrochemical Society* **1977**, *124*, 1-6.
- [195] Kenjo, T. *Journal of The Electrochemical Society* **1985**, *132*, 383-386.
- [196] Shim, J.-P.; Park, Y.-S.; Lee, H.-K.; Lee, J.-S. *Journal of Power Sources* **1998**, *74*, 151-154.
- [197] Lu, S.; Pan, J.; Huang, A.; Zhuang, L.; Lu, J. *Proceedings of the National Academy of Sciences of the United States of America* **2008**, *105*, 20611-20614.
- [198] Cheng, X.; Shi, Z.; Glass, N.; Zhang, L.; Zhang, J.; Song, D.; Liu, Z.-S.; Wang, H.; Shen, J. *Journal of Power Sources* **2007**, *165*, 739-756.

## Appendix A

### ABBREVIATIONS AND IMPORTANT VARIABLES

PEMFCs	proton exchange membrane fuel cells
HEMFCs	hydroxide exchange membrane fuel cells
DMFCs	direct methanol fuel cells
MEA	membrane electrode assembly
HOR/HER	hydrogen oxidation/evolution reaction
MOR	methanol oxidation reaction
RDS	rate determining step
TS	Tafel slope
RDE	rotating disk electrode
CV	cyclic voltammogram
SEM	scanning electron microscopy
TEM	transmission electron microscopy
HRTEM	high resolution transmission electron microscopy
XRD	X-ray diffraction pattern
XPS	X-ray photonelectron microscopy
RHE	reversible hydrogen electrode
EIS	electrochemical impedance spectroscopy
OCV	open circuit voltage
HBE	hydrogen binding energy
ECSA	electrochemical active surface area

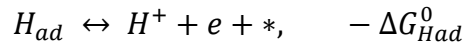
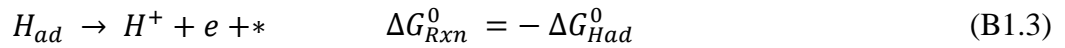
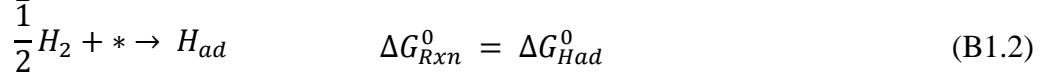
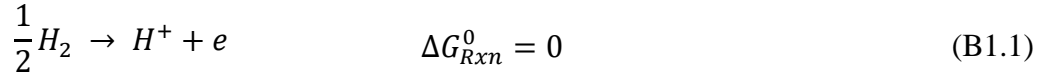
PZC	point of zero charge
$H_{\text{upd}}$	underpotential deposited hydrogen
$iR$	internal resistance
$i_k$	kinetic current (density)
$i_0$	exchange current (density)
$\alpha$	transfer coefficient
$\eta$	overpotential
$i_d$	diffusion current (density)
$i_l$	limiting current (density)
$\eta_d$	diffusion overpotetnial
$E_{\text{peak}}$	$H_{\text{upd}}$ desorption peak potentail
$E_a$	activation energy
F	Faraday constant (96,485 A·s/mol)
T	temperature
R	gas constant (8.314 J/(mol·K))

## Appendix B

### DERIVATION OF EQUATIONS

#### B.1 Derivation of HBE and $E_{\text{peak}}$ Relationship

The hydrogen oxidation reaction (Rxn. B1.1) consists of dissociative adsorption of  $H_2$  (Rxn. B1.2) and oxidation/desorption of  $H_{ad}$  to form  $H^+$  (Rxn. B1.3). Hydrogen-metal binding energy on metal surface (*HBE*) is defined by the enthalpy change ( $\Delta H_{Had}^0$ ) of Rxn B1.2 where  $\Delta H_{Had}^0 = \Delta G_{Had}^0 + T\Delta S_{Had}^0$ , with  $\Delta G_{Had}^0$  being the Gibbs energy change and  $\Delta S_{Had}^0$  the entropy change of Rxn. B1.2 at standard conditions ( $T = 298$  K,  $p_{H_2} = 1$  atm and  $a_{H_2} = 1$ ). Since the Gibbs energy change of Rxn B1.1 at standard conditions equals to 0, and Rxn B1.2 + Rxn B1.3 = Rxn B1.1, the Gibbs energy change of Rxn B1.3 is  $-\Delta G_{Had}^0$ .



At potential  $E_{SHE}$ ,  $\Delta G_{Had}^0(E_{SHE}) = \Delta G_{Had}^0 + FE_{SHE}$ , therefore,

$$K(E_{SHE}) = \frac{[H^+](1-\theta)}{\theta} = \exp\left(-\frac{\Delta G_{Had}^0(E_{SHE})}{RT}\right) = \exp\left(\frac{\Delta G_{Had}^0 + FE_{SHE}}{RT}\right)$$

$$\frac{\theta}{(1-\theta)} = [H^+] \exp\left(-\frac{\Delta G_{Had}^0}{RT}\right) \exp\left(-\frac{FE_{SHE}}{RT}\right) \quad (B1.4)$$

$$\text{Since } E_{RHE} = E_{SHE} - \frac{RT \ln[H^+]}{F}$$

$$\frac{\theta}{(1-\theta)} = \exp\left(-\frac{\Delta G_{Had}^0}{RT}\right) \exp\left(-\frac{FE_{RHE}}{RT}\right) \quad (\text{B1.5})$$

The relationship between hydrogen desorption current density and coverage is as follows:

$$i = -vQ \frac{d\theta}{dE} \quad (\text{B1.6})$$

where  $v$  is the scanning rate ( $dE/dt$ ),  $Q$  is the charge density of a fully covered surface assuming a monolayer adsorption.

At peak potential,  $i$  has a maximum value, so  $\frac{di}{dE} = 0$ ,

$$\frac{di}{dE} = -vQ \frac{d^2\theta}{dE^2} = 0 \text{ and } \frac{d^2i}{dE^2} < 0$$

$$E_{RHE} = -\frac{\Delta G_{Had}^0}{F} + \frac{RT}{F} \ln\left(\frac{1-\theta}{\theta}\right) \quad (\text{B1.7})$$

Frumkin isotherm assumes a linear variation of Gibbs free energy with surface coverage, the general relationship can be written as follows:

$$\Delta G_{Had}^0 = \Delta G_{Had,\theta=0}^0 + gRT\theta \quad (\text{B1.8})$$

where  $g$  is the dimensionless interaction parameter and it has negative values for attractive interactions and positive ones for repulsive interaction. Langmuir isotherm is a special case for Frumkin isotherm, in which the lateral interaction among adsorbates is negligible ( $g = 0$ ). From Eq. B1.7 and B1.8:

$$\frac{dE}{d\theta} = -\frac{RTg}{F} - \frac{RT}{F} \frac{1}{\theta(1-\theta)}$$

From Eq. B1.6:

$$i(E) = -vQ \frac{d\theta}{dE} = \frac{vQF}{RT} \frac{1}{g + 1/(\theta(1-\theta))}$$

Differentiate with respect to  $\theta$ :

$$\frac{di}{d\theta} = \frac{vQF}{RT} \frac{1 - 2\theta}{(g\theta(1 - \theta) + 1)^2}$$

At the maximum of cyclic voltammogram peaks,

$$\frac{di}{dE} = \frac{\frac{di}{d\theta}}{\frac{dE}{d\theta}} = \frac{\frac{vQF}{RT} \frac{1 - 2\theta}{(g\theta(1 - \theta) + 1)^2}}{-\frac{RTg}{F} - \frac{RT}{F} \frac{1}{\theta(1 - \theta)}} = -\frac{vQF^2 (1 - 2\theta)\theta(1 - \theta)}{R^2T^2 (g\theta(1 - \theta) + 1)^3} = 0$$

$$\theta = \frac{1}{2}$$

At the maximum of cyclic voltammogram peaks, the second derivative of  $i$  with respect to  $E$  should be negative,

$$\begin{aligned} \frac{d^2i}{dE^2} \Big|_{\theta=1/2} &= \frac{vQF^3 (g\theta(1 - \theta)(-2 + 6\theta - 6\theta^2) + (1 - 6\theta + 6\theta^2))\theta(1 - \theta)}{R^3T^3 (g\theta(1 - \theta) + 1)^5} \\ &= -\frac{vQF^3}{8R^3T^3 \left(\frac{g}{4} + 1\right)^4} < 0 \end{aligned}$$

$$\text{Thus, } \theta_{peak} = \frac{1}{2}$$

$$E_{peak,RHE} = -\frac{\Delta G_{Had,0=1/2}^0}{F} = -\frac{\Delta G_{Had,0=0}^0 + gRT/2}{F} \quad (\text{B1.9})$$

The change of entropy in Rxn B1.2 is

$$\Delta S_{Had}^0 = S_{Had} - S_* - \frac{1}{2}S_{H_2}^0 = -\frac{1}{2}S_{H_2}^0 \quad (\text{B1.10})$$

where  $S_{Had}$ ,  $S_*$ , and  $S_{H_2}^0$  are the entropy of adsorbed hydrogen, unoccupied sites and  $H_2$  in the gas phase at standard conditions ( $S_{H_2}^0 = 130.684 \text{ J}/(\text{mol. K})$ ), respectively. Since vibrational entropy of  $H_{ad}$  is negligible, and configurational entropies of the adsorbed hydrogen and unoccupied sites are identical, the total entropy of adsorbed hydrogen and unoccupied sites are the same ( $S_{Had} = S_*$ ), hence,  $\Delta S_{Had}^0 = -\frac{1}{2}S_{H_2}^0 = -65.342 \text{ J}/(\text{mol. K})$ .

Finally,

$$HBE = \Delta H_{Had}^0 = \Delta G_{Had, \theta=0}^0 + T\Delta S_{Had}^0 = -E_{peak, RHE}F - \frac{1}{2}gRT - \frac{1}{2}TS_{H_2}^0 \quad (B1.11)$$

For Langmuir adsorption,  $g = 0$

$$HBE = -E_{peak, RHE}F - \frac{1}{2}TS_{H_2}^0 \quad (B1.12)$$

Note that the HBE is commonly defined in surface science and computational literatures as

$$HBE = -\frac{1}{2}D_{H_2} + \Delta H_{Had}^0$$

where  $D_{H_2}$  is the dissociation energy of the  $H_2$  molecule ( $D_{H_2} = 436 \text{ kJ/mol}$ ). Thus, HBE is related to the peak potentials in CVs following expression below:

$$HBE = -\frac{1}{2}D_{H_2} - E_{peak, RHE}F - \frac{1}{2}TS_{H_2}^0 \quad (B1.13)$$

## B.2 Derivation of Exchange Current Density and $E_{peak}$ Relationship (Eq. 5.6)

The Arrhenius equation is as follows,

$$i_0 = K \exp\left(-\frac{E_a}{RT}\right) \quad (B2.1)$$

where  $i_0$  is the exchange current density,  $K$  is the pre-exponential parameter,  $E_a$  is the activation energy,  $R$  is the gas constant, and  $T$  is the temperature in Kelvin.

Brønsted-Evans-Polanyi principle states that the activation energy is proportional to the reaction enthalpy for reactions in the same family, more specifically:

$$E_a = E_0 + \beta\Delta H \quad (B2.2)$$

where  $E_0$  is the activation energy of a reaction in the same family,  $\Delta H$  is the enthalpy of reaction, and  $\beta$  is a proportionality coefficient that characterizes the position of transition state along the reaction coordinate ( $0 \leq \beta \leq 1$ ).

For HOR/HER ( $H_2 \leftrightarrow H^+ + 2e$ ), it consists of either a Tafel step ( $H_2 + 2 * \leftrightarrow 2H_{ad}$ ) or a Heyrovsky step ( $H_2 + * \leftrightarrow H_{ad} + H^+ + e$ ) followed by a Volmer step

( $H_{ad} \leftrightarrow H^+ + e + *$ ). If the Volmer step is the rate-determining step, the activation energy of HOR/HER is approximately the activation energy of the Volmer step,

$$E_a = E_{a,Volmer} = E_0 + \beta \Delta H_{H,desorption} \quad (B2.3)$$

It has been derived earlier[129] that

$$-\Delta H_{H,desorption} = \Delta H_{H,ads} = -FE_{peak} - \frac{1}{2}TS_{H_2}^0 \quad (B2.4)$$

where  $\Delta H_{H,desorption}$  is the enthalpy of H desorption,  $\Delta H_{H,ads}$  is the enthalpy of H adsorption,  $E_{peak}$  is the  $H_{upd}$  desorption peak potential,  $S_{H_2}^0$  is the standard entropy of  $H_2$ .

Hence,

$$E_a = E_0 + \beta(FE_{peak} + \frac{1}{2}TS_{H_2}^0) \quad (B2.5)$$

Substituting Eq. B2.5 into Eq. B2.1 yields,

$$i_0 = K \exp\left(-\frac{E_0 + \beta(FE_{peak} + \frac{1}{2}TS_{H_2}^0)}{RT}\right) = K \exp\left(-\frac{E_0 + \frac{1}{2}\beta TS_{H_2}^0}{RT}\right) \exp\left(-\frac{\beta FE_{peak}}{RT}\right)$$

$$\text{Let } A = K \exp\left(-\frac{E_0 + \frac{1}{2}\beta TS_{H_2}^0}{RT}\right)$$

$$i_0 = A \exp\left(-\frac{\beta FE_{peak}}{RT}\right) \quad (B2.6)$$

### B.3 Derivation of $\Delta E_a$ and $\Delta E_{peak}$ Relationship (Eq. 5.7)

If  $E_{a,1}$  and  $E_{a,2}$  are the activation energies of HOR/HER at pH1 and pH2, respectively, while  $E_{peak,1}$  and  $E_{peak,2}$  are the  $H_{upd}$  desorption peak potentials at pH1 and pH2, respectively, then according to Eq. B2.5,

$$E_{a,1} - E_{a,2} = \beta F(E_{peak,1} - E_{peak,2}) \quad (B3.1)$$

## Appendix C

### REPRINT PERMISSIONS

12/6/2015

Rightslink® by Copyright Clearance Center



RightsLink®

Home

Account  
Info

Help



**Title:** Correlating Hydrogen Oxidation/Evolution Reaction Activity with the Minority Weak Hydrogen-Binding Sites on Ir/C Catalysts

Logged in as:  
Jie Zheng

LOGOUT

**Author:** Jie Zheng, Zhongbin Zhuang, Bingjun Xu, et al

**Publication:** ACS Catalysis

**Publisher:** American Chemical Society

**Date:** Jul 1, 2015

Copyright © 2015, American Chemical Society

#### PERMISSION/LICENSE IS GRANTED FOR YOUR ORDER AT NO CHARGE

This type of permission/license, instead of the standard Terms & Conditions, is sent to you because no fee is being charged for your order. Please note the following:

- Permission is granted for your request in both print and electronic formats, and translations.
- If figures and/or tables were requested, they may be adapted or used in part.
- Please print this page for your records and send a copy of it to your publisher/graduate school.
- Appropriate credit for the requested material should be given as follows: "Reprinted (adapted) with permission from (COMPLETE REFERENCE CITATION). Copyright (YEAR) American Chemical Society." Insert appropriate information in place of the capitalized words.
- One-time permission is granted only for the use specified in your request. No additional uses are granted (such as derivative works or other editions). For any other uses, please submit a new request.

BACK

CLOSE WINDOW

Copyright © 2015 Copyright Clearance Center, Inc. All Rights Reserved. [Privacy statement](#). [Terms and Conditions](#).  
Comments? We would like to hear from you. E-mail us at [customercare@copyright.com](mailto:customercare@copyright.com)

**RightsLink®**[Home](#)[Account Info](#)[Help](#)**ACS Publications**  
Most Trusted. Most Cited. Most Read.**Title:** Platinum–Ruthenium Nanotubes and Platinum–Ruthenium Coated Copper Nanowires As Efficient Catalysts for Electro-Oxidation of MethanolLogged in as:  
Jie Zheng[LOGOUT](#)**Author:** Jie Zheng, David A. Cullen, Robert V. Forest, et al**Publication:** ACS Catalysis**Publisher:** American Chemical Society**Date:** Mar 1, 2015

Copyright © 2015, American Chemical Society

**PERMISSION/LICENSE IS GRANTED FOR YOUR ORDER AT NO CHARGE**

This type of permission/license, instead of the standard Terms & Conditions, is sent to you because no fee is being charged for your order. Please note the following:

- Permission is granted for your request in both print and electronic formats, and translations.
- If figures and/or tables were requested, they may be adapted or used in part.
- Please print this page for your records and send a copy of it to your publisher/graduate school.
- Appropriate credit for the requested material should be given as follows: "Reprinted (adapted) with permission from (COMPLETE REFERENCE CITATION). Copyright (YEAR) American Chemical Society." Insert appropriate information in place of the capitalized words.
- One-time permission is granted only for the use specified in your request. No additional uses are granted (such as derivative works or other editions). For any other uses, please submit a new request.

[BACK](#)[CLOSE WINDOW](#)

Copyright © 2015 [Copyright Clearance Center, Inc.](#) All Rights Reserved. [Privacy statement.](#) [Terms and Conditions.](#) Comments? We would like to hear from you. E-mail us at [customer-care@copyright.com](mailto:customer-care@copyright.com)

## **ECS Copyright and Permissions**

ECS does not hold the copyright on the Open access articles published in its journals. Please follow reuse instructions that correspond with the Creative Commons license on the paper.

Authors may use their own tables and figures in other scholarly research papers that they write, without writing to ECS for permission. Full credit to the original source should be given.

## **Guidelines for Use of Open Access Materials from ECS Publications**

ECS does not hold the copyright on the Open Access articles published in its journals. The copyright is held by the author(s). Please follow reuse instructions given by Creative Commons for its various licenses. ECS articles are published using either CC BY or CC BY-NC-ND licenses, here are links for more information:

CC BY: <http://creativecommons.org/licenses/by/4.0/>

CC BY-NC-ND: <http://creativecommons.org/licenses/by-nc-nd/4.0/>

Best Practices for Citing CC Licensed Articles:

[https://wiki.creativecommons.org/Best\\_practices\\_for\\_attribution](https://wiki.creativecommons.org/Best_practices_for_attribution)

The following paper was published in Journal of the Electrochemical Society as an open access article and was reproduced in Chapter 2 in this dissertation:

Zheng, J.; Yan, Y.; Xu, B. Correcting the Hydrogen Diffusion Limitation in Rotating Disk Electrode Measurements of Hydrogen Evolution Reaction Kinetics *Journal of The Electrochemical Society* **2015**, 162, F1470-F1481.